The imprint of the disc dispersal phase on the demographics of giant planets

Kristina Monsch

München 2021

The imprint of the disc dispersal phase on the demographics of giant planets

Kristina Monsch

Dissertation
der Fakultät für Physik
der Ludwig-Maximilians-Universität
München

vorgelegt von
Kristina Monsch
aus Landsberg am Lech

München, den 1. Juli 2021

Erstgutachterin: Prof. Dr. Barbara Ercolano
Zweitgutachterin: Prof. Dr. Paola Caselli
Tag der mündlichen Prüfung: 20. September 2021

Contents

List of Figures

List of Tables

Zusammenfassung

Jüngste Beobachtungsprogramme von Exoplaneten haben die Existenz einer beeindruckenden Vielfalt von Planetensystemen aufgezeigt. Dies wirft daher die Frage auf, wie Planetensysteme wie das Unsere entstehen und sich entwickeln können. Der Schlüssel zur Erklärung dieser Vielfalt liegt im Verständnis der statistischen Trends, die sich aus der jüngsten Fülle von Exoplanetendaten abzeichnen. Einer davon ist ein Peak in der Halbwertsachsenverteilung von Gasriesen, die sich bevorzugt bei Bahnradien von etwa 1–2 astronomischen Einheiten anhäufen. Es wurde kürzlich die Hypothese aufgestellt, dass dieses charakteristische Merkmal während der Zeit der Planetenmigration in der gasreichen protoplanetaren Scheibe entsteht, die durch die Auflösung der Scheibe mittels Röntgen-getriebener Photoevaporation gestoppt wird. In dieser Dissertation untersuche ich den Einfluss der Dispersionsphase der Scheibe auf den Migrationsprozess von Gasriesen, was zu einem besseren Verständnis ihrer beobachteten Demografie führt. Zu diesem Zweck habe ich mehrdimensionale, numerische Simulationen der Scheiben-Planeten-Wechselwirkung und eine als Planetenpopulationssynthese bekannte Methode verwendet. Anschließend untersuche ich, ob diese Wechselwirkung zwischen der Scheibendispersion und Planetenentwicklung einen möglichen Abdruck in der beobachteten Demografie von Gasriesen hinterlassen kann. Indem wir die beobachteten Röntgenleuchtkräfte von Sternen mit der Halbwertsachsenverteilung ihrer Gasriesen korrelieren, identifizieren wir ein auffälliges Merkmal, das auch qualitativ von unseren Simulationen vorhergesagt wird. Dies festigt daher unsere Anfangshypothese, dass Röntgen-Photoevaporation tatsächlich die Architektur von Planetensystemen prägt. Die Ergebnisse dieser umfangreichen Studie stellen wichtige Bedingungen für aktuelle Modelle der Planetenentstehung und -entwicklung dar und geben Orientierung für zukünftige Modelle, die eine genaue Behandlung der Dispersionsphase der protoplanetaren Scheibe berücksichtigen müssen.

Abstract

Recent exoplanet surveys have highlighted the existence of an impressive diversity of planetary systems, raising the question of how systems like our own can form and develop. The key to explaining their diversity lies in the understanding of the statistical trends that are now emerging from the recent wealth of exoplanet data. One of these trends is a peak in the semi-major axis distribution of gas giants that preferentially clump up at orbital radii of 1–2 astronomical units. It has recently been suggested that this characteristic feature may be established during the time of planetary migration. The migration of giant planets in the gas-rich protoplanetary disc is halted by disc dispersal via X-ray driven photoevaporation. In this thesis I aim at studying the impact of the disc dispersal phase on the migration process of gas giants, leading to a better understanding of their observed demographics. For this purpose, I have used multi-dimensional numerical simulations of disc-planet interactions and a method known as planet population synthesis. I am then investigating if this interaction between disc dispersal and planet evolution can leave any potential diagnostics in the observed demographics of giant planets. By correlating the observed X-ray luminosities of giant planet host stars with the semi-major axis distribution of their giant planets, we find a prominent feature that is also predicted qualitatively by our simulations, further strengthening the conclusion that X-ray-driven photoevaporation is indeed shaping the architecture of planetary systems. The results obtained from this extensive study pose important limitations on current models of planet formation and evolution and provide guidance for future models that need to take an accurate treatment of the disc dispersal phase into account.

Chapter 1

Introduction

The field of the discovery and characterisation of extrasolar planets, the so-called *exoplanets*, is one of the great frontiers of modern astrophysics and it has gained dramatically in importance during the last 20 years. Understanding how planetary systems, such as our own, have formed is crucial to answering the probably most fundamental question to humankind – what are the origins of life and are we alone in the Universe?

While only a handful of planets outside of our Solar System were known in the early 2000s, this number has recently increased almost exponentially thanks to dedicated missions to their discovery. This is illustrated in Figure 1.1, which shows the cumulative number of detected and confirmed exoplanets as a function of time. The bars are colour-coded based on the detection technique that was used for their discovery. The most important ones are the radial velocity and transit method, while all remaining methods are summarised as 'Other' (see Chapter 5, for details). As of May 2021, there are more than 4353 confirmed exoplanets[1] and this number is expected to continue rising steadily. This wealth of observations finally enables astrophysicists to perform statistical analyses and tests and look for correlations and trends within the underlying data. As it is expected that the initial conditions and physical processes at play during the early phases of planetary systems should be imprinted in the distribution of exoplanets that is observed today, the observed demographics of exoplanets set important constraints on planetary formation and evolution models. Therefore, confronting the outcomes of theoretical models with the actual exoplanet data is crucial in order for testing and benchmarking our understanding of the underlying processes.

A prominent trend in the exoplanet demographics is that gas giants[2] are not distributed homogeneously along the semi-major axis plane, but pile up at given locations. This can be inferred from the left panel of Figure 1.2, which shows the mass distribution of giant planets

[1] Source: NASA Exoplanet Archive, accessed on May 13, 2021.

[2] Gas giants are giant planet mainly composed of hydrogen and helium and are tens to thousands of times as massive as Earth (D'Angelo & Lissauer, 2018). While the so-called ice giants like Uranus and Neptune technically also correspond to giant planets, in the framework of this thesis, the term 'giant planet' will only refer to gas giants.

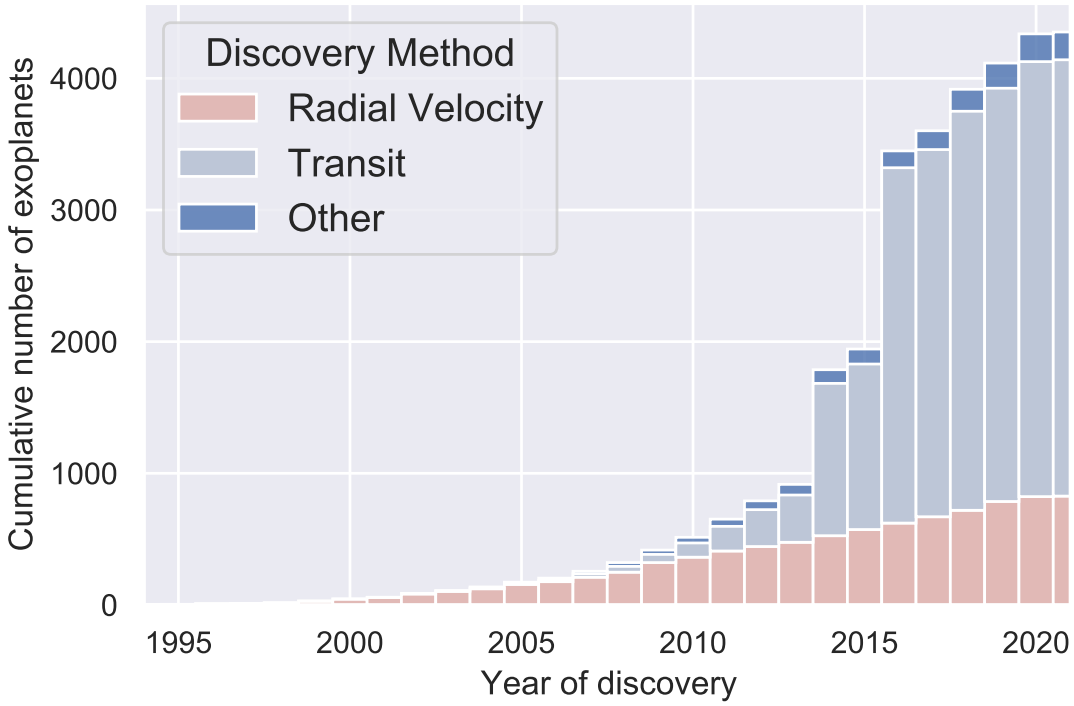

Figure 1.1: Cumulative number of exoplanets as a function of time. The differently coloured bars correspond to exoplanets detected via the radial velocity method (red), the transit method (light blue) or other techniques (dark blue). The data that was used for this diagram was taken from the NASA Exoplanet Archive.

with masses greater than 0.1 Jupiter masses[3] as a function of the distance to their host star. Three different giant planet populations can be identified from Figure 1.2 – firstly, the so-called hot Jupiters, which are orbiting their host star at distances smaller than Mercury's orbit (i.e. $\lesssim 0.1$ astronomical units[4]). Secondly, warm Jupiters, which pile up between distances of $\sim$ 1–5 au. And finally the cold Jupiters, which are located in the outermost regions of their planetary systems ($>$ 5–10 au). For comparison, also the locations of Jupiter and Saturn are overplotted, and it can be seen that they fall into the relatively empty part of parameter space. Thus, it becomes immediately apparent that already the giant planets within our own Solar System would be relatively difficult to detect with current facilities if they were exoplanets. However, future telescopes like the *James Webb* Space Telescope (JWST) or the *Nancy Grace Roman* Space Telescope (*Roman*, formerly known as WFIRST), which allow detections of gravitational microlensing events or gathering long-term spectroscopic data, are expected to extend our census of known exoplanets within this empty part of parameter space immensely, ultimately aiding in answering the question of how common planetary systems such as our own are.

If the distribution that is shown in the left panel of Figure 1.2 is collapsed into a histogram along the semi-major axis plane, it can be inferred that the resulting distribution of giant planets is not smooth but shows mountains and deserts, i.e. regions of over- and underpopulation. This

[3] *Jupiter mass*, $1\,M_\mathrm{J} = 1.898 \times 10^{27}$ kg (Williams, 2019)
[4] *Astronomical unit*, $1\,\mathrm{au} = 1.496 \times 10^{8}$ km $\equiv$ distance between Sun and Earth (Williams, 2019)

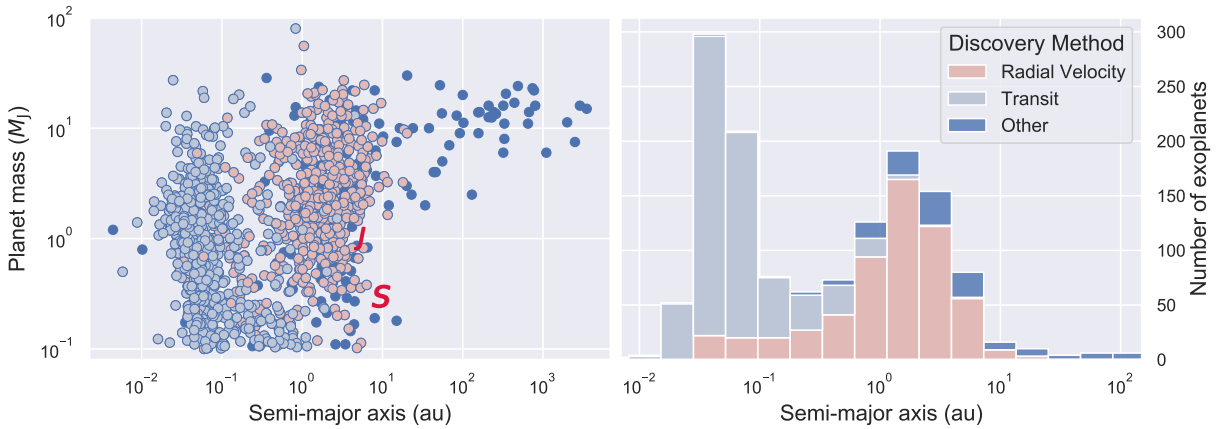

Figure 1.2: Demographics of giant planets detected via radial velocity (red), transit (light blue) and other methods (dark blue). *Left panel:* Planetary mass vs. semi-major axis distribution of confirmed giant planets with $M_p \geq 0.1\,M_J$. The letters 'J' and 'S' mark the positions of Jupiter and Saturn in this diagram. *Right panel:* Corresponding histogram for the semi-major axis distribution of these giant planets.

suggests that the giant planet formation efficiency is either different throughout the planet-forming disc, resulting in corresponding 'sweet spots' for planet formation, or that planets form in the outermost parts of the disc and get parked at given locations as they migrate inwards. The truth likely lies in a combination of both.

While the origin of hot Jupiters is still matter of debate (cf. Dawson & Johnson, 2018, for a review), it has been suggested that the pile-up of warm Jupiters, roughly located at 1–2 au, could potentially be caused by disc dispersal via internal photoevaporation, driven by highly energetic photons that are emitted by the host star. As this radiation starts clearing the disc, it opens an annular gas-free cavity that cuts off the inner disc from further mass supply by the outer disc. Planets that are located inside of this annular gap can continue migrating inwards and are either engulfed by their host star or potentially end up as hot Jupiters. At the same time, planets that are located outside the gap also migrate inwards, however they are at the latest parked once they reach the photoevaporative gap. Disc dispersal via internal photoevaporation can therefore naturally provide a parking radius for inward migrating giant planets.

This concept was confirmed theoretically with numerical simulations performed by Alexander & Pascucci (2012), who examined the irradiation of the disc by extreme ultraviolet photons. Their work was later extended by Ercolano & Rosotti (2015), who added more energetic X-ray photons to their models, as updated radiation-hydrodynamical models performed by Owen et al. (2010, 2011a, 2012) showed that X-ray-driven, photoevaporative winds are expected to dominate the total mass loss during the late stages of disc evolution. Both models were successful in reproducing the observed peak of giant planets near $\sim$ 1–2 au, however, in the case of X-ray photoevaporation, this feature was even more prominent as due to the increased mass loss rates and the more extended radial mass loss profile, more planets could be parked at larger radii. These results highlighted the importance of the photoevaporation process on shaping the orbital distribution of giant planets and thus motivated further work on investigating if an unambiguous imprint of this process may be observable in the semi-major axis versus host

star X-ray luminosity plane of gas giants. If such a characteristic feature was to be found, this would provide direct evidence for X-ray photoevaporation sculpting the observed exoplanet demographics.

Structure of this thesis

The goal of my dissertation is to identify potential observational diagnostics of X-ray-driven photoevaporation in the observed semi-major axis distribution of giant planets using numerical simulations of disc-planet interactions and find possible signatures of this process within the observational exoplanet data. The chapters 2 to 5 will provide the necessary theoretical framework for this study. Chapter 6 then describes the assembly of an observational catalogue that gathers X-ray data of giant planet host stars, which can be used to identify a possible imprint of disc dispersal within the giant planet distribution. Chapter 7 investigates in detail how the migration process of giant planets during the disc dispersal phase is affected by X-ray-driven photoevaporation. Chapter 8 shows the effect of X-ray-driven photoevaporation on a given population of giant planets and identifies how an imprint of this process may look like in an observed sample. Finally, Chapter 9 discusses how these planet formation and evolution models can be improved in the near future in order to find robust evidence for X-ray photoevaporation shaping giant planet demographics.

Chapter 2

From molecular clouds to stars and planets

Already in the 18th century, philosophers like Immanuel Kant or Pierre-Simon Laplace suspected that the Solar System must have formed from a dusty and gaseous disc orbiting the young Sun (Garcia, 2011). The existence of circumstellar discs had therefore been postulated long before their first observational evidence in the 1990s. Modern astronomy has taken a leap since then and thanks to the advent of infrared (IR) and (sub-)millimeter (mm) astronomy, it has become possible to not only directly observe the formation of stars in dense, molecular clouds, but also the formation of planetary systems orbiting these stars. These regions are inaccessible to observations in the optical wavelength bands due the high concentration of dust and molecular gas that absorb most of the visible light coming from the embedded protostars. While the dust component makes up only $\sim 1\,\%$ of the total mass budget of interstellar gas, it dominates the opacity of dense gas, as the dust grains absorb the stellar radiation very efficiently and re-emit it at longer wavelengths (Garcia, 2011). Therefore, the dust component can be easily studied in the IR and (sub-)mm bands, but also observing molecular emission in the gaseous component with high accuracy has become feasible thanks to facilities like the Very Large Array (VLA) or the Atacama Large Millimeter/Submillimeter Array (ALMA).

Even though the exact details of the star formation process are far from being fully understood, there is a strong consensus on the general picture. Figure 2.1 shows a simple cartoon of the distinct phases of the formation process of stars, their surrounding discs and for mation of planetary systems, which in their entirety, cover more than 12 orders of magnitude, both in mass and size (e.g., Shu et al., 1987). The following chapter will step-by-step describe these different evolutionary stages.

2.1 The formation of stars

Stars form in cold and dense cores embedded in giant molecular clouds within the interstellar medium (ISM, see e.g., Evans, 1999, for a review). It is observationally established that all

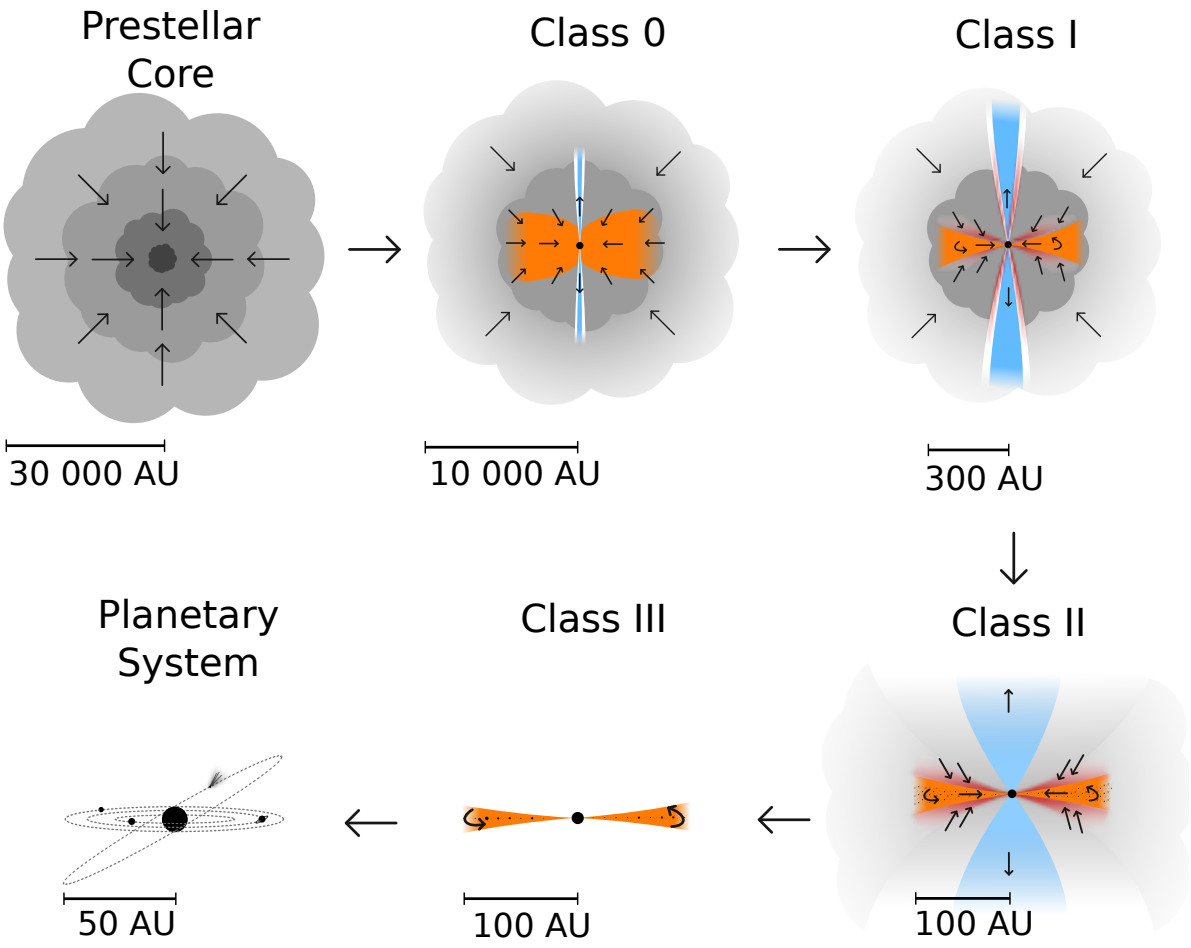

Figure 2.1: Cartoon of the different evolutionary stages of the star formation process. Image credit: Persson (2014)

star forming regions are slowly rotating, implying that they must carry a large amount of angular momentum given their immense sizes of a few parsecs (e.g., Goodman et al., 1993; Burkert & Bodenheimer, 2000). Unperturbed interstellar clouds are assumed to be in the state of hydrostatic equilibrium and thus can be considered to obey the virial theorem, which describes the relation between the potential and kinetic energy of a system of particles at thermal equilibrium: $E_{\rm kin} = -1/2\, E_{\rm pot}$.

Once the mass of a cloud exceeds the local Jeans mass (Jeans, 1902):

$$M > M_{\rm Jeans} = \left(\frac{5kT}{G\mu m_{\rm H}}\right)^{3/2} \left(\frac{3}{4\pi\rho}\right)^{1/2}, \tag{2.1}$$

its gravitational energy will exceed its thermal energy, so that the gas pressure is insufficient to support the cloud against gravitational collapse under its own self-gravity. The Jeans criterion

therefore describes under what physical conditions this collapse is initiated for a cloud of given temperature T, mass M and radius r (or density $\rho = M/r^3$), where k is the Boltzmann constant, G the gravitational constant, μ the mean molecular weight of the gas and m_{H} is the mass of the hydrogen atom (assuming that the bulk of gas within the cool ISM constitutes of molecular hydrogen). For typical conditions within molecular clouds, the Jeans mass typically ranges between 10^3-10^4 solar masses[5]. It immediately follows from Eq. 2.1 that the cooler and denser the gas, the less massive a cloud has to be in order to become gravitationally unstable.

During the collapse of the slowly rotating cloud core, the gas is compressed and starts heating up, as the released potential energy is partly transformed into kinetic energy of the gas particles (panel 1 of Figure 2.1). This increase in gas density and temperature would prevent any further collapse of the cloud core due to the growing thermal pressure that acts against the gravitational contraction, until ultimately hydrostatic equilibrium would be reached again (LeBlanc, 2010). However, as the gas can cool efficiently through the emission of IR radiation (which is, for example, produced by inelastic collisions of the gas molecules), lower masses for dense clumps within the molecular cloud can suffice in order for them to exceed the local Jeans mass and therefore also start collapsing gravitationally. This way, the molecular cloud can form a cascade of fragments with masses ranging between 0.1–100 $M_\odot$ that will later form stars (e.g., Matsumoto & Hanawa, 2003). The process of star formation is therefore the result of a fine balance between heating and cooling of the gas, which ultimately regulates the gravitational collapse of a giant molecular cloud.

With ongoing contraction, the density in the central regions of the fragments start increasing such, that these regions become opaque to thermal radiation. The collapsing core is then unable to sustain its efficient cooling through the emission of IR radiation, so that the temperatures in the central regions of the core start increasing again. The growing thermal pressure prevents any further gravitational collapse and fragmentation of the molecular cloud, as it has reached hydrostatic equilibrium again. The lowest angular momentum material from the rotating, collapsing cloud core falls towards the center (e.g., Terebey et al., 1984; Yorke et al., 1993) and a protostar embedded in a massive, infalling envelope of gas and dust is formed (panel 2 in Figure 2.1). The remaining material with higher angular momentum forms a circumstellar accretion disc, which will surround the young protostar during the first few million years of its lifetime (panel 3 and 4 in Figure 2.1). At this point, the disc contains only a fraction of the central star's mass, thereby transitioning from a protostellar to a so-called protoplanetary disc.

The massive envelope surrounding the protostar is optically thick to visible and IR radiation, and therefore, such objects can only be observed at far-IR (fIR, $\lambda \sim 25$–$350\,\mu$m, NASA/IPAC 2012), mm or even cm wavelengths (Garcia, 2011). After about ~ 0.5 Myr (Evans et al., 2009), the envelope is depleted and the young star with a surrounding disc is revealed, which can be either observed through its (sub-)mm emission, which traces the cold dust in the outskirts of the circumstellar disc (~ 100 au), or its near-IR (nIR, $\lambda \sim 0.7$–$5\,\mu$m) to mid-IR (mIR, $\lambda \sim 5$–$25\,\mu$m) emission that is sensitive to the warmer dust close to the star. Consequently, most of what we know about accretion discs surrounding young stars concerns the dust grains, but observations of the gas component using the UV-range can further provide important information on processes

[5] *Solar mass*, $1\,M_\odot = 1.988 \times 10^{30}$ kg

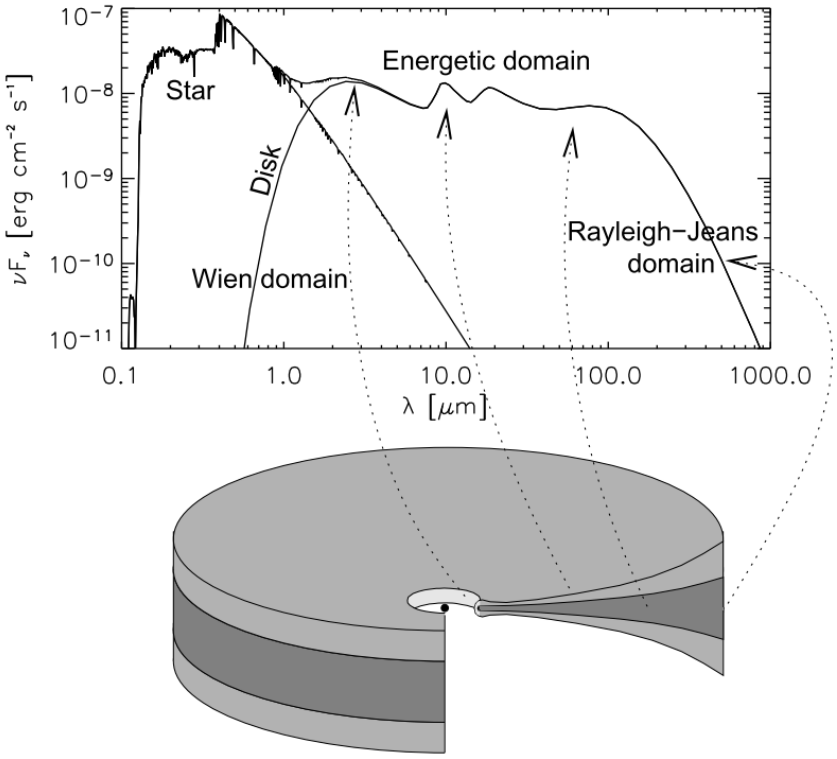

Figure 2.2: Build-up of a typical Class II spectral energy distribution (SED) of a flaring protoplanetary disc and the origin of various components. The SED of a young stellar object (YSO) can be interpreted as the superposition of the emission coming from a 'naked stellar photosphere plus the excess emission of the circumstellar material. Typically the near- and mid-infrared emission arises from small radii, while the far-infrared comes from the outer disc regions. The (sub-)millimeter emission mostly arises from the midplane of the outer disc. Image adapted from Dullemond et al. (2007) with permission by University of Arizona Press.

such as accretion or outflows that have a significant impact on shaping the innermost regions of the disc.

Even though the young star has acquired most of its final mass at this point, its internal temperatures are not yet high enough in order to initiate the nuclear fusion of hydrogen to helium in its core. Due to the missing radiation pressure, the star can therefore continue its contraction, which in turn increases the density and temperature in its core such that at some point hydrogen burning can be initiated, if the initial mass of the protostar is high enough. With the onset of nuclear fusion in the stellar interior, the star finally reaches the so-called zero-age main sequence (ZAMS), which is often referred to as the birth line of a star. At this point the star formation process is fully finished.

2.2 Young stellar objects and pre-main sequence stars

Young stellar objects (YSOs) are proto- and pre-main sequence (PMS) stars whose internal temperatures are not yet high enough in order to initiate hydrogen burning within the stellar core. They are therefore not located on the main sequence within the so-called Hertzsprung-Russel-diagram (HRD)[6]. While all main sequence stars burn hydrogen to helium in their cores via nuclear fusion, YSOs sustain their energy-levels mostly through gravitational contraction and Deuterium, as well as Lithium burning (LeBlanc, 2010). Depending on their mass, PMS stars are categorised into T Tauri and Herbig Ae/Be stars. While the former have masses between $0.07 < M_\star < 2\,M_\odot$ (i.e. spectral types M, K, G, and F), the latter have masses between 2–8 $M_\odot$. Young brown dwarfs are technically also YSOs, though their masses are below the hydrogen burning limit of $M_\star \lesssim 0.07\,M_\odot$, which is too low for the core to ever reach high enough central temperatures to initiate hydrogen burning (Stahler & Palla, 2004; Garcia, 2011, but see also Forbes & Loeb 2019).

Another important characteristic of low-mass YSOs is the presence of strong Lithium-emission coming from their photospheres, which produces an absorption line at 670.8 nm (e.g., Bildsten et al., 1997; Jeffries & Oliveira, 2005). The presence of Lithium within the stellar spectrum is highly sensitive to the mass and central temperatures of the PMS star, as it is converted to helium once they reach a critical temperature of $2.5\text{–}3 \times 10^6$ Kelvin (Bodenheimer, 1965; Skumanich, 1972)[7]. After the onset of hydrogen burning, however, this line can barely be traced anymore, which is the reason why it is generally taken as a sign of stellar youth, therefore being a very useful indicator of PMS stars (e.g., Mentuch et al., 2008; Manara et al., 2013).

Next to the strength of emission lines in their spectrum, young PMS stars are traditionally classified by the slope of their spectral energy distribution (SED) in the IR wavelength regime, the so-called spectral index α_{IR}, which was initially introduced by Lada & Wilking (1984) and first applied by Lada (1987):

$$\alpha_{\mathrm{IR}} \equiv \frac{\mathrm{d}\log(\lambda F_\lambda)}{\mathrm{d}\log(\lambda)} = \frac{\mathrm{d}\log(\nu F_\nu)}{\mathrm{d}\log(\nu)}. \tag{2.2}$$

Here, F_λ is the flux density measured at wavelength λ and Eq. 2.2 is usually equated between $\sim$ 2.2 µm and $\sim$ 25 µm, i.e. between the near- and mid-IR region of the stellar spectrum (Armitage, 2013; Garcia, 2011). The SED of a YSO is the superposition of the emission coming from the pure stellar photosphere and the so-called IR excess emission, which is a robust indicator for the presence of circumstellar material (e.g., Chiang & Goldreich, 1997). As previously mentioned in Section 2.1, nIR and mIR emission of YSOs typically stems from hot dust emission at small disc radii, while the fIR traces the cooler dust emission coming from the outer disc regions. (Sub-)mm emission mostly arises from the cool dust in the outermost

[6] The Hertzsprung-Russel-diagram describes a diagram in which the stellar luminosities/absolute magnitudes of a range of different stars are plotted against their corresponding effective temperature/spectral type. The majority of the stellar population is located on the so-called main sequence, on which they spend most of their lifetime.

[7] *Kelvin*, $1\,\mathrm{K} = -272.15^\circ\mathrm{C}$

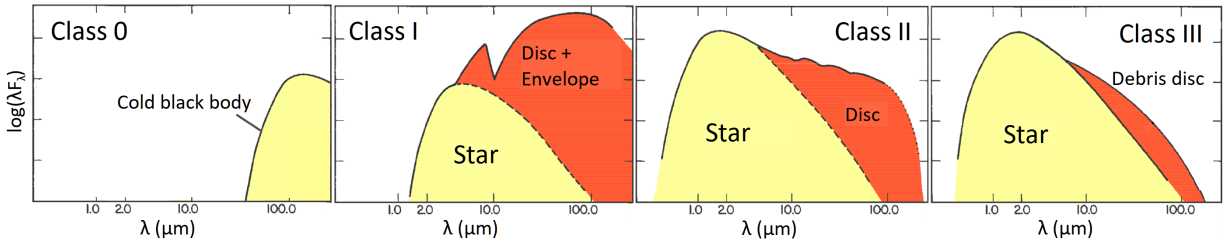

Figure 2.3: Classification of YSOs into Class 0–III based on their SED. The solid lines show the observed SED of the corresponding YSO that contains the emission of both the star (yellow area) and the disc (orange area), while the dashed lines represent the expected emission that would arise from the same central star without a disc. Figure adapted from Lada (1987).

disc regions that has settled towards the mid plane. Thus, the overall SED of a YSO that is surrounded by a circumstellar disc should basically resemble that of a stretched blackbody, where each disc annulus radiates as a blackbody with a different local temperature.

Figure 2.2 shows the structure of a typical Class II SED for a flaring protoplanetary disc and how different features of the spectrum are related to certain regions within the disc. The dust surrounding the disc absorbs the infalling stellar radiation and re-emits it at longer wavelengths. Thus a redder SED (i.e. an SED with stronger emission at longer wavelengths) is broadly associated with the presence of a higher amount of circumstellar dust (Alexander et al., 2014). The corresponding SED shapes that are used for the empirical classification scheme based on the spectral index are illustrated in Figure 2.3. The solid lines circumcise an illustrative observed SED of a YSO, which is the superposition of the emission coming from the star-disc system, while the yellow-shaded region reflects the expected emission that would arise from the photosphere of a disc-less central star ('naked photosphere').

Class 0 Class 0 objects do not show any optical and near/mid-IR excess within their SED, but have strong fIR to (sub-)mm emission. They are neither proto- nor PMS stars, as they correspond to embedded objects at the earliest evolutionary phases (i.e. $M_{\rm env} > M_\star > M_{\rm d}$)[8], namely at the onset of gravitational collapse within the giant molecular cloud (e.g., Andre et al., 1993). Their emission therefore basically corresponds to that of a cold black body.

Class I Stars with $\alpha_{\rm IR} \gtrsim 0.3$ (Greene et al., 1994) are so-called Class I objects and correspond to accreting protostars that are still embedded in a massive, infalling envelope ($M_\star > M_{\rm env} \sim M_{\rm d}$). During this phase, the protostar accretes most of its final mass (Apai & Lauretta, 2010).

Class II Class II objects ($M_{\rm d}/M_\star \sim 1\,\%$), show strong IR excess emission with $-1.6 < \alpha_{\rm IR} < -0.3$ and are also known as Classical T Tauri stars (CTTS), even though their definition is based on different properties. While CTTSs are technically defined by their Hα equivalent width that is an accretion signature, it has been

[8] $M_{\rm env}$: envelope mass; $M_\star$: mass of the central star; $M_{\rm d}$: disc mass

observed that it correlates well with the presence of nIR excess emission (Armitage, 2007a) and thus both expressions can be more or less used interchangeably. Class II objects show bright emission lines such as Hα[9], indicative of strong accretion shocks that are the result of gas free-falling onto the stellar surface via magnetically mediated accretion funnels (e.g., Herbig & Bell, 1988; White & Basri, 2003; Muzerolle et al., 2000), therefore causing the high mass-accretion rates of $\sim 10^{-8}\,M_{\odot}\,\mathrm{yr}^{-1}$ observed for young stars (Gullbring et al., 1998; Hartmann et al., 1998). These are also the phases at which giant planet formation is thought to occur as a result from the large reservoirs of gas that should be still present in the disc.

Class III Class III objects are YSOs with $\alpha_{\mathrm{IR}} < -1.6$ that have dissipated most of their surrounding disc ($M_{\mathrm{d}}/M_{\star} \ll 1\,\%$) and consequently lack any significant accretion signatures in the stellar spectrum (Stahler & Palla, 2004). They are usually equated with so-called weak-lined T Tauri stars (WTTS), due to the weak presence of Hα emission. The resulting SED of a Class III objects effectively resembles that of a pure stellar photosphere, with only a small contribution of a so-called debris disc, which is thought to be the last remnant of a circumstellar disc around a YSO. Its opacity is most likely dominated by second-generation dust produced by the collision of planetesimals (cf. Wyatt, 2008; Williams & Cieza, 2011, for reviews).

The classification scheme based on the spectral index therefore reflects the different evolutionary stages of a protostar (e.g., Adams et al., 1987; Lada, 1987; Andre & Montmerle, 1994; Kenyon & Hartmann, 1995), and correspond to panels 2–5 in Figure 2.1. The SEDs of young stars provide an extremely powerful tool for characterising star-disc systems as the shape of the SED is highly sensitive on the underlying disc structure. By allowing measurements of the disc masses, accretion rates and the temperature structure of the disc, SEDs spanning different wavelength-bands provide important constraints for theoretical models of disc evolution.

It should be added though that inclination effects have a strong impact on the resulting shape of the SED, and consequently a classification based solely on the SED may lead to erroneous conclusions. For example, Robitaille et al. (2006) found that Class II YSOs viewed at high inclinations show similar SEDs to typical Class I YSOs, while an edge-on Class I SED may show strong resemble to a Class 0 YSO (Williams & Cieza, 2011). Thus, YSOs with edge-on discs may be mistaken with highly embedded, and consequently less evolved objects, highlighting the necessity of observing young stars in multiple wavelength bands besides the IR/(sub-)mm regime, in order to fully characterise the evolutionary state of a YSO. Such an additional diagnostic could be, for example, the X-ray emission of PMS stars, which has been shown to be a robust tracer of stellar youth. This will be described in more detail in the next section.

[9]The Hα line is an absorption line of the Balmer series at 6563 Å. It arises from the transition of an excited hydrogen electron from its third lowest to its second lowest energy level (Stahler & Palla, 2004).

2.3 X-ray emission of young stars

All kinds of stars across the Hertzsprung-Russell-diagram (HRD) are known to emit at least some fraction of their total bolometric luminosity as highly energetic X-ray emission ($h\nu \approx$ 0.1–10 keV), and there is no indication for the existence of an X-ray quiet population of stars with suppressed magnetic activity (e.g., Preibisch et al., 2005). Hence understanding the processes that drive the emergence and evolution of stellar X-ray emission is crucial, not only for the study of young stars, but especially for understanding how these are impacting their surrounding circumstellar discs that ultimately harbour nascent planets. The next section will briefly summarise current knowledge and observational constraints on the X-ray emission of young, PMS stars and how it evolves over time.

Observational constraints

Helioseismological measurements[10] starting in the 1960s enabled scientists not only to study the solar structure, but also the origin of several phenomena, such as solar spots and the solar magnetic activity (e.g., Leighton et al., 1962; Ulrich, 1970; Leibacher & Stein, 1971). Even though the Sun's immediate proximity allows us to test our models of stellar structure at high precision, the origin of stellar X-rays, especially those of young stars, is far from being fully understood. Satellites like ROSAT (short for **Ro**entgen**sat**ellit), *XMM-Newton* or the *Chandra* X-ray Observatory have shed light into this field and enable us to study the magnetic activity of PMS stars through their X-ray emission.

The relative output of X-ray emission from low-mass stars compared to their total bolometric luminosity $L_{\rm bol}$ (i.e. integrated over all wavelengths of the stellar spectrum) typically ranges between $L_{\rm x}/L_{\rm bol} \approx 10^{-8}$–$10^{-3}$, with older stars showing the lowest levels of X-ray activity (e.g., Feigelson et al., 2004; Schmitt & Liefke, 2004; Telleschi et al., 2007; Wright et al., 2010). In contrast, YSOs in all evolutionary stages, from protostellar to PMS, typically emit a much higher fraction of their bolometric luminosity in X-rays, with X-ray luminosities ranging from $28 \lesssim \log(L_{\rm x}/{\rm erg\,s^{-1}}) \lesssim 32$ between $h\nu \approx 0.5$–8 keV (e.g., Preibisch et al., 2005; Güdel et al., 2007). Compared to the solar output of $26 < \log(L_{\rm x}/{\rm erg\,s^{-1}}) < 27$ within the same spectral band (with occasional flares reaching up to $\log(L_{\rm x}/{\rm erg\,s^{-1}}) \approx 28$), young stars, which have not reached the main sequence yet, generally show highly elevated X-ray levels compared to their main sequence counterparts (Feigelson et al., 2007). The decrease in X-ray luminosity of several orders of magnitude between the zero-age main sequence (ZAMS) and the solar age have made X-ray observations a commonly used tool to efficiently discriminate between young and typically older galactic field stars (e.g., Getman et al., 2005; Wright & Drake, 2009; Wright et al., 2011).

An advantage of this method is that X-ray emission is equally sensitive towards stars with and without circumstellar material, therefore avoiding the bias that is introduced when samples of stars are solely selected based on their nIR excess (Preibisch et al., 2011). Due to the high

[10] Helioseismology is the study of the internal structure and dynamics of the Sun through propagating sound waves that cause the Sun to oscillate.

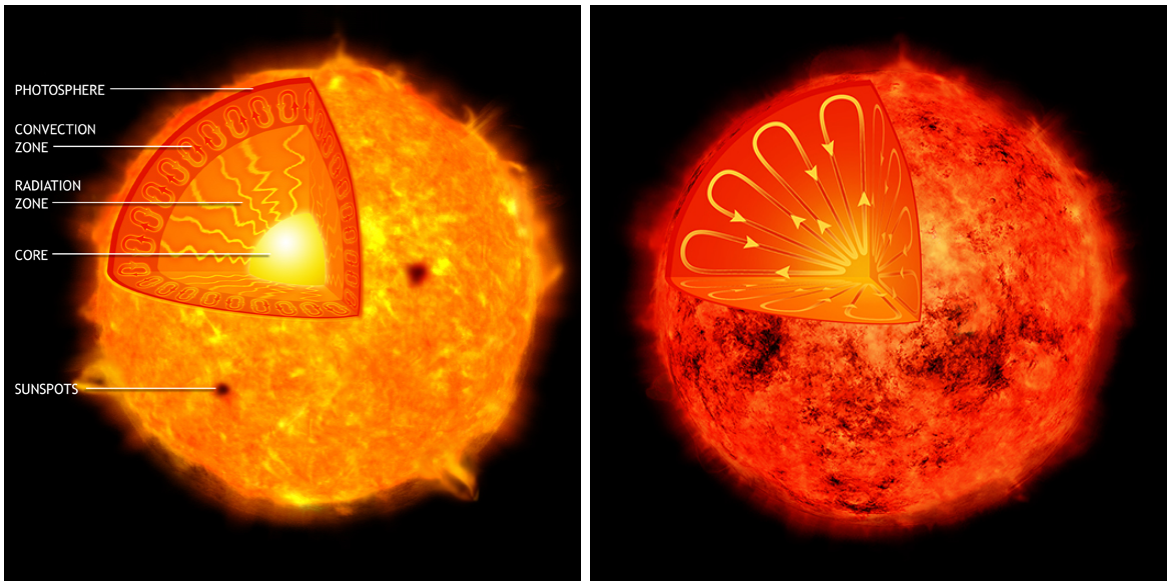

Figure 2.4: Schematic structure of a partly convective (left panel) and a fully-convective (right panel) star. Image Credit: NASA/CXC/M.Weiss

photon-energies, X-ray radiation is much less affected by absorption through interstellar hydrogen than optical light, and can therefore penetrate interstellar clouds to very high extinctions of up to $A_v \approx 500$ mag (Feigelson et al., 2007). In contrast, the nIR emission of YSOs traces the warm and hot dust in the inner regions of their circumstellar discs, resulting in an excess of IR emission in their SED between $\sim$ 1–10 µm (Apai & Lauretta, 2010). Because this emission is characteristic for young stars bearing circumstellar discs, it cannot be used to trace older stars that have already dissipated their surrounding material. Nevertheless, objects like evolved Be stars, planetary nebulae or active galactic nuclei (AGN) can show very similar nIR-excess to those of young stars, hence possibly contaminating samples selected solely based on this excess emission (e.g., Mentuch et al., 2009; Oliveira et al., 2009; Rebull et al., 2010). Using X-ray emission as an additional tracer of young stars has therefore proven to be a very successful tool (e.g., Preibisch & Zinnecker, 2002; Broos et al., 2007; Forbrich et al., 2007; Wang et al., 2011), especially as extended surveys, such as the *Chandra* Orion Ultradeep Project (COUP, cf. Getman et al., 2005), or the *XMM-Newton* Extended Survey of Taurus (XEST, cf. Güdel et al., 2007) have mapped entire star-forming regions in X-rays. By establishing basic relations between stellar properties and their X-ray emission, these surveys offer an extremely comprehensive view of the X-ray properties from the PMS stellar population.

Origin of the stellar X-Ray emission

The X-ray emission of solar- and late-type stars with spectral types ranging from F to M arises from a magnetically confined plasma at temperatures of several million Kelvins, which is known as corona (Vaiana et al., 1981). This coronal X-ray emission, as well as chromospheric Ca II or Hα emission, have been shown to be a reliable proxy of stellar magnetic activity (e.g.,

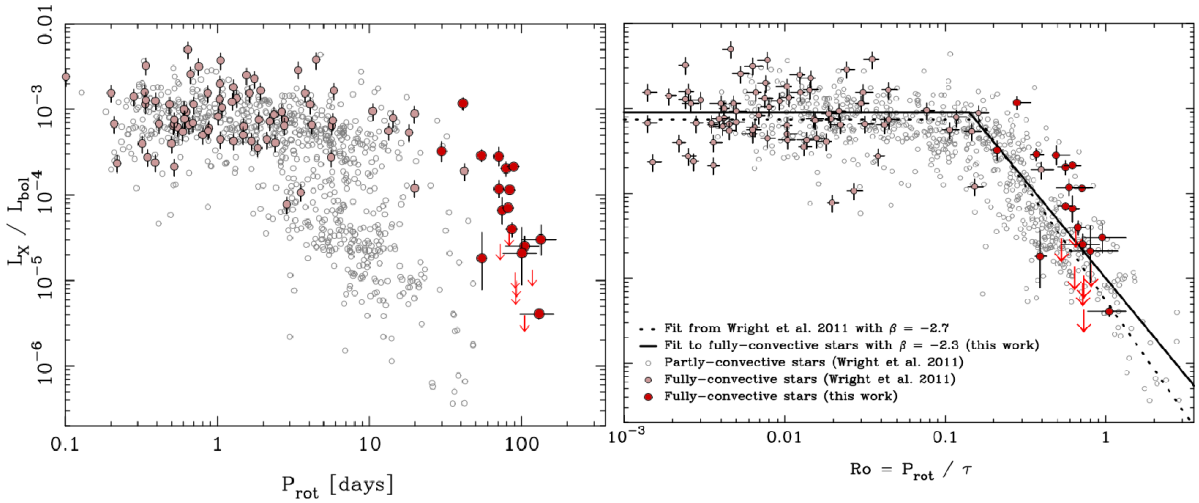

Figure 2.5: Fractional X-ray luminosity, L_x/L_{bol}, plotted against the rotation period, P_{rot} (left panel) and the Rossby number Ro $= P_{rot}/\tau$ (right panel), for fully convective stars from Wright et al. (2018, large red points), fully convective stars included in the sample of Wright et al. (2011, medium, light red points), and the remaining partly convective stars from their sample (grey empty circles). Image Credit: Wright et al. (2018).

Maggio et al., 1987; Feigelson & Montmerle, 1999; Favata & Micela, 2003; Pevtsov et al., 2003; West et al., 2008), which is believed to arise from magnetic dynamo activity. This is fueled by the so-called α–Ω dynamo (Parker, 1955), which is the result of the friction produced in a thin boundary layer known as *tachocline* (Spiegel & Zahn, 1992) between the rigidly rotating, radiative core and the base of the surrounding convective envelope within the interior of solar-type stars (cf. Parker, 1955; Wilson, 1966; Kraft, 1967). The schematic structure of a partly-convective, differentially rotating star is illustrated in the left panel of Figure 2.4, while the right panel shows the internal structure of a low-mass star that is fully convective.

Consequently, stellar magnetic activity has been tightly linked to the stellar rotation period, P_{rot}, which naturally explains why young stars, which are much faster rotators than their main sequence counterparts, show highly elevated X-ray activity. Also the observed decrease of fractional X-ray luminosity with increasing stellar age can be attributed to the rotational spin-down of the star, which is driven by mass-loss through magnetised, stellar winds (e.g., Weber & Davis, 1967; Skumanich, 1972). Further observational evidence for the theory of a magnetic dynamo is provided by the fact that stellar X-ray activity is observed to increase monotonically with stellar rotation rate (e.g., Kraft, 1967; Pallavicini et al., 1981; Noyes et al., 1984; Pizzolato et al., 2003), thus faster rotators generally show higher magnetic activity.

This is demonstrated in the left panel of Figure 2.5 that shows the fractional X-ray luminosity as a function of stellar rotation period, determined for the largest available sample of partly- and fully convective main sequence stars with existing photometric rotation periods and X-ray luminosities obtained by Wright et al. (2011, 2018). For slowly rotating stars a decrease in X-ray activity is observed, that roughly scales with $L_x/L_{bol} \propto P_{rot}^{-2.6}$ (Pallavicini et al., 1981; Pizzolato et al., 2003). This relation breaks down, however, for the most rapid rotators (i.e. stars with $P_{rot} < 2$–3 d), which reach a mass-independent saturation limit at $L_x/L_{bol} \approx -3$ (Vilhu,

1984; Micela et al., 1985), whose origin is not yet fully understood. This therefore divides the activity-rotation relation of main sequence stars into two distinct regimes: a *saturated* regime for fast-rotating stars and a *non-saturated* one for slow rotators.

However, a strong scatter of several orders of magnitude of L_x/L_{bol} can be observed for a given P_{rot}, as stars of different masses may have the same rotation periods. Therefore, it has become common to scale P_{rot} with the so-called Rossby number, $Ro \equiv P_{rot}/\tau_c$, which reduces this scatter significantly (Noyes et al., 1984). The Rossby-number connects the stellar rotation period with the convective turnover time τ_c (cf. Gilman, 1980), which is a function of stellar mass only, and therefore allows an unbiased comparison of stars of different masses. This is demonstrated in the right panel of Fig. 2.5, which shows the same sample as before, however now plotted against the Rossby number. Wright et al. (2011) have found the transition between the saturated and non-saturated regimes to occur at $Ro = 0.13 \pm 0.02$, or equivalently, rotation periods of $\sim$ 1–10 d. Wright et al. (2018) then increased the observational sample drastically and found that the activity-rotation relation can be expressed as $L_x/L_{bol} \propto Ro^{-2.3}$ in the non-saturated regime, which fits observations from late F-type through early M-type stars. The stellar mass, or equivalently spectral type, dictates the properties of the convective zone, whose size increases for later spectral types. The turnover time is therefore a measure for the depth of the convective zone and is thought to play a major role in the generation of the magnetic fields, so that stars with deeper convection zones relative to their radius (i.e. stars of later spectral types/lower masses) will show stronger dynamo activity than early-type stars for a given rotation period.

Recently, the theory of a tachocline-fueled magnetic dynamo has been questioned, however. The reason for this is that if this boundary layer between the radiative core and convective envelope was indeed to be responsible for operating a solar-type dynamo, fully convective stars that do not possess a tachocline should not be able to sustain such a dynamo. Wright & Drake (2016) observed four slowly rotating, fully convective M-type stars ($M_\star < 0.4\,M_\odot$) using the *Chandra* X-ray Observatory as well as the ROSAT satellite. Surprisingly they found that their rotation-activity relationship correlates in the same way as for partly convective stars by falling into the unsaturated regime. These results were later confirmed and consolidated by Wright et al. (2018), who extended this sample of fully convective M-dwarfs by 21 more sources (red dots in Figure 2.5). Both studies found that the rotation-activity relationships of fully and partly convective stars are indistinguishable, indicating that they possibly operate a similar type of dynamo that does not stem from a tachocline.

Further evidence coming from observational studies of young T Tauri stars, which are also thought to be fully convective, have cast doubts on the operation of a solar-like α–Ω dynamo as origin of stellar X-ray activity. Early X-ray studies from the Orion Nebula Cluster by Feigelson et al. (2002) and Flaccomio et al. (2003) could not find a significant correlation between their X-ray activity and rotation. Later studies by Preibisch et al. (2005) and Briggs et al. (2007) revealed that all T Tauri stars with known rotation periods observed within the COUP and XEST surveys do not follow the rotation period-activity relation of main sequence stars that predicts increasing X-ray activity for decreasing rotation periods, but fall well into the unsaturated regime within the (L_x/L_{bol})–Ro-relationship. On the contrary, a weakly positive correlation between L_x/L_{bol} and P_{rot} could be identified for a given Rossby-number, however,

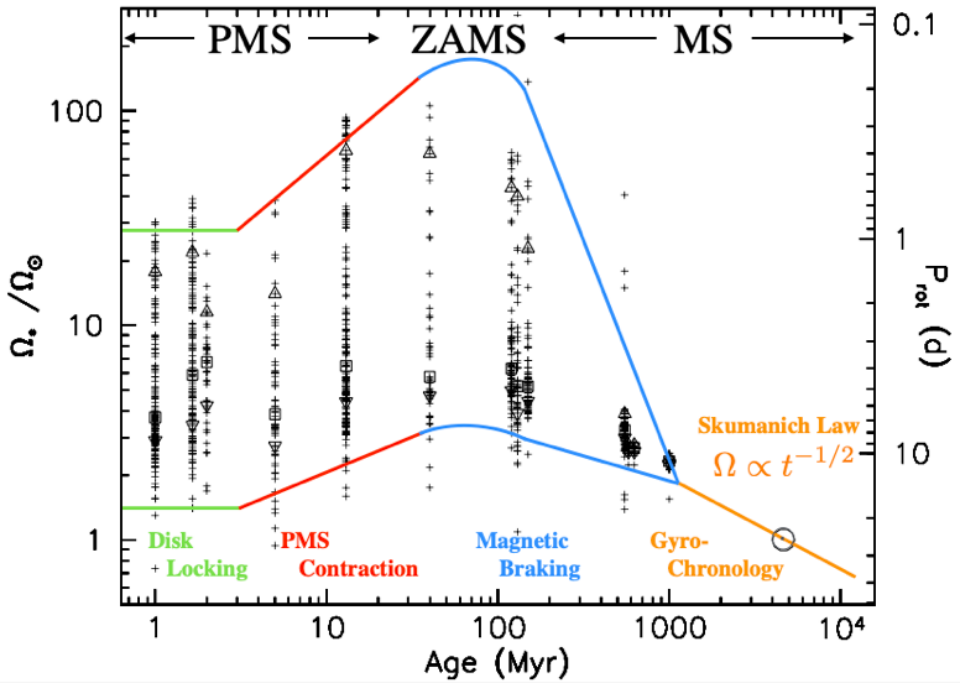

Figure 2.6: Angular velocity distributions of solar-type stars in young open clusters and the Sun as a function of cluster age. The left axis corresponds to the angular frequency $\Omega = 2\pi/P_{\mathrm{rot}}$ in units of the Sun's, while the right axis shows the rotation period P_{rot} in days. Upward and downward triangles represent the 90$^{\mathrm{th}}$ and the 25$^{\mathrm{th}}$ percentiles, the squares show the corresponding median of the observed distributions. The open circle in the lower right corner shows the location of the present Sun within the diagram. Image Credit: Gallet & Bouvier (2015) and modified by Cecilia Garraffo.

the corresponding scatter in X-ray activity is significantly larger than that observed for main sequence stars. While these results may possibly stem from selection effects, they nevertheless suggest that the tachocline may not be critical to amplifying magnetic activity, which therefore supports different models in which the magnetic dynamo may either originate throughout the convective zone or may be generated entirely by turbulence (Wright & Drake, 2016; Wright et al., 2018). Thus, studying the relationship between stellar rotation and tracers of magnetic activity are an important probe for stellar dynamo theories.

Time evolution of the X-Ray emission

Figure 2.6 shows the rotation rate distribution of solar-type stars in young open clusters as a function of cluster age. Stars in young clusters generally show a wide spread in rotation rates, in particular at relatively young ages of $\lesssim 100$ Myr. As stellar magnetic activity is tightly linked to the stellar rotation period, also for the X-ray luminosity a strong scatter covering about two orders of magnitude can be observed for such stars (e.g., Preibisch et al., 2005; Güdel et al., 2007). The origin of the intrinsic scatter both in rotation rate and X-ray luminosity are still not fully understood.

During the first few million years of stellar evolution, YSOs are surrounded by circumstellar

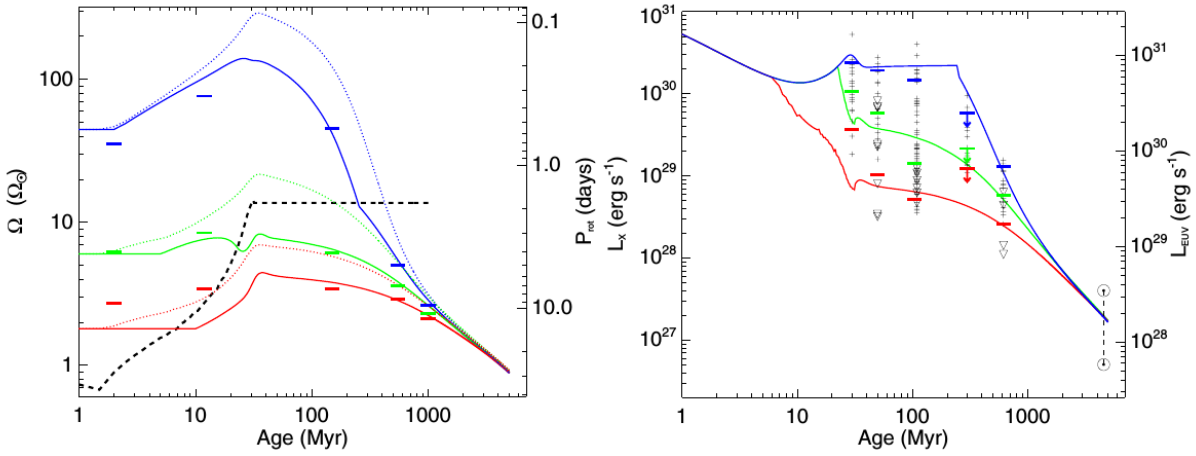

Figure 2.7: Predicted evolutionary tracks for the rotation rate (left panel) and X-ray luminosity (right panel) as a function of cluster age. The coloured lines show the 10$^{\text{th}}$ (red), 50$^{\text{th}}$ (green) and 90$^{\text{th}}$ (blue) percentiles of the rotational/X-ray luminosity distribution out of which the solid and dotted lines show the rotational evolution of the envelope and core respectively. The horizontal lines show the observational constraints on the percentiles. The two solar symbols in the right corner lie at 4.5 Gyr and show the range of L_{x} for the Sun over the course of the solar cycle. Image credit: Tu et al. (2015).

accretion discs that are connected to their host star via magnetic field lines that truncate the disc at a few stellar radii. Due to an effect known as 'disc-locking' (e.g., Cieza & Baliber, 2007), i.e. the magnetic interactions with the circumstellar disc during the first few million years of stellar evolution, discs effectively prevent the contracting star from further spinning up. This leads to almost constant rotation rates, and consequently also X-ray luminosities following $L_{\text{x}} \propto t^{-1/3}$, (cf. Preibisch & Feigelson, 2005) during the PMS phase ($\sim$ 0.1–10 Myr). This changes, however, drastically with the dispersal of the disc, as the star can continue to contract again. This results in an increase of the rotational frequency, until the star has reached the ZAMS. At this point, the star's ongoing contraction halts due to the fact that it starts losing mass and angular momentum through magnetised, stellar winds (so called 'magnetic braking', cf. Weber & Davis, 1967), which will again lead to stellar spin-down. During this phase the angular rotation frequency, and consequently also the X-ray emission of main sequence stars, decay over time in a characteristic fashion, before converging to a mass-dependent behavior for ages exceeding $\gtrsim$ 1 Gyr. Skumanich (1972) has found the empirical relation of $\Omega_{\text{rot}} \propto t^{-1/2}$, or $P_{\text{rot}} \propto t^{1/2}$, for the rotational spin down of a star as a function of its age. Further, it has been observationally established that $L_{\text{x}}/L_{\text{bol}} \propto P_{\text{rot}}^{-3}$ to P_{rot}^{-2}, resulting in the X-ray luminosity to decrease with time as $L_{\text{x}} \propto t^{-1.5}$ to $t^{-0.75}$ (e.g., Maggio et al., 1987; Güdel et al., 1997; Feigelson et al., 2004; Preibisch & Feigelson, 2005).

Tu et al. (2015, but see also Gondoin 2018) have used a similar rotational evolution model as Johnstone et al. (2015) and Gallet & Bouvier (2015) to predict the X-ray luminosity distributions as a function of stellar age, based on a range of initial rotation rates Ω for solar-mass stars (0.9–1.1 $M_{\odot}$). They found that their model predictions agree well with the observed time-dependent scatter of X-ray luminosities observed for several stellar clusters. These results are

shown in Figure 2.7, which illustrates the predicted evolutionary tracks for the rotation rate (left panel) and X-ray luminosity (right panel) as a function of cluster age. The coloured lines show the 10^{th}, 50^{th} and 90^{th} percentiles of the rotational and X-ray luminosity distribution, out of which the solid and dotted lines correspond to the evolution of the stellar envelope and core, respectively.

An important conclusion from their work that is relevant to the work presented in this thesis is that the order between different evolutionary tracks of both the rotation rate and the X-ray luminosity remains conserved before converging to the Skumanich-branch with $\Omega_{\text{rot}} \propto t^{-1/2}$ (or $L_{\text{x}} \propto t^{-1.5}$). From this follows that a given star, which is X-ray brighter (or a faster rotator) at the end of the disc-locking phase, remains a stronger X-ray emitter (or faster rotator) during the next $\lesssim$ 1–2 Gyr. This enables us to observe present-day X-ray luminosities of stars with ages of < 2 Gyr and make rough predictions about their X-ray activity at earlier times, when their disc was still present. Mapping the X-ray luminosity as a function of time further requires the precise knowledge of stellar ages, which is often difficult to infer, especially for isolated stars that are not part of an open cluster (e.g., Tout et al., 1999). Further, detailed models of stellar spin-down are needed that include the impact of stellar magnetic morphology on the efficiency of angular momentum loss during magnetic braking (e.g., Garraffo et al., 2016, 2018), which can be then coupled to models of stellar X-ray activity.

Chapter 3

The birthplaces of planets: planet-forming discs

Planets form in circumstellar accretion discs, which are a natural outcome of the star formation process. They provide the resources from which planets will assemble, and therefore the mechanisms of star and planet formation are tightly coupled. Any comprehensive theory of planet formation must be capable of producing systems hosting both close-in and very distant planets from their host star. Hence understanding the physical properties of planetary nurseries as well as the origin of their striking diversity is vital to understanding the formation process of planets. A detailed understanding of the processes and timescales on which they operate is crucial for constraining models of both star and planet formation.

While it was clear early on that circumstellar discs must hold the reservoir for planets to form, exoplanets had been solely observed around evolved main-sequence stars. Only very recently, it has been possible to observe planets that are *caught in the act* of their formation by observing Hα-emission, which traces the accretion of gas from the circumplanetary disc onto the planet (e.g., Sallum et al., 2015; Haffert et al., 2019; Keppler et al., 2018; Müller et al., 2018). In the meanwhile, more and more observational studies have provided evidence that planets must form early, possibly already in the Class 0/Class I phase (e.g., Tychoniec et al., 2020), implying that their harbouring discs should be rather referred to as *planet-forming*, rather than *protoplanetary*.

In this chapter, we first derive a theoretical framework to describe the structure and evolution of planet-forming discs. We then discuss their basic observational properties and focus specifically on discs around Class II T Tauri stars, as the formation process of planets around higher-mass Herbig Ae/Be stars is still unclear. Their evolution towards the main sequence is significantly faster than for low-mass stars, therefore giving planets around such stars little time to form (Klahr & Brandner, 2006; Garcia, 2011).

3.1 Theoretical framework

As described in the previous chapter, during the collapse of a prestellar core, the matter that surrounds the nascent protostar will form a rotating accretion disc that keeps feeding the central star during the first few million years of its evolution. Keplerian discs are stable to hydrodynamic instabilities according to Rayleigh's stability criterion (Drazin & Reid, 1981; Ruden, 1993), meaning that without a mechanism to decrease the gas particles' angular momentum, they would continue orbiting the central star indefinitely with constant angular frequency:

$$\Omega_{\mathrm{K}} = \sqrt{\frac{GM_{\star}}{R^3}}, \tag{3.1}$$

where G describes the gravitational constant, $M_{\star}$ the mass of the central star and R the radius at which the gas particle is located. The mere fact that CTTSs are observed to accrete already proves that there must be some kind of mechanism present that dissipates angular momentum. The specific angular momentum of each fluid element in the disc can be described by:

$$L = \Omega_{\mathrm{K}} R^2. \tag{3.2}$$

Combining Eq. 3.2 with Eq. 3.1 yields that $L \propto \sqrt{R}$. In order for a gas particle to spiral inwards and accrete onto the central star, it must inevitably lose angular momentum, as R decreases. For protoplanetary discs, this can be achieved through two different, not mutually exclusive, routes:

1. by redistributing angular momentum throughout the disc, or
2. by removing angular momentum entirely from the system.

Removing angular momentum entirely from the system requires an external sink to the continuity equation, such as magnetically-driven disc winds or magnetic braking due to magneto-hydrodynamic (MHD) effects. Redistributing angular momentum to the outer disc, in turn, requires a form of viscosity, which is produced through the differential rotation (i.e. shear) between two adjacent gas annuli (e.g., Shakura & Sunyaev, 1973). The latter route is especially important in the earliest phases of circumstellar discs, when they are still massive. To first order, the evolution of discs during the primordial stages is therefore driven by viscous transport and accretion, while disc winds will start to dominate at later stages, when the viscous accretion rates drop below the wind mass-loss rates. The theoretical basics of the viscous evolution of circumstellar disc will be outlined in the following.

Viscous evolution of a gas disc

The viscous evolution of a Keplerian disc can be described by the basic equations of fluid dynamics including viscosity, in particular the continuity equation and the Navier-Stokes equations. Solving this coupled system of equations in all three dimensions is a challenging task to do and usually not possible without sophisticated numerical methods. Therefore, in order to

derive an analytic solution for the disc structure, usually several assumptions have to be made beforehand. First, we split the disc into separate, infinitesimally thin annuli, which are 'glued together' in radial direction, so that they can interact with each other. Each annulus then constitutes an independent 1D vertical disc structure problem (a so-called 1+1D problem). The second assumption is that of an axis-symmetric and geometrically thin gas disc that is centred around the $z = 0$ plane (e.g., Apai & Lauretta, 2010).

Equipped with these basic assumptions, the continuity equation can be written as:

$$\frac{\partial \Sigma}{\partial t} + \frac{1}{R}\frac{\partial}{\partial R}(R\Sigma v_{\mathrm{R}}) = 0, \tag{3.3}$$

where R is the radial distance to the central star, v_{R} is the radial velocity and Σ is the gas surface density, which is defined as the vertical integral of the volume density:

$$\Sigma(R, t) \equiv \int_{-\infty}^{\infty} \rho(R, z, t)\mathrm{d}z. \tag{3.4}$$

By solving the Navier-Stokes equations in azimuthal direction and combining them with the continuity equation (Eq. 3.3) as well as the expression for the Keplerian angular frequency given by Eq. 3.1, one obtains a general expression for the dynamical evolution of a viscous accretion disc (cf. Ruden, 1993, and Lodato 2008 for detailed derivations):

$$\frac{\partial \Sigma}{\partial t} = \frac{3}{R}\frac{\partial}{\partial R}\left[R^{1/2}\frac{\partial}{\partial R}(\nu\Sigma R^{1/2})\right], \tag{3.5}$$

where $\nu \propto R^{\gamma}$ is the kinematic viscosity (Lynden-Bell & Pringle, 1974; Pringle, 1981). Eq. 3.5 is a partial differential equation, where diffusion is regulated by the viscosity ν, and consequently the evolution of a viscous disc strongly depends on the exact form of this parameter. Also, for the general case, Eq. 3.5 has no analytic solution and therefore needs to be integrated numerically if no further specifications or assumptions are made. However, by considering simplified special cases, several analytic solutions have been derived in the past, from which the *steady-state* and the *self-similar* solutions will be discussed in detail in the following.

Steady-state solution

The simplest solution to Eq. 3.5 is a steady-state solution, in which the flow in the disc is assumed to be steady, meaning that the mass accretion rate, $\mathrm{d}M/\mathrm{d}t$, stays constant over time. Considering that the mass in each of the infinitesimally thin disc annuli is described by $\mathrm{d}M = 2\pi R\Sigma\mathrm{d}R$, the mass flow can be described as:

$$\dot{M}(R) \equiv \frac{\mathrm{d}M}{\mathrm{d}t} = -2\pi R\Sigma(R)v_{\mathrm{R}} = \text{const.} \tag{3.6}$$

Given that $\dot{M}(R)$ is constant with time, $\partial\Sigma/\partial t = 0$ and the left side of Eq. 3.5 becomes zero. The steady-state evolution of Eq. 3.5 is then obtained by integrating over R, assuming that

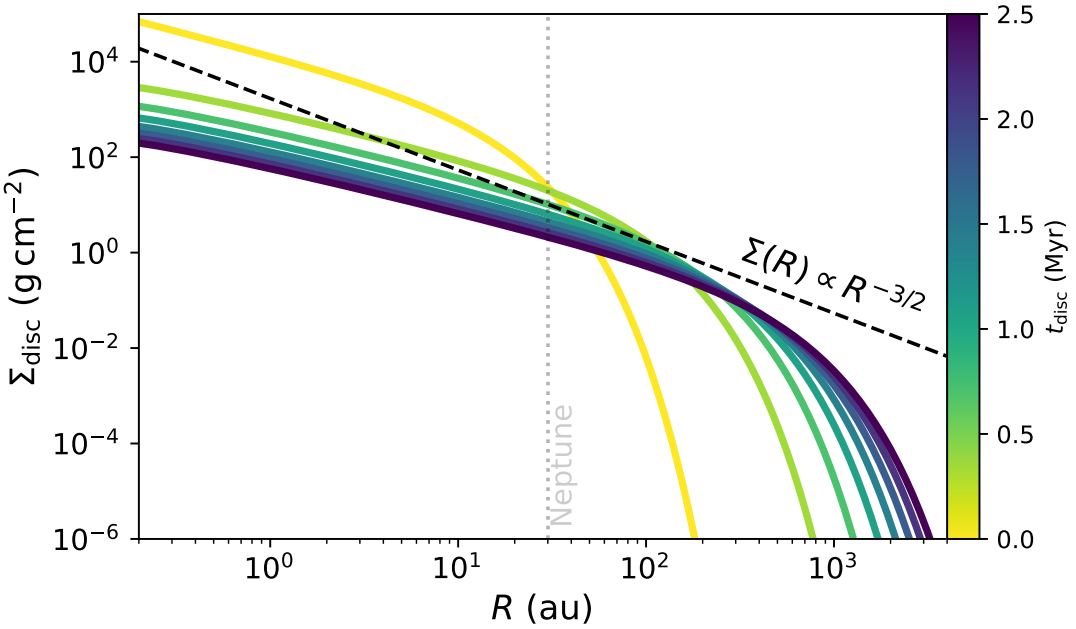

Figure 3.1: Surface density evolution and viscous spreading of a circumstellar disc for the $\gamma = 1$ case of the self-similar solution. The colour-scale shows the corresponding disc age in units of million years. The initial disc conditions were $M_\star = 1\,M_\odot$, $M_{\rm d}(0) = 0.1\,M_\odot$, $\alpha = 10^{-2}$, $H/R = 0.05$ and $R_1 = 10\,{\rm au}$. The dashed line shows the surface density scaling of $\Sigma(R) = 1700\,(R/{\rm au})^{-3/2}$ following from the minimum mass solar nebula model derived by Weidenschilling (1977) and Hayashi (1981). The dotted grey line marks the semi-major axis of Neptune in the Solar System.

the inner boundary is $R = R_{\rm in}$ and that there is no torque exerted at the inner boundary (i.e. $\mathrm{d}\Omega/\mathrm{d}R = 0$ at $R_{\rm in}$):

$$\Sigma(R) = \frac{\dot{M}}{3\pi\nu}\left(1 - \sqrt{\frac{R_{\rm in}}{R}}\right). \tag{3.7}$$

It follows from Eq. 3.7 that for $R \gg R_{\rm in}$, the accretion rate becomes $\dot{M}(R) \approx 3\pi\nu\Sigma(R)$. Thus, even though the steady-state solution does not require an a priori knowledge of the exact form or source of viscosity, the rate at which the disc evolves is nevertheless governed by the rate at which angular momentum is transported outwards, which ultimately depends on the origin and magnitude of the viscous torque (Ruden, 1993).

Self-similar solution

In reality, protoplanetary discs are not steady objects, as their accretion rates will decrease strongly over time. Therefore, on large timescales, the assumption of a constant mass accretion rate over time, as was made in the previous case, does not hold and a more general solution needs to be found. The so-called *self-similar solution* provides such a solution, however, it requires the a priori knowledge of the dependence of viscosity on the underlying disc properties.

Given that the viscosity can be written as a power-law in R, which is independent of time so that $\nu(R) \propto R^{\gamma}$, Lynden-Bell & Pringle (1974) derived a similarity solution to Eq. 3.5:

$$\Sigma(R,t) = \frac{C}{3\pi\nu_1 (R/R_1)^{\gamma}} \left(1+\frac{t}{t_\nu}\right)^{-(5/2-\gamma)/(2-\gamma)} \exp\left(-\frac{(R/R_1)^{(2-\gamma)}}{1+t/t_\nu}\right), \tag{3.8}$$

where C is a normalisation constant, R_1 is the scaling, or cut-off radius (usually assumed to be the radius, which contains two thirds of the total disc mass, cf. Williams & Cieza, 2011), $\nu_1 \equiv \nu(R_1)$ and t_ν is the so-called viscous timescale at radius R_1 (Pringle, 1981):

$$t_\nu = \frac{1}{3(2-\gamma)^2}\frac{R_1^2}{\nu_1}. \tag{3.9}$$

The solutions to Eq. 3.8 and 3.9 for different values of γ are summarised in detail in Hartmann et al. (1998). For simplicity, we will solely consider the $\gamma = 1$ case (i.e. $\nu \propto R$) in the following and only briefly outline the most relevant concepts and equations.

Given that $\gamma = 1$, Eq. 3.8 and 3.9 can be rewritten as:

$$\Sigma(R,t) = \frac{M_\mathrm{d}(0)}{2\pi R_1^2}\frac{1}{R/R_1}\left(1+\frac{t}{t_\nu}\right)^{-\frac{3}{2}} \exp\left(-\frac{R/R_1}{1+t/t_\nu}\right), \tag{3.10}$$

and

$$t_\nu = \frac{1}{3}\frac{R_1^2}{\nu_1}. \tag{3.11}$$

The radial mass distribution as a function of time is described by:

$$M_\mathrm{d}(R,t) = M_\mathrm{d}(0)\left(1+\frac{t}{t_\nu}\right)^{-\frac{1}{2}}\left[1-\exp\left(-\frac{R/R_1}{1+t/t_\nu}\right)\right], \tag{3.12}$$

where

$$M_\mathrm{d}(t) = M_\mathrm{d}(0)\left(1+\frac{t}{t_\nu}\right)^{-\frac{1}{2}}, \tag{3.13}$$

is the total disc mass. The mass accretion rate at any given disc radius is described by

$$\dot{M}_\mathrm{acc}(R,t) \equiv \frac{\mathrm{d}M}{\mathrm{d}t} = \frac{M_\mathrm{d}(0)}{2t_\nu}\frac{1}{(1+t/t_\nu)^{3/2}}\exp\left(-\frac{R/R_1}{1+t/t_\nu}\right)\left[1-\frac{2R/R_1}{1+t/t_\nu}\right], \tag{3.14}$$

which in the limit of $R \to 0\,\mathrm{au}$ becomes:

$$\dot{M}_\mathrm{acc}(0,t) = \frac{M_\mathrm{d}(0)}{2t_\nu}\frac{1}{(1+t/t_\nu)^{3/2}}. \tag{3.15}$$

Consequently the mass accretion rate onto the star scales with time as $\dot{M}_\mathrm{acc}(t) \propto t^{-1.5}$. This relation is consistent with measured accretion rates of young PMS stars from the Taurus and

Chamaeleon I molecular cloud complexes obtained by Gullbring et al. (1998) and Hartmann et al. (1998), therefore implying that $\gamma \sim 1$ is a reasonable assumption. These observational results are reassuring, since they show that the basic structure of protoplanetary discs can be described to sufficient accuracy by simple analytic considerations.

Finally, the outer disc radius can be described by:

$$R_{\mathrm{d}}(t) = \frac{R_1}{2}\left(1 + \frac{t}{t_\nu}\right). \tag{3.16}$$

It follows from Eq. 3.16 that with increasing time, the disc will grow in size, leading to the so-called 'viscous spreading' of the outer disc radius. This is a simple consequence of angular momentum conservation, as viscosity moves material with higher angular momentum to the outer regions, which will lead to the expansion of the disc. This is illustrated in Fig. 3.1, which shows the viscous evolution of the surface density structure of a planet-forming disc surrounding a $1\,M_\odot$ star, with $M_{\mathrm{d}}(0) = 0.1\,M_\odot$, $H/R = 0.05$, $R_1 = 10\,\mathrm{au}$ and $\alpha = 10^{-2}$. While the disc starts with an initial size of $\sim 200\,\mathrm{au}$, it increases up to $> 1000\,\mathrm{au}$ after only $\sim 1\,\mathrm{Myr}$. With increasing age, more and more mass will therefore be located in the outer regions of the protoplanetary disc, thus leading to an increase of R_1. Further, the surface density profile of $\Sigma(R) = 1700\,(R/\mathrm{au})^{-3/2}$ derived for the so-called minimum mass solar nebula (MMSN, Weidenschilling, 1977; Hayashi, 1981) is overplotted to highlight that the predicted surface density evolution from the self-similar solution agrees reasonably well with observed constraints for disc evolution from the Solar System.

Source of viscosity

The source of viscosity is still matter of debate, but it is certain that molecular viscosity, which arises from the random motions of gas particles, is too low in order for accretion discs to be dispersed in the observed timescales of a few million years. Turbulence or magnetic stresses possibly constitute a significant fraction of viscosity. One of the most accepted mechanisms to drive turbulence lies in the magneto-rotational instability (MRI, Balbus & Hawley, 1991), which is present in weakly magnetised, but sufficiently ionised discs. However, also the vertical shear instability (VSI, Richard & Zahn, 1999; Nelson et al., 2013; Stoll & Kley, 2014) or gravitational instability (Lin & Pringle, 1987), where spiral density waves redistribute angular momentum, have been proposed as possible origins of turbulence in protoplanetary discs.

For simplicity, we usually make the assumption that the viscosity stays constant throughout the disc. However, there is no physical reason for this assumption, and in fact, MHD calculations of a radially- and vertically-variant viscosity have recently regained more and more in importance. For example, a key requirement for MRI to work is a sufficiently ionised disc – however, discs are expected to be cold and neutral objects for most parts. While hard X-rays may provide a possible ionisation source especially for the outer disc regions (e.g., Glassgold et al., 1997), they are nevertheless not energetic enough to fully penetrate the disc, leaving the innermost disc layers mostly unperturbed. If turbulence is indeed caused by the MRI, one would expect that discs have a layered structure (e.g., Gammie, 1996), in which a 'dead zone', which is an MRI-inactive region of strongly suppressed or even absent turbulence, is encased between two actively

accreting layers (starting at ~ 1 au, with a large radial extent; e.g., Salmeron & Wardle, 2008; Terquem, 2008; Bai & Goodman, 2009; Turner & Drake, 2009). While there is no observational evidence of such dead zones yet, recent modelling efforts suggest that their existence is indeed very likely, and consequently that the viscosity is indeed not constant throughout the entire disc (cf. Armitage, 2011, for a review).

Independently of the exact origin of the underlying source of viscosity, one can parameterise the kinematic viscosity in the case of a vertically isothermal disc using the so-called 'α-prescription', which was introduced by Shakura & Sunyaev (1973):

$$\nu \equiv \alpha \frac{c_S^2}{\Omega_K} = \alpha c_S H, \tag{3.17}$$

where $c_S = \sqrt{kT/\mu m_H}$ is the isothermal sound speed, with k being the Boltzmann constant, μ the mean molecular weight of the gas molecules (assumed to be primarily hydrogen, therefore $\mu \approx 2.3$), m_H is the mass of a hydrogen atom and $H = c_S/\Omega_K$ is the vertical pressure scale height. The α-parameter ($\alpha \leq 1$) is a dimensionless number that represents the ratio of the stress over pressure and thus describes the efficiency of angular momentum transport due to turbulence. The value of α can be either constrained from observations of stellar accretion rates (e.g., Gullbring et al., 1998; Hartmann et al., 1998), from tailored models of individual systems (e.g., Hueso & Guillot, 2005) or from measurements of the turbulent velocity dispersion from molecular gas emission line broadening (e.g., Teague et al., 2016; Flaherty et al., 2020), and typically ranges between $\alpha \sim 10^{-4}$–10^{-1}.

As follows from Eq. 3.17, the viscosity depends on the temperature of the disc. The main source of heating, especially at large disc radii, is the irradiation by the central star, so that the outer layers of the disc are hotter than the central layers close to the midplane (so called 'passive discs'). It follows from the left side of Eq. 3.17 that $\nu \propto TR^{-3/2}$, and if $T \propto R^{-1/2}$, we retain our initial assumption that $\gamma \approx 1$ and consequently that $\nu \propto R$. Together with the right side of Eq. 3.17 it follows that the disc has a flaring geometry, meaning that the aspect ratio increases with increasing radius, so that $H(R) \propto R^{5/4}$ as $\nu \propto R$ and $\alpha = \text{const.}$, which is consistent with models of the vertical structure of passive discs (Chiang & Goldreich, 1997; D'Alessio et al., 1998; Dullemond et al., 2001, 2002). Indeed, this theoretical result was later verified observationally by Kenyon & Hartmann (1987), who confirmed a flaring geometry of the disc's surface to be the origin of the strong fIR excess emission of most protoplanetary discs that were observed by IRAS (Infrared Astronomical Satellite). As flared discs can capture more stellar radiation at larger radii than spatially flat discs, more radiation can be reprocessed by the dust grains, naturally resulting in flatter SEDs at fIR wavelengths (Alexander et al., 2014). However, due to the iterative absorption and re-emission of the impinging stellar photons by the dust phase, the photons propagate through the disc in a diffusive (and stochastic) way that strongly depends on the composition of the disc (Dullemond et al., 2007). Therefore, for a detailed calculation of the disc temperature, radiative transfer models are a necessary tool.

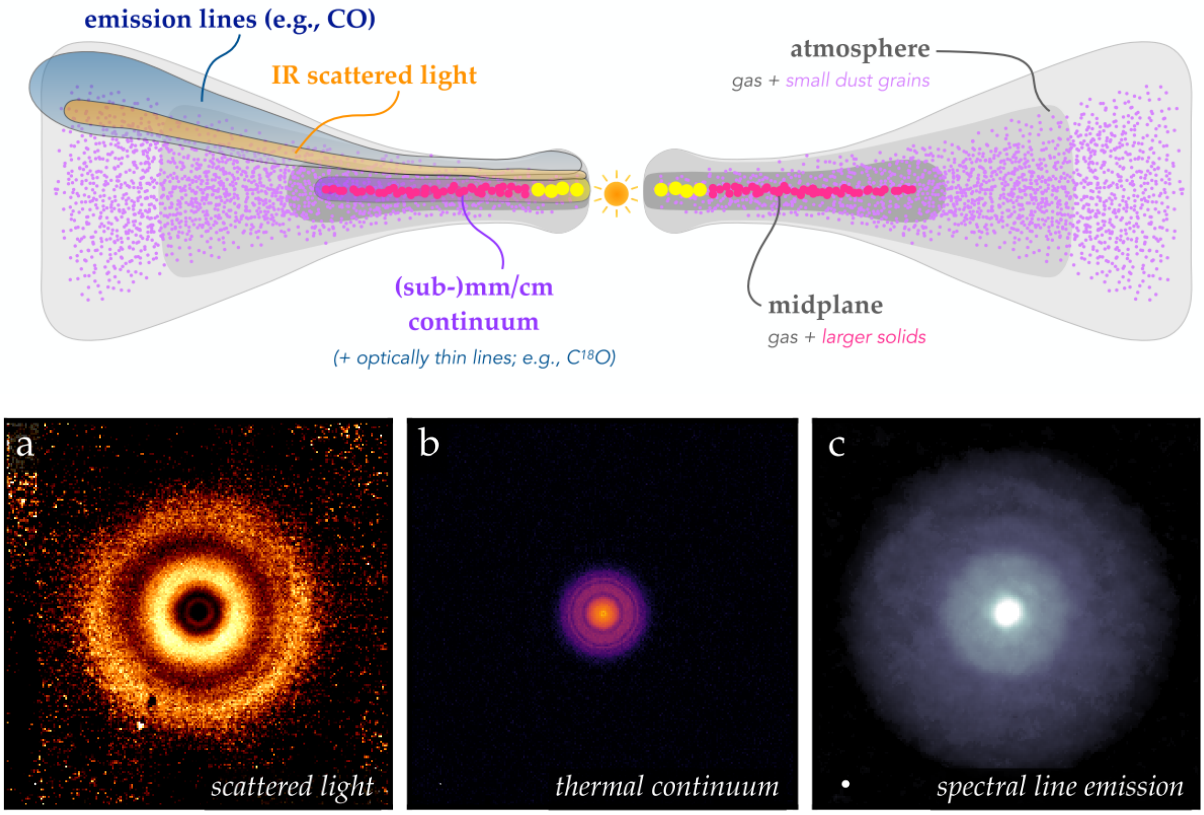

Figure 3.2: *Top:* Schematic disc structure viewed at different wavelengths. The gas phase is shown as grey-shaded region, while dust particles are marked by colours. The left side marks the origin of given emission tracers, while the right side illustrates the corresponding disc composition of these regions. *Bottom:* Comparison of TW Hya in different disc tracers: (a) scattered light from small dust grains ($\lambda = 1.6\,\mu$m, van Boekel et al., 2017), (b) thermal continuum from pebble-sized particles ($\lambda = 0.9$ mm, Andrews et al., 2016), and (c) cold molecular gas traced by CO $J = 3 - 2$ spectral line emission (Huang et al., 2018). The resolution of each observation is shown as ellipse in the lower left corner. Note that all three images are to scale and span 500 au from left to right. Image reproduced from Andrews (2020) with permission from Annual Reviews.

3.2 Observational properties

The first observational evidence for the existence of circumstellar discs surrounding young stars came from *Hubble* Space Telescope (HST) observations of the Orion Nebula Cluster (ONC) in the early 1990s, in which flattened droplet-like structures were imaged as shadows in silhouette of the bright nebular background (O'dell et al., 1993; O'dell & Wen, 1994). These structures were referred to as *proplyds*, which is an abbreviation for **pro**to**pl**anetr**y** **d**iscs, and were thought to be externally photoevaporated by the massive, luminous Trapezium stars embedded in the ONC (Stahler & Palla, 2004). However, more detailed studies of their morphology had been impeded for a long time, in part by the lacking resolving power and sensitivity of the available facilities back then but also due to the fact that circumstellar discs tend to be opaque, and thus can only be studied in detail at longer wavelengths.

Only recently, it has become possible to spatially resolve circumstellar discs thanks to facilities like ALMA (Atacama Large Millimeter/submillimeter Array) or the SPHERE (Spectro-Polarimetric High-contrast Exoplanet REsearch) instrument mounted on the Very Large Telescope (VLT), which have truly revolutionised the field. The last decade has therefore provided us with a plethora of highly-resolved images of discs surrounding all kinds of stars at different evolutionary stages, such as HL Tau ($t \lesssim$ 1–2 Myr, Briceño et al., 2002; ALMA Partnership et al., 2015), MWC 758 ($\sim$ 1–5 Myr, Meeus et al., 2012; Dong et al., 2018) or TW Hya ($\sim$ 10 Myr, Weinberger et al., 2013; Andrews et al., 2016). Dedicated protoplanetary disc surveys performed by these facilities (e.g. DSHARP, Andrews et al., 2018, or ODISEA, Cieza et al. 2020) have further established that substructures in discs are ubiquitous and that circumstellar discs are far more complex objects than previously thought. The observed substructures, such as rings, gaps, but also asymmetric ones like spirals, vortices or shadows challenge our theoretical understanding of protoplanetary discs. Many of these structures are often related to perturbations emerging from nascent planets, however, also other effects have been proposed to their explanation. As far as it is possible in this highly dynamic field, the following section will attempt at summarising the state-of-the-art of the observed properties of this very diverse class of objects – the planet-forming discs.

Disc tracers

Figure 3.2 shows the schematic structure of a circumstellar disc and highlights the disc regions from which different disc tracers originate. The lower panels show the famous TW Hya disc observed in these different tracers, highlighting the striking differences in morphology for the same disc that is observed at different wavelengths.

Scattered light emission arises when small, micron-sized dust (which is still fully coupled to the gas) reflects the impinging stellar photons. It is especially useful to study the polarisation of scattered light, which allows conclusions on the underlying properties of dust grains, such as their sizes, shapes or composition (Andrews, 2020). The thermal continuum emission comprises wavelengths between the nIR to cm, therefore being a useful tracer of dust grains subject to different temperatures. The only possibility to get a direct measurement of the disc gas is by observing spectral line emission. As can be inferred from the right panel of Figure 3.2, gas can extend to significantly larger radii than the dust phase of the disc.

Each tracer is therefore not only sensitive towards different locations in the disc, but also to different materials and in particular different physical conditions. Observing a circumstellar discs at different wavelengths is an important tool in order to obtain a global picture of their properties, which is of high relevance for connecting observational insights to theoretical models of star and planet formation.

Disc masses and composition

The masses of circumstellar discs are one of the most important quantities to determine, however, they are difficult to obtain as most of the disc mass is present in the form of cold, molecular hydrogen, which can barely be observed directly (as it has no electric dipole moment and only

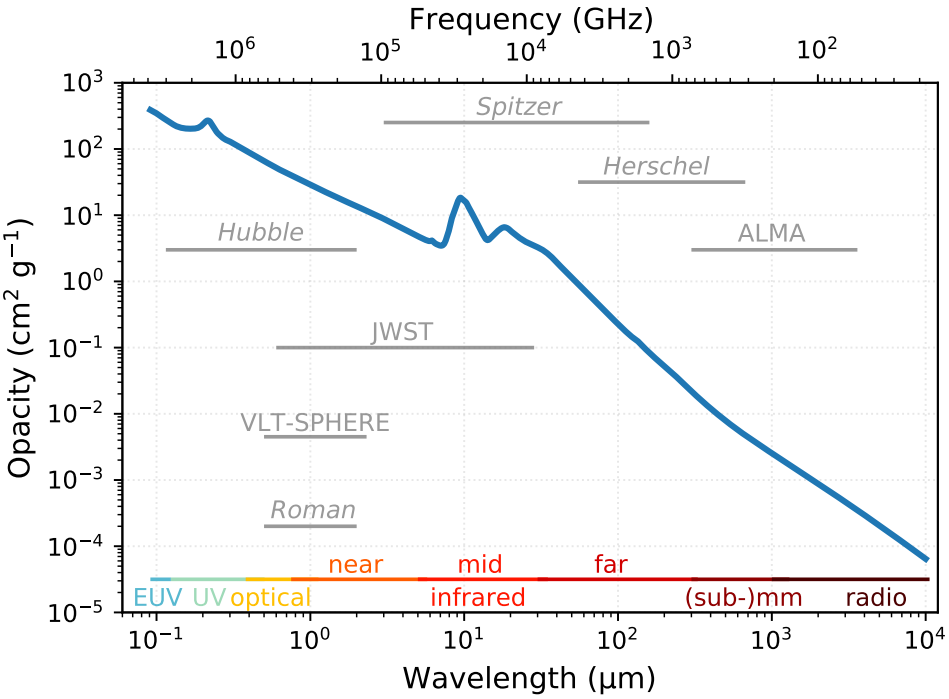

Figure 3.3: Dust opacity as a function of wavelength/frequency for a typical dust grain distribution of the Milky Way. Also shown are selected spectral windows of different telescopes. The opacity values are taken from Weingartner & Draine (2001) and Draine (2003).

emits through magnetic quadrupole transitions, cf. Williams & Cieza, 2011; Alexander et al., 2014). Therefore, it is typically assumed that the composition of circumstellar discs, which are relics from the star formation process, does not differ significantly from that of their parental cloud cores. Usually, the assumption of a dust-to-gas ratio of 1:100 is made (which is the same as in the ISM), meaning that discs are composed by 99 % of gas and 1 % of dust grains. In the diffuse ISM, dust grains are mainly composed of silicates with sizes $\lesssim 1\,\mu$m (Mathis et al., 1977; Dullemond et al., 2007), mixed with graphite and polycyclic aromatic hydrocarbons (PAHs, cf. Draine, 2003). In the cold and dense regions of protoplanetary discs, molecular gas will freeze out onto the dust grains and cover them in ice coatings (e.g., Bergin & Tafalla, 2007).

Even though the dust component makes up only a small fraction of the total mass budget of the disc, it dominates, however, its opacity. In addition, the radiation emitted by the disc can be interpreted as reprocessed emission, since dust grains absorb the incoming stellar radiation with wavelengths smaller than their physical grain size, and re-emit it at longer wavelengths. Consequently continuum emission observations at different wavelengths are required in order to probe the dust at different temperatures, and therefore different disc radii. This provides a global picture of the disc composition, ranging from the hot dust located at the dust sublimation radius ($\sim$ 500–1500 K, equivalent to radii of $\sim$ 0.1–1 au, cf. Pollack et al., 1994; Dullemond et al., 2007) to the warm dust at a few astronomical units ($\sim$ 50–150 K) up to the cold dust residing in the mass reservoir that is located in the outermost regions of the protoplanetary disc

($\gtrsim 100\,\mathrm{au}$).

While line emission from gas mass tracers (e.g. H_2, CO and their isotopologues, but also other atomic and molecular tracers) are detected (e.g., Najita et al., 2007; Williams & Cieza, 2011), the masses of protoplanetary discs are best determined by their (sub-)mm continuum emission produced by the cold dust component. The reason for this is that the dust opacity, which is a measure for the absorption efficiency of a given medium, increases immensely towards shorter wavelengths, meaning that the dust becomes optically thick in the visual to UV wavelength regime. This can be inferred from Figure 3.3, which shows the dependence of the dust opacity with the wavelength/frequency of the incident radiation for a typical dust grain distribution in the Milky Way, with opacity values taken from Weingartner & Draine (2001) and Draine (2003). The opacity has the highest levels at infrared wavelengths and decreases significantly towards longer wavelengths.

The opacity is defined via the intensity of the incoming radiation I_ν:

$$\mathrm{d}I_\nu = -\kappa I_\nu \mathrm{d}s, \tag{3.18}$$

where $\mathrm{d}I_\nu$ describes the reduction of the intensity during its path through a medium of given opacity along the length $\mathrm{d}s$. The determination of disc masses from observations at a given frequency[11] ν therefore requires an estimate of the opacity κ (Beckwith et al., 1990):

$$\kappa = 0.1 \left(\frac{\nu}{10^{12}\,\mathrm{Hz}}\right)^{\beta} \mathrm{cm}^2\,\mathrm{g}^{-1}, \tag{3.19}$$

where the opacity spectral index $\beta(\nu) \equiv \mathrm{d}\ln\kappa/\mathrm{d}\ln\nu$ is set by the grain size distribution (i.e. $n(r_\mathrm{dust}) \propto r_\mathrm{dust}^{-4}$ to r_dust^{-3} for dust grains of sizes ~ 0.003–$1.0\,\mu\mathrm{m}$, where small grain sizes dominate by number, cf. Mathis et al., 1977; Draine, 2006), the composition of the dust grains (e.g., Ossenkopf & Henning, 1994; Pollack et al., 1994), as well as the frequency of the incoming radiation. The value of β can be estimated from multi-wavelength observations (Draine, 2006).

The optical depth along the line of sight, which is a measure for the amount of absorption that occurs when the stellar light travels through the absorbing medium, can then be determined via

$$\tau_\nu \equiv \int \rho\kappa \mathrm{d}s = \kappa\Sigma, \tag{3.20}$$

where ρ is the density of the gas and Σ is the disc surface density. The MMSN (cf. Section 3.1) estimates the gas surface density structure to scale as $\Sigma(r) = 1700\,(r/\mathrm{au})^{-3/2}\,\mathrm{g\,cm}^{-2}$, and therefore for typical disc conditions at e.g. $R = 10\,\mathrm{au}$, one can assume $\beta \approx 1$ (Draine, 2006), so that $\kappa(1\,\mathrm{mm}) = 0.03\,\mathrm{cm}^2\,\mathrm{g}^{-1}$ and $\tau_\nu(1\,\mathrm{mm}) = 1$ for $\Sigma \approx 30\,\mathrm{g\,cm}^{-2}$ (Williams & Cieza, 2011). This means that only beyond 10 au the disc becomes optically thin to mm-emission, while it remains optically thick to optical and infrared radiation. Inside to this radius, one can only see the disc's surface layers, emphasizing that wavelengths longer than 1 mm are required in order to observe the innermost 10 au of the disc.

[11] Note that the symbol "ν" is used interchangeably for the viscosity (Eq. 3.17) and the frequency of electromagnetic radiation ($\nu = c/\lambda$) throughout this thesis. The corresponding meaning should be, however, clear from the context.

Assuming that most of the mm-emission is optically thin, one can then determine the total mass of the disc via:

$$M_{\mathrm{dust}} = \frac{F_\nu d^2}{\kappa B_\nu(T_{\mathrm{dust}})}, \tag{3.21}$$

where F_ν is the observed flux at a given frequency ν, d is the distance to the object and

$$B_\nu(T_{\mathrm{dust}}) = \frac{2h\nu^3}{c^2}\frac{1}{\exp(h\nu/kT_{\mathrm{dust}})-1} \tag{3.22}$$

is the Planck function evaluated at the dust temperature T_{dust}. At long wavelengths, the Planck function can be well approximated by the Rayleigh-Jeans limit ($h\nu \ll kT_{\mathrm{dust}}$, cf. Fig. 2.2), so that $\exp(h\nu/kT_{\mathrm{dust}}) - 1 \approx h\nu/kT_{\mathrm{dust}}$ and therefore

$$B_\nu(T_{\mathrm{dust}}) \approx \frac{2\nu^2 kT_{\mathrm{dust}}}{c^2}. \tag{3.23}$$

Consequently, if the dust temperature T_{dust} can be estimated from the observed spectrum (typically 10–20 K for CTTSs), the measurement of the flux density F_ν allows the determination of the disc mass, provided that both the opacity κ and the distance d to the object are known (Draine, 2006). Typical Class II disc masses obtained from (sub-)mm dust observations range between 0.001–0.1 $M_\odot$, however, the determination of precise disc masses is subject to several uncertainties and possible sources of error, such as the assumed dust-to-gas ratio or the grain size distribution.

However, one of the biggest sources of uncertainty when estimating disc masses from dust observations is the disc opacity κ, as the prescription given by Eq. 3.19 only applies to dust grains with sizes between $\sim$ 0.3–3 mm, while decreasing significantly for larger-sized bodies ($\sim$ 1 m, cf. D'Alessio et al., 2001). This implies that a large amount of mass is hidden in larger bodies than micron-sized dust as significantly more mass can be held in pebbles or even planetesimals within the same solid angle without significantly affecting the observed SED (cf. Williams, 2012). This hints towards disc masses being systematically underestimated by (sub-)mm observations, raising the question if the observed discs are even massive enough in order to form the observed population of exoplanetary systems.

Different authors have posed this question (e.g., Greaves & Rice, 2010; Najita & Kenyon, 2014, or Manara et al. 2018) and found that the dust disc masses determined from (sub-)mm continuum emission are systematically too low in order to form the observed exoplanetary systems. And indeed, Draine (2006) find that observations at a given wavelength λ can only constrain the dust grain properties up to a maximum size of $r_{\mathrm{max}} \sim 3\lambda$, showing that a significant fraction of the total disc mass may remain undetected when a disc is observed only at a single wavelength (Williams & Cieza, 2011). For example, disc masses estimated from accretion rates of T Tauri stars (measured via UV-observations) are systematically higher by about an order of magnitude ($M_{\mathrm{d}}/M_\odot \approx$ 1–20 %, e.g., Hartmann et al., 1998) than those obtained from (sub-)mm observations ($M_{\mathrm{d}}/M_\odot \approx 1$ %, e.g., Andrews & Williams, 2005, 2007; van der Marel et al., 2016), while some direct estimates from gas mass tracers yield orders of magnitude lower disc

masses than dust observations (Mannings & Sargent, 1997; Guilloteau & Dutrey, 1998; Natta, 2004). Each of these tracers are subject to different limitations and uncertainties, highlighting the necessity of using different disc mass tracers in order to obtain a global picture of the structure and evolution of protoplanetary discs.

Thus it is highly likely that observed disc masses are simply underestimated and that they represent the lower limit of true disc masses. Another valid possibility is, however, that planet formation must occur significantly earlier than previously thought, possibly already during the Class I stage (Tychoniec et al., 2018), in which disc masses are high enough in order to potentially explain the observed initial mass function of exoplanetary systems (e.g., Schib et al., 2020). One example for this is the famous HL Tau disc (ALMA Partnership et al., 2015), which has an estimated age of $\lesssim$ 1–2 Myr (Briceño et al., 2002). The gaps and vortices observed in this system can be well reproduced by 2D hydrodynamical simulations which consider the presence of several massive cores in the outer parts of the disc ($\sim$ 10–20 au, cf. Picogna & Kley, 2015). This suggests that planet formation in the outer disc must occur much earlier than the median lifetime of 2–3 Myr, possibly via gravitational instability (see Section 3.4 for details).

Disc radii

In Section 3.1, we have derived that the surface density profile of a purely viscously evolving disc can be described by an exponentially tapered profile (Eq. 3.10). This theoretical prediction has been indeed confirmed by observational studies, even though radii of protoplanetary discs are hard to determine as their outer parts are cool and consequently only emit weakly. Further, the dust and gas component are not necessarily coupled as dust grains tend to drift inwards (known as 'radial drift'). Thus observations of different disc tracers naturally provide different estimates of the outer disc radii, with molecular gas emission typically extending to larger radii than dust continuum emission, which tends to show sharp outer edges (e.g., Birnstiel & Andrews, 2014; Rosotti et al., 2019, and see also Figure 3.2).

Dust disc radii of T Tauri stars are typically found to be $\lesssim$ 200-300 au, with only few reaching radii $\gtrsim$ 500 au (e.g., Vicente & Alves, 2005; Hughes et al., 2008; Andrews et al., 2009, 2010; van der Marel et al., 2018). Further, older stars are typically found to have larger radii (e.g., Isella et al., 2009, but see also Hendler et al. 2020 who find opposite behaviour), which is consistent with the prediction of the spreading of a viscously evolving disc (cf. Figure 3.1). The reason for the discrepancy on the disc radii of older stars lies in the fact that as the disc is viscously expanding while it is being accreted onto the host star, also its opacity will decrease significantly. Thus, even though the disc may have effectively become larger, this may not be observable and consequently it may appear smaller with increasing age (see e.g., Rosotti et al., 2019).

Accretion rates

It is observationally established that protoplanetary discs show a wide range of accretion rates, ranging from 10^{-7} to $10^{-9}\,M_\odot\,\mathrm{yr}^{-1}$ (e.g., Alexander et al., 2014). The average mass accretion

rate for T Tauri stars is $\sim 10^{-8}\,M_\odot\,\mathrm{yr}^{-1}$ and is observed to decrease with stellar age as $\dot{M}_{\mathrm{acc}}(t) \propto t^{-1.5}$ to $t^{-2.8}$ (cf. Gullbring et al., 1998; Hartmann et al., 1998), which is consistent with the analytical models of disc structure that were discussed previously. Further, the accretion rate is observed to depend on stellar mass as $\dot{M}_{\mathrm{acc}} \propto M_\star^2$ (Muzerolle et al., 2005).

In order for accretion of circumstellar matter to happen, a fraction of disc material needs to loose energy and angular momentum so that it can fall into the gravitational well of the central star (D'Alessio et al., 2004). The accreted gas is thought to be channeled onto the central star along magnetospheric field lines that truncate the disc at a few stellar radii, a process known as magnetospheric accretion (Koenigl, 1991; Shu et al., 1994; Bouvier et al., 2007). As the material falls freely onto the stellar surface, energy will be released via hot accretion shocks (Calvet & Gullbring, 1998) that can be directly measured by the excess radiation over the photospheric emission. As the emitted luminosity essentially corresponds to the released potential energy (Garcia, 2011), the accretion luminosity can be written as:

$$L_{\mathrm{acc}} = \left(1 - \frac{R_\star}{R_{\mathrm{in}}}\right) \frac{GM_\star \dot{M}_{\mathrm{acc}}}{R_\star} \approx 0.8 \frac{GM_\star \dot{M}_{\mathrm{acc}}}{R_\star}, \tag{3.24}$$

where $R_\star$ is the stellar radius and R_{in} is the inner radius of the circumstellar accretion disc, which can be assumed to be $R_{\mathrm{in}} \approx 5R_\star$, resulting in the prefactor of 0.8.

Observations of Hα emission lines, which trace hot gas falling onto the star, show that magnetospheric gas accretion is an important draining process within the inner regions of the circumstellar disc (e.g., Calvet & Gullbring, 1998; Hartmann et al., 1998), especially at early times when the disc is still massive. Magnetospheric accretion has therefore a strong impact on the viscous evolution of a disc and significantly shortens its lifetime compared to models of pure viscous evolution (cf. Bouvier et al., 2007, for a review). However, due to the power-law decline of the mass accretion rate with radius, it is inefficient in removing disc mass on large scales within the observed disc lifetimes, where most of the material resides. Here, where the gravitational influence of the star becomes less strong, mass loss within the disc is mainly dominated by disc winds. High-energetic radiation, emitted by the central or a nearby star, irradiate the disc and heat the surface layers, driving escaping mass flows from the outer regions of the disc. The inner part can then be drained by viscous accretion, causing the disc to spread due to angular momentum transport, while photoevaporative winds mainly remove the outer disc mass reservoir.

Lifetimes

The lifetime of planet-forming discs is one of the most fundamental quantities to determine, as it sets a strict upper limit for the accretion of gas onto planetary cores, and therefore the formation of giant planets. Large-scale studies of nearby star-forming regions have established that the nIR excess emission, being a robust tracer of hot circumstellar dust at $\sim$ au radii, as well as spectroscopic accretion signatures that trace hot gas impinging on the stellar photosphere (e.g., Hartigan et al., 1995) disappear on timescales of only a few million years (cf. Calvet et al., 2000; Hillenbrand, 2005, for reviews).

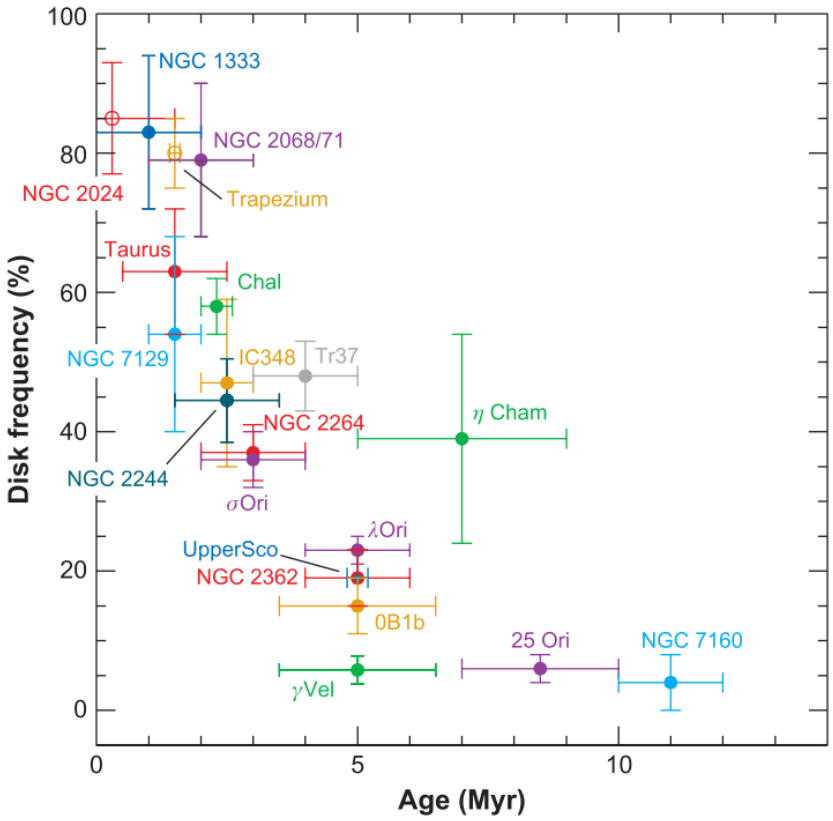

Figure 3.4: Fraction of Sun-like stars with detectable near-IR excess as a function of time. Image reproduced from Wyatt (2008, and references therein) with permission from Annual Reviews.

This is illustrated in Figure 3.4, which shows the fraction of Sun-like stars with detectable nIR-excess emission from various different open stellar clusters as a function of their age, obtained by Wyatt (2008). It can be clearly inferred that the frequency of disc-bearing stars decreases strongly from almost 90 % at < 1 Myr to less than 10 % at $\gtrsim 5$ Myr. Consequently, after about 10 Myr, most YSOs are observed to be disc-less rather than disc-bearing (e.g., Strom et al., 1989; Skrutskie et al., 1990; Haisch et al., 2001; Hernández et al., 2007; Fedele et al., 2010; Ribas et al., 2014, 2015). This decay in time is well described by an exponential function with a characteristic (or *e*-folding) time of ~ 2.5 Myr, which is often reported as the mean disc lifetime (e.g., Mamajek, 2009).

Transition discs

As nIR-emission only traces the hot dust that is located in the innermost regions of the disc, it cannot provide any evidence on the presence of dust at larger radii. Therefore one might argue that YSOs *without* a detectable nIR-excess, which is indicative of a hole in the inner disc regions could, however, host longer-lived outer discs with plenty of left-over circumstellar material emitting in the mIR regime, which can just not be detected at shorter wavelengths.

The launch of the *Spitzer* Space Telescope (*Spitzer*) had been fundamental to answering

this open question, as it offered the necessary sensitivity and wavelength coverage in order to enable observations of discs in the mIR regime. Targeted studies towards Class II and Class III objects showed, however, that there are only very few discs with lacking nIR excess, but detectable mIR emission ($\sim$ 10 % for F–M-type stars, see e.g., Skrutskie et al., 1990). These objects would be located to the lower right of primordial (i.e. Class II objects with strong nIR+mIR excess emission) and disc-less (i.e. Class III objects with very weak nIR+mIR excess emission) YSOs in the infrared $K[8\,\mu\text{m}]$–$K[24\,\mu\text{m}]$ two-colour plane, indicating a lack of disc emission at small radii, but optically thick disc emission at larger radii (e.g., Koepferl et al., 2013). Often however, these intermediate objects show stronger fIR excess than what would be expected from a typical Class II/Class III SED. Ercolano et al. (2015) attributed this to the lacking presence of an inner disc, which would normally absorb most of the stellar irradiation and therefore prevent the photons from reaching and heating the outer disc. Therefore, the large inner holes identified in such intermediate objects have been commonly interpreted as a signpost of their final dispersal. However, the scarcity of discs that are being *caught in the act* of dispersing, the so-called transition discs (TDs), necessarily implies that the transition from primordial to disc-less YSOs must occur rapidly – on the order of a few 10^5 yr, proceeding from the inside-out (e.g., Strom et al., 1989; Skrutskie et al., 1990; Wolk & Walter, 1996; D'Alessio et al., 2005; Cieza et al., 2007; Luhman et al., 2010; Ercolano et al., 2011).

TDs are a diverse class of objects and thus it is difficult to define them in an unambiguous fashion. While early studies classified TDs solely based on their IR-SED as being on the verge of dispersal, a distinct class of TDs had been identified especially with the advent of ALMA – discs with high accretion rates but large holes, and with bright mm-emission tracing large reservoirs of cold gas (e.g., Andrews et al., 2011). They further show a large variety of substructures, such as rings, gaps, but often also non-axissymmetric structures like spirals, shadows or vortices. Therefore, this new class of objects do not fall under the classical definition of TDs, as they correspond to rather massive and possibly long-lived objects that are clearly not in the process of dispersing (cf. Owen, 2016, for a review).

Based on the strength of the $\lambda = 1.33\,\text{mm}$ flux, Owen & Clarke (2012) divided the at the time available sample of TDs into mm-bright (i.e. high dust mass) and mm-faint (i.e. low dust mass) objects, with the transition occurring at $F_\nu = 30\,\text{mJy}$. They found that these two populations have entirely different distributions of hole sizes and accretion rates. While mm-faint objects generally have smaller holes ($\lesssim 10\,\text{au}$), with the vast majority only showing some rather weak accretion signatures ($\sim 10^{-10}$–$10^{-9}\,M_\odot\,\text{yr}^{-1}$), mm-bright objects typically have larger holes ($\gtrsim 20\,\text{au}$) and higher accretion rates ($\gtrsim 10^{-8}\,M_\odot\,\text{yr}^{-1}$). These completely different physical properties of both populations of TDs hint towards different formation routes. As mm-faint TDs are consistent with discs being in the process of dispersing, they are believed to be a direct consequence of disc dispersal mechanisms, such as photoevaporation or other disc-driven winds, and thus can be placed between Class II and Class III discs. In contrast, mm-bright TDs are too massive ($M_\text{d} \gtrsim 10\,M_\text{J}$, cf. van der Marel et al., 2016) for processes like photoevaporation to be dominant, as they are often found around young Class II or even Class I YSOs. Therefore, the substructures like rings and gaps that are routinely observed in their mm-surface density are typically attributed to nascent forming planets and planet-disc interactions, rather than disc dispersal.

3.3 Limitations of viscous accretion models

In Section 3.1 we have derived a simple analytical framework solely based on viscous evolution that is able to reproduce the observed morphology and physical properties of planet-forming discs to sufficient accuracy. An important consequence of this simplified treatment is, however, that it predicts the mass accretion rate onto the star to decline as $\dot{M}_{\rm acc}(t) \propto t^{-1.5}$, where $\dot{M}_{\rm acc}(R) \propto \nu\Sigma(R)$. Thus, purely viscously evolving discs should disperse in such a way that with time, they become progressively fainter at *all* wavelengths. This process would gradually become slower, as the mass accretion rate declines over time. Therefore, viscous disc evolution models predict an indefinitely long phase of expansion during the dispersion process, which is, however, in tension with the previously discussed observations of transition discs, which predict a short dispersal time ($\sim 10\,\%$ of the total disc lifetime) that proceeds from the inside out. Hence it can safely be concluded that viscous accretion alone is not the only process that is responsible for dispersing circumstellar accretion discs. While there are a range of processes that can reproduce the observed features and properties of TDs, only viscous accretion and disc winds can be considered as true global disc dispersal mechanisms, as they shape the surface density structure of the disc globally and remove both mass and angular momentum from the system. While the early phases of disc evolution can be generally considered as being solely accretion-dominated, at late stages, disc-driven winds will start to dominate the overall mass loss.

For disc-driven winds, it is not fully established yet in which flavour they occur (see Ercolano & Pascucci, 2017, for a detailed review). Given that young T Tauri stars show highly elevated levels of magnetic activity (cf. Section 2.3), it appears obvious to assume that the energetic photons coming from the central star may blow away all of the circumstellar gas. However, also non-ideal MHD-effects are very likely candidates for the origin of disc winds (e.g., Bai & Stone, 2013; Bai, 2016; Suzuki et al., 2016), even though they would entail that the classic, quite convenient α-disc model is inapplicable and therefore deprecated. This would invoke a major paradigm shift in the astrophysical community, as the α-model has been incredibly successful in explaining several key aspects of circumstellar discs, while at the same time being surprisingly simple. Further, while photoevaporative winds will only carry away mass from the disc, MHD-driven winds can remove both mass and angular momentum from the system, leading to the so-called wind-driven accretion. Consequently, clear observational diagnostics are required in order to distinguish between MHD- and photoevaporation-driven winds (e.g., Gressel et al., 2020; Weber et al., 2020), even though it is also possible that both effects act simultaneously (e.g., Wang et al., 2019; Kunitomo et al., 2020; Rodenkirch et al., 2020).

Hence, while the α-model is extremely successful in explaining several key properties of planet-forming discs, observations cannot unequivocally prove it. Future work will therefore have to focus on providing both theoretical and observed constraints on the origin of disc winds and especially the origin of turbulence in planet-forming discs.

3.4 Planet formation

Planets are born out of the dust and gas that is left over from the star formation process. The initial conditions for planet formation are thus determined by the properties of their surrounding planet-forming discs, which evolve and disperse as they give birth to planets. Interestingly, the timescales of disc dispersal are comparable to those of planet formation, suggesting that the dispersal mechanism must already dominate disc evolution at the time at which planets form. Conversely, the process of planet formation also strongly shapes the disc, making the two separate fields of planet formation and disc evolution a tightly coupled and complex problem. A too complex problem to be treated in its entirety in this thesis. Therefore, we will solely focus on the formation of gas giants in the following and only briefly summarise key aspects.

Core accretion

Giant planets are thought to form via two main routes – core accretion and gravitational instability, where the former is believed to be the dominant mechanism (cf. D'Angelo & Lissauer, 2018, for a review). Core accretion is based on a hierarchical collisional accumulation of micron-sized dust grains that collide and stick with a certain probability (which mostly depends on the relative velocity of the impact, as well as the dust composition), thereby forming a so-called planetary embryo. By accreting smaller bodies and nebular gas during their orbital motion around the star, the embryo can grow from pebble-size ($\sim$ cm to m) to a planetesimal ($\sim$ km), before finally assembling into a planetary core with typical masses between 5–15 Earth masses[12]. These cores then accrete nebular gas and reach around Jupiter mass (Laughlin et al., 2004). This requires, however, a large reservoir of icy dust and gas, which can only be found in the cool outer parts of the disc, typically at distances of 5–10 au around solar-type stars. Once the protoplanet has reached a sufficiently high mass of $\sim 30\,M_\oplus$, while the disc is still gas-rich, it will go into the so-called runaway gas accretion regime, in which it is able to efficiently accrete a gaseous envelope in the matter of only a few $\sim 10^5$ yr (Pollack et al., 1996), ultimately forming a gas-rich giant planet.

While core accretion is the currently favoured scenario for the formation of giant planets (at least at intermediate distances to the central star), there still remains a large number of open questions. For example, the just described scenario assumes that most collisions between dust grains will indeed lead to sticking and their subsequent coagulation. In reality, however, there are several barriers that need to be overcome during the assembly of planetary bodies, such as the *bouncing barrier* and the *meter-sized barrier*. These barriers describe a persistent problem in planet formation theories, where particles with sizes of ~ 1 m fail to grow further as collisions with other particles will either lead to their fragmentation rather than their coagulation, or they drift inwards so rapidly that they are lost onto the central star before they can continue growing (cf. Weidenschilling, 1977, and Morbidelli & Raymond 2016, for a review). Possible solutions to these barriers include more realistic models on the dust grain composition (e.g., Okuzumi et al., 2012; Kataoka et al., 2013), the streaming instability (Youdin & Goodman, 2005), or the so-called pebble accretion (e.g., Ormel & Klahr, 2010; Lambrechts & Johansen,

[12] *Earth mass*, $1\,M_\oplus = 5.97 \times 10^{24}$ kg (Williams, 2019)

2012). However, further theoretical work is required in order to fully assess the efficacy of these processes in different disc environments.

Gravitational instability

An alternative route to the core accretion model is the so-called gravitational instability (or disc instability), in which planets form through global gravitational instabilities that emerge in the disc (e.g., Boss, 1997; Mayer et al., 2002). The basic idea behind this scenario is the same as for the formation process of stars – a sufficiently massive disc (i.e. $M_\mathrm{d} \approx M_\star$) becomes unstable to gravitational collapse, which leads to its fragmentation and the formation of a self-gravitating clump that will later form a planet (Kuiper, 1951). Consequently, similar conditions as for the star formation process discussed in Section 2.1 (such as the local Jeans mass or the necessary cooling, cf. Rice et al., 2003) have to be fulfilled (cf. Kratter & Lodato, 2016, for a review).

The main parameter describing the disc's stability against gravitational collapse is the so-called *Safronov-Toomre criterion* (Safronov, 1960; Toomre, 1964):

$$Q = \frac{c_\mathrm{S}\kappa}{\pi G \Sigma}, \tag{3.25}$$

where c_S is the sound speed of the gas, κ is the local epicyclic frequency (for which $\kappa = \Omega_\mathrm{K}$, if the disc is Keplerian), G is the gravitational constant and Σ is the 2D surface density of the disc. A geometrically thin disc is unstable to gravitational collapse if $Q < 1$, and thus it immediately follows from Eq. 3.25 that cold and massive regions of a protoplanetary disc are more susceptible to becoming gravitationally unstable.

Models have shown that gravitational instability tends to form very massive giant planets with many even falling into the brown dwarf regime (e.g., Stamatellos & Whitworth, 2009) at large disc radii (e.g., Boss, 2011; Meru & Bate, 2011), where cold dust and gas is abundant. Therefore, the gravitational instability is typically initiated at early times, when the disc is massive and gas-rich and would be rapid, only taking a few several orbital timescales (D'Angelo & Lissauer, 2018), noting however that the actual contraction to Jupiter-size would take significantly longer (Cameron et al., 1982). This makes disc instability a viable alternative to the relatively slow formation of giant planets via core accretion, at least for planets that have formed at large radial distances to their host star, such as the famous four-planet system HR 8799 (Marois et al., 2008; Konopacky & Barman, 2018).

Further, even though gravitational instability tends to form planets at large distances of their host star, they can nevertheless migrate to small distances very rapidly, thus, providing another possible interpretation for the giant planets located at orbital distances of several astronomical units (see also Chapter 8, in which we find that planets that have potentially formed via gravitational instability preferentially pile-up outside of the desert of planets, which is formed by X-ray-driven photoevaporation). In summary, planet formation via gravitational instability may provide a promising avenue for the origin of substructures at large radii specifically observed in young T Tauri discs such as HL Tau, which are typically attributed to nascent, massive planets rather than disc dispersal.

Chapter 4

The dispersal of planet-forming discs via photoevaporative winds

As we have established in Section 3.2, the lifetimes of circumstellar discs around low-mass stars are observed to be short, hence an efficient mechanism is required that can rapidly deplete the disc both on small and large scales. This chapter will focus on giving an overview of photoevaporation, which is believed to be the dominant mechanism that drives the dispersal of discs.

4.1 Theoretical concepts

Disc dispersal via photoevaporation occurs when high-energy, stellar photons irradiate and heat the surface layers of the surrounding planet-forming disc to such temperatures ($\sim 10^3$–10^4 K), that at a given radius a thermal wind is launched, that can ultimately escape the gravitational potential of the central star (cf. Hollenbach et al., 2000; Clarke, 2011; Alexander et al., 2014; Gorti et al., 2016; Ercolano & Pascucci, 2017, for reviews). Figure 4.1 shows a sketch of the three main stages of the evolution and dispersal of discs that are subject to both viscosity and disc winds, adapted from the recent review article by Ercolano & Pascucci (2017). In this schematic picture, the disc surrounding the central star is composed of dust and gas, which is irradiated by stellar ultraviolet and X-ray photons. The accreted gas is funneled onto the central star via magnetospheric field lines that truncate the disc at a few stellar radii (see Section 3.2). It is important to note though, that Figure 4.1 includes the contribution of MHD- as well as photoevaporative winds. While it is possible that both processes can act simultaneously (cf. Section 3.3), MHD-driven winds would invoke that the evolution of the surface density and of the mass accretion rate is unlikely to be well described by the α-mechanism that was derived in Section 3.1. Hence, we will solely focus on models of photoevaporation-driven disc dispersal in the following. We note, however, that detailed investigations on the origin of disc winds are on the way (e.g., Gressel et al., 2020; Weber et al., 2020).

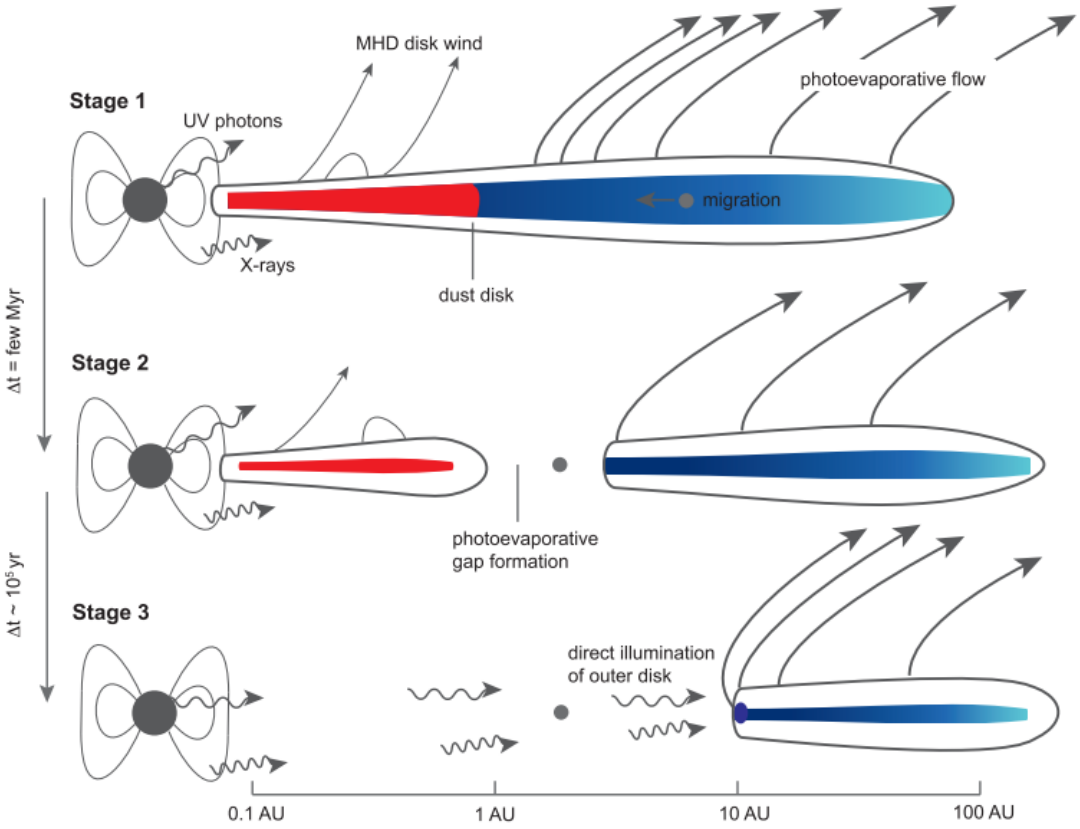

Figure 4.1: The three main stages of disc evolution and dispersal, adapted from Ercolano & Pascucci (2017) based on an earlier figure by Alexander et al. (2014).

Stage 1: Viscous evolution

In the (currently accepted) standard picture of accretion discs, for most of their lifetime disc evolution is mainly governed by viscous accretion onto the host star, while at late times, mass loss via photoevaporative winds starts to dominate. This means that even though photoevaporation may remove *some* mass already at early stages of disc evolution, the total mass loss is clearly dominated by viscous accretion, and subsequently the impact of photoevaporation on the radial surface density distribution is only marginal during the first few million years.

The surface density of the disc then gradually decreases over time and so does the mass accretion rate following $\dot{M}_{\rm acc} \propto t^{-1.5}$ (cf. Eq. 3.15), whereas the wind mass loss rate stays roughly constant. Thus, the disc's opacity gradually decreases, allowing the incident radiation coming from the host star to penetrate deeper disc layers with time. While more energetic photons (e.g. hard X-rays, far-ultraviolet) will be able to launch winds once the mass accretion rate falls below $\dot{M}_{\rm acc} \lesssim 10^{-6}\,M_\odot\,{\rm yr}^{-1}$, less energetic photons (e.g. extreme-ultraviolet, soft X-rays) will be only able to penetrate sufficiently large columns at later times, namely once $\dot{M}_{\rm acc} \lesssim 10^{-8}\,M_\odot\,{\rm yr}^{-1}$ (Gorti et al., 2009). This means that at some point in time at a given location, the viscous accretion rate drops below the wind mass loss rate, so that $\dot{M}_{\rm acc} < \dot{M}_{\rm w}$. At

this point, photoevaporation starts to dominate the overall mass loss as any gas parcels outside to this radius are inevitably blown away by the thermal disc winds, rather than being accreted onto the central star. Photoevaporation-driven mass loss then gradually starves the disc inside of the location, where $\dot{M}_{\rm acc} = \dot{M}_{\rm w}$, as it is deprived of any further mass replenishment coming from the outer disc. This leads to the formation of an evacuated annular gap, or cavity, that fully detaches the inner from the outer disc.

The location at which the gap is first opened can be described by the gravitational radius:

$$R_{\rm g} \equiv \frac{GM_\star}{c_{\rm s}^2} = \frac{GM_\star \mu m_{\rm H}}{kT}, \tag{4.1}$$

which is the radius at which the sound speed of the heated gas equals the local Keplerian velocity (i.e. $c_{\rm S} = \sqrt{GM_\star/R_{\rm g}}$). Consequently, in order for thermal winds to be launched, the temperature of the gas has to exceed the local escape temperature. Eq. 4.1 can then be written in a more convenient way as:

$$R_{\rm g} \approx 6.8\,{\rm au} \left(\frac{M_\star}{M_\odot}\right) \left(\frac{T}{10^4\,{\rm K}}\right)^{-1}, \tag{4.2}$$

where T is the temperature of the heated gas layer at the base of the flow and $M_\star$ is the mass of the central star (Liffman, 2003). However, both analytical and numerical models have shown that thermal winds can be already launched at significantly smaller radii of $\sim R_{\rm g}/5$ (e.g., Liffman, 2003; Adams et al., 2004; Font et al., 2004; Dullemond et al., 2007), which is often termed the critical radius:

$$R_{\rm crit} \approx 0.2\,R_{\rm g} \approx 1.4\,{\rm au} \left(\frac{M_\star}{M_\odot}\right) \left(\frac{T}{1000\,{\rm K}}\right)^{-1}. \tag{4.3}$$

For solar-type stars, the critical radius thus lies between $\sim$ 1–10 au.

Stage 2: Gap opening

Clarke et al. (2001) described the process of gap opening as a 'switch', which is activated as soon as the accretion rate through the disc declines to a sufficiently low level that roughly matches the photoevaporative mass loss from the disc outside 5–10 au. While the exact values for the location and time of gap opening depend on the assumed spectra of the impinging photons, Clarke et al. (2001) found that in the case of EUV photoevaporation the switch is initiated once $\dot{M}_{\rm acc} \lesssim 10^{-10}\,M_\odot\,{\rm yr}^{-1}$. At this point, the true dispersal phase of the disc begins, which will only last for a few 10^5 yr, proceeding from the inside out. Inside the cavity, the heated and ionised gas forms a bound atmosphere, which partly absorbs the incoming stellar flux, therefore preventing it from reaching and heating the inner rim of the outer disc (Armitage, 2013). Outside of the cavity, the gas particle's thermal energy exceed their gravitational binding energy, so that the gas becomes unbound and is blown away via thermally-driven disc winds.

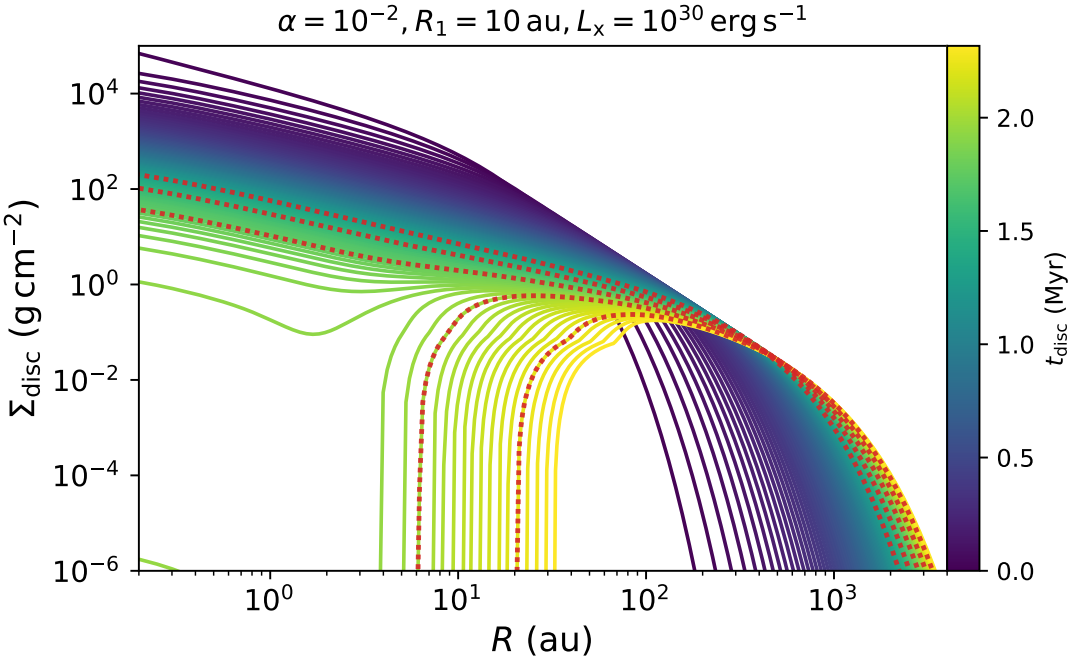

Figure 4.2: Surface density evolution of a circumstellar disc subject to viscosity and photoevaporation. The initial conditions of the disc are $M_\star = 1\,M_\odot$, $M_\mathrm{d} = 0.1\,M_\odot$, $\alpha = 10^{-2}$, $R_1 = 10\,\mathrm{au}$, $H/R = 0.05$ and $L_\mathrm{x} = 10^{30}\,\mathrm{erg\,s^{-1}}$ for the photoevaporation profile from Owen et al. (2012). The colour-coding for the solid lines shows the corresponding age of the disc at a given timestep. The red dashed lines mark the surface density profile at 55 %, 65 %, 75 %, 85 % and 95 % of the total disc lifetime, in order to illustrate the so-called 'two-timescale behaviour', which is a rather long period of viscous disc evolution, followed by the rapid dispersal of the disc due to photoevaporation.

Stage 3: Final dispersal

Since the cavity prevents any mass flow from the outer to the inner disc, the latter will be accreted onto the central star roughly on the viscous timescale ($\sim 10^5\,\mathrm{yr}$). This reduces the inner disc's opacity such, that the inner rim of the outer disc can be directly irradiated by the central star (Alexander et al., 2006a,b), which leads to the efficient heating and outward removal of the outer disc. This direct illumination triggers an even faster dispersal of the outer disc, which will only last a few $10^5\,\mathrm{yr}$ (e.g., Clarke et al., 2001; Gorti & Hollenbach, 2009).

The timescales of disc evolution are demonstrated in Figure 4.2, which shows the surface density evolution of a planet-forming disc subject to viscosity and X-ray photoevaporation. The red dotted lines highlight the disc structure at selected timesteps between 55 % to 95 % of the total disc lifetime. The observed *two-timescale behaviour* – a rather long period of viscous disc evolution, followed by the rapid dispersal of the disc due to photoevaporation – can be easily reproduced by the above described scenario. Consequently, the combination of viscous accretion theory and photoevaporation models are a very efficient route to disperse circumstellar discs within the observed disc timescales.

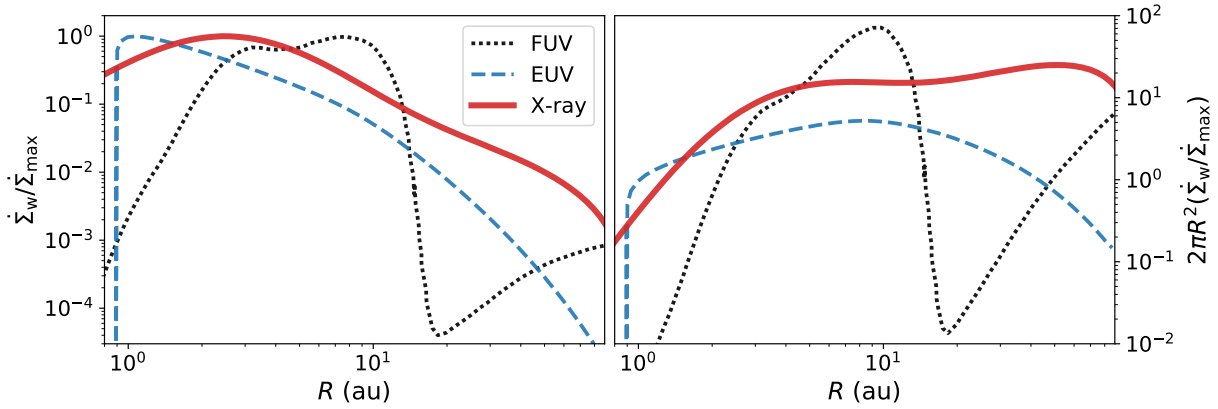

Figure 4.3: Surface mass loss profiles as a function of disc radius for different photoevaporation models around a $1\,M_\odot$ star. The left panel shows the normalised surface mass loss rates of an FUV- (dotted line, Gorti et al., 2009), an EUV- (dashed line, Font et al., 2004), and an X-ray-dominated photoevaporation profile (solid line, Owen et al., 2012). The right panel shows the same profiles scaled with $2\pi R^2$ in order to illustrate which disc region is most affected by photoevaporative mass loss. The underlying data was obtained from Alexander et al. (2014).

4.2 Photoevaporation models

While it is generally accepted that photoevaporative winds must play an important role in the dispersal of circumstellar discs, there is no consensus so far on the details of the underlying model. Photoevaporation models need to take the coupling between radiative transfer, thermodynamics as well as hydrodynamical effects into account. Hence, full radiation-hydrodynamic simulations are not only extremely computationally expensive, but their results are also highly sensitive on the assumptions and complexity of the underlying model, leading to considerable differences between different models.

The biggest difference lies in the assumed spectrum of the impinging photons, for which three wavelength regimes are of particular importance to protoplanetary discs: far-ultraviolet radiation (FUV), extreme-ultraviolet radiation (EUV) and X-rays. It is, however, still debated in the literature as to what type of radiation may be the main driver of photoevaporative winds. The radial mass loss distribution of the three profiles is demonstrated in Figure 4.3. The left panel shows the normalised mass loss rate per unit area, $\dot{\Sigma}_w/\dot{\Sigma}_{norm}$, as a function of disc radius for an EUV- (Font et al., 2004), an FUV- (Gorti et al., 2009) and an X-ray-dominated wind (Owen et al., 2012). It can be clearly seen that these different profiles have their peak at different locations, hence triggering mass loss from different regions in the planet-forming disc. This is emphasised in the right panel of Figure 4.3, that shows the normalised mass loss per interval radius, i.e. $2\pi R^2(\dot{\Sigma}_w/\dot{\Sigma}_{norm})$, and thus reflects which disc region is most affected by photoevaporative mass loss. It is important to note, however, that in Figure 4.3 only normalised mass loss rates are shown. The *total* values, however, can differ by up to two orders of magnitudes, highlighting the fact that different mass loss profiles will shape a given disc in completely different ways.

Extreme Ultraviolet (EUV)

EUV photons have high enough energies ($13.6\,\mathrm{eV} \leq h\nu < 100\,\mathrm{eV}$) to ionise hydrogen atoms in the upper layers of the disc, which are subsequently heated to nearly isothermal temperatures of $T \approx 10^4\,\mathrm{K}$ with escape velocities of $c_\mathrm{S} \approx 10\,\mathrm{km\,s^{-1}}$. The ionised and nearly isothermal atmosphere produced by EUV photoevaporation is then separated from the underlying disc by an ionisation front, which is a sharp boundary between the ionised and the neutral gas.

The heating rate due to EUV is not very sensitive to the incident spectrum, as the dominant contribution to the ionisation rate comes mainly from photons at or close to the energy threshold. Thus, the integrated mass loss rate for the EUV case depends mostly on the EUV photon rate Φ_EUV:

$$\dot{M}_\mathrm{w} \approx 1.6 \times 10^{-10} \left(\frac{\Phi_\mathrm{EUV}}{10^{42}\,\mathrm{s^{-1}}}\right)^{1/2} \left(\frac{M_\star}{M_\odot}\right)^{1/2} M_\odot\,\mathrm{yr^{-1}}, \tag{4.4}$$

resulting in mass loss rates of $\sim 10^{-10}\,M_\odot\,\mathrm{yr^{-1}}$ for typical EUV photon rates of $\Phi_\mathrm{EUV} \approx 10^{41}\,\mathrm{s^{-1}}$ observed for solar-type stars. Alexander et al. (2006a) found that this value can be increased by around an order of magnitude, if the direct irradiation of the outer disc is taken into account once the inner disc is sufficiently depleted. The critical radius can be written as:

$$R_\mathrm{crit,EUV} \approx 1.8\,\mathrm{au} \left(\frac{M_\star}{M_\odot}\right), \tag{4.5}$$

and thus, for a solar-mass star, the gap due to EUV photoevaporation will be roughly opened at $\sim 1.8\,\mathrm{au}$ (Alexander et al., 2014).

EUV photons have a penetration depth of the order $N_\mathrm{H} \approx 10^{20}\,\mathrm{cm^{-2}}$ and are thus readily absorbed by relatively small columns of neutral hydrogen (Hollenbach & Gorti, 2009; Gorti & Hollenbach, 2009). Hence, EUV observations of T Tauri stars suffer strongly from the strong absorption of the ionising photons by intervening neutral hydrogen atoms and consequently, the value for the ionising photon fluxes of T Tauri stars is only poorly constrained. Current data suggest, however, that the photon rates are generally too low ($\Phi_\mathrm{EUV} \lesssim 10^{42}\,\mathrm{s^{-1}}$), in order to drive significant mass loss. The mass loss rate is mostly concentrated around the gravitational radius of $\sim 10\,\mathrm{au}$ (cf. right panel of Figure 4.3), which makes EUV photoevaporation rather ineffective in removing the outer disc mass reservoir. This, combined with the low mass loss rate of $\dot{M}_\mathrm{w} \sim 10^{-10}\,M_\odot\,\mathrm{yr^{-1}}$, suggests that EUV photoevaporation alone cannot be an effective global disc dispersal mechanism, at least until late times of disc evolution when most of the inner disc has been already dispersed.

Far Ultraviolet (FUV)

FUV photons ($6\,\mathrm{eV} \leq h\nu \leq 13.6\,\mathrm{eV}$) can dissociate hydrogen molecules, however their energies are not sufficient to ionise hydrogen atoms. As the underlying theory of FUV-photoevaporation is the most complex out of three different profiles, the underlying mechanisms are not yet fully

understood. Still, qualitatively similar behaviour can be expected from FUV-driven photoevaporation as for the EUV case, while the strength of the winds are more comparable to those driven by X-rays.

FUV photons have penetration depths of $N_{\mathrm{H}} \sim 10^{21}$–$10^{23}\,\mathrm{cm}^{-2}$, which strongly depend on the abundance and properties of the small dust grains as well as the PAHs, as they absorb the bulk of the incoming FUV flux and re-irradiate it as thermal IR-emission (Alexander et al., 2014; Ercolano & Pascucci, 2017). Thus, FUV photons can penetrate significantly deeper columns than EUV, and therefore drive more vigorous winds with mass loss rates of $\sim 10^{-8}\,M_{\odot}\,\mathrm{yr}^{-1}$, which is about two orders of magnitude larger than for EUV-driven winds (e.g., Gorti & Hollenbach, 2009). However, FUV mass loss rates are far more uncertain than for the EUV or X-ray case, as current models are not based on hydrodynamical calculations, but solely on 1+1D thermochemical calculations that assume hydrostatic equilibrium.

In contrast to the EUV case, in which the mass loss is concentrated around the gravitational radius, the FUV surface mass loss profile peaks at around the same location (5–10 au), while also driving significant mass loss in the outermost parts of the disc (i.e. beyond $\gtrsim 100\,\mathrm{au}$, cf. right panel of Figure 4.3). Hence, in the FUV case, winds may also be launched from the outer disc regions, which in some cases, may lead to the opening of secondary gaps that are located outside of the gravitational radius. These vigorous winds in the outer disc regions may provide a possible solution to the 'relic disc problem' that was previously discussed in Section 3.2, however, hydrodynamical calculations are needed to definitely assess the importance of FUV-driven photoevaporation on the dispersal of discs.

It is important to note though, that in the photoevaporation scenario, gaps in the surface density will only open if the incident radiation field has a significant non-accretion generated component, meaning that it is mainly chromospheric or coronal in origin (Gorti et al., 2015, 2016). When this is the case, the impinging photon flux stays rather constant while the star is still surrounded by a disc, allowing its continuous heating due to the stellar irradiation. This is naturally the case for EUV or X-ray photons, but not necessarily for FUV photons, which to a significant fraction, also arise from the time-variable mass accretion onto the central star (e.g., Gorti & Hollenbach, 2009).

Thus, the FUV levels of most stars are highest when they are young, before declining to chromospheric values towards later stages, as accretion ceases (Gorti et al., 2009; Armitage, 2011). For some cases, however, the opposite behaviour may be observed, namely that the bulk of the incident FUV radiation field is produced by accretion onto the central star, while the chromospheric component is very weak or even absent. In this limiting case, the continuous irradiation of the inner disc regions cannot be sustained over the entire lifetime, thus leading to an outside-in dispersal of the disc due to viscous draining, without the opening of a photoevaporative gap (Gorti et al., 2015).

(Soft) X-rays

The last type of photons to consider in the context of disc photoevaporation are stellar X-rays ($0.1\,\mathrm{keV} \leq h\nu \leq 10\,\mathrm{keV}$). As already explained in Section 2.3, this emission arises from a magnetically confined hot plasma in the stellar corona with temperatures of several

million Kelvins. X-rays are primarily absorbed by K-shell electrons of heavy elements, such as oxygen, carbon or iron, which are subsequently ionised due to the high photon energies. The released, highly-energetic photo-electrons then continue ionising and heating the gas via collisional excitation (Alexander et al., 2014).

Early studies on X-ray-driven photoevaporation were inconclusive on the importance of X-rays in launching disc winds. While Alexander et al. (2004b) and Gorti & Hollenbach (2009) found that EUV is the dominant source of heating, Ercolano et al. (2008) and Ercolano et al. (2009a) found the opposite, namely that X-ray heating will dominate the mass loss of the disc. A major uncertainty in all of these early studies was the assumption of a hydrostatic equilibrium. While such an approach can be useful to estimate the order of magnitude of the total mass loss rates, they are unable to provide very reliable results on the radial mass loss profile.

Only when Owen et al. (2010, 2011a, 2012) coupled the radiative transfer models of X-ray photoionisation by Ercolano et al. (2008, 2009a) with 2D hydrodynamical calculations, robust estimates for the mass loss profiles could be obtained. For this purpose they considered an X-ray spectrum with an EUV component (XEUV) in order to fully account for EUV photons and their transition to soft X-rays ($0.1\,\mathrm{keV} \lesssim h\nu \lesssim 1\,\mathrm{keV}$), which have been shown to be the main driver of X-ray heating in the wind launching regions (Ercolano et al., 2009a). While hard X-rays ($h\nu > 1\,\mathrm{keV}$) can penetrate significantly deeper columns than soft X-rays, they are nevertheless unable to provide enough heating in those regions to ultimately unbind the gas. This coupled approach between radiative transfer and hydrodynamics was possible as Ercolano et al. (2009a) showed that in the full radiative transfer problem, the gas temperature, T, and the disc ionisation parameter, ξ, are well correlated. Thus, this relation can be used as an input to the hydrodynamical calculations, leading to a computationally efficient route to solve this highly complex problem.

While the mass loss rate in the EUV case is found to scale as $\dot{M}_\mathrm{w} \propto \sqrt{\Phi_\mathrm{EUV}}$, for XEUV-photoevaporation it can be described as (Owen et al., 2012):

$$\dot{M}_\mathrm{w} = 6.25 \times 10^{-9} \left(\frac{M_\star}{M_\odot}\right)^{-0.068} \left(\frac{L_\mathrm{x}}{10^{30}\,\mathrm{erg\,s^{-1}}}\right)^{1.14} M_\odot\,\mathrm{yr}^{-1}. \tag{4.6}$$

Hence it follows that $\dot{M}_\mathrm{w} \propto L_\mathrm{x}$ (which can be also derived via purely analytical considerations, cf. Owen et al., 2011a, for details), implying that the mass loss rates are strongly dependent on the X-ray properties of the central star. As X-rays are emitted in the magnetosphere, they are mostly unaffected by absorption through accretion funnels, and thus are able to penetrate significantly deeper columns of neutral gas (up to $N_\mathrm{H} \sim 10^{22}\,\mathrm{cm}^{-2}$) compared to EUV (Owen et al., 2010). Also, XEUV photoevaporation causes a broader wind profile by being able to heat the circumstellar gas at larger radii, and following Eq. 4.6, mass loss rates of $\sim 10^{-8}\,M_\odot\,\mathrm{yr}^{-1}$, which dominate at intermediate distances of 5–20 au, are achieved for solar-type stars with typical X-ray luminosities of $\sim 10^{30}\,\mathrm{erg\,s^{-1}}$. This can be inferred from the right panel of Figure 4.3, which shows that the X-ray mass loss rate increases steadily towards larger radii.

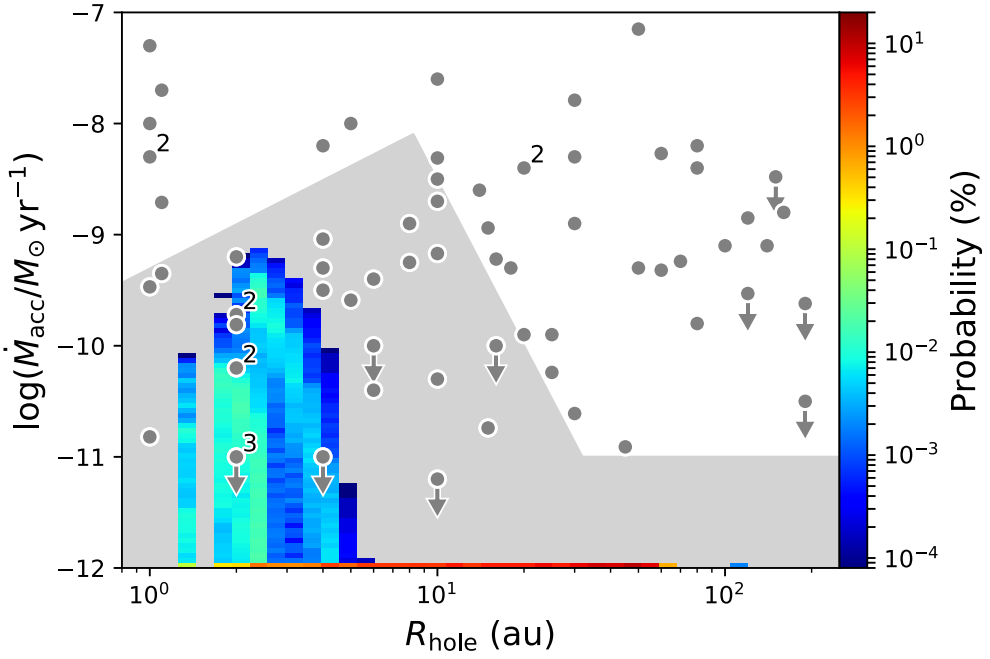

Figure 4.4: Mass accretion rate versus disc hole size of transition discs. The grey circles show observed transition discs gathered by Ercolano & Pascucci (2017, and references therein). Numbers next to circles indicate the total number of sources at that point, arrows indicate that the accretion rate is an upper limit. The coloured areas show the probability of finding a transition disc with the corresponding accretion rate and hole radius, calculated from a population synthesis of discs subject to viscosity and X-ray photoevaporation, using the model by Owen et al. (2012). The same initial conditions as in the previous setups were used, which are $M_\star = 1\,M_\odot$, $M_{\rm d} = 0.1\,M_\odot$, $R_1 = 10\,{\rm au}$, $\alpha = 10^{-2}$ and $H/R = 0.05$. X-ray luminosities were sampled randomly from the X-ray luminosity function of the Taurus cluster (Güdel et al., 2007). All discs with an accretion rate lower than $10^{-12}\,M_\odot\,{\rm yr}^{-1}$ are shown at the bottom. The grey shaded region, which was adapted from Figure 17 in Owen et al. (2012), shows the region in parameter space, in which observed transition discs can potentially be explained by disc dispersal via X-ray-driven photoevaporation.

4.3 Observed constraints on disc dispersal

Disc dispersal via photoevaporation can explain a significant fraction of transition discs within the $\dot{M}_{\rm acc}$–$R_{\rm hole}$ plane, especially those with small ($\lesssim 10\,{\rm au}$) cavities and small to intermediate accretion rates. It generally fails, however, at explaining a specific subset of transition discs, namely those with high accretion rates and large cavities ($\gtrsim 20\,{\rm au}$). Therefore, the gaps and other substructures that are regularly observed in these discs are usually attributed to disc-planet interactions caused by an embedded planet, rather than disc dispersal (e.g., Francis & van der Marel, 2020).

These two different populations of transition discs can be inferred from Figure 4.4, which shows the mass accretion rates of transition discs as a function of their cavity (or 'hole') size. The grey dots correspond to observed transition discs collected by Ercolano & Pascucci (2017, and references therein), while the colour-coded areas reflect the probability of finding a TD at a given location in $\dot{M}_{\rm acc}$–$R_{\rm hole}$ space, obtained by performing a set of population synthesis models using the 1D viscous evolution+photoevaporation code SPOCK by Ercolano & Rosotti (2015).

For this purpose, 1000 individual simulations of planet-less discs subject to viscosity and X-ray photoevaporation using the profile from Owen et al. (2012) were performed. The stellar X-ray luminosity, which is a fundamental input parameter for X-ray photoevaporation models, was sampled randomly from an observed distribution of X-ray luminosities in the Taurus cluster (Güdel et al., 2007; Owen et al., 2011a), while all remaining physical properties were identical for all discs in the model: $M_\star = 1\,M_\odot$, $M_\mathrm{d} = 0.1\,M_\odot$, $\alpha = 10^{-2}$, $R_1 = 10\,\mathrm{au}$ and $H/R = 0.05$. The grey shaded area (adapted from Figure 17 of Owen et al., 2012) encompasses the region within the $\dot{M}_\mathrm{acc}$–R_hole space that can be theoretically populated by models of disc evolution that include disc dispersal via X-ray-driven photoevaporation.

The reason, why the grey shaded region is significantly larger than the region populated by the population synthesis model lies in the fact that the model only employed a very simplistic approach. As the model only considered the gas phase and all discs had identical initial properties (i.e. mass, size and viscosity), it is obvious that such a simplistic setup cannot recreate the full diversity of observed transition discs. However, by using more realistic assumptions, for example on the carbon- and oxygen content in dispersing discs (Ercolano et al., 2018; Wölfer et al., 2019), or by including more vigorous winds into the model (Picogna et al. 2019; Woelfer et al., in preparation; Ercolano et al., subm.), it has been demonstrated that the coloured region can be extended especially towards larger hole sizes, so that disc dispersal via photoevaporation can reproduce a significant larger fraction of observed transition discs in the $\dot{M}_\mathrm{acc}$–R_hole plane.

Figure 4.4 emphasises that there are two distinct populations of transition discs, and that around half of them can be considered to be 'true transitions discs', meaning that they are on the verge of dispersal. However, one of the major caveats in photoevaporation models is the over-prediction of so-called 'relic discs', which are non-accreting transition discs with intermediate to large inner cavities (red line at the bottom of Figure 4.4). Such objects are an expected result of the inside-out dispersal of discs, however, none of those have been detected so far. A possible reason for this may lie in the fact that such discs are simply not observable in the mm-continuum due to the small amount of left-over dust that is barely emitting at the low temperatures present at large radii. Moreover, it is possible that radial drift may have already removed most of the large dust grains from the outer disc regions by the time the photoevaporative gap has opened, thus rendering these objects invisible (Ercolano et al., 2017). Consequently, future studies will have to take the dust component into account and treat it in a self-consistent manner in order to resolve the persistent issue of relic discs in photoevaporation models.

4.4 Effect on planets

As internal photoevaporation plays a key role in eventually dispersing discs, this process will also have an immediate impact on the formation and evolution of young planets. This includes, for example, increasing the dust-to-gas ratio in the disc by removing mostly gas via pressure-driven disc winds, which may possibly affect the formation of planetesimals via the streaming instability (Ercolano et al., 2018; Franz et al., 2020), the erosion of exoplanetary atmospheres (which may set the evolutionary pathway of Super Earths and Sub-Neptunes, cf. Owen & Wu, 2017) or the migration history of planets, especially gas giants (Alexander & Armitage, 2007,

2009; Alexander & Pascucci, 2012; Ercolano & Rosotti, 2015; Jennings et al., 2018; Monsch et al., 2021a,b). Some key aspects will be discussed in more detail in the following.

Disc dispersal

Photoevaporation and giant planet formation are tightly linked, mutually supporting processes. For example, Alexander & Armitage (2009) and Rosotti et al. (2013) showed that the presence of a forming giant planet outside of the gravitational radius may have an immediate effect on the onset of disc dispersal via photoevaporation. The reason for this is that the cavity, which is carved by the forming giant planet, decreases the mass flow from the outer to the inner disc, ultimately leaving the inner disc at a lower surface density compared to a planet-less disc. This in turn reduces the accretion rate onto the star, so that the switch between the accretion-dominated to the photoevaporation-dominated regime (i.e. where $\dot{M}_{\rm acc} = \dot{M}_{\rm w}$) is initiated at an earlier time compared to a planet-less disc. Consequently, under certain conditions (such as a high planet mass and late formation time), the presence of a giant planet may trigger the earlier onset of photoevaporation, ultimately leading to the faster dispersal of the disc. This can have immediate consequences on the migration speed and the final parking location of a given giant planets, which will be the main focus of Chapter 7.

Planet formation

Photoevaporation limits the time, which is available for gas giants to form, as they need to assemble a large fraction of their final mass from the gas phase of the disc. Consequently, giant planets will need to form in less than $\sim 10\,\mathrm{Myr}$, and potentially even faster, considering that most discs have a significantly shorter mean lifetime of 2–3 Myr (Najita & Kenyon, 2014; Manara et al., 2018; Tychoniec et al., 2020).

Moreover, disc dispersal via photoevaporation can also have a more direct impact on the formation of planets through different effects. Firstly, photoevaporative disc winds mostly remove the gas phase from the disc as they generally entrain only the small micron-sized dust grains, basically independent of the incident spectrum (Owen et al., 2011b; Hutchison et al., 2016b,a; Franz et al., 2020). This will gradually lead to an increase of the disc's dust-to-gas ratio, which has been suggested to possibly abet the formation of planetesimals by triggering the streaming instability (Drążkowska et al., 2016; Carrera et al., 2017; Ercolano et al., 2018). The results on the importance of photoevaporation on the formation of planetesimals coming from these studies are, however, inconclusive, which is mainly a consequence of the different employed photoevaporation profiles.

Planet demographics and migration

More importantly, viscous accretion models alone would predict the disc surface density to decline uniformly at all radii. This would imply that giant planets have a constant formation efficiency throughout the disc and consequently, one would expect to observe a homogeneous radial distribution of giant planets. This is not the case, as giant planets are observed to clump

up preferentially in a region between $\sim$ 1–2 au, which may hint towards 'sweet spots' for planet formation and/or their migration.

Further, the existence of the so-called hot Jupiters, which have orbital periods $P < 15$ d (Wang et al., 2015), are generally considered to be direct evidence of their inward migration having taken place. As the physical conditions in the inner regions of planet-forming discs are unfavourable to giant planet formation (see Section 3.4), the in situ information of hot Jupiters is unlikely. They are rather believed to form in the cold outer parts of the disc, where icy dust is still abundant, and subsequently migrate inwards during their evolution (cf. Dawson & Johnson, 2018, for a review). This implies, however, that without a mechanism to halt this process, many planets would be pushed to the very inner regions of the disc and perhaps even fall onto their host star.

Photoevaporation may provide such a parking mechanism, as it removes mass from the disc non-uniformly at given locations, where the surface mass loss profile is maximal. Thus, in a photoevaporating disc, planets are expected to pile up at given locations, namely where a gas-free cavity is opened, which will prevent any further inward migration of planets (Alexander & Armitage, 2009; Alexander & Pascucci, 2012). The observational and theoretical implications of this process on the demographics of giant planets are the main focus of Chapter 6 and Chapter 8, respectively.

Chapter 5

Extra-solar planets

The existence of planetary bodies next to Earth had been one of the great astronomical conundrums since the antiquity. While some of the inner and the outer planets in our Solar System, such as Mercury, Venus, Mars, Jupiter or Saturn had been already identified by naked eye by the ancient Babylonians, it took until the 17th century that their planetary nature could be also proven using the first telescopes (Sachs, 1974; Drake, 2003). Especially Galileo Galilei's first observation of the Jovian moons in 1610 marked one of the major milestones in astronomy, as they were direct evidence for heavenly bodies orbiting planets other than Earth. Now, almost 500 years later, we know that planets outside of our own Solar System are ubiquitous. Large-scale observational campaigns performed in the last 20 years have been incredibly successful in detecting and characterising a plethora of extrasolar planets, leading to the conclusion that statistically, every star in our Galaxy is expected to host at least one planet. Especially the *Kepler* Space Telescope has proven to be of great importance to this cause by discovering more than 2600 exoplanets using the transit method in its almost ten year-long mission. However, also other techniques, like the radial velocity method, direct imaging or gravitational microlensing have been crucial in adding to the wealth of exoplanet data that we have today. This chapter will therefore first review the properties of the observed exoplanet demographics, before briefly describing the most important techniques that were employed for their detection.

5.1 Exoplanet demographics

The most important results from past exoplanet campaigns are that exoplanets are ubiquitous (e.g., Cassan et al., 2012; Batalha, 2014) and that small planets are more common than giant planets by at least an order of magnitude (cf. Winn & Fabrycky, 2015, and Gaudi et al. 2020, for reviews). For a long time, this had not been evident, as before the *Kepler* era, the most abundant kind of detected exoplanets had been giant planets and especially the so-called hot Jupiters. The reasons for this are mostly selection effects and observational biases, as massive, close-in planets are significantly easier to detect than lower-mass planets, as will be discussed in the following sections. Further, radial velocity and transit campaigns mostly focused on

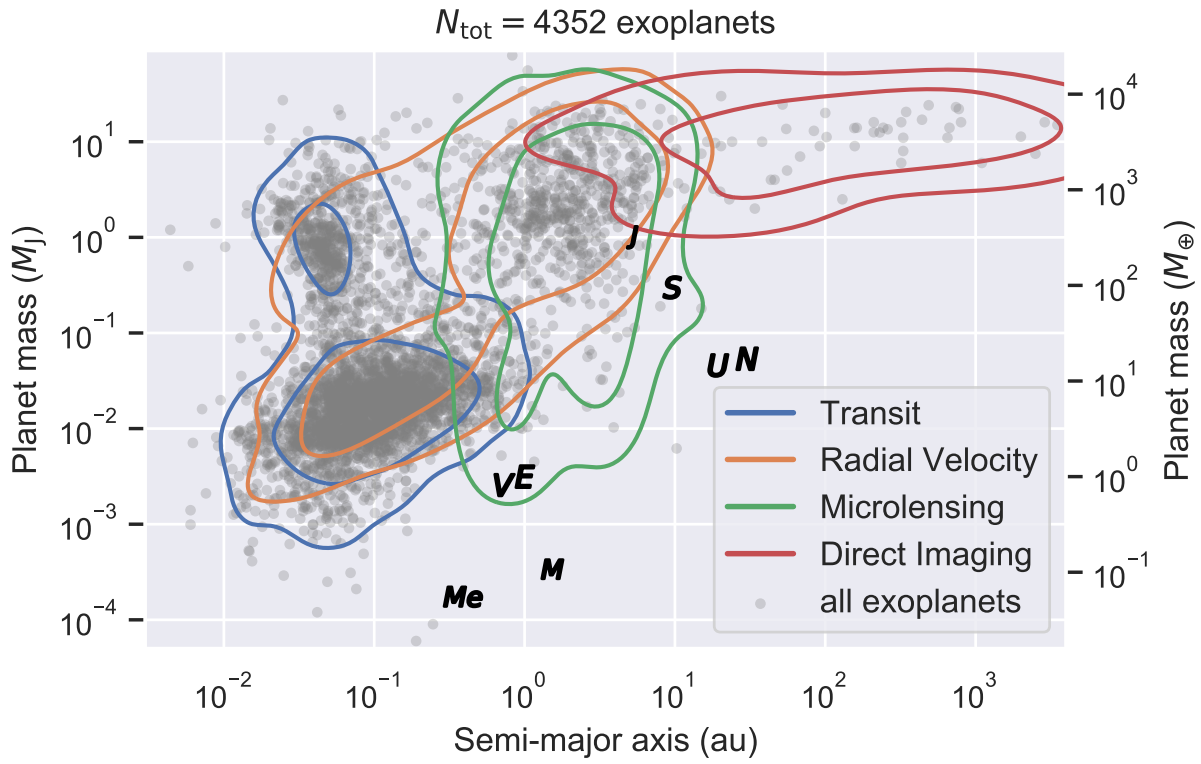

Figure 5.1: Planet mass versus semi-major axis distribution of all detected exoplanets as of May 2021 (data obtained from the NASA Exoplanet Archive). The differently coloured contours show the 68 % and 95 % percentiles for each planet distribution detected by the transit (blue), radial velocity (orange), microlensing (green) and direct imaging method (red). For comparison, we overplot the Solar System planets abbreviated with their first letters.

F, G and K-type stars. However, small planets are more easily detected around lower-mass M-dwarfs due to an increased transit probability and deeper transit depths for planets of the same size when compared to sun-like stars (cf. Dressing & Charbonneau, 2013; Mulders, 2018, and Section 5.2). Therefore, in the early years of exoplanet science, it had been thought that planets similar to Earth must be rather rare. This view has drastically changed with the first data release of the *Kepler* mission, which showed that there are many planets with radii ranging between Earth's and Neptune's, the so-called Super-Earths and Sub-Neptunes. Their discovery challenged planet formation theories at that time, which mainly focused on reproducing planets similar to those observed in our own Solar System and thus did not predict the existence of these intermediate class of planets.

There are a number of trends that can now be inferred from the exoplanet demographics (see e.g., Udry & Santos, 2007; Mulders, 2018; Santerne, 2018, and Gaudi et al. 2020, for reviews), such as the bimodality in the radius distribution of Super-Earths and Sub-Neptunes, roughly located between 1.5–2 $R_\oplus$ (the so-called 'Fulton-gap' or 'evaporation valley', cf. Fulton et al., 2017; Owen & Wu, 2017), or the higher occurrence rates of giant planets around metal-rich and more massive stars (e.g., Santos et al., 2001, 2004; Fischer & Valenti, 2005; Bond et al., 2006;

Johnson et al., 2010; Sousa et al., 2011). In contrast, low-mass planets are more frequently found around low-mass stars having a wide range of metallicities (e.g., Sousa et al., 2008; Buchhave et al., 2012; Howard et al., 2012; Mulders et al., 2015b). This suggests that planets can form in completely different environments and that stellar properties play a fundamental role in determining the efficiency of the planet formation process.

In this context it is important to derive planet occurrence rates, which account for non-detections, as well as selection effects and detection biases introduced by each exoplanet method and/or survey. For example, while some techniques are most sensitive towards massive, close-in planets, others routinely detect wide-orbit planets. Therefore unbiased occurrence rates are vital to distinguish artificial trends imposed by the underlying survey limitations from intrinsic (physical) trends within the planet/host star population. This is demonstrated in Figure 5.1, which shows the demographics of the in total 4352 detected exoplanets as of May 2021. The contours show the 68 % and 95 % percentiles for each corresponding distribution for the transit, radial velocity, microlensing and direct imaging methods, and therefore illustrate in which part of parameter space a given discovery method is most sensitive. For comparison, also the locations of the Solar System planets are overplotted. It becomes immediately apparent from Figure 5.1 that the different detection techniques, which will be discussed in the next subsections, mostly cover different parts of the planet mass versus semi-major axis plane, hence probing completely different populations of exoplanets.

For example, by using radial velocity measurements, Cumming et al. (2008) estimated the occurrence rate of gas giants (0.3–10 M_{J}) with orbital periods between 2–2000 d ($\approx$ 0.03–3 au) to be 10.5 % for solar-type stars. They found a strongly rising giant planet fraction for orbital periods beyond $P \approx 300$ d ($\sim$ 0.9 au, see also Marcy et al., 2005), however a more recent study by Bryan et al. (2016), which combines radial velocity with direct imaging data, finds the giant planet frequency to decline beyond 3–10 au, therefore suggesting a peak in the giant planet occurrence rate within these radii. This finding was later confirmed by Fernandes et al. (2019), who combined radial velocity and *Kepler* (i.e. photometrical transit) data to compute unified giant planet occurrence rates for orbital periods of up to 10^4 d considering different detection methods. They also find a break in the giant planet occurrence rate between 2–3 au, roughly corresponding to the location of the water ice line within the Solar System. They further compared their observational results with the outcomes of the planet population synthesis models by Mordasini et al. (2009); Ida et al. (2018) and Jennings et al. (2018), for which they find a generally good agreement. These robust results by Fernandes et al. (2019) suggest that massive planets on wide orbits ($>$ 10 au) are rare (see also Fulton et al., 2021), and that they are exceedingly less frequent than super-Earths or rocky planets in general (Bowler, 2016). However, the rather contradicting conclusions on the frequency of gas giants, which were obtained by using different exoplanet detection methods, highlight the different sensitivity of each method. Therefore, planetary occurrence rate studies should be treated with caution when the selection effects and observational biases of each exoplanet survey and discovery method are not taken into account, or when the conclusions are just based on a single detection method.

5.2 Detection methods

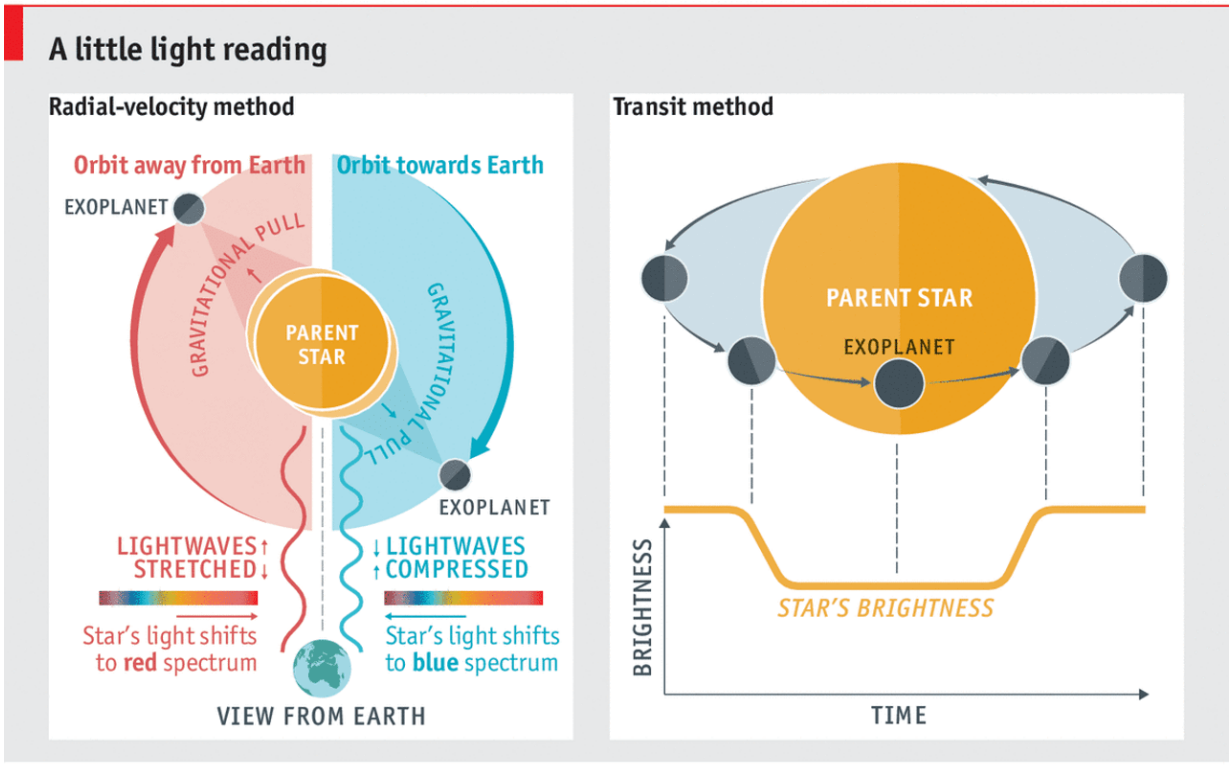

Figure 5.2: Schematic illustrations of the radial velocity (left panel) and the transit (right panel) method. Image reused from Economist (2016) with permission from *The Economist Group Limited*.

Radial velocity

The radial velocity (RV) method, or Doppler spectroscopy, is an indirect method for detecting exoplanets via the observation of shifted spectral lines within the parent star's spectrum, which are caused by the Doppler effect. More than 837 out of a total sample of 4353 exoplanets have been detected using this method. Until at least 2012, Doppler spectroscopy has been by far the most successful technique for discovering exoplanets.

The RV method uses the fact that if a star is surrounded by a companion, both bodies will orbit around a common center of mass. As the host star is generally significantly more massive than its planets, the center of mass will usually be located inside the stellar radius, leading to a 'wobbling' orbital motion of the central star. This causes the spectral lines within the parent star's spectrum to be Doppler-shifted, with the direction of this shift depending on the star's relative motion with respect to Earth, as is illustrated in the left panel of Figure 5.2. If the star is moving *towards* Earth, the spectral lines will be *blue-shifted*, meaning that they are shifted towards shorter wavelengths (i.e. higher energies) compared to their rest wavelength λ_{rest}. They

are *red-shifted* when the star is *moving away* from Earth again. The wobbling motion of the planet host star will produce a characteristic, periodic variation of the stellar spectral lines, that can be observed from Earth using high-precision spectrographs. Doppler spectroscopy may also cause false positives as stellar magnetic activity and other effects such as spectroscopic motions or granulation may generate similar RV signals as planets. Therefore, precise calibration of the instruments and a careful data reduction process play an indispensable role for the success of this discovery method (Wright, 2018).

The shift $\Delta\lambda$ of the spectral lines can be determined via:

$$\Delta\lambda \approx \frac{v_{\text{radial}}\lambda_{\text{rest}}}{c}, \tag{5.1}$$

where c is the speed of light, and v_{radial} is the radial velocity of the star. One can relate the amplitude of the Doppler shift of a spectral line to the mass and orbital properties of the planet using Kepler's third law:

$$(a_\star + a_\text{p})^3 = \frac{GT^2(M_\star + M_\text{p})}{4\pi^2}, \tag{5.2}$$

where $a_\star$ and a_p give the corresponding distance of the star/planet to the center of mass, $M_\star$ and M_P are their respective masses, G is the gravitational constant and T is the planet's orbital period around its host star. Assuming $M_\text{p} \ll M_\star$ and $a_\star \ll a_\text{p}$, which is true for most star-planet configurations, it follows that:

$$a_\text{p} \approx \sqrt[3]{\frac{GT^2M_\star}{4\pi^2}}. \tag{5.3}$$

The semi-major axis of the companion can therefore be determined if the stellar mass and the planet's orbital period are known. For nearly circular orbits, one can assume that $v \approx 2\pi a/T$, and therefore it follows from the definition of the center of mass ($a_\star M_\star = a_\text{p} M_\text{p}$) that:

$$a_\text{p} = \frac{a_\star M_\star}{M_\text{p}} = \frac{v_\star T M_\star}{2\pi M_\text{p}}. \tag{5.4}$$

The direct determination of the stellar orbital velocity, $v_\star$, is not possible as the measurement of the Doppler shift of a spectral line only provides a measure for the radial portion of the stellar orbital velocity, i.e. $v_{\text{radial}} = v_\star \sin i$, where $0° \leq i \leq 90°$ is the orbital inclination of the system. Hence it follows that:

$$a_\text{p} = \frac{v_{\text{radial}} T M_\star}{2\pi M_\text{p} \sin i}, \tag{5.5}$$

which can be substituted back into Eq. 5.3:

$$M_\text{p} \sin i = v_{\text{radial}} \sqrt[3]{\frac{M_\star^2 T}{2\pi G}} \iff v_{\text{radial}} = M_\text{p} \sin i \sqrt[3]{\frac{2\pi G}{M_\star^2 T}}. \tag{5.6}$$

Thus, Eq. 5.6 gives a direct relation between the radial velocity of the host star, which can be determined from the Doppler shift ($\Delta\lambda$) of the stellar spectral lines using Eq. 5.1, and the

planetary mass (M_p), the system's inclination (i), as well as the the orbital period (T). While i can generally not be inferred from RV measurements (see however Rodler et al., 2012), they can provide the planet's minimum mass $M_\mathrm{p} \sin i$. In conjunction with another method that can infer the system's orbital inclination (such as the transit method that will be discussed in the following subsection), one can measure the precise mass of a planet. The RV method is therefore often used as a follow-up method for the transit technique, as this can scan a large portion of the sky simultaneously in contrast to the RV method, which can only observe a small number of stars at the same time.

Following Eq. 5.6, the probability of detecting a planet using the RV method should therefore increase with larger planetary mass and smaller orbital period and stellar mass. The most common type of detected exoplanet should therefore be massive gas giants located very close to their low-mass parent star (see the blue contours in Fig. 5.1). Such kind of planets correspond to the so-called hot Jupiters, which are gas giants with orbital periods of $P \lesssim 15\,\mathrm{d}$ (Wang et al., 2015). And indeed, the first exoplanet discovered using this method was the hot Jupiter 51 Peg b, having a minimum mass of $0.47\,M_\mathrm{J}$ on a 4.23 day orbit, which induced an RV-amplitude of $59\,\mathrm{m\,s^{-1}}$ (Mayor & Queloz, 1995). For comparison, Jupiter with its 5.2 au distance to the Sun would only produce an RV-signal of $\approx 12\,\mathrm{m\,s^{-1}}$, while Earth's perturbation of the Sun's radial velocity is only $\approx 9\,\mathrm{cm\,s^{-1}}$. The detection of such weak RV-signals still proves to be very challenging with current spectroscopic instruments (Fischer et al., 2016; Wright, 2018).

Exoplanets that are similar to those in our Solar System are therefore difficult to discover from Earth using the RV method. This partly explains why most of the Solar System planets are located in an empty region in the exoplanet demographics diagram shown in Figure 5.1. Most exoplanetary systems that have been detected so far thus correspond to very different planetary systems compared to our own.

Transit

The transit method is a photometric exoplanet detection method, which is based on the observation of a dimming event in the parent star's brightness, that occurs when a companion passes, or *transits*, right in front of it. This results in a dip in the so-called lightcurve of the star, that is obtained when the star's brightness is monitored over an extended period of time. The basic geometry of such a transit and the resulting lightcurve is illustrated in the right panel of Figure 5.2. The four observables that can be extracted from such a lightcurve are the transit depth, the transit duration, the period of the planet and the corresponding duration of the ingress and egress[13] of the planet (Yee & Gaudi, 2008).

The transit method's strength lies especially in the rich set of physical properties that can be inferred from transiting planets (Deeg & Alonso, 2018). For example, the duration of the transit event allows to infer the orbital period, and therefore also the semi-major axis of the transiting planet. Further, the transit depth in the stellar lightcurve measures the reduction in stellar brightness due to the obscuring planet, and therefore enables a direct measurement of its size. And in contrast to the previously described RV method, transit photometry allows

[13] Ingress and egress mark the beginning and end of a transit event. They are defined as the time at which the projected planetary disc has first and last contact to the stellar disc, respectively.

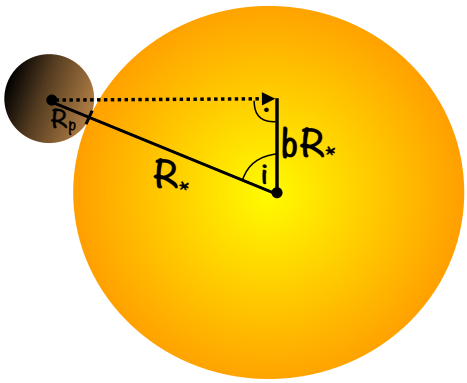

Figure 5.3: Basic transit geometry of a planet, which is at its exterior ingress (i.e. the first contact between the planetary and the stellar disc), moving from left to right.

to measure the planet's inclination, which is a necessary ingredient for estimating the planet's precise mass using additional spectroscopic RV observations.

Figure 5.3 shows a sketch of a transit event, in which the transiting planet is at its exterior ingress, i.e. when it first touches the stellar disc and is moving inwards in the direction of the stellar center. The following section will only briefly summarise the most important concepts related to planetary transits. We refer to Seager & Mallén-Ornelas (2003a), for a detailed description of a unique solution of the planet and star parameters that can be deduced from a planetary transit lightcurve. Assuming an ideally spherical star and planet, and neglecting limb darkening (i.e. that real stellar discs are fainter towards the edge), as well as the planet's flux, we can derive the transit depth in the stellar lightcurve from the cross-sectional areas of the planet and the star as:

$$\frac{\Delta F}{F} = \left(\frac{R_\mathrm{p}}{R_\star}\right)^2. \tag{5.7}$$

Here, F corresponds to the total observed stellar flux and ΔF to the decrease in total flux caused by the planetary transit. To first order the planetary radius can then be derived via:

$$R_\mathrm{p} = R_\star \sqrt{\frac{\Delta F}{F}}. \tag{5.8}$$

The total transit duration can then be determined via:

$$T_\mathrm{transit} = \frac{P}{\pi} \arcsin\left(\frac{R_\star}{a}\right) \sqrt{\frac{[1 + (R_\mathrm{p}/R_\star)]^2 - [(a/R_\star)\cos i]^2}{1 - \cos^2 i}}, \tag{5.9}$$

for which the period P can be calculated using Kepler's third law assuming circular orbits:

$$P = \sqrt{\frac{4\pi^2 a^3}{G(M_\star + M_\mathrm{p})}}. \tag{5.10}$$

Another important parameter that can be determined from the lightcurve is the so-called impact parameter $b = a\cos i/R_\star$, which can vary between $b = 0$ at the center of the stellar disc, and $b = 1$ on the cusp. It is defined as the sky-projected distance between the centers of the stellar and the planetary disc at conjunction, as illustrated in Figure 5.3:

$$b = \frac{R_\star + R_\mathrm{p}}{R_\star}\cos i. \tag{5.11}$$

From this, the orbital inclination of the system can be easily determined via

$$i = \cos^{-1}\left(\frac{bR_\star}{R_\star + R_\mathrm{p}}\right). \tag{5.12}$$

The first exoplanet that was discovered using the transit method method was the hot Jupiter HD 209458 b (Charbonneau et al., 2000; Henry et al., 2000; Mazeh et al., 2000). It had been previously hypothesised that especially hot Jupiters should be readily detectable via their transit (e.g., Borucki et al., 1985) and the detection of HD 209458 b with an only 10 cm telescope showed that already small telescopes can provide the necessary tools for exoplanet detections. The underlying geometry of the problem leads, however, to a small observing probability for a planetary transit. Assuming a circular orbit of a planet with inclination $i = 0°$, the transit probability can be described as the ratio between the sum of the stellar and the planetary radius, $R_\star + R_\mathrm{p}$, and the planet's semi-major axis a (Winn, 2010):

$$p_\mathrm{transit} = \left(\frac{R_\star + R_\mathrm{p}}{a}\right)\left(\frac{1}{1-e^2}\right). \tag{5.13}$$

In the limiting case of a circular orbit (i.e. $e = 0$) and the star being much larger than the planet ($R_\star \gg R_\mathrm{p}$), Equation 5.13 becomes:

$$p_\mathrm{transit} \approx 0.005\left(\frac{R_\star}{R_\odot}\right)\left(\frac{a}{1\,\mathrm{au}}\right)^{-1}. \tag{5.14}$$

For a hot Jupiter orbiting a solar-mass star at a distance of 0.05 au, the transit probability becomes $p_\mathrm{transit} \approx 10\,\%$, while for Jupiter located at 5.2 au, this would already decrease significantly to $p_\mathrm{transit} \approx 0.1\,\%$ or $p_\mathrm{transit} \approx 0.5\,\%$ for Earth orbiting the Sun at 1 au. This shows that it is not necessarily less likely to observe a transit for small planets, as long as they are located relatively close to the star. In turn, hot Jupiters are most likely to be seen in a transit event due to their large radius and small distance to the host star than either more distant Jupiter-like planets, or smaller, terrestrial planets. However, the low observing probability for transit events implies that in order to catch a single transiting hot Jupiter, one would need to observe *at least* 10^3 Sun-like stars.

Nevertheless, with the launch of the *Kepler* Space Telescope in 2009 (Borucki et al., 2010), the transit method has become the most successful and promising exoplanet detection technique, despite of the small observing probability of a planetary transit. More than 75 % of all known exoplanets were discovered using this method, which has only become possible due to large-scale space-based observational campaigns, which allow for the continuous observation

of a given field of stars, therefore increasing the probability of detecting a planetary transit strongly. For example, *Kepler* observed more than 5.3×10^5 stars while monitoring the Cygnus constellation, resulting in more than 2800 confirmed exoplanets (Narang et al., 2018). The recently launched *Transiting Exoplanet Survey Satellite* (TESS) mission (Ricker et al., 2015) is expected to contribute even more to the wealth of observed transiting planets, with an additional 1.3×10^5 expected observed planetary transits (Barclay et al., 2018).

Photometric transit observations in combination with spectroscopic measurements ('transit spectroscopy') additionally allow for the detailed characterisation of exoplanet compositions and their atmospheres. As the planet is transiting its parent star, the light emitted by the star passes through, and is absorbed by the planet's atmosphere. This produces specific absorption lines within the stellar spectrum that are a tracer of the chemical composition of the planetary atmosphere. For this purpose, the upcoming *James Webb* Space Telescope (JWST) is expected to provide many important contributions to the field of exoplanet research. Observations performed by JWST will not only allow the assessment of the habitability of individual planetary systems, but ultimately take us one step closer to understanding the origins of life.

Direct Imaging

The direct imaging method describes one of the few direct exoplanet detection techniques in which planets are imaged in the infrared to detect light that is reflected from their surface or atmosphere (cf. Bowler, 2016, for a review). The strength of this method therefore lies in the ability to characterise in detail the atmospheric properties of a given planet (e.g., Feng et al., 2018; Damiano et al., 2020). Direct imaging observations are generally performed within the near- and mid-infrared regime ($\approx$ 1–5 µm; e.g. via SPHERE, the Gemini Planet Imager or the upcoming *Nancy Grace Roman* Space Telescope, formerly known as WFIRST) using high-contrast adaptive optics (AO) instruments. The reason for this is that at visual wavelengths, planets are extremely faint sources compared to their host star, while in the infrared regime the ratio of the planet to stellar brightness is significantly larger due to the thermal emission coming from the planet. Young stars are therefore particularly attractive candidates for direct imaging observations, since young giant planets are most luminous at early evolutionary stages. Thus, the contrast between the planet and the star is lower than for higher stellar ages (Bowler, 2016). In order to block out the bright stellar emission during an observation, telescopes are usually equipped with coronographs.

This method has proven to be successful using both ground-based and space-based telescopes. It is particularly sensitive towards massive ($> 1\,M_\mathrm{J}$) planets, that are located at large distances, beyond $\gtrsim 10$ au to their host star. This enables us to probe a part of parameter space, that is otherwise inaccessible to more common exoplanet detections techniques, such as RV or transit, therefore allowing us to investigate alternative formation routes of giant planets such as gravitational instability. Another important constraint is that the planetary host star needs to be located close to Earth and also be monitored for an extended period of time in order to resolve the planet's orbital motion around its host star. This method can therefore provide precise measurements of the planet's orbital period and the total mass of the system ($M_\star + M_\mathrm{p}$), but the determination of individual planetary masses remains challenging with this

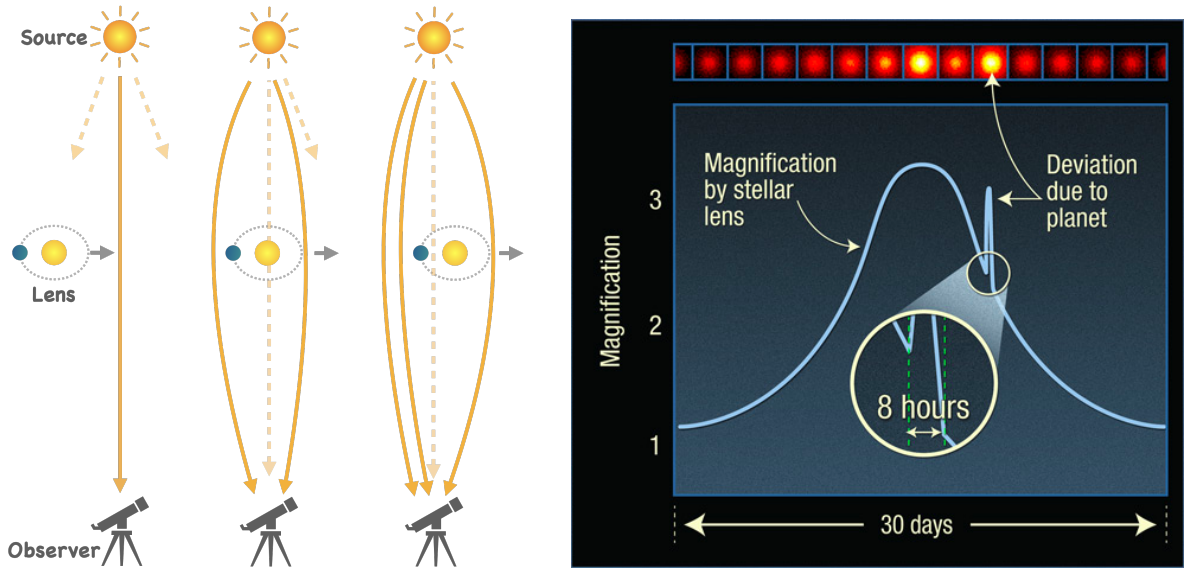

Figure 5.4: Geometry of a gravitational microlensing event and the corresponding magnification of the source star's brightness. The left panel illustrates the (not to scale) geometry of a microlensing event, in which the lens star that is hosting a planet is moving from left to right, slowly passing in front of the background source star. The solid arrows illustrate the source's light rays that are bent due to the gravitational field of the lens star including its surrounding planet. The dashed arrows show the unbent light rays that would be present if no microlensing event took place. The right panel demonstrates the corresponding magnification curve for such a configuration, in which the gravitational field of the planet causes an additional, short-lived magnification of the source star's apparent brightness. Image credit: NASA, ESA, and K. Sahu (STScI)

method (cf. Bowler, 2016, for a review).

As of May 2021, only 52 confirmed planets have been discovered via direct imaging. The probably most well-known system to have been directly imaged is the planetary system around HR 8799, hosting in total four giant planets (5–7 M_J) with projected separations between 15–70 au (Marois et al., 2008; Konopacky & Barman, 2018). Other well known objects are Fomalhaut b discovered by the HST (Kalas et al., 2005; Kalas et al., 2008) and Beta Pictoris b detected by the VLT/NaCo (Lagrange et al., 2009). Recently, it has been also possible to image accreting protoplanets around young stars that are still embedded in their natal planet-forming disc (PDS 70, cf. Keppler et al., 2018; Müller et al., 2018). However, the probably most important insight emerging from direct imaging surveys is that giant planets exist but are rare at separations of > 10 au. Assuming a hot-start evolutionary model (i.e. planets that formed via gravitational instability, cf. Section 3.4), the occurrence rate of wide-orbit giant planets is estimated to be only $0.6^{+0.7}_{-0.5}$ %, which is comparable to the likewise small frequency of hot Jupiters around Sun-like stars (Bowler, 2016).

Gravitational microlensing

Gravitational microlensing is another indirect method for the detection of exoplanets which, in contrast to all other techniques, does not rely on the detection of photons emitted from either

the star or the planet, but uses the light of another, unrelated source to prove the presence of a planet. This effect occurs when a foreground star (the 'lens') passes along the line of sight to a more distant background star (the 'source'), so that the lens' gravitational field splits the light coming from the source into two distinct images. Due to the small separation of only a few milliarcseconds between the separate images, they can typically not be resolved. They consequently appear as a single object of increased apparent brightness that can be detected from Earth using already relatively small telescopes. If the foreground star happens to host a planet, this planet will also act as a gravitational lens, further perturbing the image of the background star, which will ultimately result in a characteristic, short-lived peak in the source's apparent brightness. The configuration of such a microlensing event as well as a typical corresponding magnification curve are shown in Figure 5.4.

The sensitivity of the gravitational microlensing effect peaks for planet-star separations at the so-called Einstein radius. This is the radius of the ring image that is seen with perfect alignment between the source and the lens:

$$R_\mathrm{E} \equiv \Theta_\mathrm{E} D_\mathrm{L} \approx 2\,\mathrm{au} \sqrt{\frac{M_\mathrm{L}}{0.5\,M_\odot} \frac{D_\mathrm{L}(D_\mathrm{S} - D_\mathrm{L})}{D_\mathrm{S}(1\,\mathrm{kpc})}}. \tag{5.15}$$

Here, Θ_E is the angular size of the lensed image (or the 'physical Einstein ring radius', cf. Gaudi, 2012, for a review), D_L is the distance between the observer and the lens, M_L is the mass of the lens star's mass and D_S is the distance between the observer and the source. The Einstein radius typically corresponds to regions beyond the water ice line in planetary systems. Thus, gravitational microlensing is mostly sensitive towards planets orbiting their host star between $\sim$ 1–10 au.

Gravitational microlensing can, however, only provide weak constraints on the planet's semi-major axis as the microlensing events are usually fairly short and the orbital ellipticity is generally unknown. Similarly, only loose constraints can be obtained on the planetary mass besides measuring the planet-to-star mass ratio. However, this method's great strength lies in the ability to detect low-mass planets reaching down to Martian mass, which are inaccessible to other detection techniques. This method's major caveat is, in turn, that a given microlensing event cannot be repeated a second time as the alignment between the lens and the source star are unique events. Further, the usually large distances of several kiloparsecs between the microlensed planet host star and Earth also impede any follow-up observations using other techniques such as radial velocity or transit. Thus, gravitational microlensing can provide us with important statistical constraints on the demographics of especially lower-mass planets, but it does not allow a detailed characterisation of given planetary systems.

While the observing probability of a given microlensing event is extremely low, this can be compensated by observing a large sample of stars simultaneously. This is especially useful towards the galactic bulge, which provides a large amount of possible background stars. Due to the magnification of the star's apparent brightness during a microlensing event, also very dim stars at enormous distances (i.e. several kiloparsecs) can be observed. Therefore, planets outside the Milky Way (e.g., Dai & Guerras, 2018), as well as the so-called rogue, or free-floating planets can potentially be detected via gravitational microlensing (e.g., Mróz et al.,

2020). Further, gravitational microlensing is the only method that allows the detection of exoplanet ice giants. For example, Poleski et al. (2021) find that wide-orbit ice giants are common and that every microlensing star hosts on average $1.4^{+0.9}_{-0.6}$ ice giants. Such planets will stay inaccessible to other detection methods in the foreseeable future (e.g., Kane, 2011). Therefore, gravitational microlensing provides a unique opportunity to detect and characterise exoplanet analogues of Neptune and Uranus, which would otherwise stay hidden from us forever.

Chapter 6

X-ray properties of giant planet host stars

The content of this chapter was published in:

Monsch K., Ercolano B., Picogna G., Preibisch T., Rau M. M. (2019): "The imprint of X-ray photoevaporation of planet-forming discs on the orbital distribution of giant planets"[14], *Monthly Notices of the Royal Astronomical Society*, 483:3448

Abstract

High energy radiation from a planet host star can have strong influence on the final habitability of a system through several mechanisms. In this context we have constructed a catalogue containing the X-ray luminosities, as well as basic stellar and planetary properties of all known stars hosting giant planets ($> 0.1\,M_J$) that have been observed by the *Chandra* X-ray Observatory, *XMM-Newton* and/or ROSAT. Specifically in this chapter we present a first application of this catalogue to search for a possible imprint of X-ray photoevaporation of planet-forming discs on the present-day orbital distribution of the observed giant planets. We found a suggestive void in the semi-major axis, a, versus X-ray luminosity, L_x, plane, roughly located between $a \sim 0.05$–1 au and $L_x \sim 10^{27}$–$10^{29}\,\mathrm{erg\,s^{-1}}$, which would be expected if photoevaporation played a dominant role in the migration history of these systems. However, due to the small observational sample size, the statistical significance of this feature cannot be proven at this point.

[14] This chapter presents results from collaborative work with my coauthors, which I had the opportunity to take the lead of. In particular I was responsible for gathering the necessary X-ray and exoplanet data, cross-matching the different input catalogues, and computing the stellar X-ray fluxes and luminosities that were composed into the catalogue that is presented in this chapter. While I was advised by my coauthors, I performed all the analyses that are presented in the manuscript myself. Further, I was responsible for the composition of the manuscript.

6.1 Introduction

Recent surveys have shown a vast diversity of extra-solar planets, raising the question of how some systems end up looking like our own and/or become hospitable for life. Hints to explaining the diversity of planetary systems may be in the understanding of the statistical trends that are now emerging from the recent wealth of observational data.

One of these trends is the semi-major axis distribution of gas giants, which shows mountains and deserts, i.e. regions of over- and underpopulation. Understanding what controls the architecture of the new-born systems is crucial to assessing their habitability. As well as the location of terrestrial planets (i.e. inside or outside the habitable zone of their host star), the location of giant planets in a system is also of high importance to habitability, due to their central role in the delivery of volatiles to terrestrial planets (e.g. Quintana & Lissauer, 2014; Sánchez et al., 2018) or stopping the influx of pebbles from the outer disc, possibly preventing the early formation of terrestrial planets (e.g. Ormel et al., 2017).

The majority of exoplanets are most likely not formed in-situ. A clear evidence of this is the population of so-called "hot Jupiters", gas giants with very short orbital periods, corresponding to semi-major axes $\lesssim 0.1$ au. The finding of a hot Jupiter around V830, a young T Tauri star (Donati et al., 2016), suggests that giant planets can migrate inwards in the planet-forming disc in less than two million years. As the detection rate of hot Jupiters around young stars (6 %) seems to be higher than the detection rate around mature stars (1 %) this suggests that planet-disc interactions are the main driver of planetary migration (Donati et al., 2016; Yu et al., 2017). However, the orbital characteristics of a system are, in fact, influenced by different processes that operate at different times. At the early stages of planet evolution, young planets are subject to torques exerted on them by the gas in the protoplanetary disc, which typically results in their inward migration (e.g. Goldreich & Tremaine, 1980; Lin & Papaloizou, 1986; Kley & Nelson, 2012). After a few million years, once the gas in the disc is finally dispersed, disc-driven migration stops. The timescales for migration of giant planets formed at radii of a few astronomical units are comparable to the gas disc lifetimes of a few million years (Haisch et al., 2001), suggesting that without a mechanism to halt this process, many planets would be pushed to the very inner regions of the disc and perhaps even be lost onto their host star. Indeed, planetary population synthesis models always include simplified prescriptions for eventually dissipating the disc (e.g. Benz et al., 2014; Mordasini et al., 2015; Mordasini, 2018). Without a parking mechanism one would expect to observe a much larger fraction of hot Jupiters. Recent exoplanet surveys, however, do not show an over-abundance of hot Jupiters. On the contrary, giant planets seem to clump preferentially in a region between $\sim$ 1–2 au. What determines this peak in the distribution of giant planets is a matter of strong interest in the field today. Alexander & Pascucci (2012, henceforth AP12) suggested that internal photoevaporation driven by the host star could provide a natural parking radius for migrating giant planets, which was confirmed by numerical simulations of Ercolano & Rosotti (2015, henceforth ER15) and Jennings et al. (2018). These authors additionally showed that different photoevaporation profiles, i.e. the radially-dependent mass loss rate due to different photoevaporation models, have a dramatic influence on the final giant planet distribution for a given exoplanet population. While for most systems the orbits at the end of the gas disc

lifetimes will still be dynamically evolving, this initial migration phase is extremely important in determining the dominant exoplanet distribution characteristics, especially if it leads to non-tightly packed systems after disc dispersal.

While the influence of the photoevaporation process on the initial stages of planetesimal formation is somewhat debated in the literature (e.g. Ercolano et al., 2017), its effect at later stages, when planetary cores have already been formed and are migrating through the disc has been demonstrated. If, as suggested by ER15, disc photoevaporation driven by stellar X-rays (Ercolano et al., 2009a; Owen et al., 2010, 2011a, 2012) is affecting the observed distribution of giants, one may expect to observe a signature of this effect in the giant planet semi-major axis versus host star X-ray luminosity plane. In this work we have gathered information on the X-ray properties of giant planet-hosting stars from the three most important X-ray telescopes: the *Chandra* X-ray Observatory, *XMM-Newton* and ROSAT. These were combined with basic stellar and planetary properties from the *Extrasolar Planets Encyclopaedia*[15] (Schneider et al., 2011) to provide an extensive catalogue that can be used for investigating various processes between giant planets and their host stars.

Several previous studies already investigated different correlations between stellar and planetary properties, especially in context of the possible enhancement of stellar magnetic activity due to the presence of hot Jupiters (e.g. Lanza, 2008). Early studies by Kashyap et al. (2008) and Scharf (2010) found that hot Jupiter hosts systematically show enhanced X-ray activity. However, Poppenhaeger et al. (2010) constructed a sample of 72 planet-hosting stars within 30 pc distance from the Sun by using ROSAT and *XMM-Newton* data with which Poppenhaeger & Schmitt (2011) were able to show that there is no detectable influence of hot Jupiters enhancing the X-ray activity of their host stars. Subsequently, the study of Miller et al. (2015) and Hinkel et al. (2017) improved on several aspects, especially in terms of sample size. By including *Chandra* observations, they were able to extend their sample to fainter and more distant stars, increasing the sensitivity and reliability of their correlation tests. The analysis performed in our work is, however, significantly different to these previous studies that mainly focused on hot Jupiter systems. We study the possible connection between the architecture of giant planet systems and the X-ray emission of their parent stars, using observations of their present-day luminosities, and compare our results to predictions from numerical models of the early (< 10 Myr) evolution of these systems. Our increased sample size, largely constituted of deep *Chandra* observations, enables us to better assess the possible influence of X-ray-driven photoevaporation onto the final configuration of giant planets, with special attention to the orbital properties of "warm Jupiters", i.e. gas giants with orbital periods between 10 to 200 days.

As we use the present-day ($\sim$ Gyr) X-ray luminosities of planet hosts to relate to the evolution of the protoplanetary disc driven by the X-ray properties of the same stars at much younger ages ($\sim$ Myr), it is important to consider what is currently known about the origin and evolution of the stellar X-ray emission around low-mass stars. This is summarised in Section 6.2. The data retrieval and the resulting catalogue, which is included in the online supplementary material, is described in Section 6.3. The results are discussed in Section 6.4 and a brief

[15] `http://www.exoplanet.eu`

summary is given in Section 6.5.

6.2 Origin and Evolution of the X-Ray Emission

In this work we study the connection between the orbital configuration of extrasolar giant planets and the X-ray emission of their parent stars. The connection between these two aspects may stem from the evolutionary processes during the first few million years of the system, when the planets are still embedded in the protoplanetary disc, whose evolution and final dispersal are driven by the stellar irradiation at those young ages. Observationally, however, we can only measure the present day X-ray luminosities of the planets' host stars. It is thus important to discuss not only the origin of the X-ray emission but also how it evolves over time.

6.2.1 Origin of stellar X-ray emission

The X-ray emission of late-type stars with spectral types ranging from F to M originates from a hot, magnetically confined plasma in the stellar corona (e.g. Vaiana et al., 1981; Güdel, 2004; Jardine et al., 2006; Reale, 2014), resulting from magnetic dynamo activity produced in a boundary layer between the radiative core and the convective envelope, known as *tachocline* (e.g. Wright et al., 2011). Although there are still some open questions about the exact nature of the magnetic dynamo at work (e.g. Wright & Drake, 2016) and especially about the origin of activity saturation for very rapidly rotating stars (e.g. Kitchatinov & Olemskoy, 2015), it is well established that magnetic dynamo activity is primarily determined by the stellar rotation rate.

Numerous X-ray observations obtained during the last decades have clearly established that young stars in all evolutionary stages from protostellar to zero age main sequence (ZAMS) show highly elevated levels of X-ray activity (Preibisch et al., 1996; Feigelson & Montmerle, 1999; Preibisch & Zinnecker, 2002; Favata & Micela, 2003; Preibisch et al., 2005, 2014). Typical X-ray luminosities of solar mass young stellar objects (YSOs) during the first ~ 100 Myr are about 10^{30}–10^{31} erg s^{-1}, i.e. up to $\sim 10^4$ higher than of the current Sun. The temperatures of the X-ray emitting plasma of young stars are typically 10 to 20 MK, i.e. about ten times higher than in the solar corona.

Two fundamental results derived from particularly deep X-ray observations of young clusters are that (i) X-ray luminosity scales with stellar mass as $L_x \propto M^{1.44}$ to $M^{1.54}$ (Preibisch et al., 2005; Güdel et al., 2007) and (ii) the X-ray luminosity of T-Tauri stars (TTS) is approximately constant for ages up to 10 Myr, and then decreases following a power-law dependence of $L_x \propto t^{-0.75}$ (Preibisch & Feigelson, 2005). In light of the above described dynamo theories, the high X-ray activity levels of young stars are thought to be an ultimate consequence of their fast rotation during the first few 100 Myr of their lives (e.g. Alexander & Preibisch, 2012). The rotational evolution of stars, discussed in the next paragraph, explains the time evolution of their X-ray activity.

6.2.2 Evolution of stellar rotation

During their first few million years, YSOs are generally surrounded by circumstellar accretion discs, in which the accretion of matter from the disc onto the star is magnetically controlled (cf. Bouvier et al., 2007; Hartmann et al., 2016, for reviews). In this scenario, circumstellar discs are connected to their host star via magnetic field lines that lead to their truncation at or near the co-rotation radius, which lies typically, depending on the rotation period of the star, at a few (∼3–5) stellar radii (Bouvier et al., 2007; Preibisch, 2012). This magnetic coupling regulates the rotation rate of the star, which in turn affects the stellar X-ray emission. In particular, those field lines, which connect the stellar surface to parts of the disc that lie beyond the co-rotation radius, will tend to slow down the stellar rotation rate, as here the rotation frequency of the disc is lower than the rotation frequency of the star (cf. Bouvier et al., 2007, and references therein). This kind of magnetic coupling is assumed to be the explanation of the rather moderate rotation rates observed from young stars with ages between ~ 1 Myr and a few Myr.

When the disc has been dissipated after a few Myr, the braking effect of the magnetic coupling between the star and the disc declines and finally comes to a halt, and thus the rotation of the young star speeds up as a consequence of its continuing contraction. The highest rotation rates are established around the age of $\sim$ 30–50 Myr for solar-type stars, i.e. around the time the star reaches the ZAMS and its contraction stops. At later times, the rotation rates of young stars decrease steadily, mainly caused by the loss of angular momentum from stellar winds (e.g. Güdel, 2007; Gallet & Bouvier, 2013, 2015; Tu et al., 2015). The rotational evolution therefore depends to a large degree on the time scale over which the star is magnetospherically coupled to, and braked by the disc (e.g. Montmerle et al., 2000). Consequently, higher rotation frequencies are reached for such stars that disperse their accretion disc more quickly than for stars for which the braking effect of the magnetospheric coupling lasts longer. This therefore explains the wide range of observed rotation velocities for young stars with ages between $\sim$ 30–100 Myr and the resulting scatter in X-ray luminosity for stars of these young ages. While the decline in mean X-ray luminosity is small for the first 100 Myr compared to the observed spread in L_x for a given age (cf. Preibisch & Feigelson, 2005), at later ages, when the stellar rotation rates decrease, the range in rotational velocities (and consequently L_x) gets smaller before converging to the very low values typical for older main-sequence stars with ages of a few Gyr, such as our Sun. This behaviour closely follows the well-known Skumanich's relationship $\Omega_* \propto t^{-0.5}$ (Skumanich, 1972).

However, up to ages of about 1–2 Gyr, stars with the highest rotation rates during their early evolution are still among the fastest rotators in their current age group, i.e. the rank in rotation rates is conserved during that timescale (Gallet & Bouvier, 2013, 2015; Johnstone et al., 2015; Tu et al., 2015). This therefore justifies using the present-day observed X-ray luminosities of planet-hosting stars younger than about 1–2 Gyr as a proxy for the X-ray luminosity experienced by the same planet-disc systems at the time of giant planet migration and disc dispersal.

6.3 Observational Analysis

We used the *Extrasolar Planets Encyclopaedia*[16] (Schneider et al., 2011) to get a collection of all confirmed and unconfirmed extrasolar planets as of September 2017. In this project, we focus solely on the early dynamical evolution of giant planets that undergo so-called type II migration, therefore a lower threshold of 0.1 M_J was set for the planetary mass. In addition, all planets detected by gravitational microlensing or pulsar timing were excluded from this analysis. Since the target coordinates listed in the encyclopaedia are often unreliable, we used the stellar coordinates as listed in the SIMBAD Astronomical Database (Wenger et al., 2000) for the cross-matching. Further, we used the catalogue generated by Bailer-Jones et al. (2018)[17], in which accurate distance estimates inferred from the most recent *Gaia* Data Release 2 are given (Gaia DR2, Gaia Collaboration et al., 2016, 2018).

6.3.1 *Chandra* X-ray Observatory

We matched the stellar positions with the footprints of all ACIS and HRC observations listed in the *Chandra* archive[18]. To cover the entire field-of-view of both the ACIS and the HRC instruments, a cone search radius of 12′ and 22′ was used, respectively. We checked the accuracy of the astrometry in the *Chandra* data by comparison of X-ray source positions with the 2MASS Point Source catalogue (Skrutskie et al., 2006). At the celestial position of the planet host star in the *Chandra* image, we ran the `CIAO` script `srcflux`[19] (Fruscione et al., 2006) in order to determine the broad band (0.5–7.0 keV) X-ray fluxes for X-ray detected stars and corresponding upper limits for undetected ones. For this purpose we used the thermal Bremsstrahlung model[20] implemented in `CIAO` with a plasma temperature of $kT = 0.5$ keV and a galactic hydrogen column density of $N(\mathrm{H}) = 10^{20}\,\mathrm{cm}^{-2}$.

6.3.2 *XMM-Newton*

Count rates for *XMM-Newton* source detections were retrieved from the seventh data release of the Third *XMM-Newton* Serendipitous Source Catalogue (3XMM-DR7, Rosen et al., 2016). For undetected sources, upper limits on the source count rates were determined using the web tool FLIX[21]. This tool applies the algorithm described by Carrera et al. (2007) to estimate the upper limits of the band 8 (0.2–12.0 keV) source fluxes using the energy conversion factors (ECFs) listed in Mateos et al. (2009). To allow for the direct comparison between the source fluxes of different X-ray telescopes, the band 8 *XMM-Newton* fluxes were converted to 0.5–7.0 keV

[16] `http://www.exoplanet.eu`

[17] `http://www.mpia.de/~calj/gdr2_distances/main.html`

[18] `http://cda.harvard.edu/chaser/`

[19] `http://cxc.harvard.edu/ciao/ahelp/srcflux.html`

[20] The XSPEC model function used in this work was `xsbremss`. A detailed description of all available model functions in `CIAO` can be found at `http://cxc.harvard.edu/sherpa/ahelp/xs.html` and `https://heasarc.gsfc.nasa.gov/docs/xanadu/xspec/manual/node143.html`.

[21] `http://www.ledas.ac.uk/flix/flix_dr5.html`

to match the *Chandra* ACIS broad band fluxes using the web tool WebPIMMS[22] with $kT = 0.5\,\mathrm{keV}$, $N(\mathrm{H}) = 10^{20}\,\mathrm{cm}^{-2}$ applying the same spectral model as described in Section 6.3.1.

6.3.3 ROSAT

In order to further increase the sample of planet-hosting stars observed in X-rays, several catalogues based on the ROSAT All-Sky Survey (RASS, Voges et al., 1999, 2000; ROSAT Consortium, 2000; ROSAT Scientific Team, 2000) including the most recent second data release from 2016 (Boller et al., 2016) have been searched. These catalogues provide the count rates for detected stars, which we then converted into source fluxes using the same spectral model as discussed before. These were also converted to 0.5–7.0 keV, as described in Section 6.3.2, to match the *Chandra* broad band fluxes. Following Miller et al. (2015), we estimated approximate RASS flux upper limits using the typical detection limit of the RASS Faint Source Catalogue of $10^{-13}\,\mathrm{erg\,s^{-1}\,cm^{-2}}$. Due to the shallowness of this all-sky survey, this resulted in very crude estimates of the flux upper limits, which are several orders of magnitude larger than those estimated from *Chandra* observations. Therefore, we do not include these upper limits in our catalogue.

6.3.4 Final catalogue

Some of the targets were observed by multiple X-ray telescopes. In such cases we prioritised *Chandra* over *XMM-Newton* over ROSAT observations in our analysis, as *Chandra* offers the highest angular resolution and thus very good point source sensitivity. For stars that have been observed multiple times by a given telescope, we calculated the average flux and used this value in the analysis. For undetected X-ray sources, we used the lowest upper limit, as this corresponds to the tightest constraint on the actual source flux.

Stellar X-ray luminosities and their corresponding errors were then determined using the distance measurements either given in the *Extrasolar Planets Encyclopaedia* or from *Gaia* DR2 (Bailer-Jones et al., 2018; Gaia Collaboration et al., 2018), if available. While errors for *Chandra* data points correspond to the $\pm 1\,\sigma$ quantiles of the source fluxes, corresponding errors for *XMM-Newton* and ROSAT were calculated using the stated errors in the respective catalogue. Other uncertainties, such as in the distance or the fixed energy conversion factors were not taken into account. Therefore we expect the true errors to be larger, in the order of 20 %–30 % (cf. Kashyap et al., 2008; Poppenhaeger et al., 2010; Miller et al., 2015) We further collected measurements of the stellar rotation velocity, $v \sin i$, for the host stars in our sample by cross-matching those with the catalogues compiled by Wright et al. (2011, VizieR ID J/ApJ/743/48) and Głębocki & Gnaciński (2005, III/244) using a search radius of $3''$ and $5''$, respectively (due to high uncertainties in the source positions for the latter).

Finally, we omit the detections of unconfirmed, gap-opening planets[23] still embedded in a protoplanetary disc, as their existence is highly debated. For example, a recent study by

[22] `https://heasarc.gsfc.nasa.gov/cgi-bin/Tools/w3pimms/w3pimms.pl`

[23] These are namely TW Hya a/b, HD 100546 b, HD 98800 B b, KH 15D b and QS Vir b.

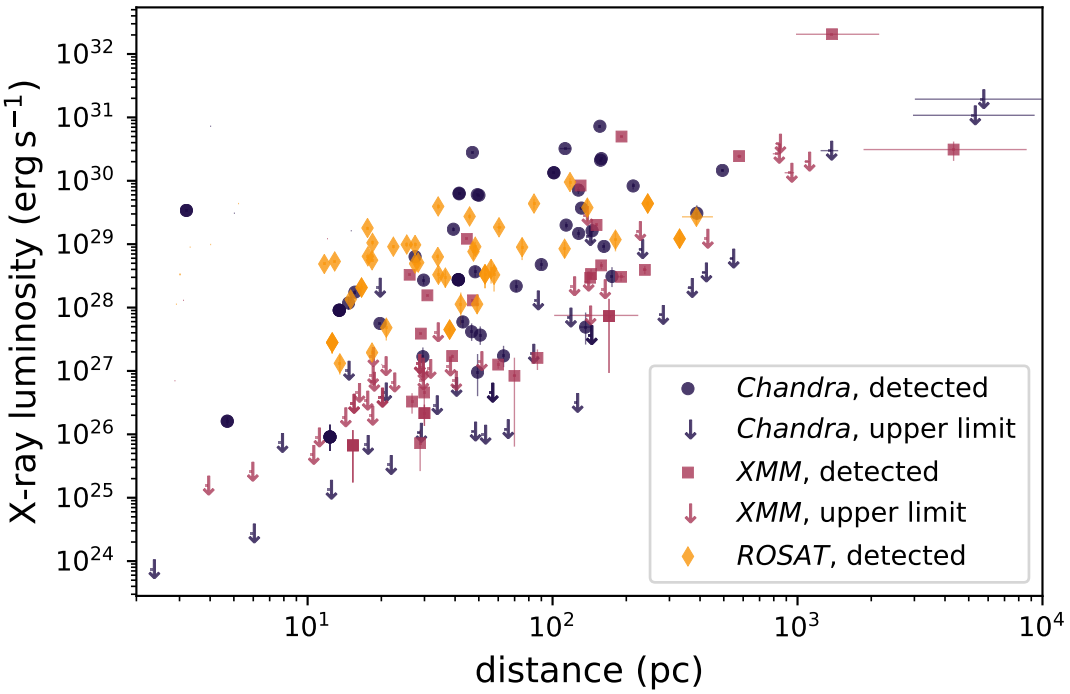

Figure 6.1: X-ray luminosity as a function of distance for the planet-hosting stars in our catalogue. Upper limits are indicated as arrows and correspond to stars that have been observed but were not detected in a given X-ray observation. This plot excludes targets where only *ROSAT* upper limits are available, as their X-ray luminosities have been crudely estimated using a fixed value for the stellar flux, as discussed in Section 6.3.3.

Ercolano et al. (2017) suggests a photoevaporative origin of the gap seen in the disc surrounding TW Hya rather than a giant planet. The current version of the catalogue therefore contains X-ray luminosities and planetary data for nearly 200 stars hosting giant planets, out of which 124 are X-ray detections and 70 upper limits.

6.4 Results and Discussion

6.4.1 Distribution of stellar and planetary properties in our catalogue

Figure 6.1 shows the X-ray luminosity distribution of all stars hosting planets with masses larger than 0.1 M_J in our catalogue as a function of distance. As expected, most detected systems are relatively nearby with distances $\lesssim 200$ pc. Owing to *Chandra*'s high sensitivity, it is however possible to infer meaningful upper limits on X-ray luminosities even for stars with distances up to 10^4 pc. While the most distant systems[24] in Figure 6.1 are more likely to be an exception, X-ray information of systems up to several hundreds of parsecs can be routinely obtained. In

[24]SWEEPS-04 & SWEEPS-11, detected within the *Sagittarius Window Eclipsing Extrasolar Planet Search* near the Galactic Bulge (SWEEPS, Sahu et al., 2006).

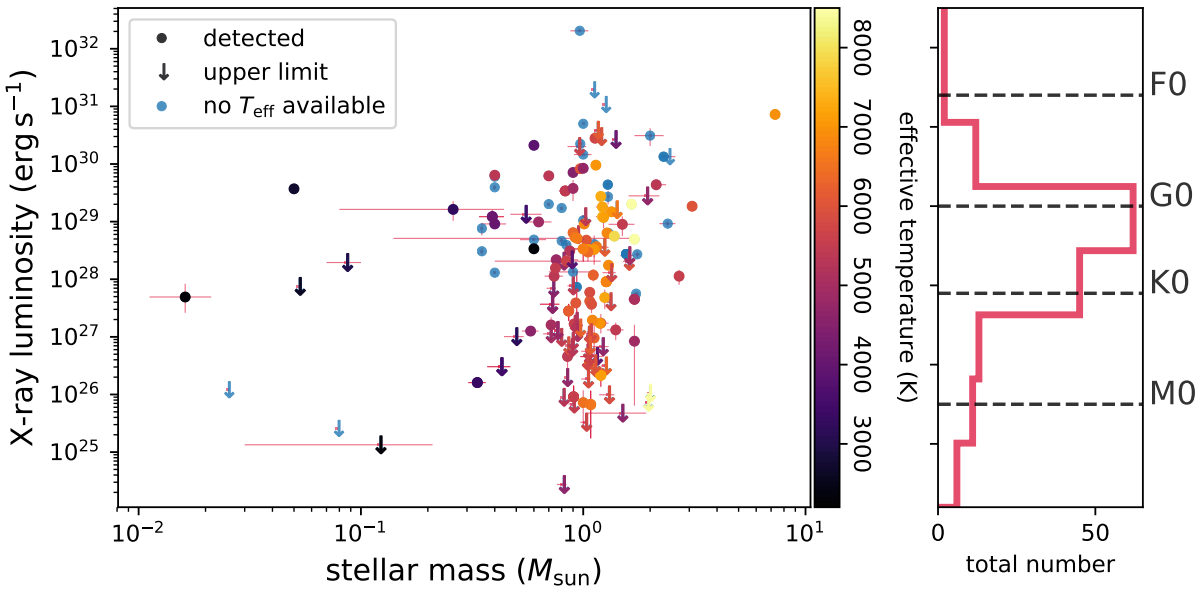

Figure 6.2: X-ray luminosity of all host-stars in our catalogue as a function of their mass, with their effective temperature shown as colours. Upper limits are indicated as arrows and correspond to stars that have been observed but were not detected in a given observation. The histogram on the right shows the distribution of effective temperatures for these stars and their corresponding spectral types.

particular the combination of shallow but abundant ROSAT and *XMM-Newton* data with highly sensitive *Chandra* observations enables us to obtain a rather complete sample and to cover a larger range of observed X-ray luminosities of giant planet hosts.

Figure 6.2 shows the resulting $L_{\rm x}$-vs-$M_{\rm star}$ distribution of the stars in our sample, with colours corresponding to the effective temperature of each star. One can immediately infer that this distribution peaks close to $\sim 1\,M_{\odot}$, thus most stars being of solar-type with effective temperatures ranging from 4000–7000 K. These stars therefore mostly resemble G- and K-type stars, as can be seen in the histogram in the right panel of Figure 6.2.

6.4.2 Observational biases and selection effects

The main goal of this chapter is to study whether X-ray-driven photoevaporation has a detectable effect on the final semi-major axis distribution of giant planet systems and therefore we will only focus on the $L_{\rm x}$–vs–a distribution of these systems in the following. However, as previously pointed out, our catalogue contains several other properties of these systems which could be used to study further correlations and effects, such as in the context of star-planet interactions or the influence of stellar irradiation on exoplanet atmospheres.

In Figure 6.3 we show the resulting X-ray luminosity distribution for all stars vs. the semi-major axes of their giant planets. The observed distribution covers several orders of magnitudes both in X-ray luminosities, $L_{\rm x}$, and in planet semi-major axes, a. Since the detection of extrasolar planets is subject to many observational biases, this results in several underpopulated regions,

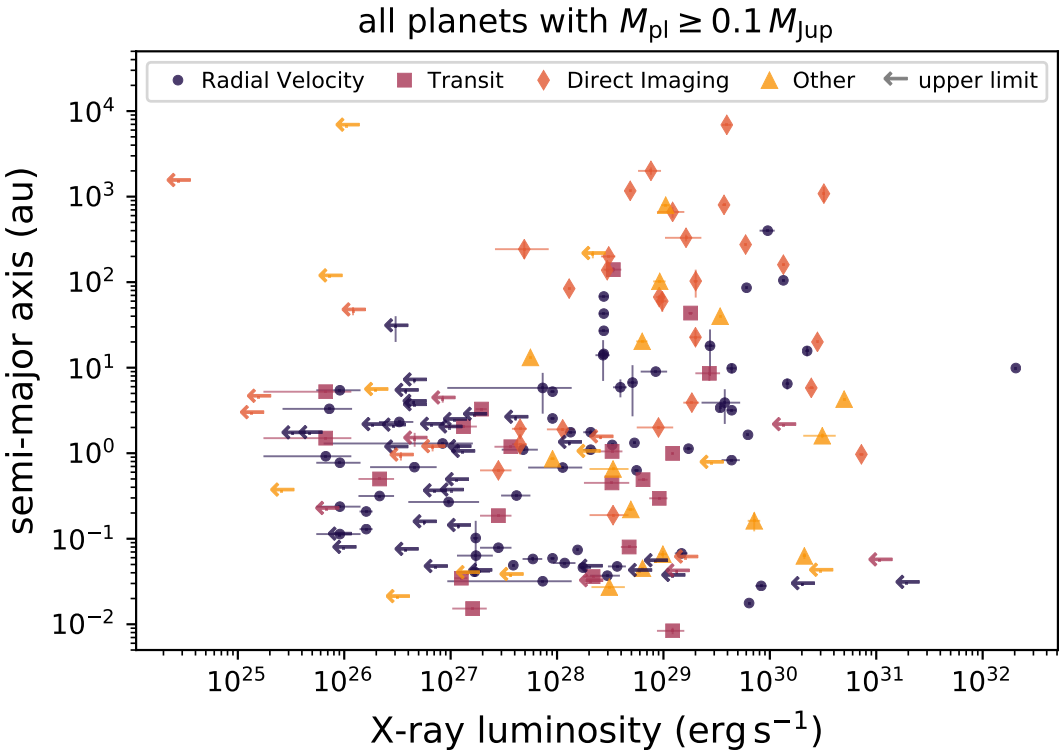

Figure 6.3: Observed semi-major axis vs. X-ray luminosity distribution of stars hosting giant planets with masses above 0.1 M_J, as discussed in Section 6.3. For multi-planet systems all planets with a mass of 0.1 M_J are plotted. The colours highlight the different exoplanet detection methods for each system. Techniques that result in only very few detections (like astrometry or transit timing variation (TTV)) in our catalogue are summarised as 'Other'. Upper limits on X-ray luminosities are shown as arrows.

especially at large semi-major axes and low X-ray luminosities. A detailed description of many possible observational biases can be found in Kashyap et al. (2008) and Miller et al. (2015), which will be further discussed in the following.

We have assigned different colours and symbols for each exoplanet detection method in Figure 6.3 to test whether they are introducing features in the overall distribution. As expected, most planets ($\sim$ 50 %) have been detected by the radial velocity (RV) method, which is specifically sensitive to high-mass planets at small to intermediate orbits (e.g. Wright, 2018). While they are present over the entire X-ray luminosity range, they are mostly concentrated at lower values of L_x, because X-ray bright stars are generally less frequently targeted by RV-surveys due to the high variability of the stellar emission. Such stars often correspond to young pre-main sequence stars whose high activity is impeding the identification of weak RV-signals (such as by low-mass or distant planets) within the stellar spectrum (e.g. Jeffers et al., 2014). However, new methods for detecting planets especially around young active stars are promising (e.g. Jones et al., 2017; Biddle et al., 2018), which could help to fill this underdense region in the L_x–a parameter space.

Similar behaviour is found for planets detected by the transit method, which are, however,

significantly less frequent than RV-detected planets in our sample. Due to the confined range of inclinations that is needed to observe planetary transits, this method is more restricted to close-in ($< 10\,\mathrm{au}$) planets (e.g. Deeg & Alonso, 2018). Further, most transiting planets are found around stars with intermediate to low X-ray activity ($L_\mathrm{x} \lesssim 10^{29}\,\mathrm{erg\,s^{-1}}$), as the presence of stellar spots on highly active stars does not only impede the detection of exoplanets but also the accurate determination of their physical properties (e.g. Boisse et al., 2011; Ballerini et al., 2012).

For large semi-major axes (i.e. $\gtrsim 10\,\mathrm{au}$), the most sensitive planet detection method is direct imaging.[25]. This technique detects young planets more easily, since they are still releasing the accretion luminosity from their formation phase (e.g. Spiegel & Burrows, 2012) and are thus brighter in the infrared. Young planets are associated with younger, and therefore more X-ray bright stars (cf. Section 6.2), which explains why the upper right part of Figure 6.3 is more densely populated compared to the upper left region.

The remaining planets detected by astrometry or transit timing variation are summarised as 'Other' in Figure 6.3. Since they only make up a small fraction of our sample ($< 10\,\%$), we do not expect them to introduce any significant features in the L_x–a-distribution. Nevertheless, this is expected to change with the recently published second data release of *Gaia*, which will likely include many new exoplanet detections by astrometry and gravitational microlensing (Perryman et al., 2014; Katz & Brown, 2017).

Our catalogue includes in total 200 giant planets which have measured X-ray luminosities of their host stars. Compared to the *Extrasolar Planets Encyclopaedia*, which included 1224 giant planets at the time the catalogue was prepared, this corresponds to 16 % of the total sample. If we restrict ourselves to wide-orbit planets only (i.e. $a > 5\,\mathrm{au}$), our catalogue covers 44 % out of the planets from the exoplanet archive (i.e. 56 vs 126 planets). To check, if the stellar properties of the wide-orbit planet host stars differ significantly from those of the remaining sample, we have searched for trends and systematics in the distribution of different stellar properties but did not find any. The upper left part of Figure 6.3 is therefore the only region where an observational bias is affecting all the detection methods. However, it is difficult to identify and account for all of these biases. Therefore, every analysis of possible correlations or trends within the data should be treated with caution, if the distorting effect of observational biases cannot be ruled out entirely (cf. Poppenhaeger & Schmitt, 2011).

6.4.3 Theoretical implications of X-ray photoevaporation onto the final locations of giant planets

Before one can begin to search for possible features within the observed distribution of exoplanets, it is important to understand how X-ray photoevaporation may be affecting the dispersal of protoplanetary discs, which is eventually halting the planet migration process and therefore likely shaping their semi-major axis distribution in a characteristic manner. However, as discussed previously in Section 6.2.2, the rank in primordial X-ray luminosities is not expected to

[25] Also microlensing can detect planets with large semi-major axes, however, since follow-up observations are often impossible, their orbital properties are loosely defined (cf. Gaudi, 2010; Winn & Fabrycky, 2015).

be conserved for stars with ages $> 2\,\mathrm{Gyr}$. To be able to link the observed properties of the giant planet hosts to their X-ray luminosities at the time of disc dispersal, we will consider only 'young' stars in the following, i.e. stars with ages below 2 Gyr.

Predictions for expected features within the observations

Mass loss by photoevaporation is concentrated at a given disc radial distance, around the so-called gravitational radius, which is roughly 1-2 au for solar type stars (Hollenbach et al., 1994; Alexander & Armitage, 2009). At this location a gap in the protoplanetary disc is formed when the mass loss rate due to photoevaporation exceeds the accretion rate through the disc. Thus naively one can expect to observe an under-density of planets around the gravitational radius for a given range of X-ray luminosities for which a vigorous wind is expected (L_x of order 10^{29}–$10^{30}\,\mathrm{erg\,s^{-1}}$). As the disc is cleared from the inside out on a short time-scale, planets that are located outside of the photoevaporative gap are stopped, once the photoevaporative gap reaches their location. On the other hand, planets which are located inside the gravitational radius continue migrating, until the inner disc is dispersed due to viscous accretion. Assuming a broad range of initial conditions (such as the formation time and location of the planet or the strength of the photoevaporative wind), this results in an under-density of giant planets located inside the gravitational radius (cf. Alexander & Pascucci, 2012).

However, as already discussed in Section 6.2.2, the stellar X-ray luminosity decreases with age as a result of stellar spin-down. While protoplanetary disc dispersal occurs at much earlier stages of the stellar lifetime ($\lesssim 10\,\mathrm{Myr}$), the planet hosts in our catalogue mostly have ages of the order Gyr, when the X-ray luminosities are generally several orders of magnitude lower. It is thus to be expected that any features that are imprinted into the early L_x–a-distribution at the time of disc dispersal would be shifted to lower X-ray luminosities with increasing age of the corresponding system. Note however that an exact mapping of present day X-ray luminosity to earlier times is very model-dependant and not trivial, and therefore this is not attempted in the present work.

Additionally, our catalogue contains stars with a range of stellar masses, which could smear out an under-density feature, given that photoevaporation opens a gap at the gravitational radius R_g, which is linearly dependant on the stellar mass. R_g is defined as

$$R_\mathrm{g} = \frac{GM_\star}{c_\mathrm{s}^2}, \tag{6.1}$$

where $M_\star$ is the mass of the central star, G the gravitational constant and c_s the sound speed of the gas (Hollenbach et al., 1994). Thus a planet population with hosts of different stellar masses will produce deserts centered at several locations, depending on the gravitational radius of the members. Nevertheless, as solar-mass objects are the most abundant in our catalogue, one could still expect to observe an under-density of objects at the location of the gravitational radius for solar-type stars (i.e. 1–2 au).

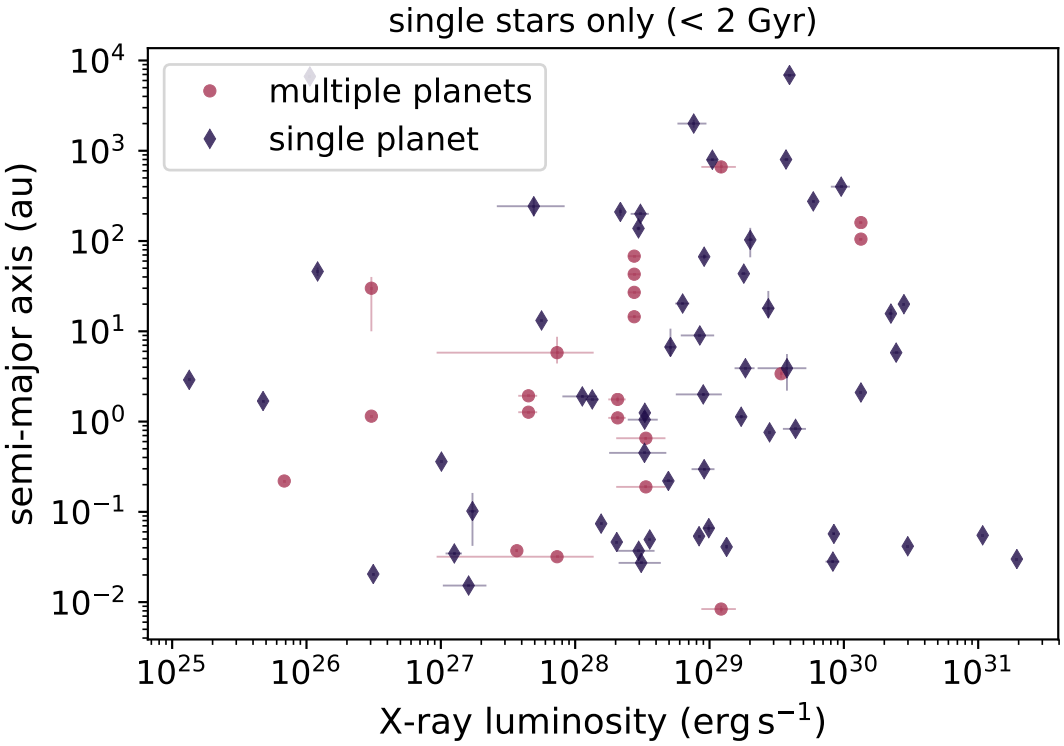

Figure 6.4: Semi-major axis vs. X-ray luminosity distribution for young (< 2 Gyr), single stars hosting confirmed giant planets in single (circles) and multiple (diamonds) planetary systems. The latter also include planets that have a planetary companion with a mass lower than the minimum mass limit of 0.1 M_J in our catalogue.

Dynamical evolution

A fundamental assumption made in our study is that the observed configuration of planetary systems resembles the one established soon after the dispersal of the protoplanetary disc. This is somewhat justified by recent results (cf. Kipping, 2018), that show that *Kepler* multi-planetary systems present a highly significant deficit in entropy compared to a randomly generated population, suggesting that they indeed keep a memory of their initial state. Therefore, the early migration phase of newly formed planets in the disc is extremely important in setting the initial conditions for any later dynamical evolution after disc dispersal.

It is therefore tempting to interpret orbital parameters (e.g. eccentricity) for the gas giants in our sample in the context of dynamical evolution, both post- and pre-disc dispersal (Dawson & Chiang, 2014; Huang et al., 2016; Petrovich & Tremaine, 2016; Anderson & Lai, 2017; Sotiriadis et al., 2017). This is, however, a non-trivial task, first of all because eccentricities and inclinations are difficult to infer from transit detections (e.g. Seager & Mallén-Ornelas, 2003b), resulting in large uncertainties in their determination. Furthermore, the naive assumption that planetary eccentricities are damped by the gaseous disc, leading to circular orbits after disc dispersal is also an over-simplification. Indeed, a forming giant planet, which is able to carve a very deep gap in the disc, can be left on significantly eccentric orbits at the end of the disc

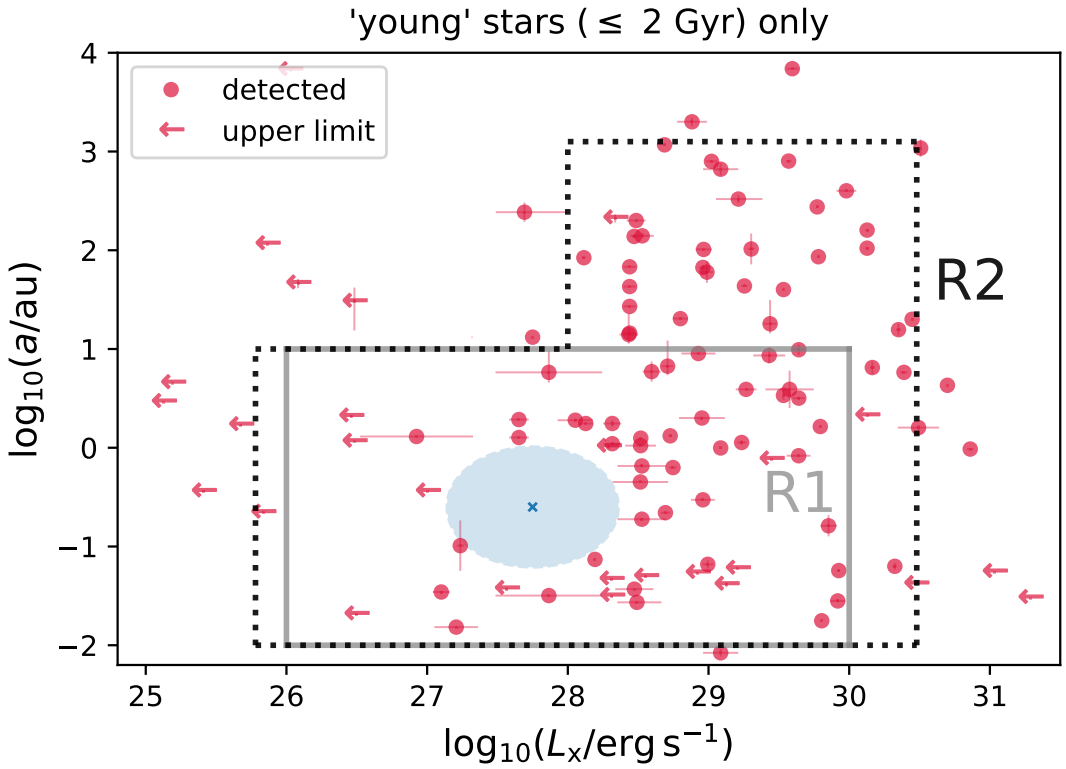

Figure 6.5: Semi-major axis vs. X-ray luminosity distribution of detected (circles) and undetected (arrows) stars in our catalogue. The grey/dotted contours show the reference regions used in the statistical analysis to test the significance of the encircled voids as described in Section 6.4.4. The blue region highlights the void, in which no young stars are found.

dispersal phase (e.g. Duffell & Chiang, 2015).

Wright et al. (2009) found that multi-planetary systems tend to have on average lower eccentricities (see also Huang et al., 2016). This behaviour is expected since planets with lower eccentricities are dynamically more stable in the long-term. Figure 6.4 shows the population of confirmed single and multiple planetary systems orbiting young (i.e. younger than 2 Gyr), single stars in our sample, where the latter also include planets that have a planetary companion with a mass below the minimum mass limit of 0.1 M_J. No significant difference is shown in the distribution of single and multiple-planetary systems for $L_x < 10^{29}$ erg s^{-1}, supporting our assumption that dynamical interactions between planets after disc dispersal do not change the overall picture. The lack of multiple-planetary systems for high L_x can be the result of faster disc photoevaporation, preventing the formation of multiple giant planet systems.

6.4.4 Deserts in the L_x-a-plane - signatures of X-ray-driven photoevaporation?

Previous work by Alexander & Pascucci (2012) and Ercolano & Rosotti (2015) suggests that signatures from X-ray-driven photoevaporation in the form of under- and overpopulation are likely to be imprinted in the final semi-major axis distribution of giant planets. While dynamical evolution of the planets after disc dispersal can alter their final location in the system drastically, their initial conditions are however set by the early evolution and migration phase while the disc is still present. Looking at the observed distribution shown in Figure 6.3 ($\sim$ Gyr), we find several underdense regions that *could* be related to X-ray-driven photoevaporation creating distinct features in the distribution of planets. These are, for example, centred on $(L_x, a) \sim (3 \times 10^{29}\,\mathrm{erg\,s^{-1}}, 0.2\,\mathrm{au})$, $(2 \times 10^{28}\,\mathrm{erg\,s^{-1}}, 5\,\mathrm{au})$ or $(10^{27}\,\mathrm{erg\,s^{-1}}, 1\,\mathrm{au})$. Nonetheless, as pointed out in Section 6.4.2, our catalogue is subject to many observational biases and selection effects that can hardly be all accounted for. Especially the underdensities seen near the edges of the L_x–a-distribution in Figure 6.5 (which is similar to Figure 6.3, however now only young stars (i.e. $< 2\,\mathrm{Gyr}$) are shown, as they are the only ones from which a memory of their primordial X-ray luminosity is to be expected, cf. Section 6.2.2) are most likely the result from observational biases rather than real physical effects, which is affirmed by the generally smaller number of data points in these regions. The only void in this distribution that cannot be readily explained by any observational biases or selection effects, is the desert centred on $[\log(L_x/\mathrm{erg\,s^{-1}}), \log(a/\mathrm{au})] \sim [27.8, -0.6]$. It is fully surrounded by 'young' stars, and as discussed in Section 6.4.2, most likely not shaped by the different exoplanet detection methods. Further, no upper limits are located on its right side, ensuring that no such limits might scatter into this gap.

However, with the current dataset it is difficult to unambiguously interpret this feature as a result of X-ray-driven photoevaporation. First of all, the small sample size reduces the voids' statistical significance. This is aggravated by the lack of knowledge of the expected void location, size and shape. In Appendix 6.A, we therefore discuss the significance of this void for two different cases: (i) without any assumptions on its location/size (Section 6.A.1) and (ii) with an a priori knowledge of its location/size (e.g. assuming a numerical model could constrain these properties (Section 6.A.2). This will allow us to forecast, how this analysis may benefit from additional observational data and more detailed numerical modelling. For this purpose we have defined two reference regions, R1 and R2, in which our observational sample is assumed to be complete and not subject to any major observational biases.

We find that the statistical significance of the observed void can only be proven in the current sample if its exact location and shape/size are known from theory. At this stage, our numerical model suffers from too many uncertainties which limits its predictive power. While an increased observational sample would certainly help to show the significance of any of the observed features, a more realistic numerical modelling is urgently needed to constrain the expected void location and size. One-dimensional approaches as those employed by AP12 and ER15 are plagued by a number of uncertainties and a systematic exploration of the result's sensitivity on the parameters used in the numerical simulations can help to better understand the underlying mechanisms. This will be the focus of a follow-up paper, which will solely aim

at improving our theoretical understanding of how X-ray-driven photoevaporation may affect the final semi-major axis distribution of giant planets.

6.5 Summary and Conclusions

We have searched for signatures of X-ray-driven photoevaporation of planet-forming discs in the present-day semi-major axis distribution of giant planets. To that end we have constructed a catalogue, containing the X-ray properties of all known planet-hosting stars, which have been observed by *Chandra*, *XMM-Newton* and/or ROSAT. This catalogue contains basic stellar and planetary properties as well as X-ray fluxes and luminosities.

The main results from a statistical analysis of the data we collected combined with theoretical considerations can be summarised as follows:

- By correlating the X-ray luminosity of the host stars with the semi-major axis distribution of their giant planets, we found a prominent under-density within the L_x-vs-a distribution, roughly centred on $(L_x, a) \sim (10^{28}\,\mathrm{erg\,s^{-1}}, 0.2\,\mathrm{au})$. To our knowledge, this void cannot be explained by any observational biases in the planet-detection process.

- Due to the limited sample size of our observations, it is currently not possible to prove the significance of this void. Certainly, missions like TESS and eROSITA will help to resolve this issue by monitoring large parts of the sky, therefore increasing the sample of X-ray observations of giant planets hosts drastically.

- The possible void hinted in the observational data ($[L_x, a] \sim [10^{28}\,\mathrm{erg\,s^{-1}}, 0.2\,\mathrm{au}]$) is at a different location from what is expected from simple theoretical considerations ($[L_x, a] \sim [10^{29}$–$10^{30}\,\mathrm{erg\,s^{-1}}, 1$–$2\,\mathrm{au}]$). While the shift in L_x is readily explainable by considering the expected decay in X-ray luminosity of stars from Myr to Gyr ages, the shift in semi-major axis is more puzzling. In the case the statistical significance of this feature is confirmed, this would point to a clear knowledge of how high energy radiation from the stellar host affects the final architecture of giant exoplanets.

Acknowledgements We thank Giovanni Rosotti and Jeff Jennings for helpful discussions and their support on using `SPOCK` for the numerical analysis. We also thank the anonymous referee for his/her extensive review, which led to the significant improvement of this paper. We acknowledge the support of the DFG priority program SPP-1992 "Exploring the Diversity of Extrasolar Planets" (DFG PR 569/13-1, ER 685/7-1) & the DFG Research Unit "Transition Disks" (FOR 2634/1, ER 685/8-1). B.E. acknowledges the support by the Munich Institute for Astro- and Particle Physics (MIAPP) of the DFG Cluster of Excellence 'Origin and Structure of the Universe'. M.M.R. is supported by DOE grant DESC0011114.

The catalogue presented in this work is mainly based on stellar and planetary properties gathered from the *Extrasolar Planets Encyclopaedia* (`http://www.exoplanet.eu`, Schneider et al., 2011). This research has made use of data obtained from the *Chandra* Data Archive and the *Chandra* Source Catalogue, and software provided by the *Chandra* X-ray Center (CXC) in the application packages `CIAO`, ChIPS, and Sherpa and of data obtained from the 3XMM *XMM-Newton* serendipitous source catalogue compiled by the 10 institutes of the XMM-Newton Survey Science Centre selected by ESA. This publication additionally makes use of data products from the Two Micron All Sky Survey, which is a joint project of the University of Massachusetts and the Infrared Processing and Analysis Center/California Institute of Technology, funded by the National Aeronautics and Space Administration and the National Science Foundation. This work has made use of data from the European Space Agency (ESA) mission *Gaia* (`https://www.cosmos.esa.int/gaia`), processed by the *Gaia* Data Processing and Analysis Consortium (DPAC, `https://www.cosmos.esa.int/web/gaia/dpac/consortium`). Funding for the DPAC has been provided by national institutions, in particular the institutions participating in the *Gaia* Multilateral Agreement.

Software: `AstroPy` (Robitaille et al., 2013), `CIAO` (Fruscione et al., 2006), `Matplotlib` (Hunter, 2007), `NumPy` (Van Der Walt et al., 2011), `SAOImage DS9` (Joye & Mandel, 2003), `SciPy` (Virtanen et al., 2020), `SPOCK` (Ercolano & Rosotti, 2015), `TOPCAT` (Taylor, 2005)

Appendix

6.A Statistical Analysis

In Section 6.4.4 we discussed that the void located at $[\log(L_x/\mathrm{erg\,s^{-1}}), \log(a/\mathrm{au})] \sim [27.8, -0.6]$ in Figure 6.5 cannot be readily explained by any observational biases. A void of similar shape and size is found in a simplified population synthesis model which we have performed using the same code and setup as Ercolano & Rosotti (2015) & Jennings et al. (2018), though it is located at lower X-ray luminosities and semi-major axes. While this shift between the observations ($\sim$ Gyr) and the simulation ($\sim$ Myr) can be somewhat qualitatively explained, it is currently not possible to predict the shifts' extent with high accuracy. This weakens the voids' significance within the observations, as either a larger observational sample or more detailed numerical models are required to obtain statistically significant results. Therefore, we will investigate the void significance for two different cases in the following, namely (i) without any assumptions on its location/size (Section 6.A.1) and (ii) with an a priori knowledge of its location/size by assuming our preliminary numerical model is constraining these properties (Section 6.A.2). However, we restrict ourselves to 'young' stars only, as they are the only category for which a memory of the primordial X-ray luminosity is expected (cf. Section 6.2.2).

6.A.1 No a-priori knowledge of the location/size of the void

Considering a randomly populated area of size A_{tot} and mean point density $n = N_{\mathrm{tot}}/A_{\mathrm{tot}}$, where N_{tot} is the total amount of data points in our reference region A_{tot}, the probability to find a void of size A_{void} is described by the Poisson formula

$$P_0(nA_{\mathrm{void}}) = \exp\left(-nA_{\mathrm{void}}\right) . \tag{6.2}$$

If one could accurately constrain the position of the under-density from theory, this would yield the probability that the void is seen in a randomly distributed dataset using Eq. 6.2. However, if the position of the under-density cannot be constrained to high enough precision using simulations, we have to consider voids of arbitrary shape and position. The mean number of voids per unit area to be expected in a random distribution was derived by Politzer & Preskill (1986) and Otto et al. (1986) to be

$$D_0(n, A_{\mathrm{void}}) = \frac{(nA_{\mathrm{void}})^2}{A_{\mathrm{void}}} \exp\left(-nA_{\mathrm{void}}\right) . \tag{6.3}$$

The prefactor to this equation takes into account that overlapping voids will be correlated instead of being independent from each other. We further note that the complexity of the tested region needs to be constrained to yield a reasonable analysis, since it will always be

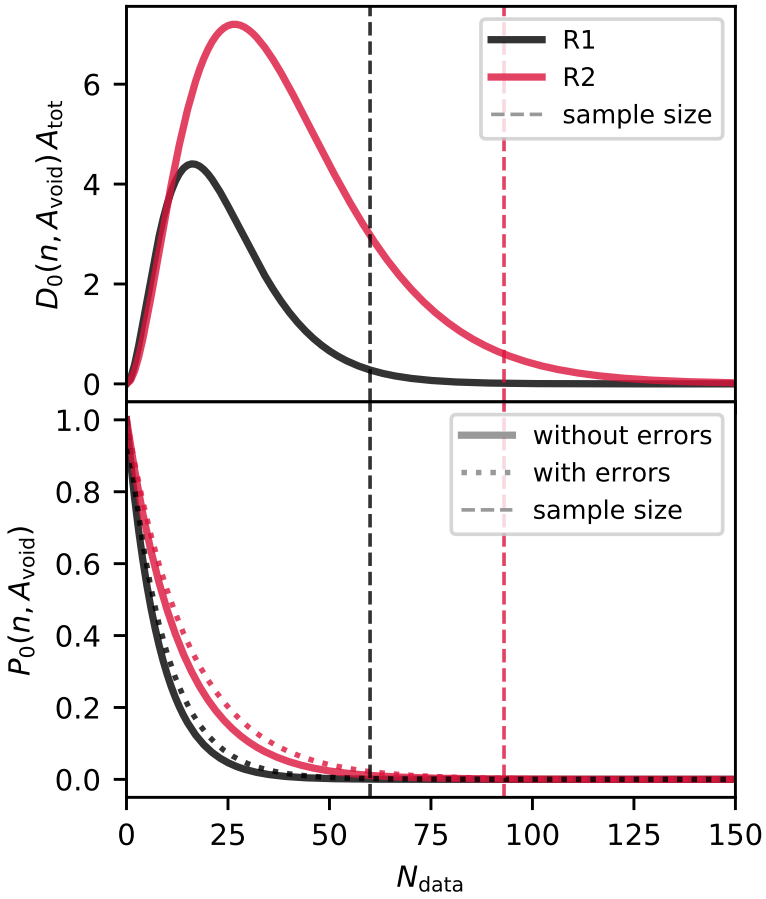

Figure 6.A.1: *Top*: Expected number of voids with fixed size and horizontal orientation, but variable position within the reference regions R1 and R2, respectively. The two solid curves show the two different scenarios for a range of possible sample sizes: only young stars (i.e. < 2 Gyr) within R1 (black) and R2 (red), respectively. The vertical lines show the actual sample size of each test. *Bottom*: The probability that the gap contains no data points without (solid lines) and with (dotted lines) including error measurements. The colours correspond to the same cases as in the upper panel.

possible to find a large region of arbitrary, complex shape in a point cloud. For simplicity, we therefore assume a cubic test region with fixed horizontal orientation, noting that choosing a circular test region reduces the expected number of voids only slightly by $\approx 10\,\%$ (Otto et al., 1986). We test against a random distribution in the $\log(L_{\rm x}/{\rm erg\,s^{-1}})$–$\log(a/{\rm au})$ plane in which the void is most apparent. We consider two cases that correspond to different choices for the reference region ($A_{\rm tot}$) as illustrated in Figure 6.5. Since R1 neglects several systems with high X-ray luminosities and large semi-major axes, we increased the reference region in R2, in which only the clearly underpopulated region at high semi-major axes (> 10 au) and low X-ray luminosities ($< 10^{28}\,{\rm erg\,s^{-1}}$) is omitted.

The top panel of Figure 6.A.1 shows the expected number of voids for a random distribution $D_0(n, A_{\rm void})\,A_{\rm tot}$, where $A_{\rm tot}$ describes the area of the reference regions R1 or R2, respectively.

The vertical lines correspond to the true sample size of each selection. Leaving the position of the void free and calculating the expected number of voids in a random distribution illustrates that for the current sample sizes, voids of the sizes considered in this study are to be expected. Thus, while the discussion in the previous section hints towards a physical origin of the observed void, with the current data its statistical significance cannot be shown. A significant increase in the sample size would be needed to allow a more detailed analysis of the presumed observational signature, which can help to refine our theoretical understanding of X-ray-driven photoevaporation.

6.A.2 A-priori knowledge of the location/size of the void

We now consider the case that the location and size of the void is known from theory. We show in the lower panel of Figure 6.A.1 the probability of finding an empty, circular region in a random distribution of sample size N_{data} at the observed position for the two different scenarios. This test investigates whether the actual number of data points that are located within the reference regions, R1 and R2, is large enough to draw any conclusions on the significance of the presumed void. The probability of finding the selected void with a priori knowledge of its location and size approaches zero for increasing N_{data}, meaning that for larger sample sizes the probability of the gap being a result of random fluctuations approaches zero. The fact that the true sample sizes all lie in the flat region of each of these curves shows that the currently available amount of data on the X-ray properties of giant planet hosts is sufficiently large to interpret this void as significant, *if* our numerical model can constrain its location and size.

We further note the measurement errors of points near the corresponding void (assuming its location and size is well-constrained) imply that there is a small chance that some of them would be placed inside the under-density. For simplicity, we therefore make the simple assumption that the measurement errors reduce the radius R_{void} of the void by $R_{\mathrm{void}} - R_{\mathrm{err}}$, where R_{err} is given by the largest error of those points that could scatter into the under-density for the respective subsample. The resulting probabilities of finding this void of reduced size at the same location for each scenario as discussed before are shown as dotted lines in the lower panel of Figure 6.A.1. Their deviation to the curves that do not take the errors into account is small and can be neglected for simplicity.

We finally note that the approach presented here considers uniformly distributed samples in the $\log L_{\mathrm{x}}$–$\log a$ plane as the random distribution. This sampling does therefore not correspond to a uniform sampling in linear L_{x}–a space, as the density of uniform samples drawn in logarithmic space, as viewed in linear space, is exponentially higher for lower values than for larger ones.

We conclude that it is currently not possible to prove the significance of the presumed void, as its exact location and shape/size is not known a priori and only roughly constrained by our preliminary theoretical investigation. An increased observational sample and/or a more sophisticated approach to the numerical modelling may in the future help show the significance of the presumed void, presenting a novel and direct way to explore the effects of disc dispersal on the final architecture of planetary systems.

Chapter 7

Giant planet migration during the disc dispersal phase

The content of this chapter was published in:

Monsch K., Picogna G., Ercolano B., Kley W. (2021): "Giant planet migration during the disc dispersal phase"[26], *Astronomy & Astrophysics*, 646:A169

Abstract

Transition discs are expected to be a natural outcome of the interplay between photoevaporation and giant planet formation. Massive planets reduce the inflow of material from the outer to the inner disc, therefore triggering an earlier onset of disc dispersal due to photoevaporation through a process known as Planet-Induced PhotoEvaporation (PIPE). In this case, a cavity is formed as material inside the planetary orbit is removed by photoevaporation, leaving only the outer disc to drive the migration of the giant planet. We investigate the impact of photoevaporation on giant planet migration and focus specifically on the case of transition discs with an evacuated cavity inside the planet location. This is important for determining under what circumstances photoevaporation is efficient at halting the migration of giant planets, thus affecting the final orbital distribution of a population of planets. For this purpose, we use 2D FARGO simulations to model the migration of giant planets in a range of primordial and transition discs subject to photoevaporation. The results are then compared to the standard prescriptions used to calculate the migration tracks of planets in 1D planet population synthesis models. The FARGO simulations show that once the disc inside the planet location is depleted of gas, planet migration ceases. This contradicts the results obtained by the impulse approximation, which predicts the accelerated inward migration of planets in discs that have been cleared inside the planetary orbit. These results suggest that the impulse approximation may not be suitable for planets embedded in transition discs. A better approximation that could be used in 1D models would involve halting planet migration once the material inside the planetary orbit is depleted of gas and the surface density at the 3:2 mean motion resonance location in the outer disc reaches a threshold value of $0.01\,\mathrm{g\,cm^{-2}}$.

[26] This chapter depends on collaborative work which I had the opportunity to take the lead of. In particular I was responsible for performing all simulations and presenting their results in the manuscript, but Giovanni Picogna helped me significantly in the preparation of this project and setting up the simulations. While I was responsible for the composition of the manuscript, I was supported by all of my coauthors in interpreting and discussing the results.

7.1 Introduction

Giant planet migration is regarded as a natural outcome of the gravitational interaction between a forming planet and the surrounding gas in the planet-forming disc. While the existence of this process was predicted more than 40 years ago (Lin & Papaloizou, 1979; Goldreich & Tremaine, 1979, 1980), its importance for planet formation theories was only realised with the first discoveries of the so-called hot Jupiters (e.g. Mayor & Queloz, 1995). These Jupiter-like planets with orbital periods of $P < 15\,\mathrm{d}$ (Wang et al., 2015) are considered to be direct evidence of planet migration having taken place. Their in situ formation at such small distances to their host stars is unlikely (see, however, Batygin et al., 2016, and Boley et al. (2016) for alternative explanations), suggesting that these planets generally formed in the outer parts of the planet-forming disc and migrated inwards during their evolution (e.g. Dawson & Johnson, 2018).

In the last few years, scattered light and (sub-)millimetre surveys have provided observations of circumstellar discs with different substructures, such as rings (e.g. ALMA Partnership et al., 2015; van Boekel et al., 2017), spirals (e.g. Benisty et al., 2015; Dong et al., 2018; Muro-Arena et al., 2020), or shadows (e.g. Benisty et al., 2017; Walsh et al., 2017). While there is a range of mechanisms that can potentially explain these substructures, such as gas pressure bumps at ice lines (e.g. Zhang et al., 2015; Okuzumi et al., 2016; Owen, 2020), photoevaporation (e.g. Ercolano et al., 2017), or non-ideal magnetohydrodynamic (MHD) effects (e.g. Hu et al., 2019), the deep gaps and other substructures in many of these systems are commonly believed to have been carved by nascent planets (e.g. Paardekooper & Mellema, 2004; Picogna & Kley, 2015; Dipierro & Laibe, 2017; Zhang et al., 2018; Veronesi et al., 2020). The discovery of the two young, accreting protoplanets PDS 70b and PDS 70c (Keppler et al., 2018; Müller et al., 2018; Haffert et al., 2019) proved that giant planets can indeed form early and that gaps and rings in so-called transition discs may offer potential indirect evidence for embedded planets (Rosotti et al., 2016; Sanchis et al., 2020) and possibly also for their migration (Meru et al., 2019; Nazari et al., 2019; Pérez et al., 2019).

Independently of when exactly giant planet formation sets in, the dispersal of the gas-phase of planet-forming discs sets not only a strict upper limit to the planet formation timescale (Pollack et al., 1996), but also to planet migration as this is the result of the exchange of angular momentum between the planet and the gas in the disc. As the migration timescale of giant planets (typically $\sim 10^5\,\mathrm{yr}$, cf. Kley & Nelson, 2012) has been shown to be much shorter than the observed lifetimes of planet-forming discs (typically $\sim 10^6$ yr, cf. Haisch et al., 2001; Mamajek, 2009; Fedele et al., 2010; Ribas et al., 2014, 2015), this elucidates the necessity of formulating planet formation theories in combination with disc dispersal mechanisms.

It is commonly believed that planet-forming discs disperse via a combination of viscous accretion and disc winds, possibly launched due to internal photoevaporation by the host star. Theoretical models predict that viscous accretion dominates for most of the disc lifetime, until the accretion rates can no longer match the mass loss rate due to disc winds, which will finally disperse the disc quickly on a timescale of a few hundred thousand years from the inside out (Alexander et al., 2014; Ercolano & Pascucci, 2017). The evolution of young stars on colour-colour diagrams of nearby star-forming regions is indeed consistent with the prediction of a fast

inside-out dispersal phase (Ercolano et al., 2009b, 2011; Koepferl et al., 2013).

Models show that the gas is heated and finally unbound, predominantly by soft X-rays ($0.1\,\mathrm{keV} \leq E \leq 1\,\mathrm{keV}$) emitted by the host star so that over a range of disc radii a vigorous disc wind is established and eventually a gap opens up in the disc. This decouples the inner from the outer disc, so that the former drains viscously onto the central star, while the latter is photoevaporated away from the inside out (Ercolano et al., 2008, 2009a; Owen et al., 2010, 2011a, 2012). The influence of extreme ultraviolet radiation (EUV, $13.6\,\mathrm{eV} \leq E \leq 0.1\,\mathrm{keV}$) on the final mass loss rates is expected to be negligible due to the fact that EUV photons are readily absorbed by atomic hydrogen in the disc atmosphere, and thus have a much smaller penetration depth (Ercolano et al., 2008, but see also Wang & Goodman (2017) and Nakatani et al. (2018)). The notion that the EUV luminosities impinging on protoplanetary discs are low compared to soft X-rays has also been observationally confirmed (Pascucci et al., 2014). Internal photoevaporation rates driven by far ultraviolet emission (FUV, $6\,\mathrm{eV} \leq E \leq 13.6\,\mathrm{eV}$) yield comparable mass loss rates of $\sim 10^{-8}\,M_{\odot}\,\mathrm{yr}^{-1}$ to the XEUV-models (Gorti et al., 2009; Gorti & Hollenbach, 2009), depending on the assumption made for the small grain population in the disc atmospheres. However, no hydrodynamical calculations exist to date for internal photoevaporation driven by FUV, and thus the mass loss profiles, $\dot{\Sigma}_{\mathrm{wind}}$, and mass loss rates, $\dot{M}_{\mathrm{wind}}$, still need to be confirmed by future calculations.

It has been numerically shown that disc dispersal via photoevaporative winds can strongly affect the migration of giant planets and therefore ultimately leave an imprint in their final semi-major axis distribution (Alexander & Armitage, 2009; Alexander & Pascucci, 2012; Ercolano & Rosotti, 2015; Jennings et al., 2018). These works also show that the final orbital distribution of giant planets strongly depends on the radial profile of the mass loss rates. It is thus in principle possible, within the limitation of the numerical models (see the discussions in Ercolano & Rosotti, 2015, and Jennings et al. (2018)), to observe an imprint of the disc dispersal phase in the present-day giant planet orbital distribution. Monsch et al. (2019) made a first attempt at finding possible signatures of X-ray-driven photoevaporation (XPE) in the observational exoplanet data, presumably established in the disc dispersal phase and driven by the highly energetic radiation emitted by the host star. To this aim, they looked for a possible link between the X-ray properties of stars hosting giant planets and their corresponding semi-major axis distribution. They assembled a catalogue of the stellar X-ray luminosities and found a suggestive void in the L_{x} versus semi-major axis plane. This void could be qualitatively explained as a consequence of disc dispersal via XPE, which stops giant planet migration at a given place in the disc for a given range of L_{x}. However, due to the small sample size, the statistical significance of this feature could not be proven with the data set at that time. Monsch et al. (2019) argued that, without having a significant increase in observational data points, accurate numerical models are required to predict the location and/or size of this gap a priori, in order to prove its statistical significance.

For such purposes, 1D planet population synthesis models are an ideal tool as they allow us to assess the impact of a range of different initial conditions on the final architecture of planetary systems (cf. Benz et al., 2014, and Mordasini 2018, for reviews). However, several simplifications have to be assumed in such models to be able to run a statistically significant amount of simulations, ultimately limiting their predictive power. In particular, approximating

a three-dimensional problem to 1D is the largest source of error since it requires the description of geometrically complex problems like angular momentum exchange between the gas disc and the planet in one dimension. This is generally achieved through prescriptions derived from more complex multi-dimensional hydrodynamical calculations.

One of these prescriptions is the so-called impulse approximation (Lin & Papaloizou, 1979), which is used to approximate the torques that are exerted by the gaseous disc on a planet. Since it yields the correct scaling as more complicated treatments (e.g. Trilling et al., 1998), it has been widely used in 1D planet population synthesis approaches to model the migration of planets embedded in gaseous discs (cf. Lubow & Ida, 2010, and Kley & Nelson (2012), for reviews). In our case, this regime corresponds to so-called type II migration, in which the planet is entrained in the viscous flow of the gas, therefore migrating at the viscous accretion speed. However, the classical paradigm of type II migration has recently been questioned, suggesting that the migration rate of the planet is not locked to the disc's viscous evolution (Duffell et al., 2014; Dürmann & Kley, 2015, and Kanagawa et al. (2018); however, see also Robert et al. (2018)). While the impulse approximation yields reasonable results for many disc-planet systems, its accuracy for more complex configurations, in which the 2D structure of the disc may be of relevance, still needs to be tested and adapted as, for example, by Liu et al. (2017), who studied the migration process of Super Earths trapped at the magnetospheric cavity of the planet-forming disc and are therefore subject to one-sided torques.

Using 2D hydrodynamical FARGO simulations, Rosotti et al. (2013, 2015) studied the interplay of giant planet formation and disc dispersal via XPE, concluding that giant planets may trigger the faster onset of disc dispersal by reducing the mass inflow into the inner disc. This effect was referred to as Planet-Induced PhotoEvaporation (PIPE). The disc around TW Hya may be a possible example of PIPE taking place as the planet, which might have carved the outer rings in the disc observed with ALMA (Andrews et al., 2016), may have also triggered the onset of photoevaporation that has cleared the disc at small radii (Ercolano et al., 2017). However, Rosotti et al. (2013, 2015) did not investigate in detail which effect this would have on the migration process of planets.

In this chapter, we extend the work by Rosotti et al. (2013) and investigate how the interplay of XPE and planet formation may affect giant planet migration. The aim is to assess whether the commonly employed impulse approximation in 1D models can correctly describe the migration of giant planets in photoevaporating discs. For this purpose, we perform 2D FARGO simulations to compare migration tracks of giant planets embedded in primordial discs to those embedded in transition discs for which the disc inside the planet has been cleared (for example by PIPE). These are then compared to results obtained from 1D simulations with the same input parameters that employ the impulse approximation.

The paper is structured as follows. In Section 7.2, we describe the 1D and 2D simulations used for this study. Section 7.3 summarises and discusses the results, while Section 7.4 highlights the limitations of our numerical model. In Section 7.5 we draw our conclusions and propose how planet migration in transition discs formed by PIPE could be handled in 1D planet population synthesis approaches.

7.2 Methods

To investigate the impact of photoevaporation on giant planet migration, we made use of both 1D and 2D simulations to compare migration tracks from the impulse approximation to those obtained from the full treatment of the underlying disc torques in two dimensions. Our study therefore only concerns the late phases of disc evolution, meaning when disc dispersal is taking place, assuming that the planet has already formed. In each of these approaches, we considered both primordial and transition discs formed by PIPE. Considering the former, we sought to study the impact of photoevaporation on the overall migration history of the planet, while considering the latter, we specifically investigated the process of giant planet migration in discs with an evacuated cavity inside the planetary orbit, so that the planet is only subject to one-sided torques acting from a rather massive outer disc.

7.2.1 X-ray photoevaporation model

We employed the XPE profile with an EUV component from the recent radiation-hydrodynamical calculations by Picogna et al. (2019) and refer the reader to that work for more details on the underlying physical model. It improves on previous work by Owen et al. (2010, 2011a, 2012) by parameterising the temperature as a function of local gas properties and the column density to the star. This results in an almost twice higher mass loss rate compared to Owen et al. (2012) and differences in the radial profile of the mass loss rate. Wölfer et al. (2019) present X-ray photoevaporation models for carbon-depleted discs, predicting even more vigorous winds with radially extended profiles. Studying the migration of giant planets in X-ray photoevaporated, carbon-depleted discs is, however, beyond the scope of this paper and will be attempted in future work. While photoevaporative winds are expected to be dusty (Franz et al., 2020), the remaining dust in the disc is not likely to affect giant planet migration significantly (see Benítez-Llambay & Pessah, 2018, for a study on the impact of dust on the migration of low-mass planets).

The strength of the photoevaporative mass loss rate is primarily determined by the stellar X-ray luminosity, which typically reaches highly elevated levels for young T Tauri stars compared to their main-sequence counterparts (e.g. Feigelson & Montmerle, 1999). We used the X-ray luminosity function determined for the Taurus molecular cloud by Güdel et al. (2007) and scale this to a stellar mass of 0.7 $M_\odot$, with a resulting median of $L_\mathrm{x} = 1.1 \times 10^{30}\,\mathrm{erg\,s^{-1}}$. To cover the intrinsic scatter of X-ray luminosities of T Tauri stars for a given stellar mass, we considered two values for the X-ray luminosity in the simulations presented here, namely $L_\mathrm{x} = 2.7 \times 10^{29}\,\mathrm{erg\,s^{-1}}$ and $L_\mathrm{x} = 1.1 \times 10^{30}\,\mathrm{erg\,s^{-1}}$.

Picogna et al. (2019) present different mass loss profiles for primordial and transition discs, which we included in our calculations. These profiles are described in detail in Appendix 7.A. For most of the disc lifetime, the viscous accretion rate onto the star ($\sim 10^{-8}\,M_\odot\,\mathrm{yr^{-1}}$ at 1 Myr, cf. Hartmann et al. 1998) exceed the mass loss rate due to photoevaporation, which for the above stated X-ray luminosities of $L_\mathrm{x} = 2.7 \times 10^{29}\,\mathrm{erg\,s^{-1}}$ and $L_\mathrm{x} = 1.1 \times 10^{30}\,\mathrm{erg\,s^{-1}}$, reaches values of $5.6 \times 10^{-9}\,M_\odot\,\mathrm{yr^{-1}}$ and $1.8 \times 10^{-8}\,M_\odot\,\mathrm{yr^{-1}}$. After the viscous accretion rate drops below the wind mass loss rate, photoevaporation will open a gap in the disc, and cut off the

inner disc from further mass supply from the outer disc. While the inner disc drains viscously onto the central star, the outer disc is irradiated directly by the stellar X-rays as soon as the column density of the remaining material inside the gap becomes less than the maximum X-ray penetration depth of roughly $2.5 \times 10^{22}\,\mathrm{cm}^{-2}$ (Ercolano et al., 2009a; Picogna et al., 2019). At this point the switch between the primordial and transition disc profile is performed in our models.

7.2.2 1D model using impulse approximation

To model the migration of a giant planet in an XEUV-irradiated disc following the impulse approximation, we used the 1D viscous evolution code SPOCK (Ercolano & Rosotti, 2015). We followed a similar setup as described by Ercolano & Rosotti (2015) and refer the reader to their work for more details on the numerical model, which we will only briefly summarise.

We modelled a planet-forming disc evolving under the influence of viscosity and X-ray photoevaporation from the host star with a mass of $0.7\,M_\odot$ and assumed an initial disc surface density profile of

$$\Sigma(R, t=0) = \frac{M_\mathrm{d}(t=0)}{2\pi R_1 R}\,\exp\left(-\frac{R}{R_1}\right), \tag{7.1}$$

where $\Sigma(R, t)$ is the gas surface density of the disc and R the distance from the star. Eq. 7.1 follows from the self-similarity solution of the diffusion equation using a time-independent power-law scaling of the disc radius with the kinematic viscosity, $\nu \propto R^\gamma$, assuming $\gamma = 1$ (cf. Lynden-Bell & Pringle, 1974; Hartmann et al., 1998). We used an initial disc mass of $M_\mathrm{d}(0) = 0.07\,M_\odot$ with a disc scaling radius of $R_1 = 18\,\mathrm{au}$, which defines the initial disc size and sets the viscous timescale of the disc (Alexander & Armitage, 2009). Following the standard α-prescription (Shakura & Sunyaev, 1973), viscosity is defined as $\nu = \alpha c_\mathrm{s} H$, where c_s is the sound speed of the gas, H the disc scale height and α a dimensionless parameter. We used $\alpha = 6.9 \times 10^{-4}$, which is consistent with models treating realistic hydrodynamical turbulence (Picogna et al., 2018), resulting in a viscous timescale of $t_\nu = 7 \times 10^5\,\mathrm{yr}$ at R_1. This combination of viscosity and disc scaling radius were chosen such that a population of discs subject to XPE from stars with an observationally motivated X-ray luminosity (cf. Section 7.2.1) have a mean disc lifetime of a few Myr as suggested by observations of young stellar clusters (Haisch et al., 2001; Mamajek, 2009; Fedele et al., 2010; Ribas et al., 2014, 2015).

The evolution of the planet-disc system can be described following the equation:

$$\frac{\partial \Sigma}{\partial t} = \frac{1}{R}\frac{\partial}{\partial R}\left[3R^{1/2}\frac{\partial}{\partial R}\left(\nu\Sigma R^{1/2}\right) - \frac{2\Lambda\Sigma R^{3/2}}{(GM_\star)^{1/2}}\right] - \dot{\Sigma}_\mathrm{w}(R, t), \tag{7.2}$$

where the first term on the right hand side describes the viscous evolution of the disc (Lynden-Bell & Pringle, 1974), the second term deals with the migration of the planet due to the torques exerted from the gas in the disc (e.g. Lin & Papaloizou, 1986), and finally, the last term is the mass loss due to photoevaporation (described by Eq. 7.12 and Eq. 7.15). Here, $M_\star$ is the stellar mass, G the gravitational constant and Λ is the rate of angular momentum transfer per

unit mass from the planet to the disc. Eq. 7.2 is discretised on a grid of $n_r = 1000$ radial cells equispaced in $R^{1/2}$, extending from 0.04 au to 10^4 au.

A fully formed planet of $M_p = 1\,M_J$ was then inserted at 5 au into the disc once it had reached a surface density of $\Sigma_0 = 10\,\mathrm{g\,cm^{-2}}$ or $100\,\mathrm{g\,cm^{-2}}$ at the planet insertion location. At this point the resolution was increased to $n_r = 4000$ and our simulations were divided into two sets – primordial and transition discs. In the former, the planet was inserted into the full disc, and was left to evolve undisturbed following disc-planet interactions. In the latter, as soon as the planet was inserted, we set the surface density to the floor value of $\Sigma_{\mathrm{floor}} = 10^{-8}\,\mathrm{g\,cm^{-2}}$ inside the planet location to manually create transition discs with an evacuated inner cavity, such as would be formed by PIPE.

Planetary accretion was modelled following Eq. 5 in Veras & Armitage (2004) and took place in both sets of our simulations, regardless of the inner disc being cleared or not. The planet then migrated at a rate given by the impulse approximation (Lin & Papaloizou, 1979, 1986):

$$\frac{\mathrm{d}a}{\mathrm{d}t} = -\left(\frac{a}{GM_\star}\right)^{1/2}\left(\frac{4\pi}{M_p}\right)\int_{R_{\mathrm{in}}}^{R_{\mathrm{out}}} R\Lambda\Sigma\mathrm{d}R. \tag{7.3}$$

The angular momentum input Λ is poorly known, and we therefore followed the formalism introduced by Armitage et al. (2002), which is a slight modification to the original one by Lin & Papaloizou (1986):

$$\Lambda(R,a) = \begin{cases} -\frac{q^2 GM_\star}{2R}\left(\frac{R}{\Delta_p}\right)^4 & \text{if } R < a \\ \frac{q^2 GM_\star}{2R}\left(\frac{a}{\Delta_p}\right)^4 & \text{if } R > a. \end{cases} \tag{7.4}$$

Here, $q = M_p/M_\star$ is the mass ratio between the planet and the star, a is the semi-major axis of the planetary orbit (assumed to be circular) and Δ_p is given by

$$\Delta_p = \max(H, |R-a|), \tag{7.5}$$

where H is the disc scale height. Δ_p corresponds to the impact parameter that ensures that material closer than one disc scale height is excluded from the torque calculation.

The simulations were stopped once the disc had been dispersed, or the planets reached $a = 0.15$ au as we do not attempt to model the interaction with the magnetospheric cavity. Table 3.1 summarises the initial conditions used for the 1D model, which are the same for both the primordial and transition disc simulations. The only parameters that were varied in the 1D simulations are the initial surface density of the disc, Σ_0, and the X-ray luminosity of the star, L_x.

7.2.3 2D FARGO simulations

To study the interaction of a giant planet embedded in an X-ray irradiated disc in 2D, we used a modified version of the hydrodynamical grid code FARGO (Masset, 2000), in which we included XPE. Before the planet is inserted, no detailed calculations of the disc structure are

SPOCK parameter	value
$M_\star$ ($M_\odot$)	0.7
M_d ($M_\odot$)	0.07
α	6.9×10^{-4}
R_1 (au)	18.
H/R	0.1
L_x (erg s^{-1})	2.7×10^{29}, 1.1×10^{30}
M_p (M_J)	1.
a_0 (au)	5.
Σ_0 (g cm^{-2})	10, 100
Σ_floor (g cm^{-2})	10^{-8}
R_in (au)	0.04
R_out (au)	10^4

Table 3.1: Initial conditions for the SPOCK simulations described in Section 7.2.2.

required due to the axis-symmetry of the system, which substantially reduces the computational expense of the simulations. However, once the planet is formed, this axis-symmetry will break as the planet induces spiral density waves and eventually carves a gap. Therefore, following the approach described in Rosotti et al. (2013), we used the surface density profile of the discs in the 1D simulations at the time of planet insertion as an input for the FARGO simulations.

We adopted a cylindrical polar coordinate system (r, ϕ, z) centred on the star. To implement a similar disc structure into FARGO as in the 1D simulations, we made use of the following relation (which is the default one in FARGO):

$$\Sigma(r) = \Sigma_0 \left(\frac{R}{l_0}\right)^{-p}, \tag{7.6}$$

where Σ_0 is the initial surface density at the base length unit of $l_0 = 5\,\mathrm{au}$ and $p = 1$ is the slope of the surface density profile. We note that this profile is different than the one described by Eq. 7.1 that was used in the 1D simulations. However, we tested that Eq. 7.6 correctly reproduces the surface density profile from SPOCK in the smaller radial domain modelled with FARGO at the time of planet insertion. Following the 1D simulations, we considered two different values of Σ_0, namely $10\,\mathrm{g\,cm^{-2}}$ and $100\,\mathrm{g\,cm^{-2}}$, while we kept the remaining parameters, unless otherwise stated, fixed to their default values. Further we assumed locally isothermal discs with a constant aspect ratio of $h = 0.1$ and a flaring index of $f = 0.25$, resulting in a mildly flared disc: $H/R = 0.1R^{0.25}$.

We modelled the disc from 0.4 au to 25 au with a resolution of $n_r = 256$ cells in radial and $n_\theta = 388$ cells in azimuthal direction using logarithmic spacing, which yielded approximately square cells at the planet location. This resolution was chosen in order to allow for a long integration time, while being able to probe the parameter space. We further performed a higher resolution simulation for comparison that gave similar results. We applied 'viscous outflow' boundary conditions at both boundaries of the radial grid to impose a steady-state

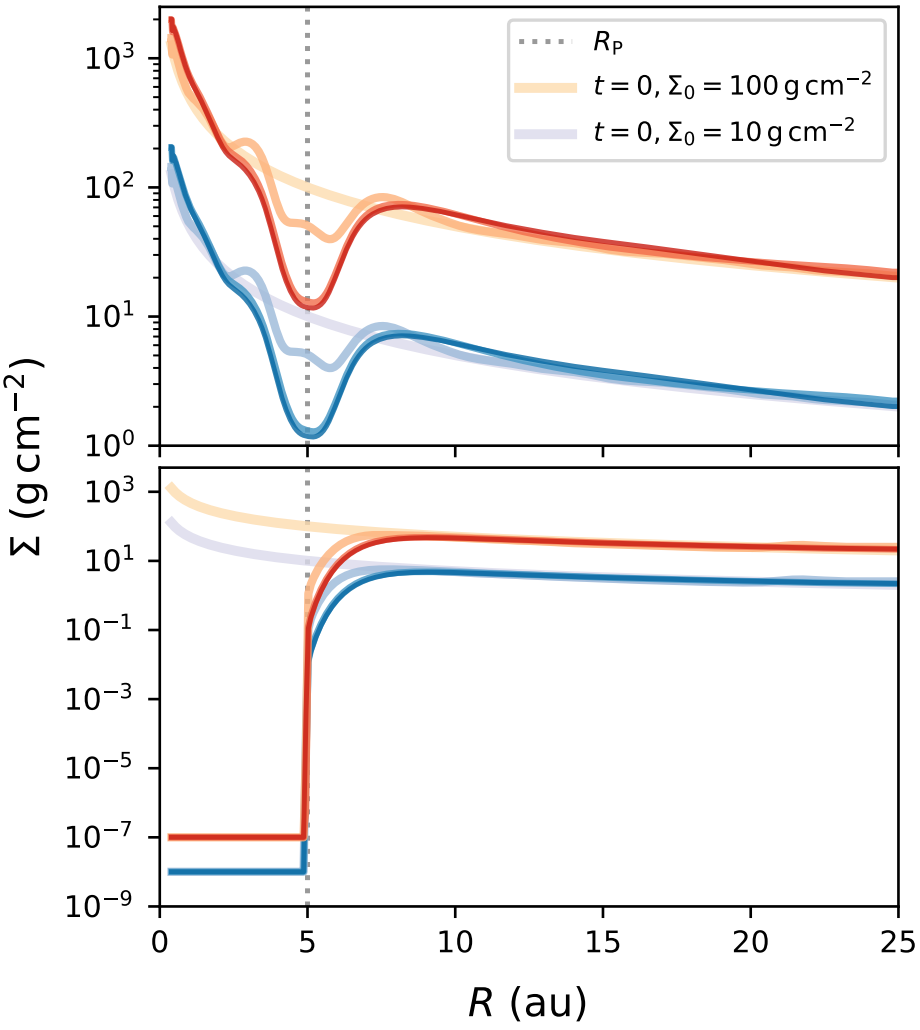

Figure 7.1: Azimuthally averaged gas surface density evolution of the primordial (top) and transition discs (bottom) modelled with FARGO. The different lines correspond to snapshots at orbit 0, 100, 1000, and 1500 for the primordial disc, and at orbit 0, 10, 150, and 200 for the transition disc. During this time, the planet position was kept fixed and photoevaporation was switched off.

accretion flow both from the outer boundary into the disc and from the inner disc onto the central star (for details, see Eq. 11 in Kley et al., 2008). The magnitude of the flow's radial velocity at the corresponding boundary radius is determined by the viscosity parameter α that was set to the same value of $\alpha = 6.9 \times 10^{-4}$ as in the 1D runs.

Photoevaporation was included as a sink-term in the continuity equation (Moeckel & Armitage, 2012; Rosotti et al., 2013):

$$\frac{\partial \Sigma}{\partial t} + \nabla \cdot (\Sigma \mathbf{v}) = -\dot{\Sigma}_{\mathrm{w}}(R, t). \tag{7.7}$$

FARGO parameter	value
Sigma0 ($\mathrm{g\,cm^{-2}}$)	10, 100
SigmaSlope	1.
SigmaFloor (Σ_0)	10^{-9}
AlphaViscosity	6.9×10^{-4}
AspectRatio	0.1
FlaringIndex	0.25
l0 (au)	5.
m0 ($M_\odot$)	0.7
mu	2.35
Nrad	256
Nsec	388
Rmin (l_0)	0.08
Rmax (l_0)	5.
RadialSpacing	Logarithmic
InnerBoundary	Viscous
OuterBoundary	Viscous
Adiabatic	No
PlanetMass (M_J)	1.
PlanetDistance (au)	5.

Table 3.2: Initial conditions that were used for the 2D FARGO simulations described in Section 7.2.3. The parameters are given in the name convention employed in the FARGO executable files. If a parameter is not specified, the default value is used. We note that FARGO employs code units, which are set by the base mass m_0, the base length l_0 and the time per orbit $t_0 = \sqrt{l_0^3/(Gm_0)} = 1/\Omega_0$, where G is the gravitational constant and Ω_0 the Keplerian orbital frequency.

The mass was removed from the disc surface density at the beginning of each time step and to prevent negative surface densities from arising, we used a floor value of $10^{-9} \times \Sigma_0$ throughout the disc. We considered the same X-ray luminosities as in the 1D model, namely $L_\mathrm{x} = 2.7 \times 10^{29}\,\mathrm{erg\,s^{-1}}$ and $L_\mathrm{x} = 1.1 \times 10^{30}\,\mathrm{erg\,s^{-1}}$ for a stellar mass of $0.7\,M_\odot$. However, to extract the impact of photoevaporation onto planet migration, we also performed control simulations without photoevaporation. Equivalently to the approach described in Section 7.2.2, we generated transition discs in FARGO by setting the surface density inside the planet location to the above stated floor value at the beginning of each transition disc simulation.

The planet was inserted at 5 au into the disc and gradually grew to its final mass of $1\,M_\mathrm{J}$ following a mass-taper function $M_\mathrm{p}(t) = m_\mathrm{taper} \times 1\,M_\mathrm{J}$, where

$$m_\mathrm{taper} = \sin^2\left(\frac{t}{4t_\mathrm{ramp-up}}\right), \tag{7.8}$$

and $t_\mathrm{ramp-up} = 10$ orbits is the ramp-up time. We note that after this step, the planet was not allowed to accrete any more disc material. The implications of this approach on the reliability of our results are discussed in detail in Section 7.4.2. The planet was kept fixed for 1500 orbits

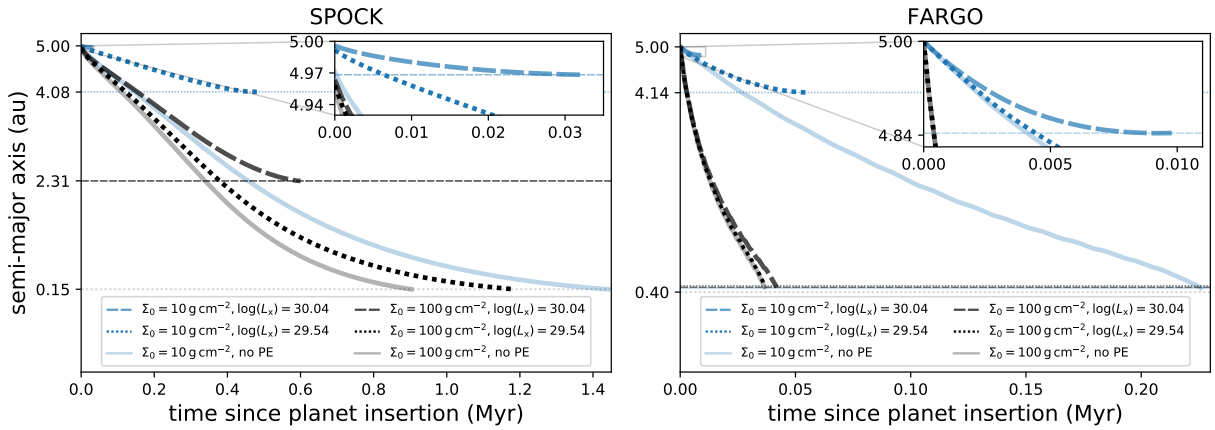

Figure 7.2: Comparison of the semi-major axis evolution of a $1\,M_\mathrm{J}$ planet in the primordial discs for different X-ray luminosities: $\log(L_\mathrm{x}/\mathrm{erg\,s^{-1}}) = 30.04$ (dashed), $\log(L_\mathrm{x}/\mathrm{erg\,s^{-1}}) = 29.54$ (dotted), and vs. no photoevaporation (solid), computed with SPOCK (left panel) and FARGO (right panel). The blue lines correspond to an initial surface density of $\Sigma_0 = 10\,\mathrm{g\,cm^{-2}}$ and the black lines to $\Sigma_0 = 100\,\mathrm{g\,cm^{-2}}$. The horizontal lines are drawn at the final planet parking locations. For SPOCK, the simulations are stopped once the planets reach 0.15 au, while for FARGO the inner grid boundary lies at 0.4 au. The upper right panels zoom into the parameter space to show the evolution of the $\log(L_\mathrm{x}/\mathrm{erg\,s^{-1}}) = 30.04$ simulations as their total disc lifetimes are significantly shorter than for the other simulations.

in the primordial discs and 200 orbits in the transition discs to 1) allow the planet to carve a deep gap in the surface density and 2) to stabilise the torques acting on the planet before it is allowed to migrate and photoevaporation is switched on. This is illustrated in Figure 7.1, which shows the azimuthally averaged surface density evolution of the primordial and transition discs at different snapshots during the first orbits, in which the planet was kept fixed. It can be seen that the disc, especially towards the outer boundaries, had reached a stable state long before the planet was released. Table 3.2 summarises the initial conditions used for the FARGO simulations.

7.3 Results and discussion

7.3.1 Migration in primordial discs subject to XPE

Figure 7.2 shows the semi-major axis evolution of the planets embedded in primordial discs, computed from SPOCK using the impulse approximation (left) and from the full 2D treatment using FARGO (right). Each line represents a different setup sampled from the two different initial disc masses of $\Sigma_0 = 10\,\mathrm{g\,cm^{-2}}$ ('low-mass disc') and $\Sigma_0 = 100\,\mathrm{g\,cm^{-2}}$ ('high-mass disc') as well as X-ray luminosities of $\log_{10}(L_\mathrm{x}/\mathrm{erg\,s^{-1}}) = 29.54$ ('low L_x') and $\log_{10}(L_\mathrm{x}/\mathrm{erg\,s^{-1}}) = 30.04$ ('high L_x'), while the remaining parameters were kept constant.

Due to the vigorous photoevaporative winds, planets embedded in the low-mass discs with high X-ray luminosities are effectively immediately parked once they are inserted into the disc. This can be seen in the subplots in the upper right corners of Figure 7.2, that zoom in the

corresponding parameter space. For this setup, the final parking locations of the planets as well as the timescales are comparable both in the 1D and 2D approach. In SPOCK, the planet migrates by about 0.03 au within 3×10^4 yr, while in FARGO it takes the planet only 10^4 yr to get parked at 4.84 au. If no photoevaporation-driven mass loss is applied, all planets migrate up to the inner radial boundary of the corresponding radial grid for both modelled disc masses, demonstrating the efficiency of X-ray photoevaporation at stopping giant planet migration.

The most significant differences in the final planet parking locations for both approaches can be observed for $\log_{10}(L_x/\mathrm{erg\,s^{-1}}) = 29.54$. In SPOCK, the planet is parked at 4.08 au after approximately 0.5 Myr for the low-mass disc, but for $\Sigma_0 = 100\,\mathrm{g\,cm^{-2}}$ it migrates up to the inner radial boundary within 1.2 Myr. This is explained by the fact that for the latter approach, the accretion rate through the disc exceeds the mass loss rate due to photoevaporation, which is then unable to remove the material around the planet that is responsible for the torques that cause its inward migration. Qualitatively similar behaviour can be observed in the FARGO simulations, in which the planet is stopped at 4.14 au after only 0.06 Myr in the low-mass disc, while for the higher-mass disc significantly faster migration compared to SPOCK is observed. However, also in this case the planet migrates up to the inner radial boundary in less than 0.05 Myr.

Consequently, while the simulations in SPOCK and FARGO both qualitatively confirm that planets are expected to migrate less with higher X-ray luminosity of the host star and that higher migration rates are obtained for more massive discs (as the torques acting on the planet directly scale with the disc's surface density, cf. Lin & Papaloizou, 1986), they also show that the absolute timescales differ strongly in the two approaches. While in FARGO the planets are parked in less than 0.3 Myr, in SPOCK they span a broader range between a few 10^5 yr to ~ 1.4 Myr. These differences can be mainly related to the different extent and surface density profile of the disc, but more importantly, to the different disc evolution in both approaches. While it is possible to model the entire disc-planet system for its full lifetime in 1D, in FARGO one has to limit the simulations to a smaller region close to the planet due to the higher computational expense of the 2D simulations. The simplifications and uncertainties involved in the 1D approach will be addressed in more detail in Section 7.4, however we additionally refer the reader to the discussion in Rosotti et al. (2013). Figure 7.2 therefore shows that a direct comparison between the timescales in 1D and 2D simulations should be treated with caution.

As mentioned above, photoevaporation is clearly more effective in the low-mass discs. Here, the migration history of the planets and the final parking location are most dramatically affected by this process. This finding is in agreement with recent results by Wise & Dodson-Robinson (2018), who showed that the impact of photoevaporation on parking planets is negligible, if the ratio of the planet to disc mass is small, so that $M_{\mathrm{disc}} \gg M_{\mathrm{p}}$. This is obvious as in high-mass discs the accretion rates exceed the photoevaporation rates such that any material removed by photoevaporation is readily replaced so that the net effect on the torques is then negligible. In this context it is however important to address the role of viscosity. The accretion rate onto the star is not directly driven by the disc mass itself, but by the disc viscosity, which in turn is set by the α parameter, the disc scale height, H, and the sound speed of the gas, c_s. In our simulations, α was kept constant while we explored a given range of disc masses. Thus, the mass accretion rate scales with the surface density of the disc, which in our simple case can

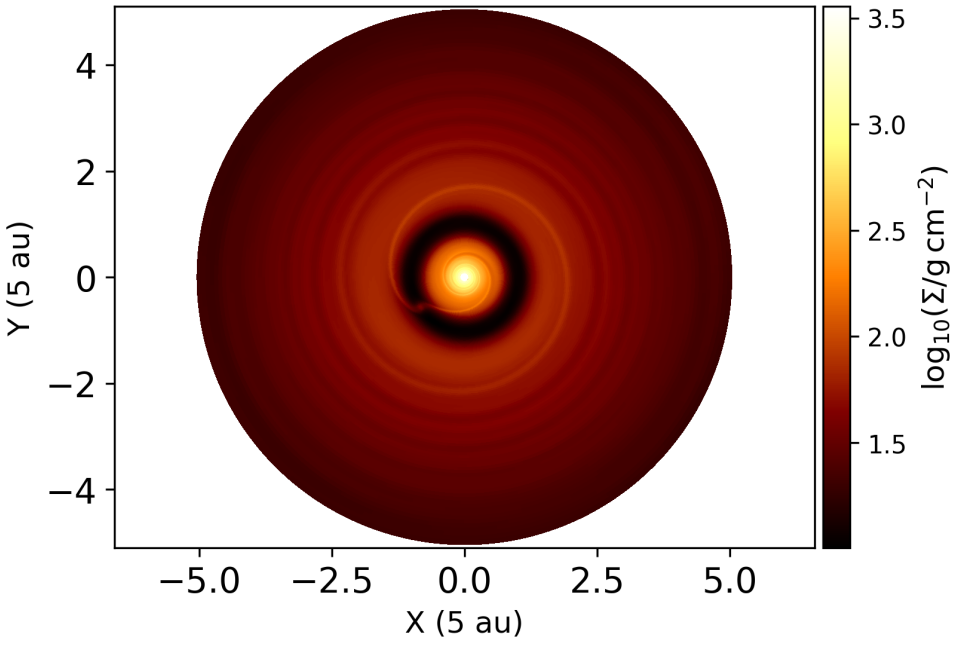

Figure 7.3: 2D surface density distribution of the $\Sigma_0 = 100\,\mathrm{g\,cm^{-2}}$ primordial disc, determined from FARGO. The surface density is plotted at orbit 1500, at which the planet is released and photoevaporation is activated.

be directly related to the disc mass. Therefore, for a given value of α, the higher-mass discs accrete at higher rates than the lower-mass discs and lie well above the photoevaporative mass loss rate. This means that the latter has negligible influence on the surface density evolution of the high-mass disc, and thus on the torques exerted on the planet. For completeness, we present the effect of different α-viscosities on the migration of the planets for the case example of $\Sigma_0 = 10\,\mathrm{g\,cm^{-2}}$ and $\log_{10}(L_\mathrm{x}/\mathrm{erg\,s^{-1}}) = 29.54$ in Appendix 7.B. We find that applying different viscosities in our simulations does not change the overall conclusion of this paper. However, it will certainly change the migration rates that are observed for the individual planets and impact their final parking location.

In conclusion, for primordial discs the impulse approximation employed in SPOCK gives a reasonably good match for the final parking locations in the low-mass discs compared to the more realistic treatment with FARGO. There is, however, a larger discrepancy for the higher-mass discs, where even in the control simulations without photoevaporation, the migration is faster in the 2D calculations. The main reason for this discrepancy is the different disc evolution between the two approaches as well as the interaction between the planet and the spiral arms that develop in the 2D simulations. These provide local enhancements to the torques acting on the planet that cannot be reproduced and accounted for in axisymmetric 1D calculations. The spiral arms induced by the planet can be seen in Figure 7.3, which shows the 2D gas surface density distribution of the primordial disc with $\Sigma_0 = 100\,\mathrm{g\,cm^{-2}}$ at orbit 1500, that is right before the planet is released and photoevaporation is activated.

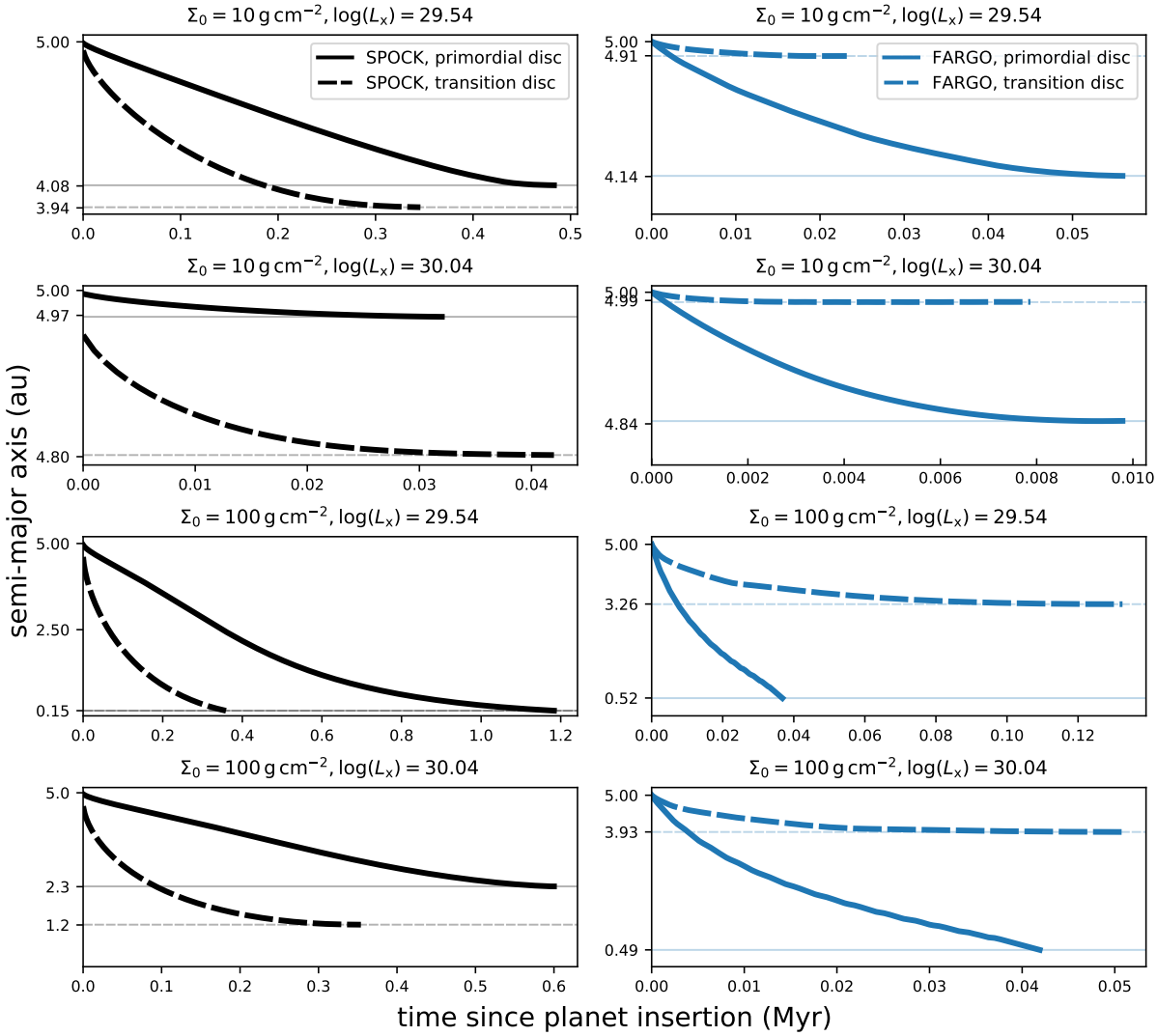

Figure 7.4: Comparison of the semi-major axis evolution and the final parking locations for different initial disc masses and X-ray luminosities, computed from `SPOCK` (left panels) and `FARGO` (right panels). The solid lines show the evolution for the planets embedded in primordial discs, while the dashed lines correspond to planets embedded in transition discs. The horizontal lines are drawn at the corresponding planet parking location from each simulation.

7.3.2 Migration of planets in primordial versus transition discs

Figure 7.4 shows a comparison of the semi-major axis evolution for the primordial and transition discs, computed with `SPOCK` and `FARGO`. Using the impulse approximation implemented in `SPOCK`, planets embedded in transition discs generally migrate farther inside than they do in primordial discs, except for the case of $100\,\mathrm{g\,cm^{-2}}$ and $\log_{10}(L_x/\mathrm{erg\,s^{-1}}) = 29.54$, where for both setups the planet is stopped at the inner radial grid. However, in all of the scenarios modelled in 1D, the planets embedded in transition discs show accelerated inward migration

compared to the planets in primordial discs. Naively, this behaviour may be expected due to the missing counteracting effect of the inner disc, so that the relatively massive outer disc can push the planet inside at an increased migration speed. However, it becomes immediately apparent from the more realistic FARGO simulations that the migration of planets subject to one-sided torques only exerted from an outer disc is not treated correctly using the impulse approximation in 1D. The FARGO results show that the planet migrates the farthest inside, if it is embedded in a primordial disc. In contrast to that, the planet migrates only weakly if it is embedded in a transition disc. The magnitude of migration depends however on the initial disc mass and the strength of the photoevaporative winds. While for $\Sigma_0 = 10\,\mathrm{g\,cm^{-2}}$ only insignificant migration can be observed for both modelled X-ray luminosities, for the higher-mass discs, the planet migrates up to 3.26 au for $\log_{10}(L_\mathrm{x}/\mathrm{erg\,s^{-1}}) = 29.54$ and up to 3.93 au for $\log_{10}(L_\mathrm{x}/\mathrm{erg\,s^{-1}}) = 30.04$. The FARGO simulations therefore show that planets in transition discs generally migrate significantly less than they do in primordial discs.

In summary, when comparing the migration tracks between SPOCK and FARGO for the transition discs only, it becomes apparent that in the latter, planets generally migrate significantly less than they do in SPOCK, while for the primordial discs no strong deviation is found, except for $100\,\mathrm{g\,cm^{-2}}$ and $\log_{10}(L_\mathrm{x}/\mathrm{erg\,s^{-1}}) = 30.04$, where the slower migration in SPOCK allows photoevaporation to deplete the disc more strongly. As a consequence, planet migration is slowed down even more and the planet is parked before it can reach the inner boundary.

7.3.3 Torques acting on the planet

To understand the origin of the different migration rates of planets embedded in primordial and transition discs, Figure 7.5 shows the evolution of the total torques (Γ_tot) acting on the planet, together with the individual contribution of the corotation (Γ_C) and Lindblad (Γ_LB) torques as a function of time. These are directly compared to the semi-major axis evolution of the planet.

The corotation torques are determined within the co-orbital region x_s (also known as horseshoe half-width, cf., Paardekooper & Papaloizou, 2009), spanning a region close to the planetary orbit from $a - x_\mathrm{s} \leq a \leq a + x_\mathrm{s}$. The width of x_s is given by

$$x_\mathrm{s} = 1.68a\sqrt{\frac{q}{h}}, \tag{7.9}$$

where a corresponds to the planet semi-major axis, $q = M_\mathrm{p}/M_\star$ is the planet to stellar mass ratio and h the disc aspect ratio (Paardekooper & Papaloizou, 2009). The contribution of the Lindblad torques are then calculated from the remaining parts of the disc. The total torque is therefore the sum of the individual corotation and Lindblad torques and the net difference between the torques interior and exterior to the planet determine its final migration rate. For most planet-disc configurations, the net difference between the torques becomes negative so that it drives inward migration (Ward, 1997), which is also the case in our simulations where no significant outward migration was observed.

The cumulative torques as a function of time were normalised by

$$\Gamma_0 = (q/h)^2 a^4 \Omega_\mathrm{P}^2 \Sigma_\mathrm{P}, \tag{7.10}$$

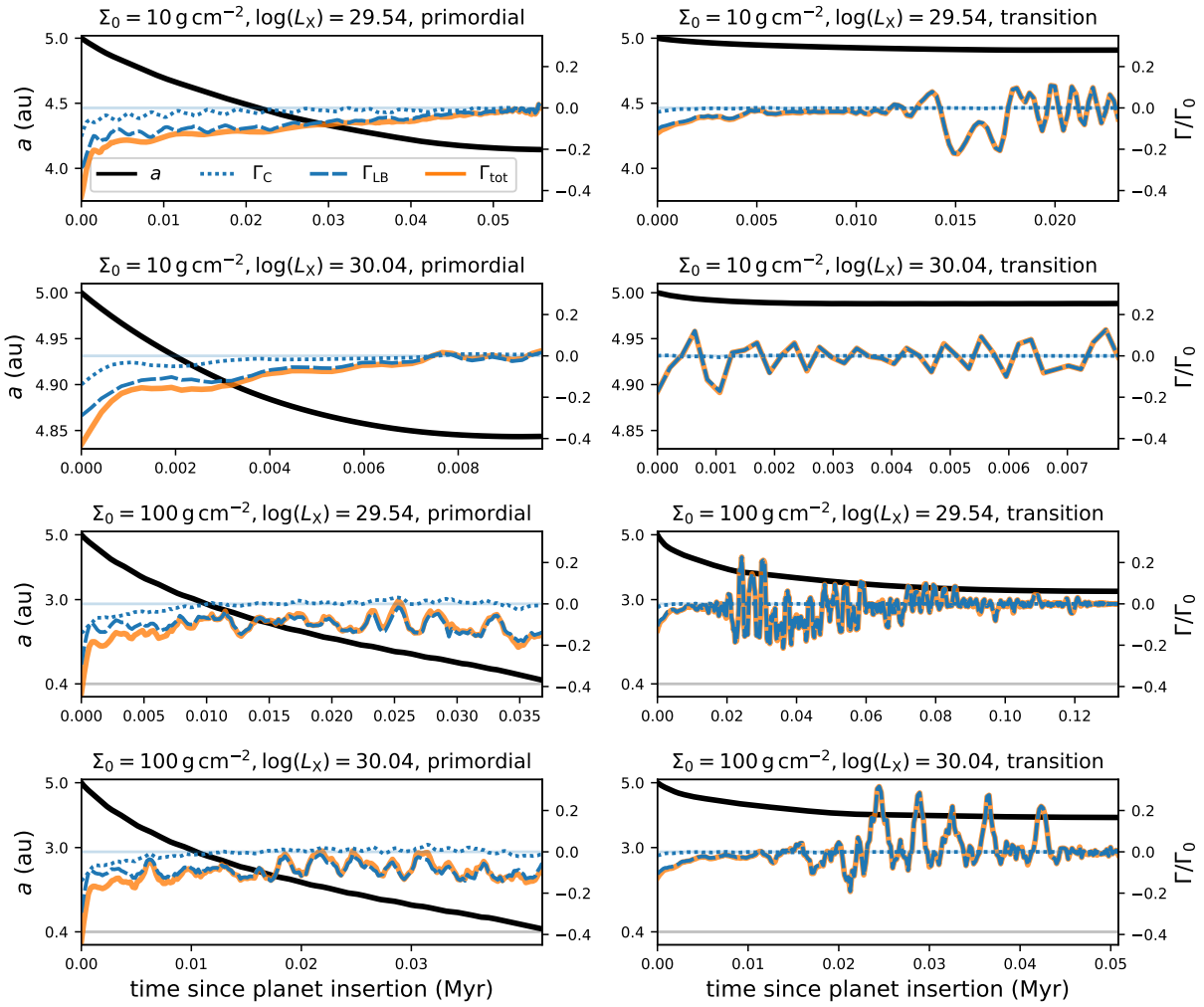

Figure 7.5: Comparison of the semi-major axis evolution (black solid) of the planet with respect to the corotation (Γ_C, blue dotted), Lindblad (Γ_{LB}, blue dashed), and total torques ($\Gamma_{tot} = \Gamma_C + \Gamma_{LB}$, orange solid) in the primordial (left panels) and transition discs (right panels), calculated from FARGO. The torques were divided by Γ_0, which is the unperturbed torque at the planet location (cf. Eq. 7.10).

which corresponds to the total torque of the unperturbed disc at the initial planet location of 5 au (see e.g. D'Angelo & Lubow, 2010; Dürmann & Kley, 2015). It is a function of the planet to stellar mass ratio q, the disc aspect ratio h, $\Sigma_P{=}\Sigma_0$ at 5 au, the orbital separation of the planet a and $\Omega_P = \sqrt{GM_\star/a^3}$. The torques were smoothed using a third order polynomial Savitzky-Golay filter (Savitzky & Golay, 1964) with a window length of 11. Fluctuations are observed in the torque evolution as the planet moves closer to the central star, in particular for the transition disc cases (right column). The cause of these fluctuations is the interaction between vortices developing at the gap edge and the photoevaporative wind with the planet, which is discussed in more detail in Appendix 7.C.

It is important to note that the transition from a primordial to a transition disc is smooth

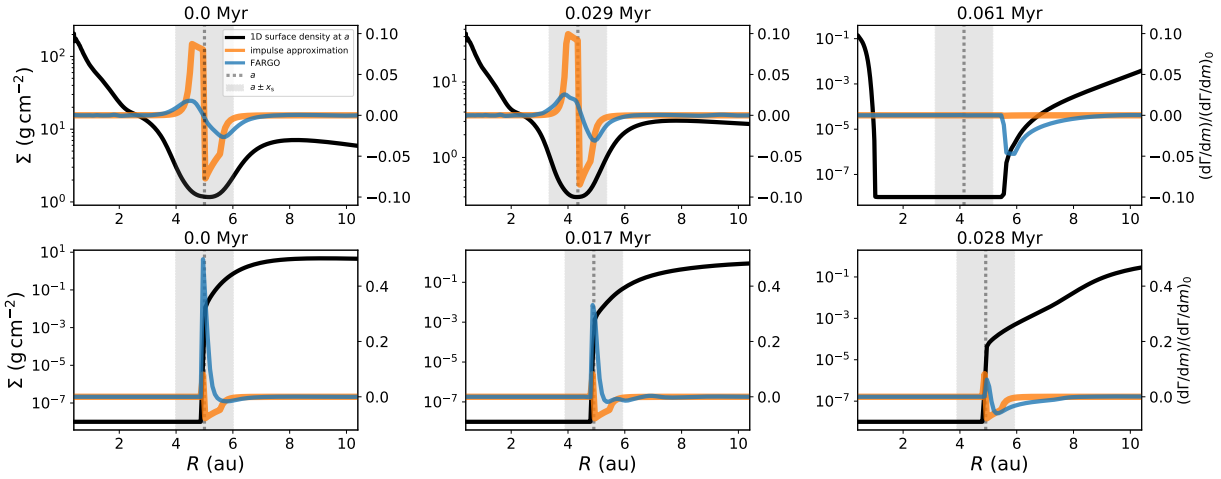

Figure 7.6: Comparison of the 1D surface density profile (solid black line) of the $\Sigma_0 = 10\,\mathrm{g\,cm^{-2}}$ and $\log_{10}(L_\mathrm{x}/\mathrm{erg\,s^{-1}}) = 29.54$ primordial (top panels) and transition disc (bottom panels) with the radial distribution of the torques per unit disc mass determined from FARGO (blue) and the impulse approximation (orange). The torques were normalised with the normalisation factor $(\mathrm{d}\Gamma/\mathrm{d}m)_0$ (cf. Eq. 7.11). The dotted line shows the planet location at the given timestep, while the shaded area encompasses $a \pm x_\mathrm{s}$.

rather than sharp. While the total torques in the former are the result of the counteracting effect from the torques interior and exterior to the planet, as the disc is slowly developing an inner cavity, the torques in the outer disc will start to dominate over those from interior to the planet. In the extreme limit of a transition disc with an evacuated inner cavity, the surface density will have a sharp cutoff at the planet location as the gap-crossing material will be either quickly accreted by the planet or be photoevaporated by the star. At this point, the planet will only be subject to the torques from the outer disc, which we refer to as 'one-sided torques'.

It can be inferred from Figure 7.5 that the absolute value of the Lindblad torques is significantly larger than those of the corotation torques. This is to be expected as the planets in our study are massive enough to open gaps in the surface density, therefore depleting the material in the corotation region. This becomes even more prominent in the transition discs since the removal of material due to the direct irradiation from the central star adds up to the planet depleting gas in its immediate surrounding, so that material close to the planet cannot complete a horseshoe orbit. Consequently, as photoevaporation depletes the regions close to the planet location, the corotation and Lindblad torques approach zero, and the planet is parked.

7.3.4 Impulse approximation versus full 2D treatment

Finally, we investigate why the impulse approximation is leading to contradicting results for transition discs compared to migration rates obtained from FARGO. The two major differences between SPOCK and FARGO are the disc evolution and the treatment of planet migration. Due to the different disc evolution (and surface density profile), it is not useful to directly compare the torques from both approaches. Therefore, in order to isolate the effect of planet migration, we computed the torques from the impulse approximation (cf. Eq. 7.4) using the 1D averaged

FARGO outputs. This way we focus only on the differences in planet migration, which is the aim of this paper.

Figure 7.6 shows the azimuthally averaged surface density profile of the primordial and transition discs in comparison to the radial distribution of the torques per unit disc mass dm directly determined from the FARGO outputs as well as through the impulse approximation. The comparison is made at three different stages of disc evolution, namely when the planet is released (first column), in the advanced stage of disc evolution (middle column) as well as right before disc dispersal (right column). The radial distribution of the specific torques are plotted in units of the normalisation factor determined by D'Angelo & Lubow (2010):

$$\left(\frac{\mathrm{d}\Gamma}{\mathrm{d}m}\right)_0 = q^2 h^{-4} a^2 \Omega_\mathrm{P}^2. \tag{7.11}$$

For the primordial discs (top row), the torques determined from the impulse approximation strongly overestimate the contribution of the corotation torques close to the planet (exerted from the region $a \pm x_\mathrm{s}$), while it underestimates the influence of the Lindblad torques at larger radii. However, as previously shown in Figure 7.5, the corotation torques are of minor importance to giant planet migration as the planet will carve a deep gap into the disc, and therefore deplete this region of material. The absolute values of the torques from FARGO are overall smaller than the ones from the impulse approximation. However, the magnitude of the Lindblad torques, which ultimately drive planet migration, is larger especially close to the planet. The difference between the calculated Lindblad torques in the two approaches is coming mainly from the lack of 2D structures, such as spiral density waves in the averaged density profiles as was previously discussed.

For the transition discs, the gas cannot perform complete horseshoe orbits since the material is removed as it crosses the planet location. The observed behaviour for the torques differs strongly between the two approaches. There are negative torques just outside the planet location pushing the planet inwards for the impulse approximation, while in FARGO strongly positive torques develop at the location of the gap edge, effectively acting as a planet trap that will prevent any further inward migration of the planet (cf. Liu et al., 2017). As the disc evolves and the photoevaporative wind depletes the gap edge this contribution becomes negligible. Here, it is important to note that our previous statement about the corotation torques not being important to giant planet migration still holds. The reason for this is that the torques shown in Figure 7.6 correspond to the specific torques, i.e. the torques were renormalised by the local disc mass $\mathrm{d}m = \Sigma\,\mathrm{d}A = 2\pi r \Sigma\,\mathrm{d}r$. Therefore, while the absolute value of the torques exerted at the gap edge are significantly stronger than in the primordial disc, the local disc mass is much more depleted and the resulting effective torque is weaker as can be inferred from Figure 7.5.

In summary, our 2D FARGO simulations show that planets that are embedded in transition discs with an evacuated cavity inside the planetary orbit migrate significantly less than they do in primordial discs. This is in contradiction with the results obtained by the impulse approximation in 1D, which predicts an accelerated inward migration for planets in discs with inner cavities. This suggests that the classic impulse approximation is not suitable to model the migration

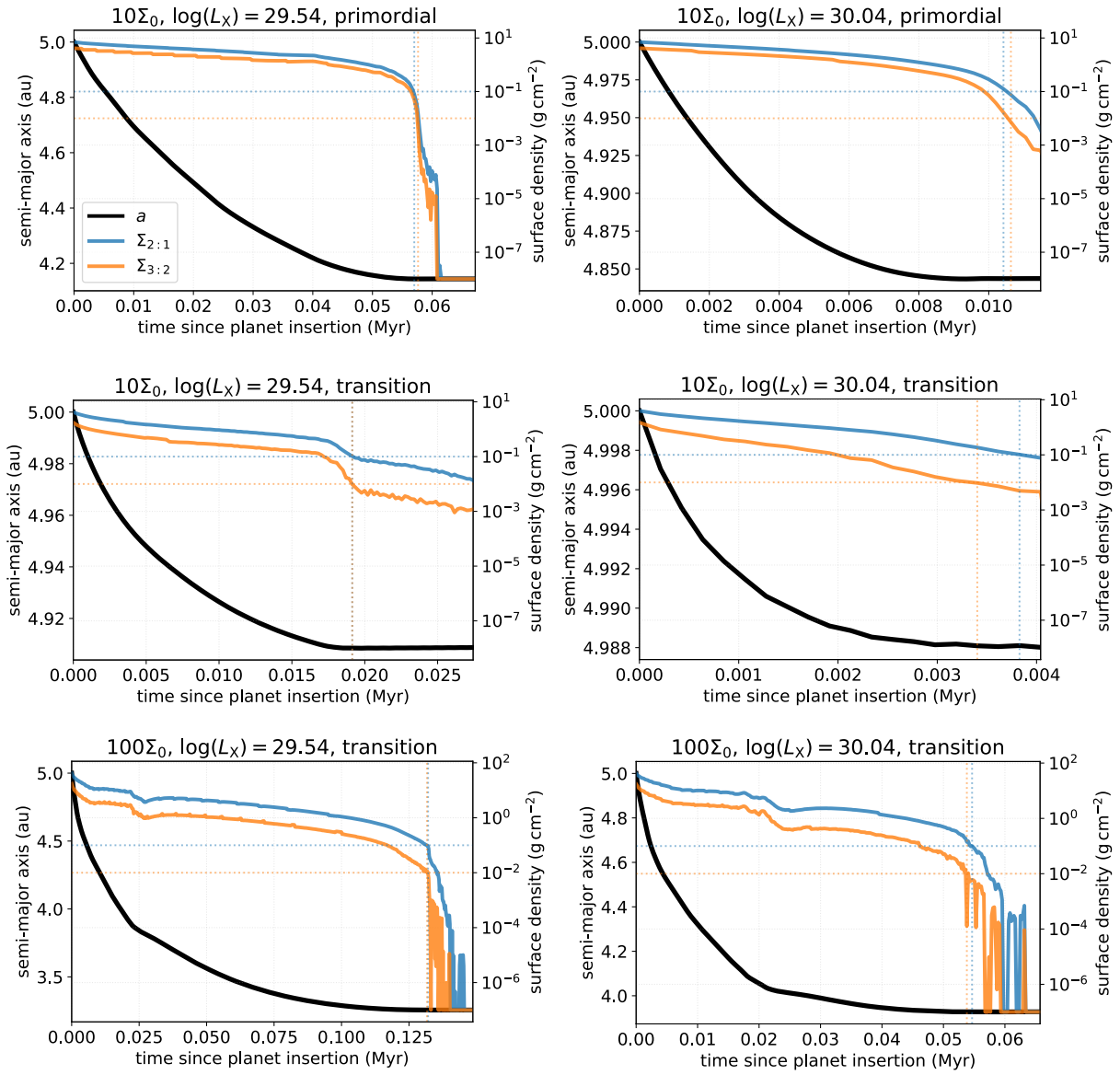

Figure 7.7: Comparison of the semi-major axis evolution (solid black) in the FARGO simulations vs. the azimuthally averaged surface density at the 2:1 (solid blue) and 3:2 (solid orange) mean motion resonance location in the corresponding disc. Only the runs in which the planet was parked due to planet-disc interactions are shown. The horizontal dotted lines are drawn at $\Sigma_{2:1} = 10^{-1}\,\mathrm{g\,cm^{-2}}$ and $\Sigma_{3:2} = 10^{-2}\,\mathrm{g\,cm^{-2}}$ and cross the corresponding vertical line where the planet is considered to be parked fully.

of planets in such discs. This has important consequences for 1D planet population synthesis calculations that employ the impulse approximation to calculate migration rates of giant planets.

7.3.5 Proposed fix for the impulse approximation in 1D models

An easy fix to the impulse approximation in 1D models could be to stop giant planet migration, once the disc inside the planetary orbit is depleted of gas. However, as shown in Figure 7.4, some modest migration of the planet embedded in a transition disc can be observed, if the outer disc is still rather massive. Stopping the planet once the disc inside the planet is depleted would likely result in too large parking radii of the planets. A better approximation that could be therefore used in such simulations is derived using Figure 7.7. Here we compare the semi-major axis evolution from the FARGO runs with the azimuthally averaged surface density that was determined at the 3:2 and 2:1 mean motion resonance locations. Both are located outside of the planetary orbit and are one of the main contributors to the outer Lindblad torques. The $\Sigma_0 = 100\,\mathrm{g\,cm^{-2}}$ runs of the primordial discs are excluded from this analysis as the planets reached the inner boundary in these simulations and were effectively not parked due to planet-disc interactions. We find that once the surface density reaches approximately $0.01\,\mathrm{g\,cm^{-2}}$ at the 3:2 mean motion resonance location and around $0.1\,\mathrm{g\,cm^{-2}}$ at the 2:1 mean motion resonance, planet migration can be considered to have stopped fully. These threshold values are independent of the initial disc mass as well as the applied X-ray luminosity tested in this work and therefore appear to be a robust proxy. However, while their eligibility for even higher disc masses still needs to be tested, it is not expected to be of relevance to realistic planet formation models. In 1D treatments of migrating planets using the impulse approximation, we therefore suggest to stop giant planet migration once the disc inside the planet is depleted and the surface density at the 3:2 mean motion resonance location (as this is closer to the planet than the 2:1 mean motion resonance) becomes less than $0.01\,\mathrm{g\,cm^{-2}}$, ensuring that the outer disc has become depleted enough to not continue pushing the planet inside.

7.4 Numerical limitations

This section will discuss the limitations of the numerical models employed in this study.

7.4.1 Viscous boundary conditions

Due to the reduced complexity of the disc structure in one dimension, it was possible to model a much larger disc extent with SPOCK than in the 2D simulations with FARGO, which only included disc radii between $0.4 - 25\,\mathrm{au}$. In such models, the choice of boundary conditions may have a significant impact on the final outcome of a simulation. While we have tested different configurations of open and closed boundaries, we found that viscous outflow boundary conditions (Kley et al., 2008) provide the most realistic setup as they impose a steady-state accretion flow from the outer to the inner disc as well as from the innermost disc onto the star (cf. Section 7.2.3). The velocity of this flow is set by the viscosity parameter α, for which we used the same value of $\alpha = 6.9 \times 10^{-4}$ both in 1D and 2D. However, as could be inferred from Figure 7.1, the discs in our model have reached a stable state before the planets were released, confirming that the choice of viscous boundary conditions is indeed appropriate for our study.

7.4.2 Planetary accretion

In the classical framework of the impulse approximation (Lin & Papaloizou, 1986), no material can cross the planetary gap so that the planet is locked inside the gap, migrating approximately on the viscous timescale. Hydrodynamical simulations have however shown that gaps formed by giant planets are more comparable to 'leaky dams' that do allow a certain mass-flow across the planetary orbit (Lubow & D'Angelo, 2006; Duffell et al., 2014; Dempsey et al., 2020). Dürmann & Kley (2015) further showed that, for some scenarios, this mass-flow can be entirely stopped if the planet is additionally accreting the gap-crossing material, therefore fully cutting off the inner from the outer disc.

In SPOCK, planetary accretion is modelled following the prescription derived by Veras & Armitage (2004), which was also used in comparable studies (Alexander & Armitage, 2009; Alexander & Pascucci, 2012; Ercolano & Rosotti, 2015). It is well known that the magnitude of this mass-flow can strongly affect the migration rate of the planet. While the fitting formula that is used in SPOCK is based on state-of-the-art numerical simulations of planet-disc interactions (Lubow et al., 1999; D'Angelo et al., 2002; Lubow & D'Angelo, 2006), its exact form is not known and may therefore carry large uncertainties.

In contrast, the simulations performed with FARGO do not include planetary accretion. This may likely be a caveat of our analysis, however, this approach was chosen to isolate the effect of XPE onto giant planet migration. Furthermore, Robert et al. (2018) find that the accretion of material onto the planet in discs with low viscosity (as it is the case in our study) should not have any significant impact on type II migration, suggesting that giant planets embedded in such discs should migrate slowly. Studying the mass-flow across the planetary orbit in photoevaporating discs is not within the scope of this paper, however, due to its likely significance to giant planet migration in high-viscosity discs, it should be investigated in more detail in future studies.

7.5 Conclusions

In this paper we have tested the impulse approximation as a 1D treatment of giant planet migration in evolving protoplanetary discs subject to photoevaporation. Our conclusions based on our comparison of 1D and 2D simulations can be summarised as follows.

1. The impulse approximation in 1D can roughly reproduce the migration history predicted by more complex 2D simulations for giant planets embedded in primordial discs with or without photoevaporation. Despite some quantitative differences, the effect on large population synthesis models is not expected to be dramatic. One exception to this is the case of planets embedded in high-mass discs with more vigorous winds. Here, the parking effect of photoevaporation is more enhanced in the 1D simulations compared to the 2D simulations. This is due to the strong non-axisymmetric density enhancements, such as spiral waves in the 2D simulations, that are absent in the 1D simulations. These regions are more resilient to photoevaporation and provide an additional contribution to the torques that are driving migration.

2. 1D simulations show higher migration rates in the case of planets embedded in transition discs, in which the material inside the planetary orbit has been cleared. On the contrary, 2D simulations of equivalent systems show that migration is effectively stopped as soon as the material inside the planetary orbit is cleared.

3. Planet population synthesis calculations should account for the above in order to accurately reproduce the orbital distribution of planets at the end of the disc clearing phase. A simple approach for 1D codes using the impulse approximation is to halt planet migration as soon as the material inside the planetary orbit has been cleared and the azimuthally averaged surface density becomes less than $0.01\,\mathrm{g\,cm^{-2}}$ at the 3:2 mean motion resonance location of the planet.

A quantitative estimate of the magnitude of the error introduced by 1D migration prescriptions is beyond the scope of this paper but will be attempted in future work.

Acknowledgements We would like to thank Sijme-Jan Paardekooper for helpful comments, and the anonymous referee for a constructive report that improved the manuscript. We acknowledge the support by the DFG priority program SPP 1992 "Exploring the Diversity of Extrasolar Planets (DFG PR 569/13-1, ER 685/7-1) & the DFG Research Unit "Transition Disks" (FOR 2634/1). This research was supported by the Excellence Cluster ORIGINS, which is funded by the Deutsche Forschungsgemeinschaft (DFG, German Research Foundation) under Germany's Excellence Strategy - EXC-2094 - 390783311. Part of the simulations have been carried out on the computing facilities of the Computational Center for Particle and Astrophysics (C2PAP).

Appendices

7.A Details on the X-ray photoevaporation model

Picogna et al. (2019) present an updated X-ray photoevaporation model, which is based on a series of radiation-hydrodynamical simulations. They focus on modelling the photoevaporative winds of solar-type stars ($M_\star = 0.7\,M_\odot$) and show how these impact the dispersal of their surrounding disc at various stages of disc evolution.

The photoevaporative surface mass loss profile, $\dot{\Sigma}_\mathrm{w}(R)$, is described by

$$\dot{\Sigma}_\mathrm{w}(R) = \ln(10)\left(\frac{6a\ln(R)^5}{R\ln(10)^6} + \frac{5b\ln(R)^4}{R\ln(10)^5} + \frac{4c\ln(R)^3}{R\ln(10)^4} + \frac{3d\ln(R)^2}{R\ln(10)^3} + \frac{2e\ln(R)}{R\ln(10)^2} + \frac{f}{R\ln(10)}\right)\frac{\dot{M}_\mathrm{w}(R)}{2\pi R}, \tag{7.12}$$

where $a = -0.5885$, $b = 4.3130$, $c = -12.1214$, $d = 16.3587$, $e = -11.4721$, $f = 5.7248$, $g = -2.8562$. The total mass loss rate is derived via $\dot{M}_\mathrm{w}(R) = \int 2\pi R\,\dot{\Sigma}_\mathrm{w}(R)\,\mathrm{d}R$ and yields:

$$\dot{M}_\mathrm{w}(R) = \dot{M}_\mathrm{w}(L_\mathrm{x}) \times 10^{a\log_{10}R^6 + b\log_{10}R^5 + c\log_{10}R^4 + d\log_{10}R^3 + e\log_{10}R^2 + f\log_{10}R + g}, \tag{7.13}$$

where

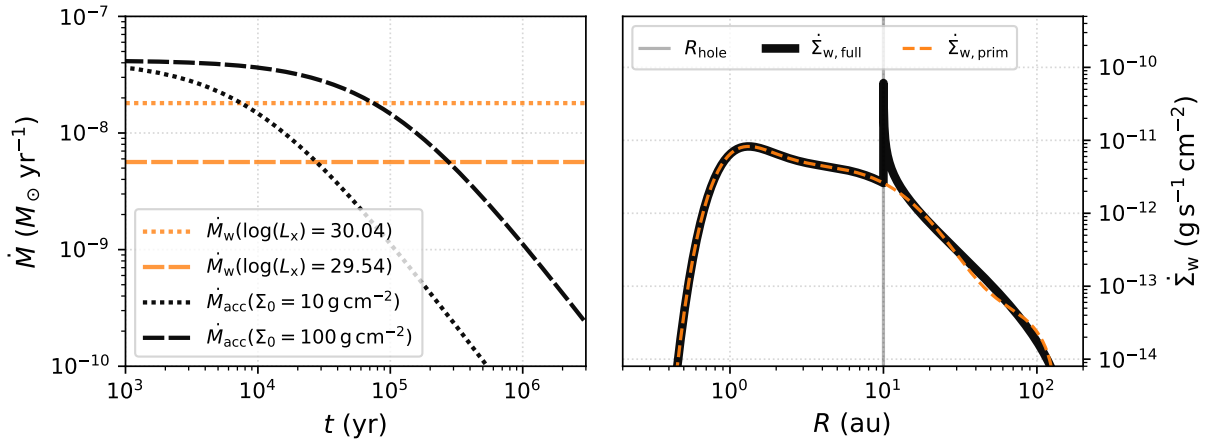

Figure 7.A.1: Comparison of the cumulative and surface mass loss profile as predicted by the XPE model by Picogna et al. (2019) to the purely viscous accretion rate onto the star. *Top panel:* Viscous accretion rate at 1 au of the $\Sigma_0 = 10\,\mathrm{g\,cm^{-2}}$ and $\Sigma_0 = 100\,\mathrm{g\,cm^{-2}}$ discs as a function of time (black lines, cf. Eq. 35 in Hartmann et al. (1998)) vs. the wind mass loss rates due to photoevaporation for $\log_{10}(L_x/\mathrm{erg\,s^{-1}}) = 29.54$ and $\log_{10}(L_x/\mathrm{erg\,s^{-1}}) = 30.04$ (orange lines, cf. Eq. 7.14). *Bottom panel:* Surface mass loss profiles as a function of disc radius. The dashed line shows the full contribution of the primordial surface mass loss profile, which is active before gap opening (Eq. 7.12). Assuming that photoevaporation has already opened a gap in the disc, with its outer radius R_{hole} lying at 10 au, and the column density of the inner disc being less than $N_{\mathrm{H}} = 2.5 \times 10^{22}\,\mathrm{cm^{-2}}$, the actual profile that is active is shown as the black solid line.

$$\log_{10}(\dot{M}_w(L_x)/(M_\odot\,\mathrm{yr^{-1}})) = A_L \exp\left\{\left[\frac{(\ln(\log_{10}(L_X)) - B_L)^2}{C_L}\right]\right\} + D_L, \tag{7.14}$$

and $A_L = -2.7326$, $B_L = 3.3307$, $C_L = -2.9868 \cdot 10^{-3}$ and $D_L = -7.2580$. For transition discs with inner holes, Eq. 7.12 becomes:

$$\dot{\Sigma}_w(R) = a b^x x^{c-1}(x\ln(b) + c)\ \frac{1.12\,\dot{M}(L_x)}{2\pi R}, \tag{7.15}$$

where $a = 0.11843$, $b = 0.99695$, $c = 0.48835$, $x = R - R_{\mathrm{gap}}$, and R_{gap} describes the gap radius.

The top panel of Figure 7.A.1 compares the viscous accretion onto the star, $\dot{M}_{\mathrm{acc}}(R, t)$ (see Eq. 35 in Hartmann et al., 1998), evaluated at 1 au of the $\Sigma_0 = 10\,\mathrm{g\,cm^{-2}}$ and $\Sigma_0 = 100\,\mathrm{g\,cm^{-2}}$ discs with the wind mass loss rate produced by photoevaporation for $\log_{10}(L_x/\mathrm{erg\,s^{-1}}) = 29.54$ and $\log_{10}(L_x/\mathrm{erg\,s^{-1}}) = 30.04$ (Eq. 7.14). It can be seen that in the early stages of disc evolution, the viscous accretion rates onto the star will exceed the photoevaporative mass loss rates. Depending on the initial disc mass and the X-ray luminosity of the star, the accretion rates will drop below the wind mass loss rate at a given time, so that photoevaporation can open an annular gap and start clearing the disc from the inside out. In the bottom panel of Figure 7.A.1, the surface mass loss profile as a function of disc radius is shown. The dashed line shows the primordial profile (Eq. 7.12), which is active before photoevaporation has opened a gap. As soon as gap opening has taken place and the column density inside this gap has decreased

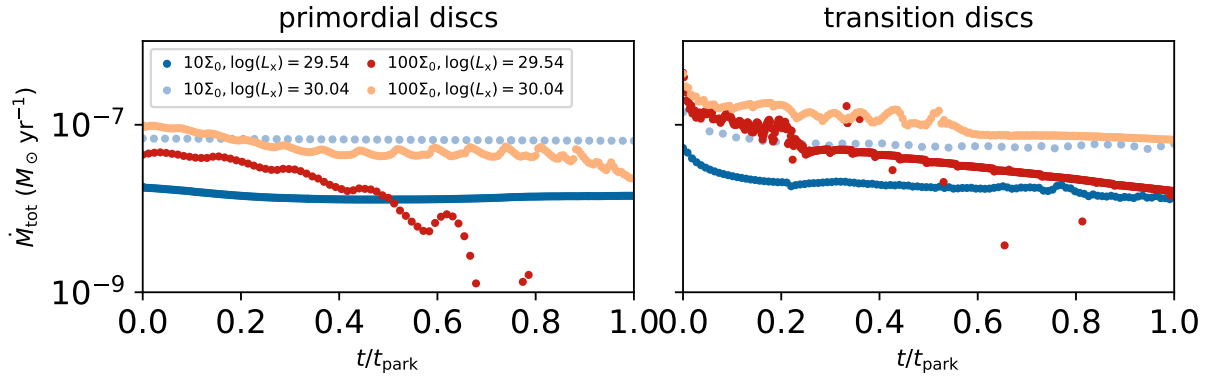

Figure 7.A.2: Total mass loss rate, $\dot{M}(t)$, of the discs modelled with FARGO as a function of $t/t_{\rm park}$, where $t_{\rm park}$ is the time it takes the planet to get parked in each simulation. The lines are plotted starting from the times at which the planet is released and photoevaporation is activated. The total mass loss rates are averaged over 100 orbits. The top panel shows $\dot{M}_{\rm tot}$ in the primordial discs, while the bottom one corresponds to transition discs.

sufficiently, the stellar X-rays can directly irradiate the outer disc, so that the photoevaporation profile switches to the transition disc one outside of the gap (Eq. 7.15). The total surface mass loss profile is therefore a combination of the primordial and the transition disc one that will intersect at the gap radius, $R_{\rm hole}$.

The total mass loss rate (i.e. including viscous accretion and photoevaporation) of the discs modelled with FARGO are shown in Figure 7.A.2. As expected, higher mass loss rates are reached both in the low- and high-mass discs with higher X-ray luminosities of the host star due to the more vigorous winds that are more efficient in removing disc material. This trend is independent of the underlying disc structure, however, in the case of transition discs, even higher absolute values of the mass loss rate compared to the primordial discs are present. Rather than being absorbed by the inner disc, the X-rays can directly irradiate the outer disc in these cases, so that the stronger, direct photoevaporation profile (Eq. 7.15) becomes immediately active. This results in higher total mass loss rates and the faster removal of the outer disc compared to the primordial discs.

Overall, the total mass loss rates stay relatively constant over the disc lifetime, especially for the low-mass discs. For the high-mass discs with $\Sigma_0 = 100\,\mathrm{g\,cm^{-2}}$ the viscous accretion rates are higher (see the discussion in Section 7.3.1) and consequently a stronger decrease in $\dot{M}_{\rm tot}$ with time is observed. This is especially prominent for $\log_{10}(L_{\rm x}/\mathrm{erg\,s^{-1}}) = 29.54$, where $\dot{M}_{\rm tot}$ quickly reaches values below $10^{-9}\,M_\odot\,\mathrm{yr^{-1}}$. Due to the high disc mass and low X-ray luminosity, photoevaporation is not strong enough to overcome viscous accretion before the planet migrates all the way to the host star (see Figure 7.4). The mass loss rate therefore follows a trend similar to that of the viscous accretion rate observed in Figure 7.A.1 (black, dashed line) as the viscous accretion rate will exceed the photoevaporation mass loss rate for a longer time. For the transition discs mostly the wind mass loss rate is contributing to the total mass loss of the disc. The evacuated inner cavity formed by PIPE prevents any accretion onto the star, and therefore all gas that crosses the planetary orbit is immediately photoevaporated

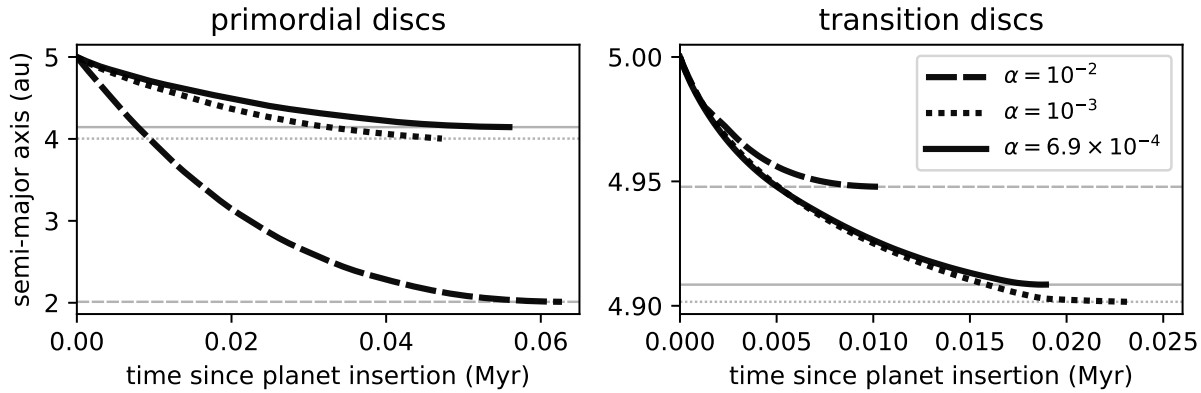

Figure 7.B.1: Semi-major axis evolution of planets embedded in primordial discs (top panel) vs. planets embedded in transition discs (bottom panel), modelled with FARGO for different α-parameters.

away.

7.B The role of viscosity

It was discussed in Section 7.3.1 that photoevaporation is more efficient in parking planets in low-mass discs. In comparison, the planets embedded in the higher-mass discs with $\Sigma_0 = 100\,\mathrm{g\,cm^{-2}}$ were effectively not parked due to planet-disc interactions or photoevaporation, but reached the inner boundary of the radial domain. The magnitude of planet migration in photoevaporating discs however crucially depends on the viscosity applied in these models. Figure 7.B.1 shows the semi-major axis evolution of a planet embedded in the $\Sigma_0 = 10\,\mathrm{g\,cm^{-2}}$ and $\log_{10}(L_\mathrm{x}/\mathrm{erg\,s^{-1}}) = 29.54$ primordial and transition discs for three different α-viscosities, namely $\alpha = [10^{-2}, 10^{-3}, 6.9 \times 10^{-4}]$.

If the viscosity is lower, the migration speed of the planet will become slower, as can be observed in the full disc simulations. The reason for this is that the gaps that are carved by the planets, are wider and deeper in low-viscosity discs, therefore the torques acting on the planet will be reduced. In contrast, for the higher viscosity cases, the planetary gap is partially refilled by inflowing gas, producing stronger torques and leading to the faster inward migration of the planet. For the transition discs opposite behaviour is observed, that is that the planet embedded in the disc with $\alpha = 10^{-2}$ is parked the earliest. However, the difference in the final parking locations compared to the other modelled disc viscosities is only marginal. The reason for this is that with higher disc viscosity, material will accumulate on a faster timescale close to the planet location in the outer disc. As was shown in Figure 7.4, one-sided torques near the gap edge will create strongly positive torques, effectively preventing any further inward migration of the planet. Consequently, with higher disc viscosity more material will be present at the gap edge, resulting in the formation of even stronger positive torques that lead to an earlier stopping of planet migration compared to transition discs with lower viscosity. In conclusion, while the choice of α may affect the final parking location of the planet, it does not change the

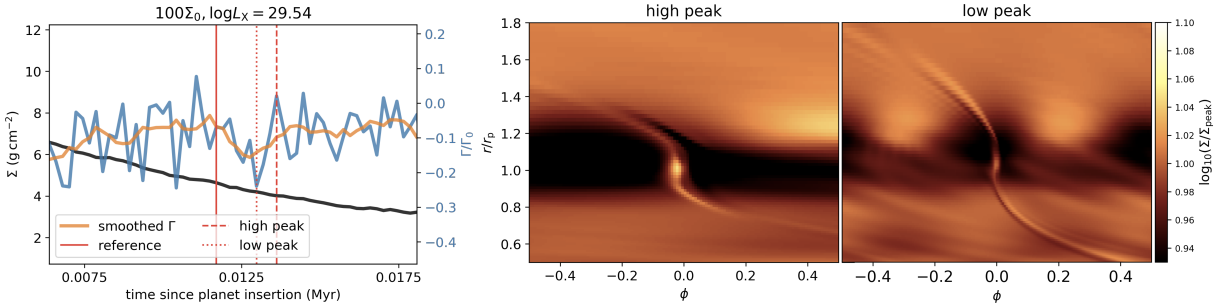

Figure 7.C.1: Asymmetries in the gas surface density close to the planet as a cause for the torque oscillations observed in Figure 7.5. *Left panel*: Torque evolution as a function of time for the low X-ray luminosity case. The blue line corresponds to the "raw" torque directly obtained from `FARGO`, while the orange line shows the smoothed torque using the previously described Savitzky-Golay filter. The black line corresponds to the azimuthally averaged surface density profile at the planet location. The torques were normalised by the normalisation factor Γ_0 (cf. Eq. 7.10). *Right panel*: Corresponding 2D surface density distribution for the high and low torque peaks with respect to the reference step.

conclusion that planet migration should cease once the disc reaches the transitional phase, in which the disc inside the planet is depleted of gas.

7.C Torque fluctuations

The torque evolution discussed in Section 7.3.3 showed strong oscillations with time, especially for the high-mass discs ($\Sigma_0 = 100\,\mathrm{g\,cm^{-2}}$) for which disc-planet interactions were more important. The case with low X-ray luminosity ($\log_{10}(L_\mathrm{x}/\mathrm{erg\,s^{-1}}) = 29.54$) showed in particular short-term oscillations while for the high X-ray case the variation was much longer with time. In Figure 7.C.1 we show the surface density distribution close to the planet location at two time steps where the torque had a low or high peak with respect to a reference step, for the low X-ray luminosity case. The surface density shows strong interaction with vortices developing in the outer gap edge that are well in agreement with the short-term oscillations. The long-term variation observed in the high X-ray flux case can be instead related to the strong interaction between the stellar irradiation and the gap edge outside the planet location, which affects the torque acting onto the planet.

Chapter 8

The imprint of X-ray photoevaporation on the orbital distribution of giant planets

The content of this chapter was published in:

Monsch K., Picogna G., Ercolano B., Preibisch T. (2021): "The imprint of X-ray photoevaporation of planet-forming discs on the orbital distribution of giant planets – II. Theoretical predictions"[27], *Astronomy & Astrophysics*, 650:A199

Abstract

Numerical models have shown that disc dispersal via internal photoevaporation driven by the host star can successfully reproduce the observed pile-up of warm Jupiters near 1–2 au. However, since a range of different mechanisms have been proposed to cause the same feature, clear observational diagnostics of disc dispersal leaving an imprint in the observed distribution of giant planets could help in constraining the dominant mechanisms. We aim to assess the impact of disc dispersal via X-ray-driven photoevaporation (XPE) on giant planet separations in order to provide theoretical constraints on the location and size of any possible features related to this process within the observed semi-major axis distribution of giant planets. For this purpose, we perform a set of 1D planet population syntheses with varying initial conditions and correlate the gas giants' final parking locations with the X-ray luminosities of their host stars in order to quantify observables of this process within the semi-major axis versus host star X-ray luminosity plane of these systems. We find that XPE does create an under-density of gas giants near the gravitational radius, with corresponding pile-ups inside and/or outside this location. However, the size and location of these features are strongly dependent on the choice of initial conditions in our model, such as the assumed formation location of the planets. XPE can strongly affect the migration process of giant planets and leave potentially observable signatures within the observed orbital separations of giant planets. However, due to the simplistic approach employed in our model, which lacks a self-consistent treatment of planet formation within an evolving disc, a quantitative analysis of the final planet population orbits is not possible. Our results, however, should strongly motivate future studies to include realistic disc dispersal mechanisms in global planet population synthesis models with self-consistent planet formation modules.

[27] This chapter depends on collaborative work which I had the opportunity to take the lead of. I performed all simulations and their corresponding analysis, and prepared all of the shown plots. My coauthors helped me significantly in the interpretation and discussion of the results.

8.1 Introduction

Planet population synthesis models have become a well-established tool for directly comparing observational data with theoretical models of planet formation and evolution. Such models are based on the simple assumption that the observed diversity of extrasolar planets stems from the diversity in initial conditions in the nurseries of planetary systems, the planet-forming discs. By stochastically varying system parameters, such as the disc mass, the dust-to-gas ratio, or the amount of planetary embryos within a system, one can directly infer and isolate the impact of specific physical processes on the overall planet formation efficiency and ultimately predict the properties of planetary systems using an ensemble of statistically independent models. By unifying as many physical processes as possible, such models therefore provide a direct link between the observed population of planetary systems and the predictions of theoretical models (see e.g. Benz et al., 2014; Mordasini, 2018, for detailed reviews)

Due to the large number of unknowns during the formation process of planets, there exists a variety of planet population synthesis models, which are centred on different aspects of the exoplanet demographics and therefore have different degrees of complexity. The most comprehensive ones connect the earliest stages of planet formation with the later dynamical evolution of the fully formed planets, long after the gas disc has been dissipated (e.g. Ida & Lin, 2004; Thommes et al., 2008; Mordasini et al., 2009; Hellary & Nelson, 2012; Coleman & Nelson, 2014; Bitsch et al., 2015; Ronco et al., 2017; Ida et al., 2018; Forgan et al., 2018; Emsenhuber et al., 2020). Based on such global approaches, some studies focus specifically on individual processes, such as the impact of pebble accretion onto planet formation and planetary system architectures (e.g. Bitsch et al., 2019; Ndugu et al., 2018, 2019; Izidoro et al., 2019) or the importance of the early infall phase from the parent molecular cloud core in setting the initial properties of protoplanetary discs (e.g. Schib et al., 2020).

However, due to the complexity of these calculations, planet population synthesis models include by necessity simplified treatments of more complicated physical processes. They typically adopt 1D parameterisations for disc and planet evolution, which are usually derived from more complex, multi-dimensional hydrodynamical calculations. Often, however, these prescriptions neglect subtler effects, or they may be only applicable to a specific subset of the modelled parameter space. One example is the so-called impulse approximation (Lin & Papaloizou, 1979, 1986), which is commonly used in 1D models to calculate the torques exerted onto planets embedded in a gaseous disc. While it yields reasonable results for most disc-planet systems, Monsch et al. (2021a) show that it fails to correctly describe the migration rates of gas giants in transition discs with evacuated inner cavities. While the impulse approximation would predict an accelerated inward migration of giant planets in such systems, these authors have shown using 2D FARGO simulations that planet migration should cease as soon as the disc inside the planetary orbit is depleted of gas. The reason for this is the formation of strongly positive torques right at the gap edge, which act as a planet trap, preventing any further inward migration of the planet. This has important consequences for the final orbital location of giant planets and should therefore be taken into account in 1D models when calculating the migration tracks of giant planets in evolving protoplanetary discs.

This illustrates the Achilles heel of planet population synthesis models as their final outcome

relies heavily on the accuracy of the employed prescriptions. For example, many models lack a detailed treatment of disc dispersal via photoevaporative winds, which are, however, a crucial ingredient in theoretical models for reproducing the observed disc lifetimes and strongly affect the final accreted gas mass of giant planets in a simulation. Models often include a combination of internal and external photoevaporation via extreme (EUV) and far-ultraviolet (FUV) photons. However, it has been shown that stellar EUV photons impinging on the circumstellar disc are already readily absorbed by small columns of neutral hydrogen and should therefore barely penetrate into the disc (e.g. Alexander et al., 2004a) and thus barely contribute to its heating and ionisation at larger radii. Photons fluxes of $\Phi \gtrsim 10^{41}\,\mathrm{s}^{-1}$ would be required to produce mass loss rates of $10^{-10}\,M_\odot\,\mathrm{yr}^{-1}$ (e.g. Alexander et al., 2006b; Alexander & Armitage, 2009). However, observations of photoevaporative winds traced by free-free emission hint towards EUV fluxes being too low to dominate the dispersal of the discs around young T Tauri stars (Pascucci et al., 2014; Macías et al., 2016); consequently by assuming purely EUV-driven winds, the impact of photoevaporation on dispersing circumstellar discs is likely to be underestimated (see however Wang & Goodman (2017) and Nakatani et al. (2018). who come to a different conclusion). Further, the importance of internal FUV-dominated photoevaporation on driving disc evolution is still matter of debate. While thermochemical models suggest significantly increased mass loss rates compared to the pure-EUV models (Gorti et al., 2009; Gorti & Hollenbach, 2009), these results still need to be confirmed by future hydrodynamical calculations. On the other hand, external photoevaporation models driven by EUV and FUV photons by nearby high-mass stars have grown in importance in recent years (Matsuyama et al., 2003a; Winter et al., 2018, 2020). In contrast to the internal models, detailed radiation-hydrodynamical calculations for external photoevaporation do exist (Facchini et al., 2016; Haworth et al., 2016, 2018) but are not employed in current planet population synthesis approaches.

8.2 The impact of disc dispersal on planetary orbits

Photoevaporative disc clearing has been suggested to have a dramatic impact on the semi-major axis distribution of giant planets (e.g. Matsuyama et al., 2003b; Hasegawa & Pudritz, 2012), and recent numerical efforts have shown that photoevaporation by EUV and/or X-ray photons can indeed reproduce the observed pile-up of Jupiter-mass planets close to 1–2 au (Alexander & Pascucci 2012; Ercolano & Rosotti 2015; however, see also Wise & Dodson-Robinson, 2018). By heating the gas in the surface layers of the disc, the gas becomes unbound beyond the so-called gravitational radius:

$$R_\mathrm{g} = \frac{GM_\star}{c_\mathrm{s}^2} \approx 8.9\,\mathrm{au}\left(\frac{T_\mathrm{gas}}{10^4\,\mathrm{K}}\right)^{-1}\left(\frac{M_\star}{M_\odot}\right), \tag{8.1}$$

where G is the gravitational constant, $M_\star$ the stellar mass, c_s the sound speed, and T_gas is the temperature of the heated gas layer (Owen et al., 2012). For X-ray-driven photoevaporation (XPE) of a $0.7\,M_\odot$ star, $T_\mathrm{gas} \approx 10^3$–$10^4\,\mathrm{K}$, so that $R_\mathrm{g} \approx 6$–$60\,\mathrm{au}$. This produces centrifugally launched, pressure-driven disc winds which result in the opening of an annular, gas-free gap inside of R_g, fully decoupling the inner from the outer disc (see Alexander et al., 2014, for a

review). Photoevaporation can therefore naturally provide a parking radius for inward migrating planets as their migration (which is a result of the angular momentum exchange between the planet and the gas-parcels in the disc) is ultimately stopped, once they reach the gas-free cavity. Planets inwards of the gap continue migrating shortly, while the inner disc is viscously drained, leading to a pile-up of planets just inside the photoevaporative gap located at the gap-opening radius (or 'critical radius'[28], henceforth R_{gap}). Planets outside of R_{gap} also continue migrating inwards; however, they are at the latest stopped once they reach the expanding photoevaporative gap. Compared to pure EUV-models (Alexander & Pascucci, 2012), XPE has been shown to be even more effective in reproducing the observed pile-up of giants close to 1–2 au (Ercolano & Rosotti, 2015). As the mass loss is more extended, it can park a larger fraction of planets, especially the more massive ones, at larger radii.

However, other models have also been proposed as possible cause for the pile-up of gas giants near 1 au, such as a reduction of type II migration rates (e.g. Ida et al., 2018) or magnetically driven disc winds that can generate pile-ups within the surface density (Suzuki et al., 2016; Chambers, 2019). Consequently, clear diagnostics for XPE shaping giant planet architectures are needed for differentiating between the possible driving mechanisms. Monsch et al. (2019) have investigated the possibility that disc dispersal via XPE may leave such an observable imprint. By self-consistently calculating the X-ray luminosities, L_{X}, of giant planet-hosting stars and correlating them with the semi-major axes, a, of their planets, they found a suggestive void within the L_{X}–a-plane, which may hint towards XPE parking the planets close to the photoevaporative gap. However, due to the limited amount of X-ray observations, they could not prove the statistical significance of this void without either increasing the sample size drastically or having an accurate theoretical model that would predict the exact location and size of this gap a priori.

Motivated by the observational study presented in Monsch et al. (2019), we aim to use theoretical models to look for possible signatures of XPE in the observed semi-major axis distribution of giant planets. For this purpose, we performed detailed 1D planet population synthesis models including giant planet migration and disc dispersal via internal photoevaporation driven by the host star. By varying key system parameters, such as the stellar X-ray luminosity, the planet mass and the planetary formation time, we predict what kind of features photoevaporation is expected to leave within the orbital distribution of gas giants. Our study is conceptually similar to previous work by Jennings et al. (2018), who have compared the impact of EUV, X-ray and FUV-photoevaporation on the orbital distribution of a given set of giant planets. Our study, in turn, solely focuses on XPE and intends to explore its impact on the migration process of giant planets as a possible origin of the over- and under-densities observed in the demographics of giant planets. We aim to provide a comprehensive model that can aid the interpretation of the void within the L_{X}–a-distribution presented in Monsch et al. (2019), within the intrinsic limitations of our 1D approach, which does not yet treat planet formation self-consistently in combination with disc evolution.

[28] Analytic models have shown that there can already be significant mass loss due to photoevaporation already starting at radii of $R_{\mathrm{crit}} \approx 0.1$–$0.2\,R_{\mathrm{g}}$ (Liffman, 2003; Adams et al., 2004; Font et al., 2004; Dullemond et al., 2007), while earlier models predicted that all gas would be fully gravitationally bound within R_{g}.

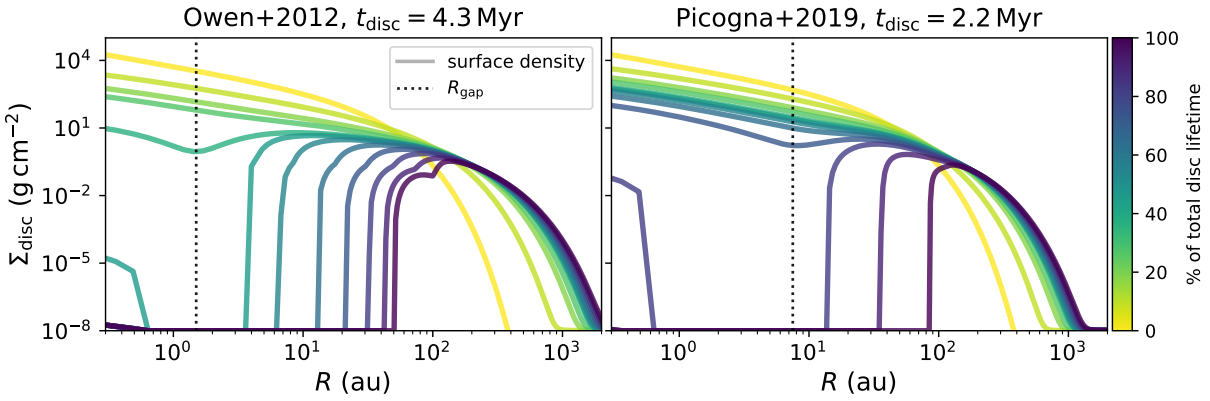

Figure 8.1: Comparison of the 1D surface density evolution as a function of disc radius for a planet-less disc of $M_{\rm d} = 0.07\,M_{\odot}$, using $L_{\rm x} = 1 \times 10^{30}\,{\rm erg\,s^{-1}}$ for the photoevaporation profiles by O12 and P19. The different lines are drawn at [0, 25, 50, 60, 70, 72, 75, 80, 85, 90, 95, 99] % of the corresponding total disc lifetime $t_{\rm disc}$. The dotted line shows the approximate location of gap opening due to photoevaporation for each model.

This chapter is structured as follows. Section 8.3 describes the X-ray photoevaporation prescription, as well as the initial setup used for the 1D planet population synthesis model. The outcome of the models is presented in Section 8.4 and discussed in the context of observational data in Section 8.5. Finally we draw our conclusion in Section 8.6.

8.3 Numerical methods

8.3.1 Photoevaporation model

In this study we investigate the impact of XPE on the orbital distribution of a population of giant planets. For this purpose, we first compare the commonly used XPE profiles derived by Owen et al. (2010, 2011a, 2012, hereafter O12) with the updated one by Picogna et al. (2019, hereafter P19). Both models were computed using radiation-hydrodynamical calculations; however P19 include a parameterisation of the temperature as a function of the local gas properties, as well as the column density to the star. Wind mass loss rates ($\dot{M}_{\rm w}$) obtained by P19 are approximately a factor of two higher compared to O12, and present significant differences in the radial mass loss profile ($\dot{\Sigma}_{\rm w}$). The relevant equations are given in Appendix 8.A, in which Figure 8.A.1 shows a direct comparison of $\dot{M}_{\rm w}(L_{\rm x})$ and $\dot{\Sigma}_{\rm w}(R)$ for both profiles. The one by P19 produces not only more vigorous winds (i.e. higher $\dot{M}_{\rm w}$), but it also extends further out into the disc (up to $\sim 120\,$au), therefore leading to the more efficient removal of the disc on a shorter timescale. Wölfer et al. (2019) present similar XPE models, however for low-metallicity discs, which are depleted in carbon. They predict significantly higher gas temperatures and photoevaporative winds in such discs due to the larger penetration depth of the X-rays. Investigating the impact of photoevaporation in carbon-depleted discs on the migration process of giant planets is beyond the scope of this paper, but will be attempted in future work.

Figure 8.1 shows the 1D surface density evolution of a planet-less disc with an initial mass

of $M_{\rm d} = 0.07\,M_{\odot}$, applying the two different photoevaporation profiles with a reference X-ray luminosity of $L_{\rm x} = 1 \times 10^{30}\,{\rm erg\,s^{-1}}$ for a $0.7\,M_{\odot}$ star. The total disc lifetimes differ by almost 2 Myr (i.e. $t_{\rm disc,\,Owen} = 4.3\,{\rm Myr}$ versus $t_{\rm disc,\,Picogna} = 2.2\,{\rm Myr}$), as expected from the enhanced efficiency of the updated photoevaporation profile by P19. Once the viscous accretion rate onto the star falls below the photoevaporative wind mass loss rate, photoevaporation opens a gap in the disc, cutting the inner disc off from further mass-supply by the outer disc. While the profile by O12 opens a gap at 1–2 au between 70–72 % of the corresponding total disc lifetime, the profile by P19 opens it at slightly larger radii of around 7–8 au after 85–90 % $\times\, t_{\rm disc,\,Picogna}$. The latter photoevaporation profile will therefore leave the surface density structure of the disc relatively unperturbed for a larger fraction of the total disc lifetime and cause gap opening at later stages of the disc's global evolution. The reason for this is that the $\dot{\Sigma}_{\rm w}$-profile from O12 peaks around 1–2 au and declines relatively steeply beyond that, so that the mass loss will be mostly concentrated near the peak of $\dot{\Sigma}_{\rm w}$. Even though the profile by P19 peaks even closer inside, it is, in contrast, flatter at larger disc radii, leading to the more efficient removal of material also outside of the peak of $\dot{\Sigma}_{\rm w}$. Therefore, the gap will open at later stages compared to the total disc lifetime (which is, nevertheless, significantly shorter for the P19 model) and at larger radii in this case.

From this point on, the disc enters the transition disc phase. As the inner disc is viscously accreted onto the host star, its opacity is reduced quickly (approximately on the viscous timescale), so that the outer disc can be directly irradiated by the central star (Alexander et al., 2006a,b). This leads to the very efficient dispersal of the outer disc, roughly on a timescale of a few 10^5 yr. Both O12 and P19 present different mass loss profiles for primordial and transition discs, which are implemented in our model (Eq. 8.11 and Eq. 8.16, respectively). The switch between both profiles is performed once a gap has opened in the disc and the radial column density inside this gap becomes less than the maximum X-ray penetration depth of $\sim 2.5 \times 10^{22}\,{\rm cm^{-2}}$ (Ercolano et al., 2009a; Picogna et al., 2019).

8.3.2 1D planet population synthesis

To model the orbital evolution of giant planets in a population of young disc-bearing stars, we used the 1D viscous evolution code `SPOCK`. We follow a similar setup as described by Ercolano & Rosotti (2015); Jennings et al. (2018) and Monsch et al. (2021a), which are mostly based on previous models by Armitage (2007b), Alexander & Armitage (2009), and Alexander & Pascucci (2012). We will therefore only briefly summarise our numerical model and refer the reader to Ercolano & Rosotti (2015) for a more detailed description of the employed code.

Each model follows the combined evolution of a single giant planet embedded in a protoplanetary disc subject to viscosity and XPE driven by the host star. The surface density evolution of the coupled planet-disc system can be described via the equation:

$$\frac{\partial \Sigma}{\partial t} = \frac{1}{R}\frac{\partial}{\partial R}\left[3R^{1/2}\frac{\partial}{\partial R}\left(\nu\Sigma R^{1/2}\right) - \frac{2\Lambda\Sigma R^{3/2}}{(GM_{\star})^{1/2}}\right] - \dot{\Sigma}_{\rm w}(R,t). \tag{8.2}$$

The first term on the right hand side of Eq. 8.2 describes the viscous evolution of the disc (Lynden-Bell & Pringle, 1974), the second term treats the migration of the planet (Lin &

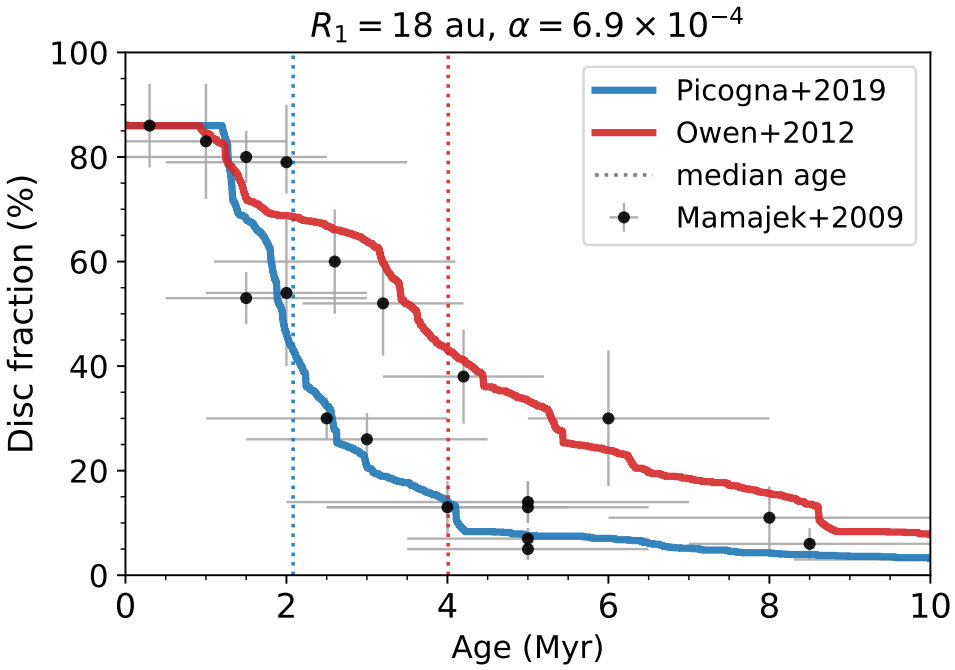

Figure 8.2: Disc fraction as a function of time from two evolving disc populations using the XPE profiles by P19 (solid blue line) and O12 (solid red line). For each model, 1000 simulations were performed, using different X-ray luminosities that were sampled randomly from the XLF of Taurus. The dotted lines show the corresponding median disc lifetimes of each distribution. The black dots show observed disc fractions compiled by Mamajek (2009). The simulated disc fractions were scaled to 86 % in order to account for binary interactions (cf. Owen et al., 2011a).

Papaloizou, 1979, 1986; Armitage et al., 2002) and $\dot{\Sigma}_{\rm w}(R,t)$ corresponds to the surface mass loss profile due to photoevaporation. Here, $\Sigma(R,t)$ describes the gas surface density of the disc, $M_\star = 0.7\,M_\odot$ is the stellar mass, R the distance from the star and G is the gravitational constant.

Eq. 8.2 was discretised on a grid of 1000 radial cells (which is increased to 4000 at the time of planet insertion), equispaced in $R^{1/2}$ and extending from 0.04 au to 10^4 au. Further we adopted the self-similarity solution of the diffusion equation by Lynden-Bell & Pringle (1974) for the surface density profile of the disc, assuming a time-independent power-law scaling of the disc radius with the kinematic viscosity, $\nu \propto R^\gamma$, where $\gamma = 1$ (cf. Section 4 in Hartmann et al., 1998):

$$\Sigma(R, t=0) = \frac{M_{\rm d}(t=0)}{2\pi R_1 R} \exp\left(-\frac{R}{R_1}\right). \tag{8.3}$$

Here, $M_{\rm d}(t=0) = 0.07\,M_\odot$ is the initial disc mass at time zero. The disc scaling radius R_1 describes the location of the exponential cutoff of the surface density profile. Together with the kinematic viscosity $\nu = \alpha c_{\rm s} H$, where $c_{\rm s}$ is the sound speed of the gas, H the disc scale height, and α the dimensionless Shakura-Sunyaev parameter (Shakura & Sunyaev, 1973), it

sets the viscous timescale $t_\nu = R_1^2/(3\nu)$. We assume locally isothermal discs with an aspect ratio of $H/R = 0.1$ at R_1, which results in flared discs following $H \propto R^{5/4}$ and a midplane temperature structure scaling as $T_{\mathrm{mid}} \propto R^{-1/2}$, so that $T_{\mathrm{mid}} \approx [2100\,\mathrm{K}, 4\,\mathrm{K}]$ at the inner and outer boundary, respectively.

The values for R_1 and α need to be chosen such that, combined with the effect of viscous accretion and mass loss due to photoevaporation, observationally supported median disc lifetimes ranging between 1–3 Myr are obtained (e.g. Haisch et al., 2001; Mamajek, 2009; Fedele et al., 2010; Ribas et al., 2014, 2015). We therefore followed the approach described by Owen et al. (2011a) and constructed populations of evolving protoplanetary discs using different combinations of R_1 and α. The results from this test are summarised in Figure 8.2, which shows the disc fraction as a function of time from both XPE models tested in our study, using in total 1000 individual simulations in which the X-ray luminosities were sampled stochastically from the X-ray luminosity function (XLF) of the Taurus cluster (Güdel et al., 2007). Following Owen et al. (2011a), the resulting distributions were scaled to 86 %, assuming an initial close binary fraction of 14 % for NGC 2024 (Haisch et al., 2001). As it has an estimated age of 0.3 Myr, this stellar cluster is likely too young for discs to have been destroyed by planet formation or photoevaporation entirely. We found that $R_1 = 18\,\mathrm{au}$ and $\alpha = 6.9 \times 10^{-4}$, which yields a viscous timescale of $t_\nu = 7 \times 10^5\,\mathrm{yr}$ at R_1, reproduces the observed disc fractions compiled by Mamajek (2009) best. Due to the increased photoevaporative mass loss rates, the profile by P19 generates shorter median disc lifetimes than the one by O12; however, both lie well within the observed spread in the disc fractions. In order to extract the effect of the XPE profile itself on the resulting orbital distribution of giant planets, we kept the same initial disc profile for all simulations in the remainder of this paper, regardless of the photoevaporation profile.

While we employ a value of disc viscosity, which is roughly consistent with recent observations of low disc turbulence (e.g. Flaherty et al., 2018), it is important to notice that realistic disc lifetimes could also be achieved by using different combinations of R_1 and α within one model as there is no a priori reason for them to be fixed in a population of discs. This approach was for example followed in a study similar to ours performed by Ercolano et al. (2018), who found, however, that their results do not change qualitatively, showing the robustness of these models against the specific choice of the underlying disc viscosity. Nevertheless, the implications of using a higher value of disc viscosity, as was for example done by Alexander & Pascucci (2012), are explored in detail in Appendix 8.B.

We modelled giant planets with masses ranging from 0.5–5 M_J, which were inserted between 5–20 au into the disc. The choice for the range of insertion locations is solely based on the simple assumption that most giant planets form outside the water snow-line due to more favourable initial conditions (e.g. Kennedy & Kenyon, 2008; Guilera et al., 2020). Around solar analogues, the water snow line is expected to lie between 2–5 au (Mulders et al., 2015a), therefore assuming 5 au as the minimum planet 'formation' location is a rather conservative choice. While the planets are allowed to accrete mass from the disc, their formation itself is not simulated in our code. Therefore, the formation times of the planets were drawn randomly from a uniform distribution between 0.25 Myr (which we assume to be the minimum time required to form a gas giant in the core accretion paradigm, cf. Pollack et al., 1996) and t_c, where

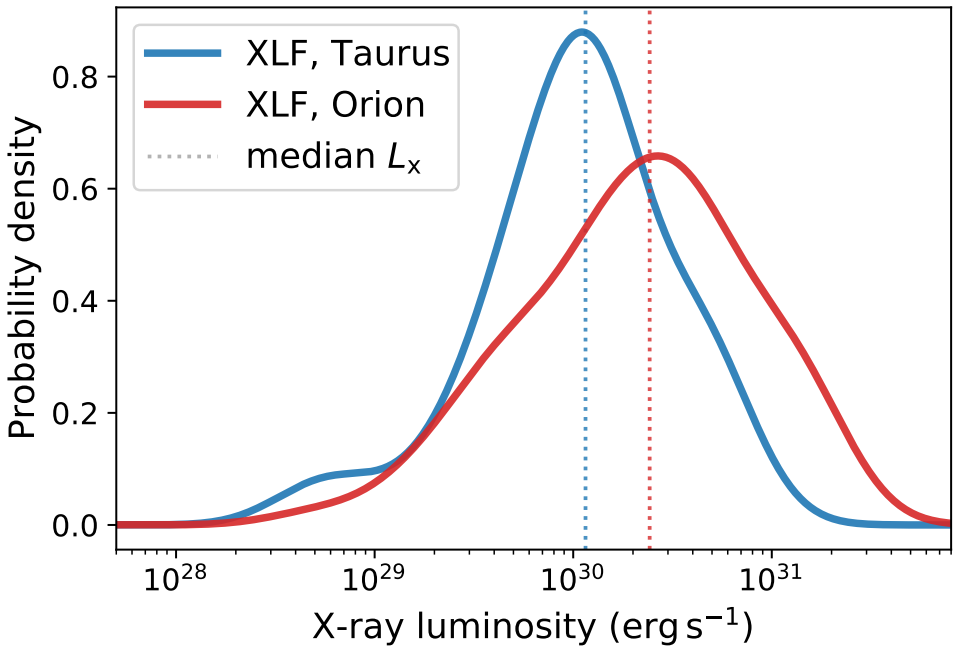

Figure 8.3: XLFs for pre-main-sequence stars located in the Taurus Cluster (0.5–1 $M_\odot$, Güdel et al., 2007; Owen et al., 2011a) and the Orion Nebula Cluster (0.5–0.9 $M_\odot$, Preibisch & Feigelson, 2005). The dotted lines are drawn at the median X-ray luminosity for each corresponding XLF.

$$t_c = \frac{t_\nu}{3}\left(\frac{3M_d(t=0)}{2t_\nu \dot{M}_w}\right)^{2/3}, \tag{8.4}$$

is the time at which photoevaporation starts to clear the disc (Clarke et al., 2001; Ruden, 2004). For $L_x = 1\times10^{30}\,\mathrm{erg\,s^{-1}}$, this corresponds to a disc clearing timescale of approximately $t_c = 1.8\,\mathrm{Myr}$ for the profile by O12 and $t_c = 1\,\mathrm{Myr}$ for the profile by P19. We further ensure that all discs are massive enough to actually form a giant planet via core accretion (if the planet is, for example, inserted at late stages of disc evolution), and therefore require the dust disc mass to be $\Sigma_{dust} = 0.01\Sigma_{gas} \geq 10\,M_\oplus$ at the time of planet insertion.

Planet accretion is modelled following Eq. 5 in Veras & Armitage (2004), whose implications will be discussed in more detail in Appendix 8.C. The planets then migrate in the disc following the impulse approximation (Lin & Papaloizou, 1979, 1986; Armitage et al., 2002):

$$\frac{da}{dt} = -\left(\frac{a}{GM_\star}\right)^{1/2}\left(\frac{4\pi}{M_p}\right)\int_{R_{in}}^{R_{out}} R\Lambda\Sigma dR, \text{ where} \tag{8.5}$$

$$\Lambda(R,a) = \begin{cases} -\frac{q^2GM_\star}{2R}\left(\frac{R}{\Delta_p}\right)^4 & \text{if } R<a \\ \frac{q^2GM_\star}{2R}\left(\frac{a}{\Delta_p}\right)^4 & \text{if } R>a. \end{cases} \tag{8.6}$$

Eq. 8.5 describes the evolution of the planetary semi-major axes as a function of time, the underlying 1D disc surface density, Σ, and the rate of the specific angular momentum transfer

Parameter	Value
$M_\star$ ($M_\odot$)	0.7
M_d ($M_\odot$)	0.07
α	6.9×10^{-4}
R_s (au)	18.
H/R	0.1
M_p (M_J)	[0.5, 5.]
t_form (Myr)	[0.25, t_c]
R_in (au)	0.04
R_out (au)	10^4
$\log(L_\mathrm{x}/\mathrm{erg\,s^{-1}})$	[27, 32]

Table 8.1: Initial conditions for the SPOCK simulations described in Section 8.3.2.

from the planet to the disc (i.e. the specific torques), $\Lambda(R, a)$. Here, $q = M_\mathrm{p}/M_\star$ is the planet to star mass-ratio and $\Delta_\mathrm{p} = \max(H, |R - a|)$ is the impact parameter, which ensures that only material outside of one disc scale height, $H = 0.1R$, is included into the torque calculation. We implemented the proposed fix by Monsch et al. (2021a) to the impulse approximation, which parks the planet as soon as the maximum surface density inside the planet location becomes $\Sigma \leq 10^{-6}\,\mathrm{g\,cm^{-2}}$ (i.e. the inner disc is dispersed) and $\Sigma \leq 10^{-2}\,\mathrm{g\,cm^{-2}}$ at the 3:2 resonance location outside the planet (to make sure that the outer disc is depleted enough to not continue pushing the planet inside). Further, each simulation is at the latest stopped at $t = 10\,\mathrm{Myr}$ or once the planet reaches $a \leq 0.15\,\mathrm{au}$ as we do not attempt to model the formation of hot Jupiter systems.

We considered observationally motivated X-ray luminosities following XLFs for pre-main-sequence stars in the Taurus cluster ($M_\star = 0.5$–$1\,M_\odot$, Güdel et al., 2007; Owen et al., 2011a) and the Orion Nebula Cluster ($M_\star = 0.5$–$0.9\,M_\odot$, Preibisch & Feigelson, 2005), which are shown in Figure 8.3. The difference between both XLFs is relatively small and lies mostly towards higher X-ray luminosities, which can be related to the different treatment of stellar flares (see Owen et al., 2011a, for a detailed discussion). Both cover a spread of about two orders of magnitude in X-ray luminosities, but in order to study the full extent in L_x-parameter space in our simulations, we sampled the X-ray luminosities linearly between $\log(L_\mathrm{x}/\mathrm{erg\,s^{-1}}) = 27$–$32$ (i.e. both extreme ends of the XLFs) using in total 1000 bins. To facilitate the identification of any L_x-specific features, we further oversampled given L_x-ranges (depending on the simulation) with another 500 bins. Table 8.1 summarises the initial conditions for the discs modelled in our study, while Table 8.2 collects the setups used for the different simulations.

8.4 Results

Figures 8.4 and 8.5 collect the outcome from the different population syntheses, each performed with in total 1500 disc-planet systems employing the photoevaporation profiles by O12 and P19. Each row shows the resulting L_x–a-distribution for different insertion locations of the planets

Name	a_{insert}	PE-profile	oversampled $\log L_{\mathrm{x}}$	$a_{\mathrm{final}} = 0.15$ au	comments
`Owen_5au`	5 au	O12	28.7–31.0	33.9 %	
`Owen_10au`	10 au	O12	28.7–31.0	23.1 %	
`Owen_20au`	20 au	O12	28.0–29.6	10.1 %	
`Owen_IPMF`	5–20 au	O12	29.0–31.0	17.8 %	uniform-random sampling of a_{insert} & planet mass sampled from IPMF
`Picogna_5au`	5 au	P19	28.0–30.5	40.3 %	
`Picogna_10au`	10 au	P19	28.0–30.5	25.1 %	
`Picogna_20au`	20 au	P19	28.0–29.5	12.6 %	
`Picogna_IPMF`	5–20 au	P19	28.0–29.5	23.0 %	uniform-random sampling of a_{insert} & planet mass sampled from IPMF

Table 8.2: Summary of the setups used for the different population synthesis models presented in Section 8.4.

(ranging from 5–20 au; see Table 8.2). The colours in the left column reflect the formation time of the planets relative to the disc clearing time (given by Eq. 8.4), so that $t_{\mathrm{form}}/t_{\mathrm{c}} < 1$, while in the right column colours correspond to the initial planetary mass. Further, the XLFs shown in Figure 8.3 were over-plotted in the right panels to demonstrate which parts of L_{x}-parameter space have been oversampled strongly due to the linear sampling of $\log L_{\mathrm{x}}$ in our model. The sizes of the data points additionally scale linearly with the value of the XLF of Taurus at the corresponding L_{x} to emphasise which part of L_{x}-parameter space would be most likely to be observed in a true sample. The crowding of planets at 0.15 au is an artefact resulting from our numerical setup, at which the simulations are forced to stop. In reality, however, these planets would either end up as hot Jupiters or be engulfed by their host star. The fraction of planets that reached the inner grid boundary are summarised for each simulation in Table 8.2. The following subsections will discuss each row of Figure 8.4 and Figure 8.5 separately.

8.4.1 Model `Owen_5au`

For the population synthesis presented in the top row of Figure 8.4, planets were inserted at 5 au into the disc. The black lines highlight three different regimes in the L_{x}–a-distribution, in which the final location of the giant planets is dominated by different effects:

1. $t_{\mathrm{c}} \gg 10$ Myr (left)
2. $t_{\mathrm{c}} \ll t_{\mathrm{m}}$ (right)
3. $10\,\mathrm{Myr} > t_{\mathrm{c}} > t_{\mathrm{m}}$ (centre)

These will be discussed in detail in the following.

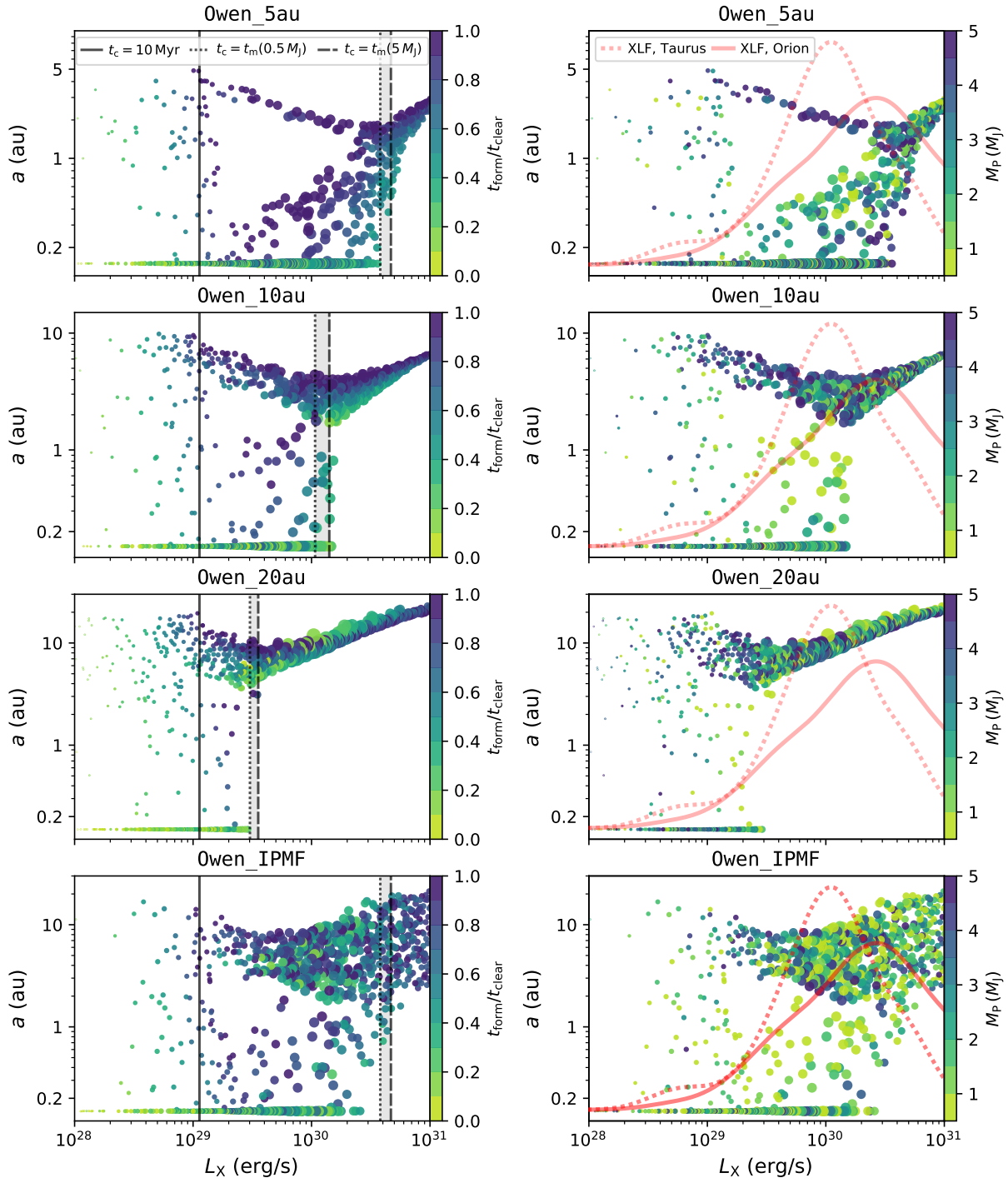

Figure 8.4: Comparison of the final L_x–a-distributions for the `Owen_XX` models using the photoevaporation profile by O12. The different rows show the outcomes of the population synthesis models using different insertion locations of the planets (5 au, 10 au, 20 au and random insertion locations). Colours in the left column correspond to the formation time of the planet with respect to the disc clearing time due to photoevaporation. In the right column, colours reflect the initial planetary mass. The black lines highlight the different regimes, in which the final planet parking location is set by different effects. These are discussed in detail in Section 8.4.1. The red lines in the right panels correspond to the XLFs as shown in Figure 8.3. Additionally, the data points were weighted linearly following the XLF in Taurus so that their size reflects the observing probability at a given L_x. This step was performed in order to emphasise which regions in L_x-parameter space are strongly over-crowded due to the linear sampling of log L_x in our model.

$t_c \gg 10\,\mathrm{Myr}$ **(left)**

For $L_x \lesssim 10^{29}\,\mathrm{erg\,s^{-1}}$, the disc clearing timescale becomes larger than 10 Myr, which is the time at which our simulations are forced to stop (e.g. $t_c \approx 63\,\mathrm{Myr}$ for $L_x = 10^{28}\,\mathrm{erg\,s^{-1}}$). In this regime, the type II migration timescale of the planets is much shorter than the disc clearing time, meaning that the surface density has already decreased significantly due to viscous accretion onto the host star once photoevaporation sets in and starts clearing the disc. At this point, the ratio of the disc mass to planet mass is so low that the planets have already stopped migrating, before photoevaporation could possibly affect or even halt their inward migration. Consequently, for low L_x, photoevaporation becomes ineffective in parking giant planets in the disc, and therefore they simply continue migrating until the simulations are forced to end at 10 Myr. Thus, for $L_x \lesssim 10^{29}\,\mathrm{erg\,s^{-1}}$, planets randomly populate semi-major axes between 5 au and the star, depending on their formation time and initial mass. In reality, however, planets in very weakly photoevaporating discs would continue to form and migrate inwards until accretion onto the star causes the surface density to become low enough to halt planet formation and migration. Thus, while the random population in our model is a direct consequence of the maximum disc lifetime assumed in our simulations, the distribution of planets in this regime is still expected to be random if planet formation were to be treated self-consistently within our model.

$t_c \ll t_m$ **(right)**

For $L_x \gtrsim 5 \times 10^{30}\,\mathrm{erg\,s^{-1}}$, t_c becomes shorter than the migration timescale of the most massive planets in our numerical model, meaning that photoevaporation produces such vigorous winds in this regime that it disperses the discs, before the planets could cross R_{gap}. Further, the range for the possible formation times of the planets becomes very small for high L_x as t_c is only marginally larger than 0.25 Myr (e.g. $t_c = 0.33\,\mathrm{Myr}$ for $L_x = 10^{31}\,\mathrm{erg\,s^{-1}}$), which is the minimum time required to form a giant planet in our model. Thus, for increasing X-ray luminosities, photoevaporation becomes more efficient in dispersing the circumstellar material and consequently parking the planets quickly after they are inserted into the disc, creating a diagonally shaped tail towards higher L_x.

$10\,\mathrm{Myr} > t_c > t_m$ **(centre)**

In this regime, the disc clearing timescale is shorter than 10 Myr, meaning that for each X-ray luminosity within this range, disc dispersal via XPE will be initiated before the simulations reach their maximum run time. Further, the migration timescale, t_m, for a planet of $0.5\,M_J$ (dotted line) or $5\,M_J$ (dashed line) that is formed at the earliest possible time of 0.25 Myr in our model (assuming a disc without photoevaporation), becomes shorter than the disc clearing time. This means that the planet may reach the inner boundary (depending on its insertion time and mass) before photoevaporation starts clearing the disc. Therefore, the X-ray luminosities ranging between $t_c = t_m(0.5\,M_J)$ and $t_c = t_m(5\,M_J)$ can be considered as an upper limit, for which a planet of given mass in our setup is potentially able to cross R_{gap}, before photoevaporation could potentially open a gap at this location. In contrast, for higher L_x, photoevaporation

will disperse the disc before planets can cross $R_{\rm gap}$, so that all planets are parked soon after they have been inserted into the disc. Therefore, $10\,{\rm Myr} > t_{\rm c} > t_{\rm m}(5\,M_{\rm J})$ defines the range in $L_{\rm x}$-parameter space, in which one would expect to observe an under-density of planets in the $L_{\rm x}$–a-distribution, caused by disc dispersal via photoevaporation. This is because photoevaporation opens an annular gap at $R_{\rm gap}$ in the disc on timescales comparable to the migration timescales of the planets, which will force the planets to either edge of the gap, with the majority sneaking by before gap opening. This creates a void of planets in the observed $L_{\rm x}$–a-distribution, which is centred on $R_{\rm gap}$.

Indeed, for intermediate X-ray luminosities of $\sim 10^{29}\,{\rm erg\,s^{-1}}$ to $\sim 5 \times 10^{30}\,{\rm erg\,s^{-1}}$, a large triangular-shaped desert of planets centred on $\sim 1\,{\rm au}$ can be observed. The insertion location of planets lies close to $R_{\rm gap}$ in the `Owen_5au` model, so that only planets that formed late relative to the disc clearing time (i.e. $t_{\rm form}/t_{\rm c} \gtrsim 0.7$) are parked outside of the gap. Assuming that the planet formation efficiency at 5 au right before the onset of disc dispersal is considerably low, such planets could for example correspond to planets that formed earlier in the outermost parts of the planet-forming disc, possibly due to gravitational instability or pebble accretion, and have migrated up to 5 au just before photoevaporative disc clearing was initiated. It is therefore highly suggestive that the insertion location of the planets plays the most important role in determining the final parking location of the planets in our model. To investigate this further, we will later discuss the impact of different planet insertion locations on our results.

Planet-mass distributions

As inferred from Eq. 8.5, the migration rate of a planet depends on its mass. Therefore it is to be expected that distinct trends for planets of different masses can be observed in the orbital distribution of giant planets as more massive planets will reach higher migration rates, therefore reaching smaller radii before photoevaporation starts clearing the disc.

From the top right panel in Figure 8.4 it becomes apparent that planets with $M_{\rm p} \gtrsim 2.5\,M_{\rm J}$ accumulate outside of the observed void, which is roughly centred on 1 au. These planets are so massive that they strongly suppress the inflow of material across the planetary orbit, which reduces the opacity of the inner disc such that photoevaporation can start clearing the inner disc earlier as would be expected without the presence of a giant planet. This effect is termed Planet-Induced PhotoEvaporation (PIPE) and was first identified by Alexander & Armitage (2009) and Rosotti et al. (2013) as a direct consequence of the strong coupling between planet formation and protoplanetary disc clearing. As photoevaporation opens a gap in the disc, it fully decouples the inner from the outer disc, so that any further inflow of material from the outer disc is inhibited. For planets triggering PIPE, gap opening due to photoevaporation is therefore always initiated before they can cross $R_{\rm gap}$, leading to their pile-up just outside of this location. In contrast, all lower-mass gas giants with $M_{\rm p} \lesssim 2.5\,M_{\rm J}$ are able to cross this location before gap opening as they do not trigger PIPE. Therefore they will either pile up just inside the gas-free cavity or keep migrating inside, depending on how fast the inner disc is dispersed. The final parking location of planets located inside of $R_{\rm gap}$ at the time of gap opening therefore ultimately depends on their formation time, meaning only planets that are formed late and consequently also crossed $R_{\rm gap}$ at later stages, will be able to survive, while

all remaining planets migrate all the way onto the star and therefore pile up at 0.15 au in our model. This result is consistent with recent work by Emsenhuber et al. (2020), who also found that giant planets need to acquire their full mass up until shortly before the dispersal of the disc to prevent their strong inward migration, which would otherwise bring them to the inner edge of the disc.

8.4.2 Model `Owen_10au`

The numerical setup used to obtain the results shown in the second row of Figure 8.4 is conceptually the same as for model `Owen_5au`; however, now planets were inserted at 10 au into the disc. Even though a void of planets is observed again in the L_x–a-distribution, its size is significantly reduced compared to the previous model. This is easily explained because, due to the longer migration timescales of planets embedded at 10 au, photoevaporation will have more time to reduce the disc surface density and therefore eventually park the planets before they can cross R_{gap}. In the previous model, only very massive planets that reached the inner disc at late times (i.e. planets that were formed late in our model) accumulated outside of the void. Now planets with a broader range of masses and formation times ($t_{form}/t_c \gtrsim 0.5$) can be parked outside of the photoevaporative gap. Consequently also the total number density of planets inside 1 au is significantly reduced compared to the previous model.

As expected, left of $t_c = 10$ Myr no significant difference in the planet distribution can be observed (except of the higher number density of planets since fewer planets migrate up to 0.15 au) as photoevaporation does not play a significant role in this regime. Just as was observed in the previous model, also here planets are parked at random semi-major axes. However, the right edge of the void, which is confined by $t_c = t_m$, has now significantly moved towards lower X-ray luminosities. This creates an even sharper and longer tail of planets towards higher L_x as, due to the longer migration timescales, fewer planets will be able to cross R_{gap} before XPE starts clearing the disc. The final parking locations will therefore solely be set by the disc clearing timescale, which decreases with higher L_x.

8.4.3 Model `Owen_20au`

In this model, the planets were inserted at 20 au into the disc. The void that was observed in the previous two models has now shrunken dramatically and only extends from $\sim 1 \times 10^{30}\,\mathrm{erg\,s^{-1}}$ to $4 \times 10^{30}\,\mathrm{erg\,s^{-1}}$. Right of $t_c = t_m$, the final parking locations of the planets are solely set by the disc clearing time as the migration timescales of planets, which are formed at 20 au, is significantly longer than for planets inserted at 10 au or 5 au. In this regime, photoevaporation has now significantly more time to disperse the disc and open a gap, before any planet could cross this location. Consequently also the mass-distribution of planets outside of the void has become wider as more and more lower-mass planets can be parked outside R_{gap}, which ultimately results in a reduced number density of planets inside of 1 au.

8.4.4 Model `Owen_IPMF`

The previously presented models are extremely idealised. Firstly they assume that planets form at a single location, while in reality, planets are expected to form over a broad range of radii within the planet-forming disc. However, each insertion location of the planet leaves distinct features in the observed L_x–a-distribution and it becomes clear that the outcome of our population synthesis models is therefore extremely sensitive to the assumed formation location of the planets. Secondly, the planet mass was sampled randomly from a flat distribution, ranging from 0.5–5 M_J. Such an approach is reasonable to ensure that all planet-mass bins contain a statistically significant number of planets, which ultimately enables us to identify any planet-mass related features in the final L_x–a distribution (such as the pile-up of higher-mass planets outside the void in the `Owen_5au` model). However, the true distribution of giant planets is strongly non-uniform as observational data suggest that it declines with planetary mass, approximately following $\mathrm{d}N/\mathrm{d}M_p \propto M_p^{-\gamma}$, with $\gamma \approx 1$ (e.g. Marcy et al., 2005; Ananyeva et al., 2020).[29] Our previous approach is therefore not representative of the true sample of giant planets, and our results using a flat initial planet mass function (IPMF) should be treated with caution when directly compared to an observational sample. Nevertheless, in order to understand how disc dispersal via photoevaporation may affect the migration history of planets, one must first understand how these different initial conditions in our numerical model impact the final outcome.

Thus, in a new population synthesis we sampled the insertion location of the planets randomly from a uniform distribution between 5–20 au, and the planet mass from a $1/M_p$-distribution as is suggested by observations. We emphasise that we do not make any assumptions on how the planets in our model form, but solely assume that most giant planets need to form somewhere outside the water snow line, in order to acquire their gaseous atmosphere. While this approach is still highly idealised, it is nevertheless useful for understanding what kind of feature would be expected in the observed L_x–a-distribution of giant planets.

It becomes apparent from the lowest left panel of Figure 8.4 that the narrow, diagonally shaped tail, which was present in all previous models has now almost disappeared entirely. This is because the `Owen_IPMF` model is expected to be a superposition of the previous models with single planet insertion locations. Consequently, for each given insertion location one would expect the tail to shift along the y-axis and further change its length, leading to the random population of the tail between the upper boundary set by the `Owen_20au` model, and the lower boundary set by the `Owen_5au` model. Due to the larger amount of planets now inserted at larger distances from the star, mostly low-mass planets can cross the photoevaporative gap location before gap opening, while the majority of especially higher-mass planets gets parked outside of it. The reason for this is that with increasing insertion location, only planets with decreasing mass can cross the gap location as was seen in the `Owen_5au` model. Additionally,

[29] We note that this planet mass function was derived from observational data of planet hosts with ages $\sim$ Gyr and may therefore not represent the primordial mass distribution of exoplanets (see for example Carrera et al., 2018). However, global planet population synthesis approaches, such as the Bern model, seem to reproduce the observed $1/M_p$-planet mass distribution reasonably well (see Figure 5 in Benz et al., 2014, which is adapted from Mordasini et al. 2012).

due to the more realistic planet mass-sampling in this population synthesis, the resulting sample now includes significantly more lower-mass planets, which do not trigger PIPE. Therefore, most of the planets will cross R_{gap} before photoevaporation becomes dominant and opens a gap.

8.4.5 Model `Picogna_5au`

Figure 8.5 is conceptually similar to Figure 8.4; however now the photoevaporation profile by P19 was applied. A similar triangular void, such as the one identified in the `Owen_5au` model, can be observed in the intermediate L_{x}-regime. However, now the pile-up of massive planets outside of the void is entirely missing. This can be explained by the fact that the photoevaporation profile by P19 causes the photoevaporative gap to open at larger radii of 7–8 au compared to the profile by O12, which opens the gap between 1–2 au (cf. Figure 8.1). This means that in this model, planets are inserted already inside of R_{gap}, meaning that no planet can be parked outside of it. Consequently, also no tail of planets extending towards higher L_{x} can be observed. Even though photoevaporation still impacts planet migration by reducing the disc surface density, which in turn affects their migration rates, the final parking locations of the planets in this given model will be mainly set by their formation times as well as their mass.

The region at which photoevaporation becomes ineffective in affecting planet migration (i.e. left of $L_{\mathrm{x}}(t_{\mathrm{c}} = 10\,\mathrm{Myr})$) has now shifted towards a lower L_{x} of $\sim 7 \times 10^{28}\,\mathrm{erg\,s^{-1}}$. The reason for this is that the cumulative mass loss rate following from the P19 profile is higher than the one from O12 for such low L_{x}, therefore strongly increasing the impact of photoevaporation in this regime. In contrast, the region at which the clearing timescale becomes shorter than the migration timescale of the planets (i.e. right of $L_{\mathrm{x}}(t_{\mathrm{c}} = t_{\mathrm{m}})$) has now shifted towards higher L_{x}; however, also showing a larger range of the migration timescale for the lowest- and highest-mass planets in our model. While the profile by P19 generally predicts higher mass loss rates, it saturates towards $10^{-7}\,M_{\odot}\,\mathrm{yr}^{-1}$ for high L_{x} (see the left panel of Figure 8.A.1), while the one by O12 would predict an exponential increase in $\dot{M}_{\mathrm{w}}$ in this regime. This means that for $L_{\mathrm{x}} \gtrsim 5 \times 10^{30}\,\mathrm{erg\,s^{-1}}$ the impact of photoevaporation on planet migration is weaker when using the updated profile by P19. However, P19 argue that at high X-ray luminosities the theory from O12 breaks down as only the flat region of the ξ-T relation (see their section 3.3 for a detailed explanation) is accessible to the X-rays.

8.4.6 Model `Picogna_10au`

In this model, the planets were inserted at 10 au, which lies outside the location of 7–8 au, at which photoevaporation opens a gap. Therefore, planets are now expected to be parked outside of R_{gap} again, and indeed a desert of planets in the L_{x}–a-distribution can be observed for this setup. The void is similar in radial extent as the one in the `Owen_10au` model, but now encompasses a smaller range of X-ray luminosities (6×10^{29}–$5 \times 10^{30}\,\mathrm{erg\,s^{-1}}$) due to the more vigorous winds resulting from the updated photoevaporation profile. A small pile-up of higher-mass giant planets, comparable to the one observed in model `Owen_5au`, can be observed; however, now it includes significantly fewer planets. The reason for this is that the insertion

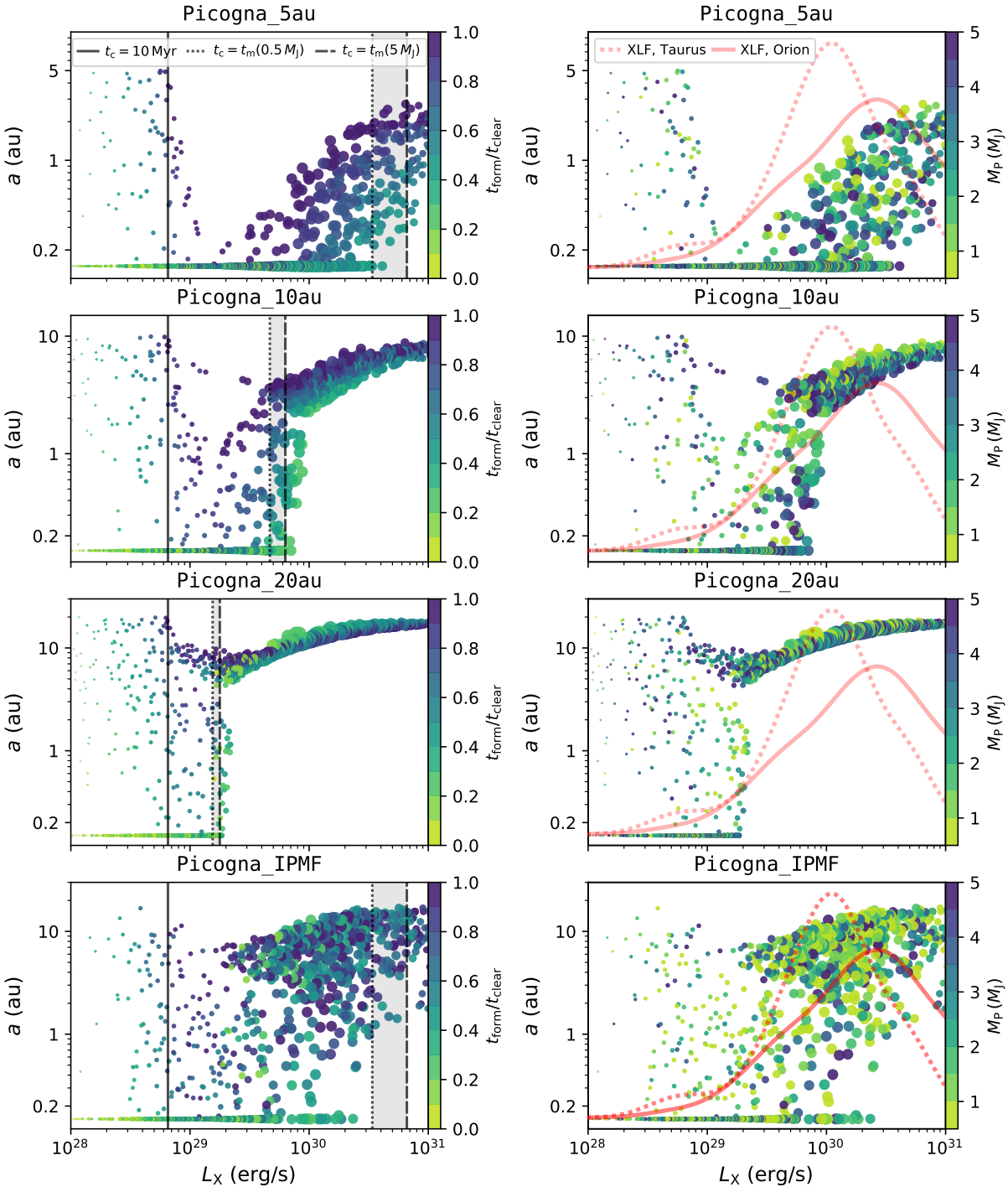

Figure 8.5: Same as Figure 8.4, but now the photoevaporation profile from P19 was applied.

location of planets at 10 au is only marginally larger than the radius at which photoevaporation will open the gap in the P19 profile. Therefore, only a small fraction of planets with favourable initial conditions, namely with a high mass and late formation times, can be parked outside of the gap. All remaining planets cross the location of gap opening before photoevaporation becomes dominant.

8.4.7 Model `Picogna_20au`

Similar to the `Owen_20au` model, also here practically no desert of planets caused by photoevaporation is observed anymore. Due to the long migration timescales of the planets, most planets are parked outside of R_{gap} as photoevaporation can open the gap before the majority of planets can cross this location. The number density of planets inside of the void appears to be larger than for the `Owen_20au`, possibly due to the higher mass loss rates that disperse the disc more quickly. Therefore, more planets are parked before they reach the inner grid boundary of 0.15 au. Similarly, also for low X-ray luminosities in the $t_{\mathrm{c}} > 10$ Myr regime more planets are parked across the entire semi-major axis range. Due to the higher mass loss rates, the disc can be depleted more efficiently. Nevertheless, photoevaporation can only weakly impact the final planet parking locations and consequently the planets will still be mostly parked at random locations.

8.4.8 Model `Picogna_IPMF`

The final semi-major axis distribution of planets in the `Picogna_IPMF` model is similar to the one in model `Owen_IPMF`; however, now the number of planets inside of the observed void is significantly larger. As was seen in the previous models, the photoevaporation profile by P19 opens the gap at larger radii, and therefore planets inserted between 10–20 au are more likely to cross R_{gap} before photoevaporation opens the gap.

Towards higher L_{x}, the broad tail of planets appears to have a fuzzier boundary towards lower semi-major axes. As mentioned above, for this photoevaporation profile, weaker winds are expected at higher L_{x}, meaning that photoevaporation is less efficient in parking the planets in this regime compared to the profile by O12. Therefore, the planets' parking location is more strongly dependent on the randomly sampled initial conditions rather than the disc clearing time, and consequently no sharp cutoff of planets can be observed.

8.5 Discussion

8.5.1 The effect of different photoevaporation profiles

Conceptually, both photoevaporation profiles leave similar imprints in the final L_{x}–a-distribution of giant planets. While for $L_{\mathrm{x}} \lesssim 10^{29}\,\mathrm{erg\,s^{-1}}$ giant planet migration is barely affected by disc dispersal via XPE, for $L_{\mathrm{x}} \gtrsim 5\text{–}7 \times 10^{30}\,\mathrm{erg\,s^{-1}}$ photoevaporation is the dominant mechanism that stops the inward migration of planets inserted at 5 au due to the rapid dispersal of the

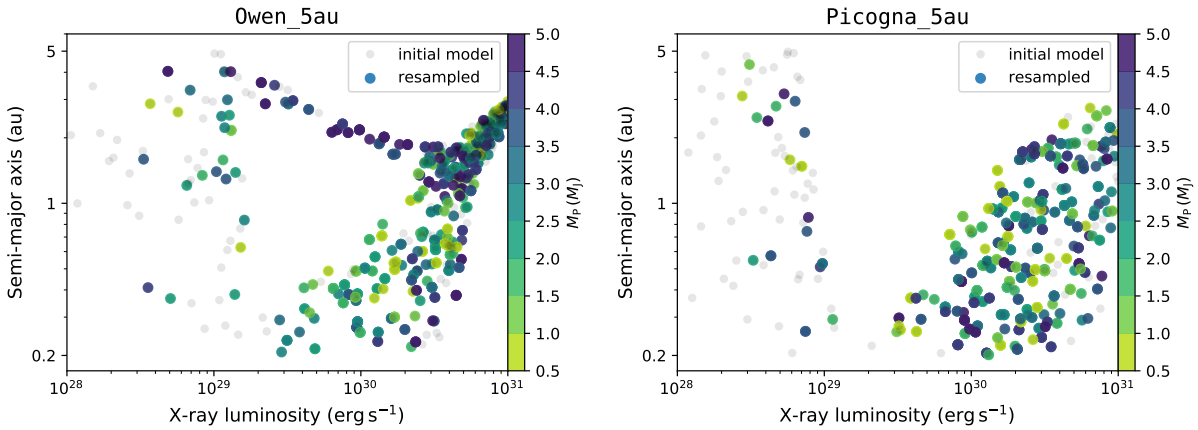

Figure 8.6: Final L_X–a-distribution assuming a realistic sampling of the X-ray luminosity. Grey dots show the initial `Owen_5au` and `Picogna_5au` models. Based on the XLF of Taurus, each data point was weighted correspondingly and the data were resampled 1500 times, which is shown as the colour-coded sample. Also the pile-up of planets at 0.15 au were removed from both samples as it corresponds to a numerical artefact rather than a real feature.

circumstellar material. For both profiles, an under-density of planets at intermediate values of L_X can be observed; however its radial extent strongly depends on the insertion location of the planets.

Only for planet insertion locations of 5 au, major differences between the final L_X–a-distribution resulting from the two photoevaporation profiles can be observed. This is because the one by P19 opens a gap at larger radii compared to the one by O12. Planets inserted at 5 au are therefore already located inside of R_{gap} for the models using the photoevaporation profile by P19. Nevertheless, besides the pile-up of high-mass planets in the `Owen_5au` model, a similarly strong under-density of planets can be observed in both cases, showing that the exact form of the XPE profile does not affect our overall conclusion, namely that for a given range of X-ray luminosities, disc dispersal via XPE will cause a dearth of planets between 1–10 au.

The profile by P19 can be considered as the more realistic one, due to the more accurate treatment of the temperature structure of the disc within the radiation-hydrodynamical calculations. The fact that the observed void of planets for the `Picogna_IPMF` model appears to be less strongly confined than for the `Owen_IPMF` one suggests, however, that it may be difficult to observe an imprint of XPE within the observed distribution of giant planets. In order to investigate this further, we compare the outcomes of our numerical models with actual observational data of exoplanet systems in the following.

8.5.2 Comparison with observations

X-ray luminosity sampling

Owen et al. (2011a) argue that the XLF derived from the Taurus cluster is more appropriate as an input to XPE models than the XLF derived for the Orion Nebula Cluster. They argue

that due to the removal of flares in the Taurus sample (that is a result of the shorter exposure time of these observations), it can better resemble the quiescent X-ray luminosities of young pre-main-sequence stars. However, stellar flares are a common phenomenon for young stars and need to be accounted for in order to obtain realistic values for stellar X-ray luminosities. The XLF for Orion is based on observations with significantly longer exposure times than the one for Taurus and therefore the stochastic effects of particularly strong X-ray flares are much more washed out by the much longer temporal baseline.

However, as the X-ray luminosity was sampled linearly between $\log(L_x/\mathrm{erg\,s^{-1}}) = 27$–$32$ rather than from an observed XLF, the amount of planets residing at the lowest and highest values of L_x is strongly overestimated in our models. In order to account for the observational selection function, we resampled the simulated data 1500 times using weights that match the observed XLFs as shown in Figure 8.3. The resulting L_x–a-distributions of the `Owen_5au` and `Picogna_5au` models (using the XLF of Taurus) are shown in Figure 8.6 and are directly compared to the initial models using linear sampling of $\log(L_x)$. While the number density of points is strongly reduced for $L_x \lesssim 10^{29}\,\mathrm{erg\,s^{-1}}$, the borders of the desert of planets is still well resolved. Within the limitations of our numerical model, this desert of planets therefore corresponds to a potentially observable feature within the L_x–a-distribution of giant planets and their host stars.

Semi-major axis distribution

Each panel in Figure 8.7 shows the resulting semi-major axis distribution from our population syntheses, obtained using a Gaussian kernel density estimate (KDE) implemented in `SciPy` (Virtanen et al., 2020), for which we applied Scott's Rule (Scott, 1992) in order to determine an appropriate bin width for the underlying data. All planets with $a < 0.2\,\mathrm{au}$ were removed from the sample prior to calculating the KDE, in order to remove the numerical artefact at 0.15 au. To allow an unbiased comparison between the simulations and the observations, we used both XLFs for the following analysis; however, we find that besides in those models, where the planet is inserted at 5 au, no significant difference can be observed in the resulting orbital separations. This approach therefore ensures that the synthetic semi-major axis distribution can be directly compared to the observed distribution of giant planets[30], which was scaled to the maximum of the corresponding model using the XPE profile by O12, in order to facilitate the readability. To allow a fair comparison between both samples, also for the observed data all planets with $a < 0.2\,\mathrm{au}$ were removed before calculating the KDE.

As previously discussed, the gap opened by photoevaporation is located at different radii in our models, depending on the applied photoevaporation profile. While it lies at $R_{\mathrm{gap}} = 1$–$2\,\mathrm{au}$ for O12, it is located at $R_{\mathrm{gap}} = 7$–$8\,\mathrm{au}$ for P19. Consequently, one would expect to observe an under-density of planets close to these radii within the orbital distribution of giant planets, and pile-ups of planets closely in- and outside of R_{gap}. Indeed, all of our models show such an under-density of planets in the L_x–a-distribution with pile-ups close to the location of gap opening; however their location and extent changes significantly with varying formation location

[30]These data were retrieved from the NASA Exoplanet Archive on 17 December 2020: `https://exoplanetarchive.ipac.caltech.edu/`.

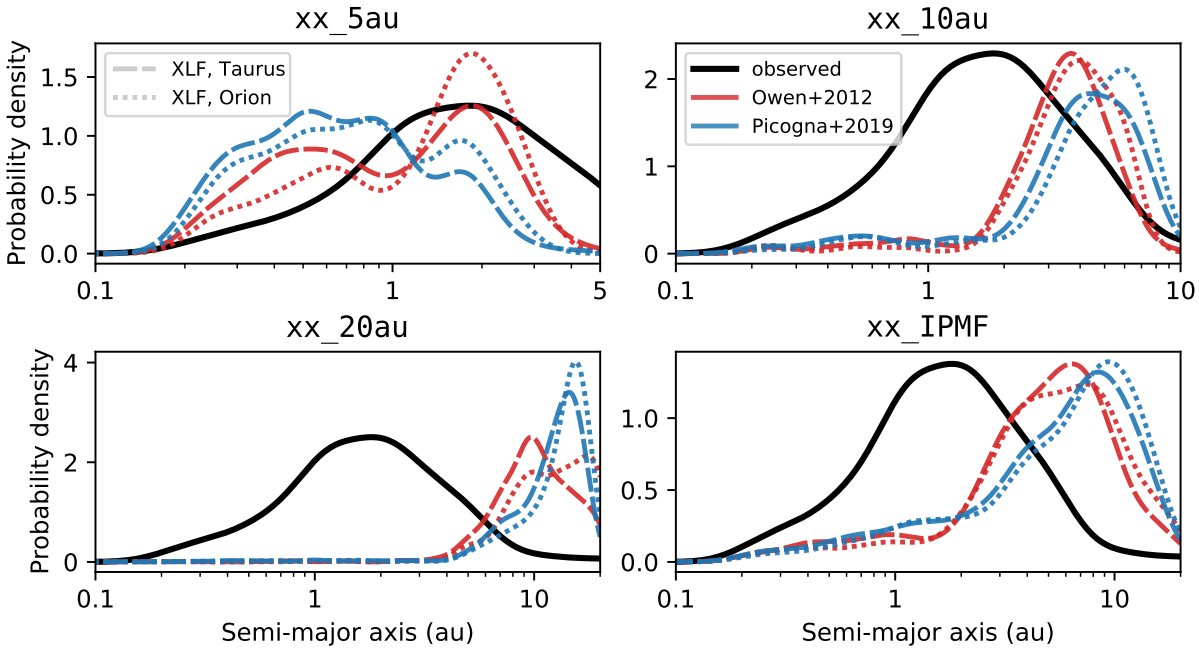

Figure 8.7: Final semi-major axis distributions, calculated using a Gaussian KDE. The blue and red lines correspond to the results from the simulations presented in this study, while the black lines show the observed distribution of giant planets obtained from the NASA Exoplanet Archive. For both datasets, all planets with $a < 0.2$ au were removed prior to calculating the KDE. As is described in detail in Section 8.5.2, the resulting semi-major axis distributions were re-weighted following the XLFs for Taurus and Orion, which are shown in Figure 8.3.

of the planets. This becomes even more apparent in the semi-major axis distribution of the giant planets, which shows that especially the choice of the insertion location of the planets has a dramatic effect on their final parking location.

While the observed sample of giant planets peaks between 1–3 au, most of the models from our study predict planets to pile up at larger radii, roughly between 3–10 au. Only model `Owen_5au` successfully reproduces the observed pile-up of giants close to 1 au; however, it over-predicts the amount of planets inside of this location. While our model is clearly able to produce a pile-up of giant planets, showing its ability in providing a parking mechanism for inward migrating planets, the discrepancy between the observed and the synthetic distribution of planets implies that our numerical model still has some significant caveats.

In particular the missing self-consistent treatment of planet formation is the biggest caveat of our study as fixed formation locations of the planets leave significantly distinct features in the resulting distribution of gas giants. However, by sampling the planet formation location randomly between 5–20 au, we are implicitly assuming a constant planet formation efficiency throughout large parts of the planet-forming disc. It could be observed in our models that giant planets pile up at larger radii with increasing insertion locations, and that the models in which the planets are inserted at 5 au (only for `Owen_5au`) or 10 au are more successful in reproducing the observed peak at 1–2 au, which may hint towards giant planet formation being more likely

between 5–10 au, rather than at radii > 20 au.

This conclusion would be indeed in agreement with observational studies that measured giant planet occurrence rates. For example, by using RV measurements, Cumming et al. (2008) measured the probability for solar-type stars hosting gas giants (0.3–10 M_J) with orbital periods between 2–2000 d ($\approx$ 0.03–3 au) to be 10.5 %. However, they proposed a strongly rising giant planet fraction for orbital periods beyond $P \approx 300$ d ($\sim$ 0.9 au; see also Marcy et al., 2005), while more recent studies such as the one performed by Bryan et al. (2016), which combines RV measurements with direct imaging data, find the giant planet frequency to decline beyond 3–10 au, therefore suggesting a peak in the giant planet occurrence rate within these radii (see however Wittenmyer et al., 2020, who find that the occurrence rate of giant planets plateaus beyond 1 au). This finding was later confirmed by Fernandes et al. (2019), who further combined RV and *Kepler* data to compute unified giant planet occurrence rates for orbital periods of up to 10^4 d. However, while our models may suggest a preferential location for giant planet formation, no robust conclusion can be extracted until a self-consistent treatment of planet formation is included into our model.

L_x–a-distribution

What can be inferred from our models is, however, that photoevaporation is indeed expected to create a desert of planets within the L_x–a-distribution of disc-planet systems. Yet, depending on the photoevaporation profile applied, and the assumed insertion location of the planets, its location and size are different, showing the strong dependence of our results on the initial conditions employed in our numerical setup. This strongly limits their predictive power when directly compared to observational data.

Further, it is important to note the planet distributions presented in Figure 8.4 and Figure 8.5 are the result of very specific initial conditions in highly idealised models and should be therefore interpreted carefully. Their sole purpose is to investigate if internal XPE can leave a potentially observable imprint in the orbital distribution of giant planets; however, no exact statements about the location or size of such features can be made at this point. One reason for this is the previously mentioned missing treatment of planet formation in our model, and therefore the strong dependence on the assumed planet formation locations. However, another strong limitation is that the simulations presented in our study were performed at the time of disc dispersal, meaning at ages < 10 Myr, while extrasolar planets are mainly detected around evolved main-sequence stars with ages of $\sim$ Gyr, with only very few exceptions (e.g. PDS 70, Keppler et al., 2018; Müller et al., 2018; Haffert et al., 2019). Consequently, any features imprinted in the earliest phases of the disc-planet systems could shift and possibly even be washed out with time due to other processes taking place that are neglected in our approach (e.g. multi-planetary systems and the resulting N-body interactions before and after gas-disc dispersal that may possibly even cause outward migration of the planets; see for example Rometsch et al., 2020). Using theoretical arguments, Monsch et al. (2019) predict that such a void as observed in our population synthesis models, would be expected to shift to lower L_x with time due to the spin-down of stellar rotation rates with increasing age and the resulting decrease in their magnetic activity, which is tightly linked to the stellar X-ray activity (see e.g.

Güdel, 2007; Brun & Browning, 2017, for reviews). Mapping the observed X-ray luminosities of planet-hosting stars to earlier times is non-trivial as the origin of the X-ray emission of late-type stars with spectral types ranging from F to M is still not fully understood. While quantitative arguments about the decrease in X-ray luminosity as a function of time can be made (e.g. Gallet & Bouvier, 2013; Tu et al., 2015, and see the discussion in Monsch et al. 2019), it is well beyond the scope of this paper to explicitly calculate the L_x-evolutionary tracks for all stars in our sample. At this point, our model is therefore not able to provide the exact location or size of any XPE related features within the L_x–a-distribution of giant planets, which would be, however, needed for proving the statistical significance of the void observed by Monsch et al. (2019). Certainly, an increase in observational data could help to resolve this issue, and current facilities like eROSITA are expected to soon provide a plethora of X-ray observations of planet-hosting stars.

Additionally, for a realistic comparison between theoretical models and observational data, it is further necessary to derive realistic occurrence rates from the synthetic planet distributions, which account for selection effects and detection biases introduced by each exoplanet detection technique and/or survey. This could be feasible, for example, by using the `epos` package developed by Mulders et al. (2019), which was successfully tested for the Bern planet population synthesis models. Since our model does not treat planet formation, but only investigates how XPE is expected to impact giant planet distributions qualitatively, we refrained from performing any detailed comparisons between simulated and observed giant planet occurrence rates. However, in the framework of global population synthesis models, whose goal it is not only to reproduce the exoplanet distributions qualitatively, but also quantitatively, using packages like `epos` is indispensable.

8.6 Conclusion

In this paper, we have explored the impact of disc dispersal via XPE onto giant planet migration and focused specifically on how this process can impact the final parking location of giant planets in planetary systems. The main results can be summarised as follows:

1. By performing a set of detailed 1D planet population synthesis models with the code `SPOCK`, we have found that XPE can indeed create a characteristic void, or under-density, of planets in the semi-major axis versus host star X-ray luminosity plane, as was previously suggested by Monsch et al. (2019). By opening an annular gap within the dispersing disc, XPE can provide a parking radius for inward migrating giant planets, so that they pile up both out- and inside of this cavity.

2. A comparison between the XPE models by Owen et al. (2012) with the more recent ones by Picogna et al. (2019) showed no qualitative difference in the resulting orbital separations of giant planets. However, due to an improved treatment of the underlying kinetic structure of the disc, the latter is more efficient in dispersing the discs, leading to gap opening at larger radii compared to the model of Owen et al. (2012), consequently resulting in pile-ups of giants located at larger radii.

3. The location and especially the size of this desert created by XPE in the L_x–a-distribution is strongly dependent on the choice of initial conditions used in our model, specifically the insertion location of the planets. This impedes a direct comparison to the catalogue obtained by Monsch et al. (2019), which would need robust measurements of the exact location and size of the void created by XPE in order to confirm that XPE may indeed leave an observational imprint in the observed L_x–a-distribution of giant planets.

Our study has shown that XPE could be expected to imprint the final semi-major axis versus host star X-ray luminosity plane, and this may potentially explain the observed pile-up of Jupiter-mass planets close to ~ 1 au. However, with our current models we are unable to make more quantitative statements. Global population synthesis models including a self-consistent treatment of planet formation and realistic disc dispersal mechanisms are needed in order to get robust results on the L_x–a-distribution of giant planet systems that can be directly compared to observations.

Acknowledgements We thank the referee, Richard Alexander, for carefully reading the manuscript as well as his helpful comments that have improved the quality of this paper. We acknowledge the support of the DFG priority program SPP 1992 "Exploring the Diversity of Extrasolar Planets" (DFG PR 569/13-1, ER 685/7-1) & the DFG Research Unit "Transition Disks" (FOR 2634/1, ER 685/8-1). We further acknowledge the support by the DFG Cluster of Excellence "Origin and Structure of the Universe". This research has made use of the NASA Exoplanet Archive, which is operated by the California Institute of Technology, under contract with the National Aeronautics and Space Administration under the Exoplanet Exploration Program.

Appendices

8.A Comparison of the different photoevaporation profiles

Figure 8.A.1 shows a comparison of the integrated mass loss rate, $\dot{M}_w(L_x)$, and the surface mass loss profile, $\dot{\Sigma}_w(R)$, from Owen et al. (2012) and Picogna et al. (2019), respectively. For the plots showing $\dot{\Sigma}_{w,full}$ it is assumed that photoevaporation of a $0.7\,M_\odot$ star already opened a gap in the disc, which has moved up to 10 au, while the inner disc had been drained. At this point, the inner edge of the outer disc lies at 10 au, and the column density of the inner disc is less than $2.5 \times 10^{22}\,\mathrm{cm}^{-2}$, so that the outer disc is directly irradiated by the stellar X-rays. Inside of 10 au the primordial ('diffuse') profile is therefore active (which is valid as long as photoevaporation has not opened a gap yet), and outside of 10 au the transitional ('direct') profile (which is valid after gap opening). The equations plotted in Figure 8.A.1 are explained in the following.

8.A.1 Owen et al. (2012)

In Appendix B1 of Owen et al. (2012), the total mass loss rate in primordial discs as a function of X-ray luminosity is described by:

$$\dot{M}_w(L_x) = 6.25 \times 10^{-9} \left(\frac{M_\star}{M_\odot}\right)^{-0.068} \left(\frac{L_x}{10^{30}\,\mathrm{erg\,s^{-1}}}\right)^{1.14} M_\odot\,\mathrm{yr}^{-1}. \tag{8.7}$$

The mass loss rate is only weakly dependent on the stellar mass and gives an almost linear scaling with the X-ray luminosity. The normalised mass loss profile is given by $\dot{M}_\mathrm{w}(R) = \int 2\pi R\,\dot{\Sigma}_\mathrm{w}(R)\,\mathrm{d}R$, where

$$\begin{aligned}\dot{\Sigma}_\mathrm{w}(x > 0.7) \;=\; & 10^{(a_1\log(x)^6+b_1\log(x)^5+c_1\log(x)^4+d_1\log(x)^3+e_1\log(x)^2+f_1\log(x)+g_1)} \\ & \times\left(\frac{6a_1\ln(x)^5}{x^2\ln(10)^7}+\frac{5b_1\ln(x)^4}{x^2\ln(10)^6}+\frac{4c_1\ln(x)^3}{x^2\ln(10)^5}+\frac{3d_1\ln(x)^2}{x^2\ln(10)^4}\right. \\ & \left.+\frac{2e_1\ln(x)}{x^2\ln(10)^3}+\frac{f_1}{x^2\ln(10)^2}\right)\times\exp\left[-\left(\frac{x}{100}\right)^{10}\right], \end{aligned} \tag{8.8}$$

with $a_1 = 0.15138$, $b_1 = -1.2182$, $c_1 = 3.4046$, $d_1 = -3.5717$, $e_1 = -0.32762$, $f_1 = 3.6064$, $g_1 = -2.4918$, and

$$x = 0.95\left(\frac{R}{\mathrm{au}}\right)\left(\frac{M_\star}{M_\odot}\right)^{-1}. \tag{8.9}$$

Eq. 8.9 describes the dimensionless radius (in dependence of the stellar mass) from which on photoevaporation becomes effective, and therefore $\dot{\Sigma}_\mathrm{w}(x < 0.7) = 0$. In the case of transition discs with inner holes, Eq. 8.7 and Eq. 8.8 change to:

$$\dot{M}_\mathrm{w}(L_\mathrm{x}) = 4.8\times10^{-9}\left(\frac{M_\star}{M_\odot}\right)^{-0.148}\left(\frac{L_\mathrm{x}}{10^{30}\,\mathrm{erg\,s^{-1}}}\right)^{1.14} M_\odot\,\mathrm{yr}^{-1},\ \text{and} \tag{8.10}$$

$$\dot{\Sigma}_\mathrm{w}(y) = \left[\frac{a_2b_2\exp(b_2y)}{R}+\frac{c_2d_2\exp(d_2y)}{R}+\frac{e_2f_2\exp(f_2y)}{R}\right]\times\exp\left[-\left(\frac{y}{57}\right)^{10}\right]. \tag{8.11}$$

Here, $a_2 = -0.438226$, $b_2 = -0.10658387$, $c_2 = 0.5699464$, $d_2 = 0.010732277$, $e_2 = -0.131809597$, $f_2 = -1.32285709$, and:

$$y = 0.95\,(R - R_\mathrm{hole})\left(\frac{M_\star}{M_\odot}\right)^{-1}, \tag{8.12}$$

with $\dot{\Sigma}_\mathrm{w}(y < 0) = 0$.

8.A.2 Picogna et al. (2019)

In Section 3.1 of Picogna et al. (2019), the primordial mass loss rate and surface mass loss profile are defined as:

$$\log\left(\dot{M}_\mathrm{w}(L_\mathrm{x})/(M_\odot\,\mathrm{yr}^{-1})\right) = A_\mathrm{L}\exp\left\{\left[\frac{(\ln(\log(L_X)) - B_\mathrm{L})^2}{C_\mathrm{L}}\right]\right\} + D_\mathrm{L}, \tag{8.13}$$

with $A_\mathrm{L} = -2.7326$, $B_\mathrm{L} = 3.3307$, $C_\mathrm{L} = -2.9868\cdot10^{-3}$, $D_\mathrm{L} = -7.2580$, and

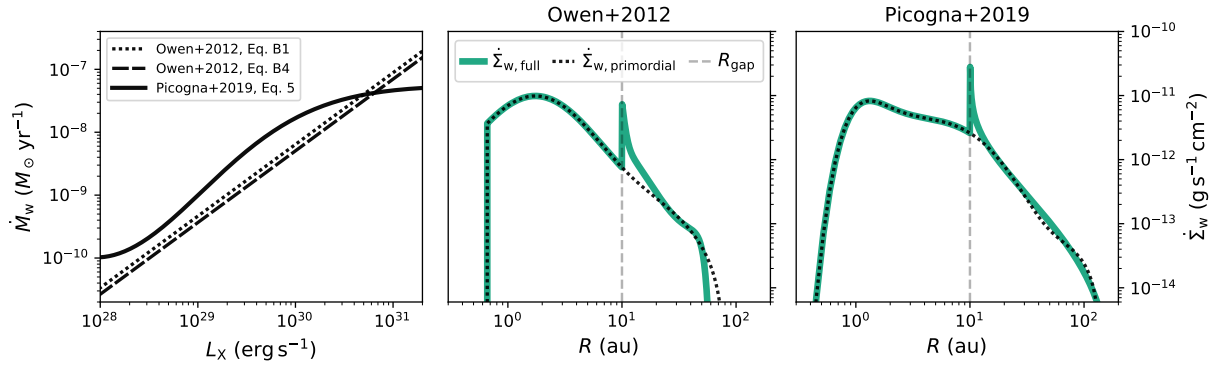

Figure 8.A.1: Comparison of the integrated mass loss rates as a function of the X-ray luminosity (left panel) and the surface mass loss profiles as a function of disc radius (centre and right panel) for the photoevaporation profiles by Owen et al. (2012) and Picogna et al. (2019). For the plots showing $\dot{\Sigma}_{w,full}$ it is assumed that photoevaporation already opened a gap in the disc, which has moved up to 10 au, while the inner disc was drained. At this point, the inner edge of the outer disc is located at 10 au, and the column density of the inner disc is less than 2.5×10^{22} cm^{-2}. Inside of 10 au the primordial profile is active (Eq. 8.8 and Eq. 8.14, respectively), and outside of 10 au the transition disc profile (Eq. 8.11 and Eq. 8.16, respectively). The solid lines show the total mass loss profile, while the dotted lines only highlight the primordial profile for each case (i.e. assuming photoevaporation had not opened a gap and the disc is still in its primordial stage).

$$\dot{\Sigma}_w(R) = \ln(10)\left(\frac{6a\ln(R)^5}{R\ln(10)^6} + \frac{5b\ln(R)^4}{R\ln(10)^5} + \frac{4c\ln(R)^3}{R\ln(10)^4} + \frac{3d\ln(R)^2}{R\ln(10)^3} + \frac{2e\ln(R)}{R\ln(10)^2} + \frac{f}{R\ln(10)}\right)\frac{\dot{M}_w(R)}{2\pi R}\, M_\odot\,\mathrm{au}^{-2}\,\mathrm{yr}^{-1}, \text{ with} \tag{8.14}$$

$$\dot{M}_w(R) = 10^{(a\log R^6 + b\log R^5 + c\log R^4 + d\log R^3) + e\log R^2 + f\log R + g)}\,\dot{M}_w(L_x), \tag{8.15}$$

and $a = -0.5885$, $b = 4.3130$, $c = -12.1214$, $d = 16.3587$, $e = -11.4721$, $f = 5.7248$, and $g = -2.8562$. For transition discs with inner holes, Eq. 8.14 will change to:

$$\dot{\Sigma}_w(R) = ab^x x^{c-1}(x\ln(b) + c)\,\frac{1.12\,\dot{M}(L_x)}{2\pi R}\, M_\odot\,\mathrm{au}^{-2}\,\mathrm{yr}^{-1} \tag{8.16}$$

where $x = (R - R_{gap})$, $a = 0.11843$, $b = 0.99695$ and $c = 0.48835$.

8.B The effect of disc viscosity on the gap location

We additionally tested the effect of a larger value for the disc viscosity ($\alpha = 10^{-2}$), which is the same value that was used in previous work by Alexander & Pascucci (2012). We note, however, that if we kept $R_1 = 18$ au and the remaining initial conditions of the discs in our model the same, unreasonably short total disc lifetimes would be obtained. Therefore we performed the

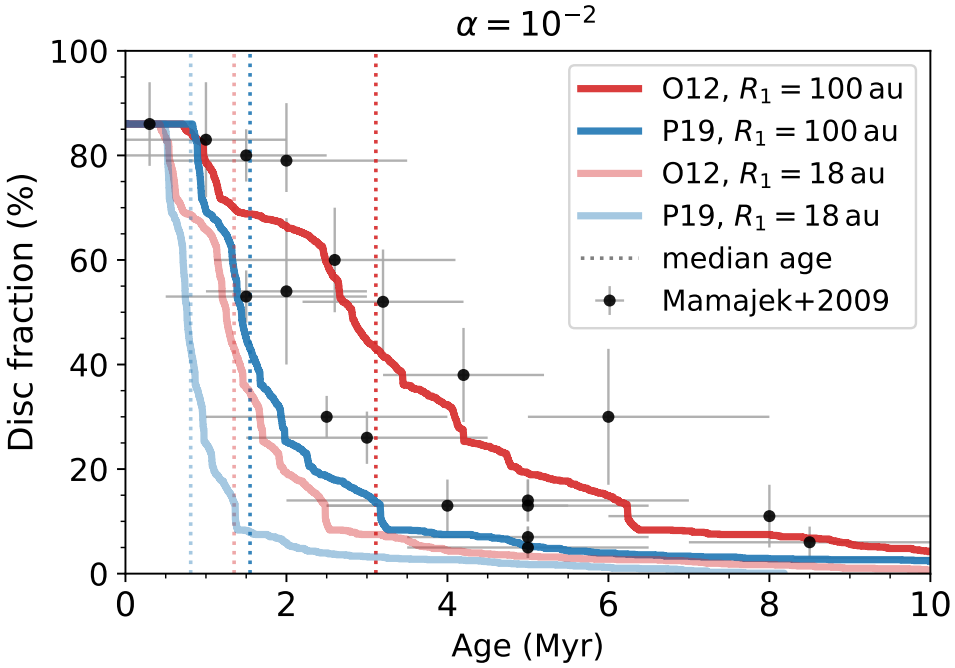

Figure 8.B.1: Same as Figure 8.2, but now a fixed viscosity parameter of $\alpha = 10^{-2}$ is assumed, while only R_1 and the photoevaporation profile are varied within the different runs.

same test as previously described in Section 8.3.2 in order to obtain an appropriate combination of R_1 and $\alpha = 10^{-2}$ that matches observed disc fractions as a function of cluster age. The results are shown in Figure 8.B.1. While Alexander & Pascucci (2012) considered EUV-dominated winds in their disc models, XPE yields more than two orders of magnitude higher wind mass loss rates. Combined with the stronger accretion onto the host star due to the higher viscosity, this would result in too short median disc lifetimes of $\lesssim 1$ Myr if $R_1 = 18$ au is used in our models. In combination with higher disc viscosities of $\alpha = 10^{-2}$, we found $R_1 = 100$ au to yield more realistic median disc lifetimes of 1–3 Myr.

Using these two sets of R_1 and α, we reran the `Owen_5au` models in order to test the effect of the viscosity parameter on the desert of planets that is observed in the L_x–a-distribution of giant planet systems. The results are shown in Figure 8.B.2. For the case of $R_1 = 18$ au and $\alpha = 10^{-2}$, the desert of planets that could be observed in the L_x–a-distribution of the `Owen_5au` model, has now mostly disappeared. Only towards $L_x \lesssim 10^{29}$ erg s^{-1} can a small desert of planets close to the insertion location of 5 au can be seen. This is, however, to be expected as with $R_1 = 18$ au most of the disc mass is concentrated relatively close to the host star. Combined with a large value of $\alpha = 10^{-2}$ for the disc viscosity, this would yield a viscous timescale of 4.8×10^4 yr at R_1, leading to the significantly faster accretion of the disc material onto the host star than compared to the `Owen_5au` model, for which $t_\nu = 7 \times 10^5$ yr. In this model, the discs would be accreted so quickly that already smaller X-ray luminosities of the star would suffice in order to disperse the discs via XPE, explaining why the void of planets has shifted towards lower values of L_x.

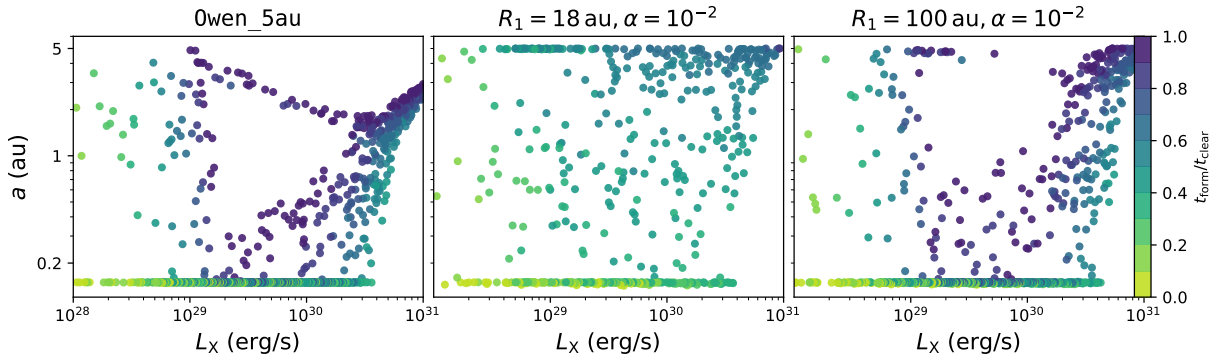

Figure 8.B.2: Comparison of the resulting L_x–a-distributions using different values for α and R_1. The left panel shows the `0wen_5au` using the default values of $\alpha = 6.9 \times 10^{-4}$ and $R_1 = 18\,\mathrm{au}$, while in the middle and right panels $R_1 = 18\,\mathrm{au}, \alpha = 10^{-2}$ and $R_1 = 100\,\mathrm{au}, \alpha = 10^{-2}$ were used.

In contrast, for $R_1 = 100\,\mathrm{au}$ and $\alpha = 10^{-2}$ a clearly confined desert of planets can be observed again. While it is located at approximately the same range of X-ray luminosities as in the `0wen_5au` model, its radial size is slightly decreased. This can be related to the different properties of the disc (e.g. different mass at a given radius and different viscosity) and the resulting different migration speed of the individual planets. Due to the higher viscosity, more planets will end up at the inner grid and possibly end up as hot Jupiters. Nevertheless, the effect of higher-mass planets being parked outside of the desert can also be observed for higher α in this case, even though with significantly reduced number density.

In conclusion, the evidence for an XPE-related desert of planets within the L_x–a-distribution of giant planets is not sensitive to the exact choice of the disc viscosity as long as the models reproduce the observed disc lifetimes in combination with viscous accretion and XPE.

8.C The effect of planet accretion on the gap location

In our 1D model, the mass-flow of the gap-crossing material is modelled following the prescription derived by Veras & Armitage (2004), which is based on 2D hydrodynamical simulations performed by Lubow et al. (1999) and D'Angelo et al. (2002):

$$\frac{\epsilon}{\epsilon_{\max}} \simeq 1.668 \left(\frac{M_p}{M_J}\right)^{1/3} \exp\left(-\frac{M_p}{1.5 M_J}\right) + 0.04. \tag{8.17}$$

Here, $\epsilon = \dot{M}_p/\dot{M}_{disc}$ describes the efficiency of mass accretion across the planetary gap that is, the ratio of the planetary accretion rate to the viscous disc accretion rate at large radii (Veras & Armitage, 2004). The parameter ϵ_{max} is an adjustable parameter that can be used to test the results' dependence on the efficiency of planetary accretion. In this work it was set to $\epsilon_{max} = 0.5$ to enable a direct comparison to previous work (Alexander & Pascucci, 2012; Ercolano & Rosotti, 2015; Jennings et al., 2018).

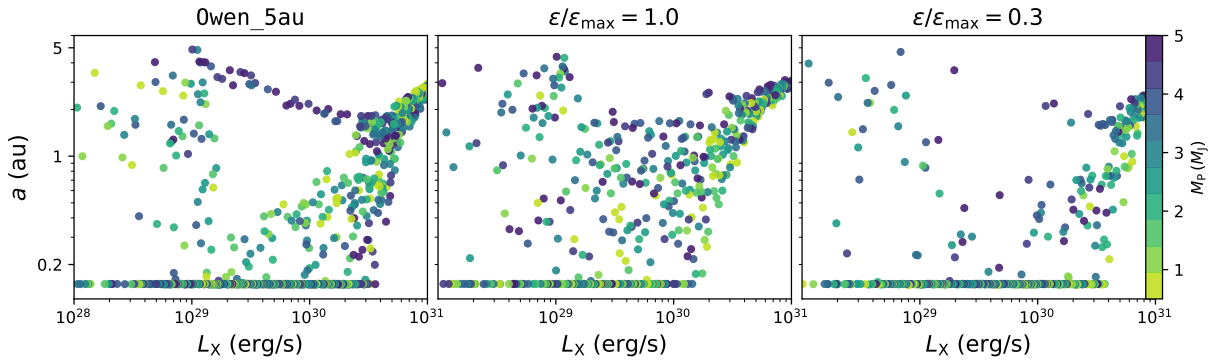

Figure 8.C.1: Comparison of the resulting L_X–a-distributions using different values for the planetary accretion efficiency. The left panel shows the default model using Eq. 8.17, while in the other two models, it was set to a constant value of $\epsilon/\epsilon_{max} = 1.0$ (centre) and $\epsilon/\epsilon_{max} = 0.3$ (right). The colour-coding represents the planet mass.

Alexander & Pascucci (2012) argue, however, that the accretion efficiency has the biggest impact on setting the final parking location of the planets in their model. We therefore ran different models based on the `Owen_5au` one, in which the accretion efficiency was set to a constant value of $\epsilon/\epsilon_{max} = 1$ and $\epsilon/\epsilon_{max} = 0.3$ as was tested by Alexander & Pascucci (2012). The resulting L_X–a-distributions are shown in Figure 8.C.1. For $\epsilon/\epsilon_{max} = 1$ (i.e. $M_p \approx 0.5\,M_J$), the void created by XPE shifts towards larger radii and has mostly disappeared due to the insertion of planets at 5 au. In contrast to the `Owen_5au` model, there is no significant difference in the radial distribution for planets of different masses, and the strong bifurcation between lower- and higher-mass giants that was observed previously has entirely disappeared. For $\epsilon/\epsilon_{max} = 0.3$ (i.e. $M_p \approx 2.5\,M_J$), most planets end up at the inner boundary. However, the desert of planets observed in the `Owen_5au` model can still be weakly surmised. This confirms that also our model is strongly dependent on the underlying planetary accretion prescription. Consequently, detailed hydrodynamical calculations of the accretion process of planets embedded in photoevaporating discs are required to provide more realistic prescriptions that can be implemented into 1D planet population synthesis approaches.

In contrast to the strong dependence on the planetary accretion prescription, Alexander & Pascucci (2012) only find a weak dependence on the planet mass and especially on their insertion location (i.e. the underlying assumption on where and when planets form). The latter conclusion is in contradiction with our results, but the discrepancy can be readily understood as their model only treats EUV-driven photoevaporation, for which the mass loss is mostly concentrated around the gravitational radius (i.e. ~ 1 au). Consequently the surface density at larger radii will be less strongly depleted compared to a disc irradiated by X-rays, for which the mass loss extends to much larger radii. In a purely EUV-irradiated disc, the final parking location of a planet inserted at 5 au or 10 au is therefore solely set by its unperturbed type II migration rates, which mostly depend on the local disc surface density and viscosity. Only once the planets reach the innermost parts of the disc, their migration tracks will be directly affected by photoevaporation. In contrast, planets embedded in a disc irradiated by X-ray dominated

winds will be subject to weaker gas torques already at the time of their formation, and therefore be parked at larger radii compared to a model assuming EUV-dominated winds.

Chapter 9

Final remarks

The last two decades have revolutionised the field of exoplanet science. Not only has our census of known exoworlds increased immensely, but we have also been incredibly successful in observing their nurseries – the planet-forming discs. With more and more data emerging, we are able to gather more insight into the underlying physical processes that are responsible for the statistical signatures we observe today. This recent wealth of observational data thereby finally allows us to test our theoretical models of planet formation and evolution to unprecedented precision. And more often than not we falsify theories, hence adding another piece into the big jigsaw puzzle that is modern astronomy.

Main results

Motivated by a prominent pile up of warm Jupiters between semi-major axes of $\sim$ 1–2 au, in **Chapter 6** we have proposed a scenario of X-ray photoevaporation-driven disc dispersal as a possible origin of the observed mountains and deserts in the demographics of gas giants. By assembling an extensive catalogue that contains the X-ray luminosities of giant planet host stars, and correlating those with the semi-major axis distribution of their giant planets, we could identify an under-density of planets in the L_x–a-plane, roughly centred on $(L_x, a) \approx (10^{28}\,\mathrm{erg\,s^{-1}}, 0.2\,\mathrm{au})$. While this desert could be qualitatively explained as a consequence of disc dispersal via X-ray-driven photoevaporation, which stops giant planet migration at a given place in the disc and for a given range of X-ray luminosities, its statistical significance could not be proven with the data set available at that time. The statistical tests performed on this data showed that unless the size and location of this feature are known a priori, a significant increase in observational data points would be required in order to statistically prove the existence of a desert.

In further theoretical work, we have then attempted to use theoretical models of planet-disc interactions to better constrain the expected morphology of the desert in the L_x–a-plane. During this process, we have identified several shortcomings in the current state-of-the-art numerical models. In **Chapter 7**, we have performed an extensive comparison between 1D and 2D treatments of type II migration in evolving protoplanetary discs, in order to test the

accuracy of simplified treatments with more realistic, higher-dimensional models. We found that the impulse approximation in 1D can roughly reproduce the migration history of giant planets embedded in primordial discs as is predicted by more complex 2D simulations. Despite some quantitative differences, the effect on large population synthesis models is not expected to be a dominant modelling systematic. This changes, however, for the case of transition discs with evacuated inner cavities, in which the 1D models generally predict higher migration rates, while 2D simulations of equivalent system show that the inward migration is effectively stopped once the material inside the planetary orbit is cleared. Finally, we proposed improvements and revised recipes for planetary migration rates calculated by the impulse approximation, that would enhance the predictive power of 1D population synthesis calculations of planets in evolving protoplanetary discs.

In **Chapter 8**, we performed a large set of detailed 1D planet population synthesis calculations in order to quantify the impact of the disc dispersal phase on the semi-major axis distribution of a population of giant planets. We confirmed the suggestion made in Chapter 6 that this process can indeed leave a characteristic under-density, or desert of planets in the semi-major axis versus host star X-ray luminosity plane. The location and especially the size of this desert is, however, strongly dependent on the choice of the initial conditions that are employed in the 1D model, thus impeding a direct comparison to the observational catalogue presented in Chapter 6.

Conclusion

Piece by piece we have established that X-ray-driven photoevaporation is indeed expected to leave a distinct imprint in the semi-major axis distribution of giant planets, which may potentially explain the observed pile-up of Jupiter-mass planets close to $\sim 1\,\mathrm{au}$. However, our current models are still unable to make more quantitative statements, as they are extremely sensitive on the underlying simplifications and assumptions made. A definitive proof of the void in the L_x–a-distribution would mean that, statistically, the location of gas giants in a planetary system is set during the time of planet formation and migration inside the planet-forming disc, and that successive dynamical interaction after its dispersal only have a small effect on setting the final architecture of a planetary system.

Future work

Thus, global population synthesis models including a self-consistent treatment of planet formation and realistic disc dispersal mechanisms that may reduce this degeneracy are urgently needed in order to get a more quantitative understanding of the power of X-ray-driven photoevaporation on setting the final parking locations of giant planets. Future work should therefore focus on implementing modern prescriptions of internal photoevaporation into global population synthesis approaches. However, these models should also improve on the prescriptions that are used for different physical effects, as we have shown that simplified treatments of more complex processes can result in significantly distorted conclusions. Another important aspect is to investigate in detail the evolution of the stellar magnetic activity as a function of time,

both during and after the disc-locking phase. The decrease in X-ray luminosities may not only have a profound effect on the dispersal of the disc, and therefore on the final parking location of giant planets, but it may also significantly impact both the chemistry as well as the dispersal of planetary atmospheres.

Observationally, several improvements can be expected in the near future. Not only is our census of known exoplanets steadily increasing, but it is especially increasing for planet around *young* stars, which are still magnetically active, and thus X-ray bright. Strong stellar activity is impeding the identification of RV-signals within the stellar spectrum, especially those of lower-mass or distant planets. Thus, increasing our census of planets around these X-ray bright stars is of particularly high value to decreasing the selection effects that are present in the observed L_{x}–a-distribution of giant planets. Further, it is to be expected that many of the newly discovered planet hosts will have X-ray counterparts detected by *Chandra*, *XMM-Newton* or ROSAT, and in particular by the recently launched eROSITA-satellite. An increased dataset will allow us to reevaluate the statistical significance of the observed gap, consequently enabling us to accurately test theories of stellar photoevaporation and its influence on the dispersal of their surrounding discs. This will significantly improve our understanding of the underlying physical processes that shape the architecture of planetary systems.

List of Acronyms

Acronym	Full name
Telescopes:	
ALMA	Atacama Large Millimeter/submillimeter Array
HST	*Hubble* Space Telescope
eROSITA	Extended Roentgen Survey with an Imaging Telescope Array
IRAS	Infrared Astronomical Satellite
JWST	*James Webb* Space Telescope
PLATO	Planetary Transits and Oscillations of stars
ROSAT	Röntgensatellit
SPHERE	Spectro-Polarimetric High-contrast Exoplanet REsearch
TESS	Transiting Exoplanet Survey Satellite
VLT	Very Large Telescope
Spectral ranges:	
EUV	extreme-ultraviolet
fIR	far-infrared
FUV	far-ultraviolet
IR	infrared
mm	millimeter
mIR	mid-infrared
nIR	near-infrared
XEUV	soft X-rays including EUV
Other:	
AGN	Active galactic nucleus
HRD	Hertzsprung-Russel diagram
ISM	Interstellar medium
MRI	Magneto-rotational instability
PMS	Pre-main sequence

PAH	Polycyclic aromatic hydrocarbon
SED	Spectral energy distribution
TD	Transition disc
VSI	Vertical shear instability
XPE	X-ray-driven photoevaporation
YSO	Young stellar object
ZAMS	Zero-age main sequence

List of (Astro-)Physical constants

Name	Symbol	Number	CGS-Unit
Physical constants:			
Boltzmann constant	k	1.381×10^{-16}	$\mathrm{erg\,K^{-1}}$
Electron volt	eV	1.602×10^{-12}	erg
Gravitational constant	G	6.67×10^{-8}	$\mathrm{cm^3\,g^{-1}\,s^{-2}}$
Hydrogen atom mass	m_H	1.6733×10^{-24}	g
Planck constant	h	6.626×10^{-27}	erg s
Proton mass	m_p	1.6726×10^{-24}	g
Speed of light	c	2.998×10^{-10}	$\mathrm{cm\,s^{-1}}$
Astrophysical constants:			
Astronomical unit	au	1.496×10^{13}	cm
Earth mass	$M_\oplus$	5.974×10^{27}	g
Jupiter mass	M_J	1.899×10^{30}	g
Parsec	pc	3.086×10^{18}	cm
Solar mass	$M_\odot$	1.989×10^{33}	g
Solar radius	$R_\odot$	6.963×10^{10}	cm

List of publications

Monsch K., Picogna G., Ercolano B., Preibisch T. (2021): "The imprint of X-ray photoevaporation of planet-forming discs on the orbital distribution of giant planets: II. Theoretical Predicstions", *Astronomy & Astrophysics*, 650:A199

Monsch K., Picogna G., Ercolano B., Kley W. (2021): "Giant planet migration during the disc dispersal phase", *Astronomy & Astrophysics*, 646:A169

Günther H. M., Principe D. A., Melis C., **Monsch K.**, Schneider P. C., Czesla, S., Wright N. J., Kashyap V. L., Schmitt J. H. M. M., Newton E. R., Drake J. J., Huenemoerder D. P.(2019): "White paper for Chandra cool attitude targets (CAT): Stellar activity with TESS and Chandra", *arXiv:1903.01547*

Monsch K., Ercolano B., Picogna G., Preibisch T., Rau M. M. (2019): "The imprint of X-ray photoevaporation of planet-forming discs on the orbital distribution of giant planets", *Monthly Notices of the Royal Astronomical Society*, 483:3448

Monsch K., Pineda J., Liu H. B., Zucker, C., How-Huan Chen, H., Pattle, K., Offner, S. S. R., Di Francesco, J., Ginsburg, A., Ercolano, B., Arce, H. G., Friesen, R., Kirk, H., Caselli, P., Goodman, A. A. (2018): "Dense gas kinematics and a narrow filament in the Orion A OMC 1 region using NH_3", *The Astrophysical Journal*, 861:77

Bibliography

Adams, F. C., Hollenbach, D., Laughlin, G., & Gorti, U. 2004, Photoevaporation of Circumstellar Disks Due to External Far-Ultraviolet Radiation in Stellar Aggregates, *The Astrophysical Journal*, **611**:360–379

Adams, F. C., Lada, C. J., & Shu, F. H. 1987, Spectral Evolution of Young Stellar Objects, *The Astrophysical Journal*, **312**:788

Alexander, F., & Preibisch, T. 2012, X-ray activity and rotation of the young stars in IC 348, *Astronomy and Astrophysics*, **539**:A64

Alexander, R., Pascucci, I., Andrews, S., Armitage, P., & Cieza, L. 2014, The Dispersal of Protoplanetary Disks, in *Protostars and Planets VI*, p. 475

Alexander, R. D., & Armitage, P. J. 2007, Dust dynamics during protoplanetary disc clearing, *Monthly Notices of the Royal Astronomical Society*, **375**:500–512

Alexander, R. D., & Armitage, P. J. 2009, Giant Planet Migration, Disk Evolution, and the Origin of Transitional Disks, *The Astrophysical Journal*, **704**:989–1001

Alexander, R. D., Clarke, C. J., & Pringle, J. E. 2004a, On the origin of ionizing photons emitted by T Tauri stars, *Monthly Notices of the Royal Astronomical Society*, **348**:879–884

Alexander, R. D., Clarke, C. J., & Pringle, J. E. 2004b, The effects of X-ray photoionization and heating on the structure of circumstellar discs, *Monthly Notices of the Royal Astronomical Society*, **354**:71–80

Alexander, R. D., Clarke, C. J., & Pringle, J. E. 2006a, Photoevaporation of protoplanetary discs - I. Hydrodynamic models, *Monthly Notices of the Royal Astronomical Society*, **369**:216–228

Alexander, R. D., Clarke, C. J., & Pringle, J. E. 2006b, Photoevaporation of protoplanetary discs - II. Evolutionary models and observable properties, *Monthly Notices of the Royal Astronomical Society*, **369**:229–239

Alexander, R. D., & Pascucci, I. 2012, Deserts and pile-ups in the distribution of exoplanets due to photoevaporative disc clearing, *Monthly Notices of the Royal Astronomical Society*, **422**:82–86

ALMA Partnership, Brogan, C. L., Pérez, L. M., et al. 2015, The 2014 ALMA Long Baseline Campaign: First Results from High Angular Resolution Observations toward the HL Tau Region, *The Astrophysical Journal Letters*, **808**:L3

Ananyeva, V. I., Ivanova, A. E., Venkstern, A. A., et al. 2020, Mass distribution of exoplanets considering some observation selection effects in the transit detection technique, *Icarus*, **346**:113773

Anderson, K. R., & Lai, D. 2017, Moderately eccentric warm Jupiters from secular interactions with exterior companions, *Monthly Notices of the Royal Astronomical Society*, **472**:3692–3705

Andre, P., & Montmerle, T. 1994, From T Tauri Stars to Protostars: Circumstellar Material and Young Stellar Objects in the rho Ophiuchi Cloud, *The Astrophysical Journal*, **420**:837

Andre, P., Ward-Thompson, D., & Barsony, M. 1993, Submillimeter Continuum Observations of rho Ophiuchi A: The Candidate Protostar VLA 1623 and Prestellar Clumps, *The Astrophysical Journal*, **406**:122

Andrews, S. M. 2020, Observations of Protoplanetary Disk Structures, *Annual Review of Astronomy and Astrophysics*, **58**:483–528

Andrews, S. M., & Williams, J. P. 2005, Circumstellar Dust Disks in Taurus-Auriga: The Submillimeter Perspective, *The Astrophysical Journal*, **631**:1134–1160

Andrews, S. M., & Williams, J. P. 2007, A Submillimeter View of Circumstellar Dust Disks in ρ Ophiuchi, *The Astrophysical Journal*, **671**:1800–1812

Andrews, S. M., Wilner, D. J., Espaillat, C., et al. 2011, Resolved Images of Large Cavities in Protoplanetary Transition Disks, *The Astrophysical Journal*, **732**:42

Andrews, S. M., Wilner, D. J., Hughes, A. M., Qi, C., & Dullemond, C. P. 2009, Protoplanetary Disk Structures in Ophiuchus, *The Astrophysical Journal*, **700**:1502–1523

Andrews, S. M., Wilner, D. J., Hughes, A. M., Qi, C., & Dullemond, C. P. 2010, Protoplanetary Disk Structures in Ophiuchus. II. Extension to Fainter Sources, *The Astrophysical Journal*, **723**:1241–1254

Andrews, S. M., Wilner, D. J., Zhu, Z., et al. 2016, Ringed Substructure and a Gap at 1 au in the Nearest Protoplanetary Disk, *The Astrophysical Journal Letters*, **820**:L40

Andrews, S. M., Huang, J., Pérez, L. M., et al. 2018, The Disk Substructures at High Angular Resolution Project (DSHARP). I. Motivation, Sample, Calibration, and Overview, *The Astrophysical Journal Letters*, **869**:L41

Apai, D. A., & Lauretta, D. S. 2010, Protoplanetary Dust: Astrophysical and Cosmochemical Perspectives

Armitage, P. J. 2007a, Lecture notes on the formation and early evolution of planetary systems, *arXiv e-prints*, arXiv:astro-ph/0701485

Armitage, P. J. 2007b, Massive Planet Migration: Theoretical Predictions and Comparison with Observations, *The Astrophysical Journal*, **665**:1381–1390

Armitage, P. J. 2011, Dynamics of Protoplanetary Disks, *Annual Review of Astronomy and Astrophysics*, **49**:195–236

Armitage, P. J. 2013, Astrophysics of Planet Formation

Armitage, P. J., Livio, M., Lubow, S. H., & Pringle, J. E. 2002, Predictions for the frequency and orbital radii of massive extrasolar planets, *Monthly Notices of the Royal Astronomical Society*, **334**:248–256

Bai, X.-N. 2016, Towards a Global Evolutionary Model of Protoplanetary Disks, *The Astrophysical Journal*, **821**:80

Bai, X.-N., & Goodman, J. 2009, Heat and Dust in Active Layers of Protostellar Disks, *The Astrophysical Journal*, **701**:737–755

Bai, X.-N., & Stone, J. M. 2013, Wind-driven Accretion in Protoplanetary Disks. I. Suppression of the Magnetorotational Instability and Launching of the Magnetocentrifugal Wind, *The Astrophysical Journal*, **769**:76

Bailer-Jones, C. A. L., Rybizki, J., Fouesneau, M., Mantelet, G., & Andrae, R. 2018, Estimating Distance from Parallaxes. IV. Distances to 1.33 Billion Stars in Gaia Data Release 2, *Astronomical Journal*, **156**:58

Balbus, S. A., & Hawley, J. F. 1991, A Powerful Local Shear Instability in Weakly Magnetized Disks. I. Linear Analysis, *The Astrophysical Journal*, **376**:214

Ballerini, P., Micela, G., Lanza, A. F., & Pagano, I. 2012, Multiwavelength flux variations induced by stellar magnetic activity: effects on planetary transits, *Astronomy and Astrophysics*, **539**:A140

Barclay, T., Pepper, J., & Quintana, E. V. 2018, A Revised Exoplanet Yield from the Transiting Exoplanet Survey Satellite (TESS), *Astrophysical Journal Supplement Series*, **239**:2

Batalha, N. M. 2014, Exploring exoplanet populations with NASA's Kepler Mission, *Proceedings of the National Academy of Science*, **111**:12647–12654

Batygin, K., Bodenheimer, P. H., & Laughlin, G. P. 2016, In Situ Formation and Dynamical Evolution of Hot Jupiter Systems, *The Astrophysical Journal*, **829**:114

Beckwith, S. V. W., Sargent, A. I., Chini, R. S., & Guesten, R. 1990, A Survey for Circumstellar Disks around Young Stellar Objects, *Astronomical Journal*, **99**:924

Benisty, M., Juhasz, A., Boccaletti, A., et al. 2015, Asymmetric features in the protoplanetary disk MWC 758, *Astronomy and Astrophysics*, **578**:L6

Benisty, M., Stolker, T., Pohl, A., et al. 2017, Shadows and spirals in the protoplanetary disk HD 100453, *Astronomy and Astrophysics*, **597**:A42

Benítez-Llambay, P., & Pessah, M. E. 2018, Torques Induced by Scattered Pebble-flow in Protoplanetary Disks, *The Astrophysical Journal Letters*, **855**:L28

Benz, W., Ida, S., Alibert, Y., Lin, D., & Mordasini, C. 2014, Planet Population Synthesis, in *Protostars and Planets VI*, p. 691

Bergin, E. A., & Tafalla, M. 2007, Cold Dark Clouds: The Initial Conditions for Star Formation, *Annual Review of Astronomy and Astrophysics*, **45**:339–396

Biddle, L. I., Johns-Krull, C. M., Llama, J., Prato, L., & Skiff, B. A. 2018, K2 Reveals Pulsed Accretion Driven by the 2 Myr Old Hot Jupiter CI Tau b, *The Astrophysical Journal Letters*, **853**:L34

Bildsten, L., Brown, E. F., Matzner, C. D., & Ushomirsky, G. 1997, Lithium Depletion in Fully Convective Pre-Main-Sequence Stars, *The Astrophysical Journal*, **482**:442–447

Birnstiel, T., & Andrews, S. M. 2014, On the Outer Edges of Protoplanetary Dust Disks, *The Astrophysical Journal*, **780**:153

Bitsch, B., Izidoro, A., Johansen, A., et al. 2019, Formation of planetary systems by pebble accretion and migration: growth of gas giants, *Astronomy and Astrophysics*, **623**:A88

Bitsch, B., Lambrechts, M., & Johansen, A. 2015, The growth of planets by pebble accretion in evolving protoplanetary discs, *Astronomy and Astrophysics*, **582**:A112

Bodenheimer, P. 1965, Studies in Stellar Evolution. II. Lithium Depletion during the Pre-Main Contraction., *The Astrophysical Journal*, **142**:451

Boisse, I., Bouchy, F., Hébrard, G., et al. 2011, Disentangling between stellar activity and planetary signals, *Astronomy and Astrophysics*, **528**:A4

Boley, A. C., Granados Contreras, A. P., & Gladman, B. 2016, The In Situ Formation of Giant Planets at Short Orbital Periods, *The Astrophysical Journal Letters*, **817**:L17

Boller, T., Freyberg, M. J., Trümper, J., et al. 2016, Second ROSAT all-sky survey (2RXS) source catalogue, *Astronomy and Astrophysics*, **588**:A103

Bond, J. C., Tinney, C. G., Butler, R. P., et al. 2006, The abundance distribution of stars with planets, *Monthly Notices of the Royal Astronomical Society*, **370**:163–173

Borucki, W. J., Scargle, J. D., & Hudson, H. S. 1985, Detectability of extrasolar planetary transits, *The Astrophysical Journal*, **291**:852–854

Borucki, W. J., Koch, D., Basri, G., et al. 2010, Kepler Planet-Detection Mission: Introduction and First Results, *Science*, **327**:977–980

Boss, A. P. 1997, Giant planet formation by gravitational instability., *Science*, **276**:1836–1839

Boss, A. P. 2011, Formation of Giant Planets by Disk Instability on Wide Orbits Around Protostars with Varied Masses, *The Astrophysical Journal*, **731**:74

Bouvier, J., Alencar, S. H. P., Harries, T. J., Johns-Krull, C. M., & Romanova, M. M. 2007, Magnetospheric Accretion in Classical T Tauri Stars, in *Protostars and Planets V*, p. 479

Bowler, B. P. 2016, Imaging Extrasolar Giant Planets, *Publications of the Astronomical Society of the Pacific*, **128**:102001

Briceño, C., Luhman, K. L., Hartmann, L., Stauffer, J. R., & Kirkpatrick, J. D. 2002, The Initial Mass Function in the Taurus Star-forming Region, *The Astrophysical Journal*, **580**:317–335

Briggs, K. R., Güdel, M., Telleschi, A., et al. 2007, The X-ray activity-rotation relation of T Tauri stars in Taurus-Auriga, *Astronomy and Astrophysics*, **468**:413–424

Broos, P. S., Feigelson, E. D., Townsley, L. K., et al. 2007, The Young Stellar Population in M17 Revealed by Chandra, *Astrophysical Journal Supplement Series*, **169**:353–385

Brun, A. S., & Browning, M. K. 2017, Magnetism, dynamo action and the solar-stellar connection, *Living Reviews in Solar Physics*, **14**:4

Bryan, M. L., Knutson, H. A., Howard, A. W., et al. 2016, Statistics of Long Period Gas Giant Planets in Known Planetary Systems, *The Astrophysical Journal*, **821**:89

Buchhave, L. A., Latham, D. W., Johansen, A., et al. 2012, An abundance of small exoplanets around stars with a wide range of metallicities, *Nature*, **486**:375–377

Burkert, A., & Bodenheimer, P. 2000, Turbulent Molecular Cloud Cores: Rotational Properties, *The Astrophysical Journal*, **543**:822–830

Calvet, N., & Gullbring, E. 1998, The Structure and Emission of the Accretion Shock in T Tauri Stars, *The Astrophysical Journal*, **509**:802–818

Calvet, N., Hartmann, L., & Strom, S. E. 2000, Evolution of Disk Accretion, in *Protostars and Planets IV*, p. 377

Cameron, A. G. W., Decampli, W. M., & Bodenheimer, P. 1982, Evolution of giant gaseous protoplanets embedded in the primitive solar nebula, *Icarus*, **49**:298–312

Carrera, D., Davies, M. B., & Johansen, A. 2018, Towards an initial mass function for giant planets, *Monthly Notices of the Royal Astronomical Society*, **478**:961–970

Carrera, D., Gorti, U., Johansen, A., & Davies, M. B. 2017, Planetesimal Formation by the Streaming Instability in a Photoevaporating Disk, *The Astrophysical Journal*, **839**:16

Carrera, F. J., Ebrero, J., Mateos, S., et al. 2007, The XMM-Newton serendipitous survey. III. The AXIS X-ray source counts and angular clustering, *Astronomy and Astrophysics*, **469**:27–46

Cassan, A., Kubas, D., Beaulieu, J. P., et al. 2012, One or more bound planets per Milky Way star from microlensing observations, *Nature*, **481**:167–169

Chambers, J. 2019, An Analytic Model for an Evolving Protoplanetary Disk with a Disk Wind, *The Astrophysical Journal*, **879**:98

Charbonneau, D., Brown, T. M., Latham, D. W., & Mayor, M. 2000, Detection of Planetary Transits Across a Sun-like Star, *The Astrophysical Journal Letters*, **529**:L45–L48

Chiang, E. I., & Goldreich, P. 1997, Spectral Energy Distributions of T Tauri Stars with Passive Circumstellar Disks, *The Astrophysical Journal*, **490**:368–376

Cieza, L., & Baliber, N. 2007, Testing the Disk Regulation Paradigm with Spitzer Observations. II. A Clear Signature of Star-Disk Interaction in NGC 2264 and the Orion Nebula Cluster, *The Astrophysical Journal*, **671**:605–615

Cieza, L., Padgett, D. L., Stapelfeldt, K. R., et al. 2007, The Spitzer c2d Survey of Weak-Line T Tauri Stars. II. New Constraints on the Timescale for Planet Building, *The Astrophysical Journal*, **667**:308–328

Cieza, L. A., González-Ruilova, C., Hales, A. S., et al. 2020, The Ophiuchus DIsc Survey Employing ALMA (ODISEA) – III. The evolution of substructures in massive discs at 3–5 au resolution, *Monthly Notices of the Royal Astronomical Society*, **501**:2934–2953

Clarke, C. 2011, The Dispersal of Disks around Young Stars, in *Physical Processes in Circumstellar Disks around Young Stars*, pp. 355–418

Clarke, C. J., Gendrin, A., & Sotomayor, M. 2001, The dispersal of circumstellar discs: the role of the ultraviolet switch, *Monthly Notices of the Royal Astronomical Society*, **328**:485–491

Coleman, G. A. L., & Nelson, R. P. 2014, On the formation of planetary systems via oligarchic growth in thermally evolving viscous discs, *Monthly Notices of the Royal Astronomical Society*, **445**:479–499

Cumming, A., Butler, R. P., Marcy, G. W., et al. 2008, The Keck Planet Search: Detectability and the Minimum Mass and Orbital Period Distribution of Extrasolar Planets, *Publications of the Astronomical Society of the Pacific*, **120**:531

Dai, X., & Guerras, E. 2018, Probing Extragalactic Planets Using Quasar Microlensing, *The Astrophysical Journal Letters*, **853**:L27

D'Alessio, P., Calvet, N., & Hartmann, L. 2001, Accretion Disks around Young Objects. III. Grain Growth, *The Astrophysical Journal*, **553**:321–334

D'Alessio, P., Calvet, N., Hartmann, L., Muzerolle, J., & Sitko, M. 2004, Models of Accretion Disks Around Young Stars, in *Star Formation at High Angular Resolution, Vol. 221*, p. 403

D'Alessio, P., Cantö, J., Calvet, N., & Lizano, S. 1998, Accretion Disks around Young Objects. I. The Detailed Vertical Structure, *The Astrophysical Journal*, **500**:411–427

D'Alessio, P., Hartmann, L., Calvet, N., et al. 2005, The Truncated Disk of CoKu Tau/4, *The Astrophysical Journal*, **621**:461–472

Damiano, M., Hu, R., & Hildebrandt, S. R. 2020, Multi-orbital-phase and Multiband Characterization of Exoplanetary Atmospheres with Reflected Light Spectra, *The Astronomical Journal*, **160**:206

D'Angelo, G., Henning, T., & Kley, W. 2002, Nested-grid calculations of disk-planet interaction, *Astronomy and Astrophysics*, **385**:647–670

D'Angelo, G., & Lissauer, J. J. 2018, Formation of Giant Planets, in *Handbook of Exoplanets*, p. 140

D'Angelo, G., & Lubow, S. H. 2010, Three-dimensional Disk-Planet Torques in a Locally Isothermal Disk, *The Astrophysical Journal*, **724**:730–747

Dawson, R. I., & Chiang, E. 2014, A class of warm Jupiters with mutually inclined, apsidally misaligned close friends, *Science*, **346**:212–216

Dawson, R. I., & Johnson, J. A. 2018, Origins of Hot Jupiters, *Annual Review of Astronomy and Astrophysics*, **56**:175–221

Deeg, H. J., & Alonso, R. 2018, Transit Photometry as an Exoplanet Discovery Method, in *Handbook of Exoplanets*

Dempsey, A. M., Lee, W.-K., & Lithwick, Y. 2020, Pileups and Migration Rates for Planets in Low-mass Disks, *The Astrophysical Journal*, **891**:108

Dipierro, G., & Laibe, G. 2017, An opening criterion for dust gaps in protoplanetary discs, *Monthly Notices of the Royal Astronomical Society*, **469**:1932–1948

Donati, J. F., Moutou, C., Malo, L., et al. 2016, A hot Jupiter orbiting a 2-million-year-old solar-mass T Tauri star, *Nature*, **534**:662–666

Dong, R., Liu, S.-y., Eisner, J., et al. 2018, The Eccentric Cavity, Triple Rings, Two-armed Spirals, and Double Clumps of the MWC 758 Disk, *The Astrophysical Journal*, **860**:124

Draine, B. T. 2003, Interstellar Dust Grains, *Annual Review of Astronomy and Astrophysics*, **41**:241–289

Draine, B. T. 2006, On the Submillimeter Opacity of Protoplanetary Disks, *The Astrophysical Journal*, **636**:1114–1120

Drake, S. 2003, Galileo at Work: His Scientific Biography, Dover phoenix editions (Dover Publications), p. 153

Drazin, P., & Reid, W. 1981, Hydrodynamic Stability, Cambridge Monographs on Mechanics (Cambridge University Press)

Dressing, C. D., & Charbonneau, D. 2013, The Occurrence Rate of Small Planets around Small Stars, *The Astrophysical Journal*, **767**:95

Drążkowska, J., Alibert, Y., & Moore, B. 2016, Close-in planetesimal formation by pile-up of drifting pebbles, *Astronomy and Astrophysics*, **594**:A105

Duffell, P. C., & Chiang, E. 2015, Eccentric Jupiters via Disk-Planet Interactions, *The Astrophysical Journal*, **812**:94

Duffell, P. C., Haiman, Z., MacFadyen, A. I., dOrazio, D. J., & Farris, B. D. 2014, The Migration of Gap-opening Planets is Not Locked to Viscous Disk Evolution, *The Astrophysical Journal Letters*, **792**:L10

Dullemond, C. P., Dominik, C., & Natta, A. 2001, Passive Irradiated Circumstellar Disks with an Inner Hole, *The Astrophysical Journal*, **560**:957–969

Dullemond, C. P., Hollenbach, D., Kamp, I., & D'Alessio, P. 2007, Models of the Structure and Evolution of Protoplanetary Disks, in *Protostars and Planets V*, p. 555

Dullemond, C. P., van Zadelhoff, G. J., & Natta, A. 2002, Vertical structure models of T Tauri and Herbig Ae/Be disks, *Astronomy and Astrophysics*, **389**:464–474

Dürmann, C., & Kley, W. 2015, Migration of massive planets in accreting disks, *Astronomy and Astrophysics*, **574**:A52

Economist, T. 2016, How to find exoplanets, *The Economist Group Limited*, [online; accessed 18 June 2021]

Emsenhuber, A., Mordasini, C., Burn, R., et al. 2020, The New Generation Planetary Population Synthesis (NGPPS). I. Bern global model of planet formation and evolution, model tests, and emerging planetary systems, *arXiv e-prints*, arXiv:2007.05561

Ercolano, B., Clarke, C. J., & Drake, J. J. 2009a, X-Ray Irradiated Protoplanetary Disk Atmospheres. II. Predictions from Models in Hydrostatic Equilibrium, *The Astrophysical Journal*, **699**:1639–1649

Ercolano, B., Clarke, C. J., & Hall, A. C. 2011, The clearing of discs around late-type T Tauri stars: constraints from the infrared two-colour plane, *Monthly Notices of the Royal Astronomical Society*, **410**:671–678

Ercolano, B., Clarke, C. J., & Robitaille, T. P. 2009b, The transition disc frequency in M stars, *Monthly Notices of the Royal Astronomical Society*, **394**:L141–L145

Ercolano, B., Drake, J. J., Raymond, J. C., & Clarke, C. C. 2008, X-Ray-Irradiated Protoplanetary Disk Atmospheres. I. Predicted Emission-Line Spectrum and Photoevaporation, *The Astrophysical Journal*, **688**:398–407

Ercolano, B., Koepferl, C., Owen, J., & Robitaille, T. 2015, Far-infrared signatures and inner hole sizes of protoplanetary discs undergoing inside-out dust dispersal, *Monthly Notices of the Royal Astronomical Society*, **452**:3689–3695

Ercolano, B., & Pascucci, I. 2017, The dispersal of planet-forming discs: theory confronts observations, *Royal Society Open Science*, **4**:170114

Ercolano, B., & Rosotti, G. 2015, The link between disc dispersal by photoevaporation and the semimajor axis distribution of exoplanets, *Monthly Notices of the Royal Astronomical Society*, **450**:3008–3014

Ercolano, B., Rosotti, G. P., Picogna, G., & Testi, L. 2017, A photoevaporative gap in the closest planet-forming disc, *Monthly Notices of the Royal Astronomical Society*, **464**:L95–L99

Ercolano, B., Weber, M. L., & Owen, J. E. 2018, Accreting transition discs with large cavities created by X-ray photoevaporation in C and O depleted discs, *Monthly Notices of the Royal Astronomical Society*, **473**:L64–L68

Evans, Neal J., I. 1999, Physical Conditions in Regions of Star Formation, *Annual Review of Astronomy and Astrophysics*, **37**:311–362

Evans, Neal J., I., Dunham, M. M., Jørgensen, J. K., et al. 2009, The Spitzer c2d Legacy Results: Star-Formation Rates and Efficiencies; Evolution and Lifetimes, *Astrophysical Journal Supplement Series*, **181**:321–350

Facchini, S., Clarke, C. J., & Bisbas, T. G. 2016, External photoevaporation of protoplanetary discs in sparse stellar groups: the impact of dust growth, *Monthly Notices of the Royal Astronomical Society*, **457**:3593–3610

Favata, F., & Micela, G. 2003, Stellar Coronal Astronomy, *Space Science Reviews*, **108**:577–708

Fedele, D., van den Ancker, M. E., Henning, T., Jayawardhana, R., & Oliveira, J. M. 2010, Timescale of mass accretion in pre-main-sequence stars, *Astronomy and Astrophysics*, **510**:A72

Feigelson, E., Townsley, L., Güdel, M., & Stassun, K. 2007, X-Ray Properties of Young Stars and Stellar Clusters, in *Protostars and Planets V*, p. 313

Feigelson, E. D., Broos, P., Gaffney, James A., I., et al. 2002, X-Ray-emitting Young Stars in the Orion Nebula, *The Astrophysical Journal*, **574**:258–292

Feigelson, E. D., & Montmerle, T. 1999, High-Energy Processes in Young Stellar Objects, *Annual Review of Astronomy and Astrophysics*, **37**:363–408

Feigelson, E. D., Hornschemeier, A. E., Micela, G., et al. 2004, The Chandra Deep Field-North Survey. XVII. Evolution of Magnetic Activity in Old Late-Type Stars, *The Astrophysical Journal*, **611**:1107–1120

Feng, Y. K., Robinson, T. D., Fortney, J. J., et al. 2018, Characterizing Earth Analogs in Reflected Light: Atmospheric Retrieval Studies for Future Space Telescopes, *The Astronomical Journal*, **155**:200

Fernandes, R. B., Mulders, G. D., Pascucci, I., Mordasini, C., & Emsenhuber, A. 2019, Hints for a Turnover at the Snow Line in the Giant Planet Occurrence Rate, *The Astrophysical Journal*, **874**:81

Fischer, D. A., & Valenti, J. 2005, The Planet-Metallicity Correlation, *The Astrophysical Journal*, **622**:1102–1117

Fischer, D. A., Anglada-Escude, G., Arriagada, P., et al. 2016, State of the Field: Extreme Precision Radial Velocities, *Publications of the Astronomical Society of the Pacific*, **128**:066001

Flaccomio, E., Damiani, F., Micela, G., et al. 2003, Chandra X-Ray Observation of the Orion Nebula Cluster. II. Relationship between X-Ray Activity Indicators and Stellar Parameters, *The Astrophysical Journal*, **582**:398–409

Flaherty, K., Hughes, A. M., Simon, J. B., et al. 2020, Measuring Turbulent Motion in Planet-forming Disks with ALMA: A Detection around DM Tau and Nondetections around MWC 480 and V4046 Sgr, *The Astrophysical Journal*, **895**:109

Flaherty, K. M., Hughes, A. M., Teague, R., et al. 2018, Turbulence in the TW Hya Disk, *The Astrophysical Journal*, **856**:117

Font, A. S., McCarthy, I. G., Johnstone, D., & Ballantyne, D. R. 2004, Photoevaporation of Circumstellar Disks around Young Stars, *The Astrophysical Journal*, **607**:890–903

Forbes, J. C., & Loeb, A. 2019, On the Existence of Brown Dwarfs More Massive than the Hydrogen Burning Limit, *The Astrophysical Journal*, **871**:227

Forbrich, J., Preibisch, T., Menten, K. M., et al. 2007, Simultaneous X-ray, radio, near-infrared, and optical monitoring of young stellar objects in the Coronet cluster, *Astronomy and Astrophysics*, **464**:1003–1013

Forgan, D. H., Hall, C., Meru, F., & Rice, W. K. M. 2018, Towards a population synthesis model of self-gravitating disc fragmentation and tidal downsizing II: the effect of fragment-fragment interactions, *Monthly Notices of the Royal Astronomical Society*, **474**:5036–5048

Francis, L., & van der Marel, N. 2020, Dust-depleted Inner Disks in a Large Sample of Transition Disks through Long-baseline ALMA Observations, *The Astrophysical Journal*, **892**:111

Franz, R., Picogna, G., Ercolano, B., & Birnstiel, T. 2020, Dust entrainment in photoevaporative winds: The impact of X-rays, *Astronomy and Astrophysics*, **635**:A53

Fruscione, A., McDowell, J. C., Allen, G. E., et al. 2006, CIAO: Chandra's data analysis system, in *Society of Photo-Optical Instrumentation Engineers (SPIE) Conference Series, Vol. 6270*, p. 62701V

Fulton, B. J., Petigura, E. A., Howard, A. W., et al. 2017, The California-Kepler Survey. III. A Gap in the Radius Distribution of Small Planets, *Astronomical Journal*, **154**:109

Fulton, B. J., Rosenthal, L. J., Hirsch, L. A., et al. 2021, The California Legacy Survey II. Occurrence of Giant Planets Beyond the Ice line, *arXiv e-prints*, arXiv:2105.11584

Gaia Collaboration, Prusti, T., de Bruijne, J. H. J., et al. 2016, The Gaia mission, *Astronomy and Astrophysics*, **595**:A1

Gaia Collaboration, Brown, A. G. A., Vallenari, A., et al. 2018, Gaia Data Release 2. Summary of the contents and survey properties, *Astronomy and Astrophysics*, **616**:A1

Gallet, F., & Bouvier, J. 2013, Improved angular momentum evolution model for solar-like stars, *Astronomy and Astrophysics*, **556**:A36

Gallet, F., & Bouvier, J. 2015, Improved angular momentum evolution model for solar-like stars. II. Exploring the mass dependence, *Astronomy and Astrophysics*, **577**:A98

Gammie, C. F. 1996, Layered Accretion in T Tauri Disks, *The Astrophysical Journal*, **457**:355

Garcia, P. J. V. 2011, Physical Processes in Circumstellar Disks around Young Stars

Garraffo, C., Drake, J. J., & Cohen, O. 2016, The missing magnetic morphology term in stellar rotation evolution, *Astronomy and Astrophysics*, **595**:A110

Garraffo, C., Drake, J. J., Dotter, A., et al. 2018, The Revolution Revolution: Magnetic Morphology Driven Spin-down, *The Astrophysical Journal*, **862**:90

Gaudi, B. S. 2010, Exoplanetary Microlensing, *arXiv e-prints*, arXiv:1002.0332

Gaudi, B. S. 2012, Microlensing Surveys for Exoplanets, *Annual Review of Astronomy and Astrophysics*, **50**:411–453

Gaudi, B. S., Christiansen, J. L., & Meyer, M. R. 2020, The Demographics of Exoplanets, *arXiv e-prints*, arXiv:2011.04703

Getman, K. V., Feigelson, E. D., Grosso, N., et al. 2005, Membership of the Orion Nebula Population from the Chandra Orion Ultradeep Project, *Astrophysical Journal Supplement Series*, **160**:353–378

Gilman, P. A. 1980, Differential rotation in stars with convection zones, in *IAU Colloq. 51: Stellar Turbulence, Vol. 114*, pp. 19–37

Glassgold, A. E., Najita, J., & Igea, J. 1997, X-Ray Ionization of Protoplanetary Disks, *The Astrophysical Journal*, **480**:344–350

Głębocki, R., & Gnaciński, P. 2005, Systematic errors in the determination of stellar rotational velocities, in *ESA Special Publication, Vol. 560, 13th Cambridge Workshop on Cool Stars, Stellar Systems and the Sun*, p. 571

Goldreich, P., & Tremaine, S. 1979, The excitation of density waves at the Lindblad and corotation resonances by an external potential., *The Astrophysical Journal*, **233**:857–871

Goldreich, P., & Tremaine, S. 1980, Disk-satellite interactions, *The Astrophysical Journal*, **241**:425–441

Gondoin, P. 2018, Magnetic activity evolution on Sun-like stars, *Astronomy and Astrophysics*, **616**:A154

Goodman, A. A., Benson, P. J., Fuller, G. A., & Myers, P. C. 1993, Dense Cores in Dark Clouds. VIII. Velocity Gradients, *The Astrophysical Journal*, **406**:528

Gorti, U., Dullemond, C. P., & Hollenbach, D. 2009, Time Evolution of Viscous Circumstellar Disks due to Photoevaporation by Far-Ultraviolet, Extreme-Ultraviolet, and X-ray Radiation from the Central Star, *The Astrophysical Journal*, **705**:1237–1251

Gorti, U., & Hollenbach, D. 2009, Photoevaporation of Circumstellar Disks By Far-Ultraviolet, Extreme-Ultraviolet and X-Ray Radiation from the Central Star, *The Astrophysical Journal*, **690**:1539–1552

Gorti, U., Hollenbach, D., & Dullemond, C. P. 2015, The Impact of Dust Evolution and Photoevaporation on Disk Dispersal, *The Astrophysical Journal*, **804**:29

Gorti, U., Liseau, R., Sándor, Z., & Clarke, C. 2016, Disk Dispersal: Theoretical Understanding and Observational Constraints, *Space Science Reviews*, **205**:125–152

Greaves, J. S., & Rice, W. K. M. 2010, Have protoplanetary discs formed planets?, *Monthly Notices of the Royal Astronomical Society*, **407**:1981–1988

Greene, T. P., Wilking, B. A., Andre, P., Young, E. T., & Lada, C. J. 1994, Further Mid-Infrared Study of the rho Ophiuchi Cloud Young Stellar Population: Luminosities and Masses of Pre–Main-Sequence Stars, *The Astrophysical Journal*, **434**:614

Gressel, O., Ramsey, J. P., Brinch, C., et al. 2020, Global Hydromagnetic Simulations of Protoplanetary Disks with Stellar Irradiation and Simplified Thermochemistry, *arXiv e-prints*, arXiv:2005.03431

Güdel, M. 2004, X-ray astronomy of stellar coronae, *Astronomy and Astrophysics Reviews*, **12**:71–237

Güdel, M. 2007, The Sun in Time: Activity and Environment, *Living Reviews in Solar Physics*, **4**:3

Güdel, M., Guinan, E. F., & Skinner, S. L. 1997, The X-Ray Sun in Time: A Study of the Long-Term Evolution of Coronae of Solar-Type Stars, *The Astrophysical Journal*, **483**:947–960

Güdel, M., Briggs, K. R., Arzner, K., et al. 2007, The XMM-Newton extended survey of the Taurus molecular cloud (XEST), *Astronomy and Astrophysics*, **468**:353–377

Guilera, O. M., Sándor, Z., Ronco, M. P., Venturini, J., & Miller Bertolami, M. M. 2020, Giant planet formation at the pressure maxima of protoplanetary disks. II. A hybrid accretion scenario, *Astronomy and Astrophysics*, **642**:A140

Guilloteau, S., & Dutrey, A. 1998, Physical parameters of the Keplerian protoplanetary disk of DM Tauri, *Astronomy and Astrophysics*, **339**:467–476

Gullbring, E., Hartmann, L., Briceño, C., & Calvet, N. 1998, Disk Accretion Rates for T Tauri Stars, *The Astrophysical Journal*, **492**:323–341

Haffert, S. Y., Bohn, A. J., de Boer, J., et al. 2019, Two accreting protoplanets around the young star PDS 70, *Nature Astronomy*, **3**:749–754

Haisch, Karl E., J., Lada, E. A., & Lada, C. J. 2001, Disk Frequencies and Lifetimes in Young Clusters, *The Astrophysical Journal Letters*, **553**:L153–L156

Hartigan, P., Edwards, S., & Ghandour, L. 1995, Disk Accretion and Mass Loss from Young Stars, *The Astrophysical Journal*, **452**:736

Hartmann, L., Calvet, N., Gullbring, E., & D'Alessio, P. 1998, Accretion and the Evolution of T Tauri Disks, *The Astrophysical Journal*, **495**:385–400

Hartmann, L., Herczeg, G., & Calvet, N. 2016, Accretion onto Pre-Main-Sequence Stars, *Annual Review of Astronomy and Astrophysics*, **54**:135–180

Hasegawa, Y., & Pudritz, R. E. 2012, Evolutionary Tracks of Trapped, Accreting Protoplanets: The Origin of the Observed Mass-Period Relation, *The Astrophysical Journal*, **760**:117

Haworth, T. J., Boubert, D., Facchini, S., Bisbas, T. G., & Clarke, C. J. 2016, Photochemical-dynamical models of externally FUV irradiated protoplanetary discs, *Monthly Notices of the Royal Astronomical Society*, **463**:3616–3629

Haworth, T. J., Clarke, C. J., Rahman, W., Winter, A. J., & Facchini, S. 2018, The FRIED grid of mass-loss rates for externally irradiated protoplanetary discs, *Monthly Notices of the Royal Astronomical Society*, **481**:452–466

Hayashi, C. 1981, Structure of the Solar Nebula, Growth and Decay of Magnetic Fields and Effects of Magnetic and Turbulent Viscosities on the Nebula, *Progress of Theoretical Physics Supplement*, **70**:35–53

Hellary, P., & Nelson, R. P. 2012, Global models of planetary system formation in radiatively-inefficient protoplanetary discs, *Monthly Notices of the Royal Astronomical Society*, **419**:2737–2757

Hendler, N., Pascucci, I., Pinilla, P., et al. 2020, The Evolution of Dust Disk Sizes from a Homogeneous Analysis of 1-10 Myr old Stars, *The Astrophysical Journal*, **895**:126

Henry, G. W., Marcy, G. W., Butler, R. P., & Vogt, S. S. 2000, A Transiting "51 Peg-like" Planet, *The Astrophysical Journal Letters*, **529**:L41–L44

Herbig, G. H., & Bell, K. R. 1988, Third Catalog of Emission-Line Stars of the Orion Population : 3 : 1988

Hernández, J., Calvet, N., Briceño, C., et al. 2007, Spitzer Observations of the Orion OB1 Association: Disk Census in the Low-Mass Stars, *The Astrophysical Journal*, **671**:1784–1799

Hillenbrand, L. A. 2005, Observational Constraints on Dust Disk Lifetimes: Implications for Planet Formation, *arXiv e-prints*, arXiv:astro-ph/0511083

Hinkel, N. R., Mamajek, E. E., Turnbull, M. C., et al. 2017, A Catalog of Stellar Unified Properties (CATSUP) for 951 FGK-Stars within 30 pc, *The Astrophysical Journal*, **848**:34

Hollenbach, D., & Gorti, U. 2009, Diagnostic Line Emission from Extreme Ultraviolet and X-ray-illuminated Disks and Shocks Around Low-mass Stars, *The Astrophysical Journal*, **703**:1203–1223

Hollenbach, D., Johnstone, D., Lizano, S., & Shu, F. 1994, Photoevaporation of disks around massive stars and application to ultracompact H II regions, *The Astrophysical Journal*, **428**:654–669

Hollenbach, D. J., Yorke, H. W., & Johnstone, D. 2000, Disk Dispersal around Young Stars, in *Protostars and Planets IV*, pp. 401–428

Howard, A. W., Marcy, G. W., Bryson, S. T., et al. 2012, Planet Occurrence within 0.25 AU of Solar-type Stars from Kepler, *Astrophysical Journal Supplement Series*, **201**:15

Hu, X., Zhu, Z., Okuzumi, S., et al. 2019, Nonideal MHD Simulation of HL Tau Disk: Formation of Rings, *The Astrophysical Journal*, **885**:36

Huang, C., Wu, Y., & Triaud, A. H. M. J. 2016, Warm Jupiters Are Less Lonely than Hot Jupiters: Close Neighbors, *The Astrophysical Journal*, **825**:98

Huang, J., Andrews, S. M., Dullemond, C. P., et al. 2018, The Disk Substructures at High Angular Resolution Project (DSHARP). II. Characteristics of Annular Substructures, *The Astrophysical Journal Letters*, **869**:L42

Hueso, R., & Guillot, T. 2005, Evolution of protoplanetary disks: constraints from DM Tauri and GM Aurigae, *Astronomy and Astrophysics*, **442**:703–725

Hughes, A. M., Wilner, D. J., Qi, C., & Hogerheijde, M. R. 2008, Gas and Dust Emission at the Outer Edge of Protoplanetary Disks, *The Astrophysical Journal*, **678**:1119–1126

Hunter, J. D. 2007, Matplotlib: A 2D Graphics Environment, *CSE*, **9**:90–95

Hutchison, M. A., Laibe, G., & Maddison, S. T. 2016a, On the maximum grain size entrained by photoevaporative winds, *Monthly Notices of the Royal Astronomical Society*, **463**:2725–2734

Hutchison, M. A., Price, D. J., Laibe, G., & Maddison, S. T. 2016b, On dust entrainment in photoevaporative winds, *Monthly Notices of the Royal Astronomical Society*, **461**:742–759

Ida, S., & Lin, D. N. C. 2004, Toward a Deterministic Model of Planetary Formation. I. A Desert in the Mass and Semimajor Axis Distributions of Extrasolar Planets, *The Astrophysical Journal*, **604**:388–413

Ida, S., Tanaka, H., Johansen, A., Kanagawa, K. D., & Tanigawa, T. 2018, Slowing Down Type II Migration of Gas Giants to Match Observational Data, *The Astrophysical Journal*, **864**:77

Isella, A., Carpenter, J. M., & Sargent, A. I. 2009, Structure and Evolution of Pre-main-sequence Circumstellar Disks, *The Astrophysical Journal*, **701**:260–282

Izidoro, A., Bitsch, B., Raymond, S. N., et al. 2019, Formation of planetary systems by pebble accretion and migration: Hot super-Earth systems from breaking compact resonant chains, *arXiv e-prints*, arXiv:1902.08772

Jardine, M., Collier Cameron, A., Donati, J.-F., Gregory, S. G., & Wood, K. 2006, X-ray emission from T Tauri stars, *Monthly Notices of the Royal Astronomical Society*, **367**:917–927

Jeans, J. H. 1902, The Stability of a Spherical Nebula, *Philosophical Transactions of the Royal Society of London Series A*, **199**:1–53

Jeffers, S. V., Barnes, J. R., Jones, H. R. A., et al. 2014, Is it possible to detect planets around young active G and K dwarfs?, *Monthly Notices of the Royal Astronomical Society*, **438**:2717–2731

Jeffries, R. D., & Oliveira, J. M. 2005, The lithium depletion boundary in NGC 2547 as a test of pre-main-sequence evolutionary models, *Monthly Notices of the Royal Astronomical Society*, **358**:13–29

Jennings, J., Ercolano, B., & Rosotti, G. P. 2018, The comparative effect of FUV, EUV and X-ray disc photoevaporation on gas giant separations, *Monthly Notices of the Royal Astronomical Society*, **477**:4131–4141

Johnson, J. A., Aller, K. M., Howard, A. W., & Crepp, J. R. 2010, Giant Planet Occurrence in the Stellar Mass-Metallicity Plane, *Publications of the Astronomical Society of the Pacific*, **122**:905

Johnstone, C. P., Güdel, M., Brott, I., & Lüftinger, T. 2015, Stellar winds on the main-sequence. II. The evolution of rotation and winds, *Astronomy and Astrophysics*, **577**:A28

Jones, D. E., Stenning, D. C., Ford, E. B., et al. 2017, Improving Exoplanet Detection Power: Multivariate Gaussian Process Models for Stellar Activity, *ArXiv e-prints*, arXiv:1711.01318

Joye, W. A., & Mandel, E. 2003, New Features of SAOImage DS9, in *Astronomical Society of the Pacific Conference Series, Vol. 295, Astronomical Data Analysis Software and Systems XII*, p. 489

Kalas, P., Graham, J. R., & Clampin, M. 2005, A planetary system as the origin of structure in Fomalhaut's dust belt, *Nature*, **435**:1067–1070

Kalas, P., Graham, J. R., Chiang, E., et al. 2008, Optical Images of an Exosolar Planet 25 Light-Years from Earth, *Science*, **322**:1345

Kanagawa, K. D., Tanaka, H., & Szuszkiewicz, E. 2018, Radial Migration of Gap-opening Planets in Protoplanetary Disks. I. The Case of a Single Planet, *The Astrophysical Journal*, **861**:140

Kane, S. R. 2011, Detecting the signatures of Uranus and Neptune, *Icarus*, **214**:327–333

Kashyap, V. L., Drake, J. J., & Saar, S. H. 2008, Extrasolar Giant Planets and X-Ray Activity, *The Astrophysical Journal*, **687**:1339–1354

Kataoka, A., Tanaka, H., Okuzumi, S., & Wada, K. 2013, Fluffy dust forms icy planetesimals by static compression, *Astronomy and Astrophysics*, **557**:L4

Katz, D., & Brown, A. G. A. 2017, Gaia: on the road to DR2, in *SF2A-2017: Proceedings of the Annual meeting of the French Society of Astronomy and Astrophysics*, pp. 259–263

Kennedy, G. M., & Kenyon, S. J. 2008, Planet Formation around Stars of Various Masses: The Snow Line and the Frequency of Giant Planets, *The Astrophysical Journal*, **673**:502–512

Kenyon, S. J., & Hartmann, L. 1987, Spectral Energy Distributions of T Tauri Stars: Disk Flaring and Limits on Accretion, *The Astrophysical Journal*, **323**:714

Kenyon, S. J., & Hartmann, L. 1995, Pre-Main-Sequence Evolution in the Taurus-Auriga Molecular Cloud, *Astrophysical Journal Supplement Series*, **101**:117

Keppler, M., Benisty, M., Müller, A., et al. 2018, Discovery of a planetary-mass companion within the gap of the transition disk around PDS 70, *Astronomy and Astrophysics*, **617**:A44

Kipping, D. 2018, Do planets remember how they formed?, *Monthly Notices of the Royal Astronomical Society*, **473**:784–795

Kitchatinov, L. L., & Olemskoy, S. V. 2015, Dynamo saturation in rapidly rotating solar-type stars, *Research in Astronomy and Astrophysics*, **15**:1801

Klahr, H., & Brandner, W. 2006, Planet Formation

Kley, W., & Nelson, R. P. 2012, Planet-Disk Interaction and Orbital Evolution, *Annual Review of Astronomy and Astrophysics*, **50**:211–249

Kley, W., Papaloizou, J. C. B., & Ogilvie, G. I. 2008, Simulations of eccentric disks in close binary systems, *Astronomy and Astrophysics*, **487**:671–687

Koenigl, A. 1991, Disk Accretion onto Magnetic T Tauri Stars, *The Astrophysical Journal Letters*, **370**:L39

Koepferl, C. M., Ercolano, B., Dale, J., et al. 2013, Disc clearing of young stellar objects: evidence for fast inside-out dispersal, *Monthly Notices of the Royal Astronomical Society*, **428**:3327–3354

Konopacky, Q. M., & Barman, T. S. 2018, HR8799: Imaging a System of Exoplanets, in *Handbook of Exoplanets*, p. 36

Kraft, R. P. 1967, Studies of Stellar Rotation. V. The Dependence of Rotation on Age among Solar-Type Stars, *The Astrophysical Journal*, **150**:551

Kratter, K., & Lodato, G. 2016, Gravitational Instabilities in Circumstellar Disks, *Annual Review of Astronomy and Astrophysics*, **54**:271–311

Kuiper, G. P. 1951, On the Origin of the Solar System, *Proceedings of the National Academy of Science*, **37**:1–14

Kunitomo, M., Suzuki, T. K., & Inutsuka, S.-i. 2020, Dispersal of protoplanetary discs by the combination of magnetically driven and photoevaporative winds, *Monthly Notices of the Royal Astronomical Society*, **492**:3849–3858

Lada, C. J. 1987, Star formation: from OB associations to protostars., in *Star Forming Regions, Vol. 115*, p. 1

Lada, C. J., & Wilking, B. A. 1984, The nature of the embedded population in the rho Ophiuchi dark cloud : mid-infrared observations., *The Astrophysical Journal*, **287**:610–621

Lagrange, A. M., Gratadour, D., Chauvin, G., et al. 2009, A probable giant planet imaged in the β Pictoris disk. VLT/NaCo deep L'-band imaging, *Astronomy and Astrophysics*, **493**:L21–L25

Lambrechts, M., & Johansen, A. 2012, Rapid growth of gas-giant cores by pebble accretion, *Astronomy and Astrophysics*, **544**:A32

Lanza, A. F. 2008, Hot Jupiters and stellar magnetic activity, *Astronomy and Astrophysics*, **487**:1163–1170

Laughlin, G., Bodenheimer, P., & Adams, F. C. 2004, The Core Accretion Model Predicts Few Jovian-Mass Planets Orbiting Red Dwarfs, *The Astrophysical Journal Letters*, **612**:L73–L76

LeBlanc, F. 2010, An Introduction to Stellar Astrophysics

Leibacher, J. W., & Stein, R. F. 1971, A New Description of the Solar Five-Minute Oscillation, *Astrophysics Letters*, **7**:191–192

Leighton, R. B., Noyes, R. W., & Simon, G. W. 1962, Velocity Fields in the Solar Atmosphere. I. Preliminary Report., *The Astrophysical Journal*, **135**:474

Liffman, K. 2003, The Gravitational Radius of an Irradiated Disk, *Publications of the Astronomical Society of Australia*, **20**:337–339

Lin, D. N. C., & Papaloizou, J. 1979, Tidal torques on accretion discs in binary systems with extreme mass ratios., *Monthly Notices of the Royal Astronomical Society*, **186**:799–812

Lin, D. N. C., & Papaloizou, J. 1986, On the tidal interaction between protoplanets and the protoplanetary disk. III - Orbital migration of protoplanets, *The Astrophysical Journal*, **309**:846–857

Lin, D. N. C., & Pringle, J. E. 1987, A viscosity prescription for a self-gravitating accretion disc, *Monthly Notices of the Royal Astronomical Society*, **225**:607–613

Liu, B., Ormel, C. W., & Lin, D. N. C. 2017, Dynamical rearrangement of super-Earths during disk dispersal. I. Outline of the magnetospheric rebound model, *Astronomy and Astrophysics*, **601**:A15

Lodato, G. 2008, Classical disc physics, *New Astronomy Review*, **52**:21–41

Lubow, S. H., & D'Angelo, G. 2006, Gas Flow across Gaps in Protoplanetary Disks, *The Astrophysical Journal*, **641**:526–533

Lubow, S. H., & Ida, S. 2010, Planet Migration, *arXiv e-prints*, arXiv:1004.4137

Lubow, S. H., Seibert, M., & Artymowicz, P. 1999, Disk Accretion onto High-Mass Planets, *The Astrophysical Journal*, **526**:1001–1012

Luhman, K. L., Allen, P. R., Espaillat, C., Hartmann, L., & Calvet, N. 2010, The Disk Population of the Taurus Star-Forming Region, *Astrophysical Journal Supplement Series*, **186**:111–174

Lynden-Bell, D., & Pringle, J. E. 1974, The evolution of viscous discs and the origin of the nebular variables., *Monthly Notices of the Royal Astronomical Society*, **168**:603–637

Macías, E., Anglada, G., Osorio, M., et al. 2016, Imaging the Photoevaporating Disk and Radio Jet of GM Aur, *The Astrophysical Journal*, **829**:1

Maggio, A., Sciortino, S., Vaiana, G. S., et al. 1987, Einstein Observatory Survey of X-Ray Emission from Solar-Type Stars: The Late F and G Dwarf Stars, *The Astrophysical Journal*, **315**:687

Mamajek, E. E. 2009, Initial Conditions of Planet Formation: Lifetimes of Primordial Disks, in *American Institute of Physics Conference Series, Vol. 1158, American Institute of Physics Conference Series*, pp. 3–10

Manara, C. F., Beccari, G., Da Rio, N., et al. 2013, Accurate determination of accretion and photospheric parameters in young stellar objects: The case of two candidate old disks in the Orion Nebula Cluster, *Astronomy and Astrophysics*, **558**:A114

Manara, C. F., Morbidelli, A., & Guillot, T. 2018, Why do protoplanetary disks appear not massive enough to form the known exoplanet population?, *Astronomy and Astrophysics*, **618**:L3

Mannings, V., & Sargent, A. I. 1997, A High-Resolution Study of Gas and Dust around Young Intermediate-Mass Stars: Evidence for Circumstellar Disks in Herbig Ae Systems, *The Astrophysical Journal*, **490**:792–802

Marcy, G., Butler, R. P., Fischer, D., et al. 2005, Observed Properties of Exoplanets: Masses, Orbits, and Metallicities, *Progress of Theoretical Physics Supplement*, **158**:24–42

Marois, C., Macintosh, B., Barman, T., et al. 2008, Direct Imaging of Multiple Planets Orbiting the Star HR 8799, *Science*, **322**:1348

Masset, F. 2000, FARGO: A fast eulerian transport algorithm for differentially rotating disks, *Astronomy and Astrophysics, Supplement*, **141**:165–173

Mateos, S., Saxton, R. D., Read, A. M., & Sembay, S. 2009, Statistical evaluation of the flux cross-calibration of the XMM-Newton EPIC cameras, *Astronomy and Astrophysics*, **496**:879–889

Mathis, J. S., Rumpl, W., & Nordsieck, K. H. 1977, The size distribution of interstellar grains., *The Astrophysical Journal*, **217**:425–433

Matsumoto, T., & Hanawa, T. 2003, Fragmentation of a Molecular Cloud Core versus Fragmentation of the Massive Protoplanetary Disk in the Main Accretion Phase, *The Astrophysical Journal*, **595**:913–934

Matsuyama, I., Johnstone, D., & Hartmann, L. 2003a, Viscous Diffusion and Photoevaporation of Stellar Disks, *The Astrophysical Journal*, **582**:893–904

Matsuyama, I., Johnstone, D., & Murray, N. 2003b, Halting Planet Migration by Photoevaporation from the Central Source, *The Astrophysical Journal Letters*, **585**:L143–L146

Mayer, L., Quinn, T., Wadsley, J., & Stadel, J. 2002, Formation of Giant Planets by Fragmentation of Protoplanetary Disks, *Science*, **298**:1756–1759

Mayor, M., & Queloz, D. 1995, A Jupiter-mass companion to a solar-type star, *Nature*, **378**:355–359

Mazeh, T., Naef, D., Torres, G., et al. 2000, The Spectroscopic Orbit of the Planetary Companion Transiting HD 209458, *The Astrophysical Journal Letters*, **532**:L55–L58

Meeus, G., Montesinos, B., Mendigutía, I., et al. 2012, Observations of Herbig Ae/Be stars with Herschel/PACS. The atomic and molecular contents of their protoplanetary discs, *Astronomy and Astrophysics*, **544**:A78

Mentuch, E., Brandeker, A., van Kerkwijk, M. H., Jayawardhana, R., & Hauschildt, P. H. 2008, Lithium Depletion of Nearby Young Stellar Associations, *The Astrophysical Journal*, **689**:1127–1140

Mentuch, E., Abraham, R. G., Glazebrook, K., et al. 2009, A Near-Infrared Excess in the Continuum of High-redshift Galaxies: A Tracer of Star Formation and Circumstellar Disks?, *The Astrophysical Journal*, **706**:1020–1035

Meru, F., & Bate, M. R. 2011, On the fragmentation criteria of self-gravitating protoplanetary discs, *Monthly Notices of the Royal Astronomical Society*, **410**:559–572

Meru, F., Rosotti, G. P., Booth, R. A., Nazari, P., & Clarke, C. J. 2019, Is the ring inside or outside the planet?: the effect of planet migration on dust rings, *Monthly Notices of the Royal Astronomical Society*, **482**:3678–3695

Micela, G., Sciortino, S., Serio, S., et al. 1985, Einstein X-ray survey of the Pleiades : the dependence of X-ray emission on stellar age., *The Astrophysical Journal*, **292**:172–180

Miller, B. P., Gallo, E., Wright, J. T., & Pearson, E. G. 2015, A Comprehensive Statistical Assessment of Star-Planet Interaction, *The Astrophysical Journal*, **799**:163

Moeckel, N., & Armitage, P. J. 2012, Hydrodynamic outcomes of planet scattering in transitional discs, *Monthly Notices of the Royal Astronomical Society*, **419**:366–376

Monsch, K., Ercolano, B., Picogna, G., Preibisch, T., & Rau, M. M. 2019, The imprint of X-ray photoevaporation of planet-forming discs on the orbital distribution of giant planets, *Monthly Notices of the Royal Astronomical Society*, **483**:3448–3458

Monsch, K., Picogna, G., Ercolano, B., & Kley, W. 2021a, Giant planet migration during the disc dispersal phase, *Astronomy and Astrophysics*, **646**:A169

Monsch, K., Picogna, G., Ercolano, B., & Preibisch, T. 2021b, The imprint of X-ray photoevaporation of planet-forming discs on the orbital distribution of giant planets - II. Theoretical predictions, *Astronomy and Astrophysics*, **650**:A199

Montmerle, T., Grosso, N., Tsuboi, Y., & Koyama, K. 2000, Rotation and X-Ray Emission from Protostars, *The Astrophysical Journal*, **532**:1097–1110

Morbidelli, A., & Raymond, S. N. 2016, Challenges in planet formation, *Journal of Geophysical Research (Planets)*, **121**:1962–1980

Mordasini, C. 2018, Planetary Population Synthesis, in *Handbook of Exoplanets*, p. 143

Mordasini, C., Alibert, Y., & Benz, W. 2009, Extrasolar planet population synthesis. I. Method, formation tracks, and mass-distance distribution, *Astronomy and Astrophysics*, **501**:1139–1160

Mordasini, C., Alibert, Y., Benz, W., Klahr, H., & Henning, T. 2012, Extrasolar planet population synthesis . IV. Correlations with disk metallicity, mass, and lifetime, *Astronomy and Astrophysics*, **541**:A97

Mordasini, C., Mollière, P., Dittkrist, K.-M., Jin, S., & Alibert, Y. 2015, Global models of planet formation and evolution, *International Journal of Astrobiology*, **14**:201–232

Mróz, P., Poleski, R., Gould, A., et al. 2020, A Terrestrial-mass Rogue Planet Candidate Detected in the Shortest-timescale Microlensing Event, *The Astrophysical Journal Letters*, **903**:L11

Mulders, G. D. 2018, Planet Populations as a Function of Stellar Properties, in *Handbook of Exoplanets*, p. 153

Mulders, G. D., Ciesla, F. J., Min, M., & Pascucci, I. 2015a, The Snow Line in Viscous Disks around Low-mass Stars: Implications for Water Delivery to Terrestrial Planets in the Habitable Zone, *The Astrophysical Journal*, **807**:9

Mulders, G. D., Mordasini, C., Pascucci, I., et al. 2019, The Exoplanet Population Observation Simulator. II. Population Synthesis in the Era of Kepler, *The Astrophysical Journal*, **887**:157

Mulders, G. D., Pascucci, I., & Apai, D. 2015b, An Increase in the Mass of Planetary Systems around Lower-mass Stars, *The Astrophysical Journal*, **814**:130

Müller, A., Keppler, M., Henning, T., et al. 2018, Orbital and atmospheric characterization of the planet within the gap of the PDS 70 transition disk, *Astronomy and Astrophysics*, **617**:L2

Muro-Arena, G. A., Ginski, C., Dominik, C., et al. 2020, Spirals inside the millimeter cavity of transition disk SR 21, *arXiv e-prints*, arXiv:2003.08189

Muzerolle, J., Calvet, N., Briceño, C., Hartmann, L., & Hillenbrand, L. 2000, Disk Accretion in the 10 MYR Old T Tauri Stars TW Hydrae and Hen 3-600A, *The Astrophysical Journal Letters*, **535**:L47–L50

Muzerolle, J., Luhman, K. L., Briceño, C., Hartmann, L., & Calvet, N. 2005, Measuring Accretion in Young Substellar Objects: Approaching the Planetary Mass Regime, *The Astrophysical Journal*, **625**:906–912

Najita, J. R., & Kenyon, S. J. 2014, The mass budget of planet-forming discs: isolating the epoch of planetesimal formation, *Monthly Notices of the Royal Astronomical Society*, **445**:3315–3329

Najita, J. R., Strom, S. E., & Muzerolle, J. 2007, Demographics of transition objects, *Monthly Notices of the Royal Astronomical Society*, **378**:369–378

Nakatani, R., Hosokawa, T., Yoshida, N., Nomura, H., & Kuiper, R. 2018, Radiation Hydrodynamics Simulations of Photoevaporation of Protoplanetary Disks by Ultraviolet Radiation: Metallicity Dependence, *The Astrophysical Journal*, **857**:57

Narang, M., Manoj, P., Furlan, E., et al. 2018, Properties and Occurrence Rates for Kepler Exoplanet Candidates as a Function of Host Star Metallicity from the DR25 Catalog, *Astronomical Journal*, **156**:221

NASA/IPAC. 2012, Near, Mid and Far-Infrared, [online; accessed on 25 June 2021]

Natta, A. 2004, Circumstellar Disks in Pre-Main Sequence Stars, in *Astronomical Society of the Pacific Conference Series, Vol. 324, Debris Disks and the Formation of Planets*, p. 20

Nazari, P., Booth, R. A., Clarke, C. J., et al. 2019, Revealing signatures of planets migrating in protoplanetary discs with ALMA multiwavelength observations, *Monthly Notices of the Royal Astronomical Society*, **485**:5914–5923

Ndugu, N., Bitsch, B., & Jurua, E. 2018, Planet population synthesis driven by pebble accretion in cluster environments, *Monthly Notices of the Royal Astronomical Society*, **474**:886–897

Ndugu, N., Bitsch, B., & Jurua, E. 2019, Are the observed gaps in protoplanetary discs caused by growing planets?, *Monthly Notices of the Royal Astronomical Society*, **488**:3625–3633

Nelson, R. P., Gressel, O., & Umurhan, O. M. 2013, Linear and non-linear evolution of the vertical shear instability in accretion discs, *Monthly Notices of the Royal Astronomical Society*, **435**:2610–2632

Noyes, R. W., Hartmann, L. W., Baliunas, S. L., Duncan, D. K., & Vaughan, A. H. 1984, Rotation, convection, and magnetic activity in lower main-sequence stars., *The Astrophysical Journal*, **279**:763–777

O'dell, C. R., & Wen, Z. 1994, Postrefurbishment Mission Hubble Space Telescope Images of the Core of the Orion Nebula: Proplyds, Herbig-Haro Objects, and Measurements of a Circumstellar Disk, *The Astrophysical Journal*, **436**:194

O'dell, C. R., Wen, Z., & Hu, X. 1993, Discovery of New Objects in the Orion Nebula on HST Images: Shocks, Compact Sources, and Protoplanetary Disks, *The Astrophysical Journal*, **410**:696

Okuzumi, S., Momose, M., Sirono, S.-i., Kobayashi, H., & Tanaka, H. 2016, Sintering-induced Dust Ring Formation in Protoplanetary Disks: Application to the HL Tau Disk, *The Astrophysical Journal*, **821**:82

Okuzumi, S., Tanaka, H., Kobayashi, H., & Wada, K. 2012, Rapid Coagulation of Porous Dust Aggregates outside the Snow Line: A Pathway to Successful Icy Planetesimal Formation, *The Astrophysical Journal*, **752**:106

Oliveira, I., Merín, B., Pontoppidan, K. M., et al. 2009, Optical Characterization of A New Young Stellar Population in the Serpens Molecular Cloud, *The Astrophysical Journal*, **691**:672–686

Ormel, C. W., & Klahr, H. H. 2010, The effect of gas drag on the growth of protoplanets. Analytical expressions for the accretion of small bodies in laminar disks, *Astronomy and Astrophysics*, **520**:A43

Ormel, C. W., Liu, B., & Schoonenberg, D. 2017, Formation of TRAPPIST-1 and other compact systems, *Astronomy and Astrophysics*, **604**:A1

Ossenkopf, V., & Henning, T. 1994, Dust opacities for protostellar cores., *Astronomy and Astrophysics*, **291**:943–959

Otto, S., Politzer, H. D., Preskill, J., & Wise, M. B. 1986, The significance of voids, *The Astrophysical Journal*, **304**:62–74

Owen, J. E. 2016, The Origin and Evolution of Transition Discs: Successes, Problems, and Open Questions, *Publications of the Astronomical Society of Australia*, **33**:e005

Owen, J. E. 2020, Snow lines can be thermally unstable, *Monthly Notices of the Royal Astronomical Society*, **495**:3160–3174

Owen, J. E., & Clarke, C. J. 2012, Two populations of transition discs?, *Monthly Notices of the Royal Astronomical Society*, **426**:L96–L100

Owen, J. E., Clarke, C. J., & Ercolano, B. 2012, On the theory of disc photoevaporation, *Monthly Notices of the Royal Astronomical Society*, **422**:1880–1901

Owen, J. E., Ercolano, B., & Clarke, C. J. 2011a, Protoplanetary disc evolution and dispersal: the implications of X-ray photoevaporation, *Monthly Notices of the Royal Astronomical Society*, **412**:13–25

Owen, J. E., Ercolano, B., & Clarke, C. J. 2011b, The imprint of photoevaporation on edge-on discs, *Monthly Notices of the Royal Astronomical Society*, **411**:1104–1110

Owen, J. E., Ercolano, B., Clarke, C. J., & Alexander, R. D. 2010, Radiation-hydrodynamic models of X-ray and EUV photoevaporating protoplanetary discs, *Monthly Notices of the Royal Astronomical Society*, **401**:1415–1428

Owen, J. E., & Wu, Y. 2017, The Evaporation Valley in the Kepler Planets, *The Astrophysical Journal*, **847**:29

Paardekooper, S. J., & Mellema, G. 2004, Planets opening dust gaps in gas disks, *Astronomy and Astrophysics*, **425**:L9–L12

Paardekooper, S. J., & Papaloizou, J. C. B. 2009, On the width and shape of the corotation region for low-mass planets, *Monthly Notices of the Royal Astronomical Society*, **394**:2297–2309

Pallavicini, R., Golub, L., Rosner, R., et al. 1981, Relations among stellar X-ray emission observed from Einstein, stellar rotation and bolometric luminosity., *The Astrophysical Journal*, **248**:279–290

Parker, E. N. 1955, Hydromagnetic Dynamo Models., *The Astrophysical Journal*, **122**:293

Pascucci, I., Ricci, L., Gorti, U., et al. 2014, Low Extreme-ultraviolet Luminosities Impinging on Protoplanetary Disks, *The Astrophysical Journal*, **795**:1

Pérez, S., Casassus, S., Baruteau, C., et al. 2019, Dust Unveils the Formation of a Mini-Neptune Planet in a Protoplanetary Ring, *Astronomical Journal*, **158**:15

Perryman, M., Hartman, J., Bakos, G. Á., & Lindegren, L. 2014, Astrometric Exoplanet Detection with Gaia, *The Astrophysical Journal*, **797**:14

Persson, M. V. 2014, Current view of protostellar evolution, [online; accessed 23 June 2021]

Petrovich, C., & Tremaine, S. 2016, Warm Jupiters from Secular Planet-Planet Interactions, *The Astrophysical Journal*, **829**:132

Pevtsov, A. A., Fisher, G. H., Acton, L. W., et al. 2003, The Relationship Between X-Ray Radiance and Magnetic Flux, *The Astrophysical Journal*, **598**:1387–1391

Picogna, G., Ercolano, B., Owen, J. E., & Weber, M. L. 2019, The dispersal of protoplanetary discs - I. A new generation of X-ray photoevaporation models, *Monthly Notices of the Royal Astronomical Society*, **487**:691–701

Picogna, G., & Kley, W. 2015, How do giant planetary cores shape the dust disk?. HL Tauri system, *Astronomy and Astrophysics*, **584**:A110

Picogna, G., Stoll, M. H. R., & Kley, W. 2018, Particle accretion onto planets in discs with hydrodynamic turbulence, *Astronomy and Astrophysics*, **616**:A116

Pizzolato, N., Maggio, A., Micela, G., Sciortino, S., & Ventura, P. 2003, The stellar activity-rotation relationship revisited: Dependence of saturated and non-saturated X-ray emission regimes on stellar mass for late-type dwarfs, *Astronomy and Astrophysics*, **397**:147–157

Poleski, R., Skowron, J., Mróz, P., et al. 2021, Wide-orbit exoplanets are common. Analysis of nearly 20 years of OGLE microlensing survey data, *arXiv e-prints*, arXiv:2104.02079

Politzer, H. D., & Preskill, J. P. 1986, Poisson clusters and Poisson voids, *Physical Review Letters*, **56**:99–102

Pollack, J. B., Hollenbach, D., Beckwith, S., et al. 1994, Composition and Radiative Properties of Grains in Molecular Clouds and Accretion Disks, *The Astrophysical Journal*, **421**:615

Pollack, J. B., Hubickyj, O., Bodenheimer, P., et al. 1996, Formation of the Giant Planets by Concurrent Accretion of Solids and Gas, *Icarus*, **124**:62–85

Poppenhaeger, K., Robrade, J., & Schmitt, J. H. M. M. 2010, Coronal properties of planet-bearing stars, *Astronomy and Astrophysics*, **515**:A98

Poppenhaeger, K., & Schmitt, J. H. M. M. 2011, A Correlation Between Host Star Activity and Planet Mass for Close-in Extrasolar Planets?, *The Astrophysical Journal*, **735**:59

Preibisch, T. 2012, The reliability of age measurements for Young Stellar Objects from Hertzsprung-Russell or color-magnitude diagrams, *Research in Astronomy and Astrophysics*, **12**:1–25

Preibisch, T., & Feigelson, E. D. 2005, The Evolution of X-Ray Emission in Young Stars, *Astrophysical Journal Supplement Series*, **160**:390–400

Preibisch, T., Mehlhorn, M., Townsley, L., Broos, P., & Ratzka, T. 2014, Chandra X-ray observation of the H ii region Gum 31 in the Carina nebula complex, *Astronomy and Astrophysics*, **564**:A120

Preibisch, T., & Zinnecker, H. 2002, X-Ray Properties of the Young Stellar and Substellar Objects in the IC 348 Cluster: The Chandra View, *Astronomical Journal*, **123**:1613–1628

Preibisch, T., Zinnecker, H., & Herbig, G. H. 1996, ROSAT X-ray observations of the young cluster IC 348., *Astronomy and Astrophysics*, **310**:456–473

Preibisch, T., Kim, Y.-C., Favata, F., et al. 2005, The Origin of T Tauri X-Ray Emission: New Insights from the Chandra Orion Ultradeep Project, *Astrophysical Journal Supplement Series*, **160**:401–422

Preibisch, T., Hodgkin, S., Irwin, M., et al. 2011, Near-infrared Properties of the X-ray-emitting Young Stellar Objects in the Carina Nebula, *Astrophysical Journal Supplement Series*, **194**:10

Pringle, J. E. 1981, Accretion discs in astrophysics, *Annual Review of Astronomy and Astrophysics*, **19**:137–162

Quintana, E. V., & Lissauer, J. J. 2014, The Effect of Planets Beyond the Ice Line on the Accretion of Volatiles by Habitable-zone Rocky Planets, *The Astrophysical Journal*, **786**:33

Reale, F. 2014, Coronal Loops: Observations and Modeling of Confined Plasma, *Living Reviews in Solar Physics*, **11**:4

Rebull, L. M., Padgett, D. L., McCabe, C. E., et al. 2010, The Taurus Spitzer Survey: New Candidate Taurus Members Selected Using Sensitive Mid-Infrared Photometry, *Astrophysical Journal Supplement Series*, **186**:259–307

Ribas, Á., Bouy, H., & Merín, B. 2015, Protoplanetary disk lifetimes vs. stellar mass and possible implications for giant planet populations, *Astronomy and Astrophysics*, **576**:A52

Ribas, Á., Merín, B., Bouy, H., & Maud, L. T. 2014, Disk evolution in the solar neighborhood. I. Disk frequencies from 1 to 100 Myr, *Astronomy and Astrophysics*, **561**:A54

Rice, W. K. M., Armitage, P. J., Bate, M. R., & Bonnell, I. A. 2003, The effect of cooling on the global stability of self-gravitating protoplanetary discs, *Monthly Notices of the Royal Astronomical Society*, **339**:1025–1030

Richard, D., & Zahn, J.-P. 1999, Turbulence in differentially rotating flows. What can be learned from the Couette-Taylor experiment, *Astronomy and Astrophysics*, **347**:734–738

Ricker, G. R., Winn, J. N., Vanderspek, R., et al. 2015, Transiting Exoplanet Survey Satellite (TESS), *Journal of Astronomical Telescopes, Instruments, and Systems*, **1**:014003

Robert, C. M. T., Crida, A., Lega, E., Méheut, H., & Morbidelli, A. 2018, Toward a new paradigm for Type II migration, *Astronomy and Astrophysics*, **617**:A98

Robitaille, T. P., Whitney, B. A., Indebetouw, R., Wood, K., & Denzmore, P. 2006, Interpreting Spectral Energy Distributions from Young Stellar Objects. I. A Grid of 200,000 YSO Model SEDs, *Astrophysical Journal Supplement Series*, **167**:256–285

Robitaille, T. P., Tollerud, E. J., Greenfield, P., et al. 2013, Astropy: A community Python package for astronomy, *Astronomy and Astrophysics*, **558**:A33

Rodenkirch, P. J., Klahr, H., Fendt, C., & Dullemond, C. P. 2020, Global axisymmetric simulations of photoevaporation and magnetically driven protoplanetary disk winds, *Astronomy and Astrophysics*, **633**:A21

Rodler, F., Lopez-Morales, M., & Ribas, I. 2012, Weighing the Non-transiting Hot Jupiter τ Boo b, *The Astrophysical Journal Letters*, **753**:L25

Rometsch, T., Rodenkirch, P. J., Kley, W., & Dullemond, C. P. 2020, Migration jumps of planets in transition discs, *Astronomy and Astrophysics*, **643**:A87

Ronco, M. P., Guilera, O. M., & de Elía, G. C. 2017, Formation of solar system analogues - I. Looking for initial conditions through a population synthesis analysis, *Monthly Notices of the Royal Astronomical Society*, **471**:2753–2770

ROSAT Consortium. 2000, VizieR Online Data Catalog: Second ROSAT PSPC Catalog (ROSAT, 2000), *VizieR Online Data Catalog*, **9030**

ROSAT Scientific Team. 2000, VizieR Online Data Catalog: ROSAT HRI Pointed Observations (1RXH) (ROSAT Team, 2000), *VizieR Online Data Catalog*, **9028**

Rosen, S. R., Webb, N. A., Watson, M. G., et al. 2016, The XMM-Newton serendipitous survey. VII. The third XMM-Newton serendipitous source catalogue, *Astronomy and Astrophysics*, **590**:A1

Rosotti, G. P., Ercolano, B., & Owen, J. E. 2015, The long-term evolution of photoevaporating transition discs with giant planets, *Monthly Notices of the Royal Astronomical Society*, **454**:2173–2182

Rosotti, G. P., Ercolano, B., Owen, J. E., & Armitage, P. J. 2013, The interplay between X-ray photoevaporation and planet formation, *Monthly Notices of the Royal Astronomical Society*, **430**:1392–1401

Rosotti, G. P., Juhasz, A., Booth, R. A., & Clarke, C. J. 2016, The minimum mass of detectable planets in protoplanetary discs and the derivation of planetary masses from high-resolution observations, *Monthly Notices of the Royal Astronomical Society*, **459**:2790–2805

Rosotti, G. P., Tazzari, M., Booth, R. A., et al. 2019, The time evolution of dusty protoplanetary disc radii: observed and physical radii differ, *Monthly Notices of the Royal Astronomical Society*, **486**:4829–4844

Ruden, S. P. 1993, The evolution of protoplanetary disks., in *Astronomical Society of the Pacific Conference Series, Vol. 36, Planets Around Pulsars*, pp. 197–215

Ruden, S. P. 2004, Evolution of Photoevaporating Protoplanetary Disks, *The Astrophysical Journal*, **605**:880–891

Sachs, A. 1974, Babylonian Observational Astronomy, *Philosophical Transactions of the Royal Society of London Series A*, **276**:43–50

Safronov, V. S. 1960, On the gravitational instability in flattened systems with axial symmetry and non-uniform rotation, *Annales d'Astrophysique*, **23**:979

Sahu, K. C., Casertano, S., Bond, H. E., et al. 2006, Transiting extrasolar planetary candidates in the Galactic bulge, *Nature*, **443**:534

Sallum, S., Follette, K. B., Eisner, J. A., et al. 2015, Accreting protoplanets in the LkCa 15 transition disk, *Nature*, **527**:342–344

Salmeron, R., & Wardle, M. 2008, Magnetorotational instability in protoplanetary discs: the effect of dust grains, *Monthly Notices of the Royal Astronomical Society*, **388**:1223–1238

Sánchez, M. B., de Elía, G. C., & Darriba, L. A. 2018, Role of gaseous giants in the dynamical evolution of terrestrial planets and water delivery in the habitable zone, *Monthly Notices of the Royal Astronomical Society*, **481**:1281–1289

Sanchis, E., Picogna, G., Ercolano, B., Testi, L., & Rosotti, G. 2020, Detectability of embedded protoplanets from hydrodynamical simulations, *Monthly Notices of the Royal Astronomical Society*, **492**:3440–3458

Santerne, A. 2018, Populations of Extrasolar Giant Planets from Transit and Radial Velocity Surveys, in *Handbook of Exoplanets*, p. 154

Santos, N. C., Israelian, G., & Mayor, M. 2001, The metal-rich nature of stars with planets, *Astronomy and Astrophysics*, **373**:1019–1031

Santos, N. C., Israelian, G., & Mayor, M. 2004, Spectroscopic [Fe/H] for 98 extra-solar planet-host stars. Exploring the probability of planet formation, *Astronomy and Astrophysics*, **415**:1153–1166

Savitzky, A., & Golay, M. J. E. 1964, Smoothing and Differentiation of Data by Simplified Least Squares Procedures., *Anal. Chem.*, **36**:1627–1639

Scharf, C. A. 2010, Possible Constraints on Exoplanet Magnetic Field Strengths from Planet-star Interaction, *The Astrophysical Journal*, **722**:1547–1555

Schib, O., Mordasini, C., Wenger, N., Marleau, G. D., & Helled, R. 2020, The influence of infall on the properties of protoplanetary discs, *arXiv e-prints*, arXiv:2011.05996

Schmitt, J. H. M. M., & Liefke, C. 2004, NEXXUS: A comprehensive ROSAT survey of coronal X-ray emission among nearby solar-like stars, *Astronomy and Astrophysics*, **417**:651–665

Schneider, J., Dedieu, C., Le Sidaner, P., Savalle, R., & Zolotukhin, I. 2011, Defining and cataloging exoplanets: the exoplanet.eu database, *Astronomy and Astrophysics*, **532**:A79

Scott, D. W. 1992, Multivariate Density Estimation

Seager, S., & Mallén-Ornelas, G. 2003a, A Unique Solution of Planet and Star Parameters from an Extrasolar Planet Transit Light Curve, *The Astrophysical Journal*, **585**:1038–1055

Seager, S., & Mallén-Ornelas, G. 2003b, A Unique Solution of Planet and Star Parameters from an Extrasolar Planet Transit Light Curve, *The Astrophysical Journal*, **585**:1038–1055

Shakura, N. I., & Sunyaev, R. A. 1973, Black holes in binary systems. Observational appearance., *Astronomy and Astrophysics*, **500**:33–51

Shu, F., Najita, J., Ostriker, E., et al. 1994, Magnetocentrifugally Driven Flows from Young Stars and Disks. I. A Generalized Model, *The Astrophysical Journal*, **429**:781

Shu, F. H., Adams, F. C., & Lizano, S. 1987, Star Formation in Molecular Clouds: Observation and Theory, *Annual Review of Astronomy and Astrophysics*, **25**:23–81

Skrutskie, M. F., Dutkevitch, D., Strom, S. E., et al. 1990, A Sensitive 10-Micron Search for Emission Arising from Circumstellar Dust Associated with Solar-Type Pre-Main-Sequence Stars, *Astronomical Journal*, **99**:1187

Skrutskie, M. F., Cutri, R. M., Stiening, R., et al. 2006, The Two Micron All Sky Survey (2MASS), *Astronomical Journal*, **131**:1163–1183

Skumanich, A. 1972, Time Scales for CA II Emission Decay, Rotational Braking, and Lithium Depletion, *The Astrophysical Journal*, **171**:565

Sotiriadis, S., Libert, A.-S., Bitsch, B., & Crida, A. 2017, Highly inclined and eccentric massive planets. II. Planet-planet interactions during the disc phase, *Astronomy and Astrophysics*, **598**:A70

Sousa, S. G., Santos, N. C., Israelian, G., Mayor, M., & Udry, S. 2011, Spectroscopic stellar parameters for 582 FGK stars in the HARPS volume-limited sample. Revising the metallicity-planet correlation, *Astronomy and Astrophysics*, **533**:A141

Sousa, S. G., Santos, N. C., Mayor, M., et al. 2008, Spectroscopic parameters for 451 stars in the HARPS GTO planet search program. Stellar [Fe/H] and the frequency of exo-Neptunes, *Astronomy and Astrophysics*, **487**:373–381

Spiegel, D. S., & Burrows, A. 2012, Spectral and Photometric Diagnostics of Giant Planet Formation Scenarios, *The Astrophysical Journal*, **745**:174

Spiegel, E. A., & Zahn, J. P. 1992, The solar tachocline., *Astronomy and Astrophysics*, **265**:106–114

Stahler, S. W., & Palla, F. 2004, The Formation of Stars

Stamatellos, D., & Whitworth, A. P. 2009, The properties of brown dwarfs and low-mass hydrogen-burning stars formed by disc fragmentation, *Monthly Notices of the Royal Astronomical Society*, **392**:413–427

Stoll, M. H. R., & Kley, W. 2014, Vertical shear instability in accretion disc models with radiation transport, *Astronomy and Astrophysics*, **572**:A77

Strom, K. M., Strom, S. E., Edwards, S., Cabrit, S., & Skrutskie, M. F. 1989, Circumstellar Material Associated with Solar-Type Pre-Main-Sequence Stars: A Possible Constraint on the Timescale for Planet Building, *Astronomical Journal*, **97**:1451

Suzuki, T. K., Ogihara, M., Morbidelli, A., Crida, A., & Guillot, T. 2016, Evolution of protoplanetary discs with magnetically driven disc winds, *Astronomy and Astrophysics*, **596**:A74

Taylor, M. B. 2005, TOPCAT & STIL: Starlink Table/VOTable Processing Software, in *Astronomical Society of the Pacific Conference Series, Vol. 347, Astronomical Data Analysis Software and Systems XIV, ed. P. Shopbell, M. Britton, & R. Ebert*, p. 29

Teague, R., Guilloteau, S., Semenov, D., et al. 2016, Measuring turbulence in TW Hydrae with ALMA: methods and limitations, *Astronomy and Astrophysics*, **592**:A49

Telleschi, A., Güdel, M., Briggs, K. R., Audard, M., & Palla, F. 2007, X-ray emission from T Tauri stars and the role of accretion: inferences from the XMM-Newton extended survey of the Taurus molecular cloud, *Astronomy and Astrophysics*, **468**:425–442

Terebey, S., Shu, F. H., & Cassen, P. 1984, The collapse of the cores of slowly rotating isothermal clouds, *The Astrophysical Journal*, **286**:529–551

Terquem, C. E. J. M. L. J. 2008, New Composite Models of Partially Ionized Protoplanetary Disks, *The Astrophysical Journal*, **689**:532–538

Thommes, E. W., Matsumura, S., & Rasio, F. A. 2008, Gas Disks to Gas Giants: Simulating the Birth of Planetary Systems, *Science*, **321**:814

Toomre, A. 1964, On the gravitational stability of a disk of stars., *The Astrophysical Journal*, **139**:1217–1238

Tout, C. A., Livio, M., & Bonnell, I. A. 1999, The ages of pre-main-sequence stars, *Monthly Notices of the Royal Astronomical Society*, **310**:360–376

Trilling, D. E., Benz, W., Guillot, T., et al. 1998, Orbital Evolution and Migration of Giant Planets: Modeling Extrasolar Planets, *The Astrophysical Journal*, **500**:428–439

Tu, L., Johnstone, C. P., Güdel, M., & Lammer, H. 2015, The extreme ultraviolet and X-ray Sun in Time: High-energy evolutionary tracks of a solar-like star, *Astronomy and Astrophysics*, **577**:L3

Turner, N. J., & Drake, J. F. 2009, Energetic Protons, Radionuclides, and Magnetic Activity in Protostellar Disks, *The Astrophysical Journal*, **703**:2152–2159

Tychoniec, Ł., Tobin, J. J., Karska, A., et al. 2018, The VLA Nascent Disk and Multiplicity Survey of Perseus Protostars (VANDAM). IV. Free-Free Emission from Protostars: Links to Infrared Properties, Outflow Tracers, and Protostellar Disk Masses, *Astrophysical Journal Supplement Series*, **238**:19

Tychoniec, Ł., Manara, C. F., Rosotti, G. P., et al. 2020, Dust masses of young disks: constraining the initial solid reservoir for planet formation, *Astronomy and Astrophysics*, **640**:A19

Udry, S., & Santos, N. C. 2007, Statistical Properties of Exoplanets, *Annual Review of Astronomy and Astrophysics*, **45**:397–439

Ulrich, R. K. 1970, The Five-Minute Oscillations on the Solar Surface, *The Astrophysical Journal*, **162**:993

Vaiana, G. S., Cassinelli, J. P., Fabbiano, G., et al. 1981, Results from an extensive Einstein stellar survey, *The Astrophysical Journal*, **245**:163–182

van Boekel, R., Henning, T., Menu, J., et al. 2017, Three Radial Gaps in the Disk of TW Hydrae Imaged with SPHERE, *The Astrophysical Journal*, **837**:132

van der Marel, N., Verhaar, B. W., van Terwisga, S., et al. 2016, The (w)hole survey: An unbiased sample study of transition disk candidates based on Spitzer catalogs, *Astronomy and Astrophysics*, **592**:A126

van der Marel, N., Williams, J. P., Ansdell, M., et al. 2018, New Insights into the Nature of Transition Disks from a Complete Disk Survey of the Lupus Star-forming Region, *The Astrophysical Journal*, **854**:177

Van Der Walt, S., Colbert, S. C., & Varoquaux, G. 2011, The NumPy array: a structure for efficient numerical computation, *ArXiv e-prints*, arXiv:1102.1523

Veras, D., & Armitage, P. J. 2004, Outward migration of extrasolar planets to large orbital radii, *Monthly Notices of the Royal Astronomical Society*, **347**:613–624

Veronesi, B., Ragusa, E., Lodato, G., et al. 2020, Is the gap in the DS Tau disc hiding a planet?, *Monthly Notices of the Royal Astronomical Society*, **495**:1913–1926

Vicente, S. M., & Alves, J. 2005, Size distribution of circumstellar disks in the Trapezium cluster, *Astronomy and Astrophysics*, **441**:195–205

Vilhu, O. 1984, The nature of magnetic activity in lower main sequence stars., *Astronomy and Astrophysics*, **133**:117–126

Virtanen, P., Gommers, R., Oliphant, T. E., et al. 2020, SciPy 1.0: fundamental algorithms for scientific computing in Python, *Nature Methods*, **17**:261–272

Voges, W., Aschenbach, B., Boller, T., et al. 1999, The ROSAT all-sky survey bright source catalogue, *Astronomy and Astrophysics*, **349**:389–405

Voges, W., Aschenbach, B., Boller, T., et al. 2000, ROSAT all-sky survey faint source catalogue., *IAU Cirulars*, **7432**

Walsh, C., Daley, C., Facchini, S., & Juhász, A. 2017, CO emission tracing a warp or radial flow within $\lesssim$100 au in the HD 100546 protoplanetary disk, *Astronomy and Astrophysics*, **607**:A114

Wang, J., Fischer, D. A., Horch, E. P., & Huang, X. 2015, On the Occurrence Rate of Hot Jupiters in Different Stellar Environments, *The Astrophysical Journal*, **799**:229

Wang, J., Feigelson, E. D., Townsley, L. K., et al. 2011, A Chandra ACIS Study of the Young Star Cluster Trumpler 15 in Carina and Correlation with Near-infrared Sources, *Astrophysical Journal Supplement Series*, **194**:11

Wang, L., Bai, X.-N., & Goodman, J. 2019, Global Simulations of Protoplanetary Disk Outflows with Coupled Non-ideal Magnetohydrodynamics and Consistent Thermochemistry, *The Astrophysical Journal*, **874**:90

Wang, L., & Goodman, J. 2017, Hydrodynamic Photoevaporation of Protoplanetary Disks with Consistent Thermochemistry, *The Astrophysical Journal*, **847**:11

Ward, W. R. 1997, Protoplanet Migration by Nebula Tides, *Icarus*, **126**:261–281

Weber, E. J., & Davis, Leverett, J. 1967, The Angular Momentum of the Solar Wind, *The Astrophysical Journal*, **148**:217–227

Weber, M. L., Ercolano, B., Picogna, G., Hartmann, L., & Rodenkirch, P. J. 2020, The interpretation of protoplanetary disc wind diagnostic lines from X-ray photoevaporation and analytical MHD models, *Monthly Notices of the Royal Astronomical Society*, **496**:223–244

Weidenschilling, S. J. 1977, The Distribution of Mass in the Planetary System and Solar Nebula, *Astrophysics and Space Science*, **51**:153–158

Weinberger, A. J., Anglada-Escudé, G., & Boss, A. P. 2013, Distance and Kinematics of the TW Hydrae Association from Parallaxes, *The Astrophysical Journal*, **762**:118

Weingartner, J. C., & Draine, B. T. 2001, Dust Grain-Size Distributions and Extinction in the Milky Way, Large Magellanic Cloud, and Small Magellanic Cloud, *The Astrophysical Journal*, **548**:296–309

Wenger, M., Ochsenbein, F., Egret, D., et al. 2000, The SIMBAD astronomical database. The CDS reference database for astronomical objects, *Astronomy and Astrophysics, Supplement*, **143**:9–22

West, A. A., Hawley, S. L., Bochanski, J. J., et al. 2008, Constraining the Age-Activity Relation for Cool Stars: The Sloan Digital Sky Survey Data Release 5 Low-Mass Star Spectroscopic Sample, *Astronomical Journal*, **135**:785–795

White, R. J., & Basri, G. 2003, Very Low Mass Stars and Brown Dwarfs in Taurus-Auriga, *The Astrophysical Journal*, **582**:1109–1122

Williams, D. R. N. 2019, Planetary Fact Sheet, [online; accessed 18 June 2021]

Williams, J. P. 2012, Astronomical evidence for the rapid growth of millimeter-sized particles in protoplanetary disks, *Meteoritics and Planetary Science*, **47**:1915–1921

Williams, J. P., & Cieza, L. A. 2011, Protoplanetary Disks and Their Evolution, *Annual Review of Astronomy and Astrophysics*, **49**:67–117

Wilson, O. C. 1966, Stellar Convection Zones, Chromospheres, and Rotation, *The Astrophysical Journal*, **144**:695

Winn, J. N. 2010, Transits and Occultations, *arXiv e-prints*, arXiv:1001.2010

Winn, J. N., & Fabrycky, D. C. 2015, The Occurrence and Architecture of Exoplanetary Systems, *Annual Review of Astronomy and Astrophysics*, **53**:409–447

Winter, A. J., Clarke, C. J., Rosotti, G., et al. 2018, Protoplanetary disc truncation mechanisms in stellar clusters: comparing external photoevaporation and tidal encounters, *Monthly Notices of the Royal Astronomical Society*, **478**:2700–2722

Winter, A. J., Kruijssen, J. M. D., Chevance, M., Keller, B. W., & Longmore, S. N. 2020, Prevalent externally driven protoplanetary disc dispersal as a function of the galactic environment, *Monthly Notices of the Royal Astronomical Society*, **491**:903–922

Wise, A. W., & Dodson-Robinson, S. E. 2018, Photoevaporation Does Not Create a Pileup of Giant Planets at 1 au, *The Astrophysical Journal*, **855**:145

Wittenmyer, R. A., Wang, S., Horner, J., et al. 2020, Cool Jupiters greatly outnumber their toasty siblings: occurrence rates from the Anglo-Australian Planet Search, *Monthly Notices of the Royal Astronomical Society*, **492**:377–383

Wölfer, L., Picogna, G., Ercolano, B., & van Dishoeck, E. F. 2019, Radiation-hydrodynamical models of X-ray photoevaporation in carbon-depleted circumstellar discs, *Monthly Notices of the Royal Astronomical Society*, **490**:5596–5614

Wolk, S. J., & Walter, F. M. 1996, A Search for Protoplanetary Disks Around Naked T Tauri Stars, *Astronomical Journal*, **111**:2066

Wright, J. T. 2018, Radial Velocities as an Exoplanet Discovery Method, in *Handbook of Exoplanets*

Wright, J. T., Upadhyay, S., Marcy, G. W., et al. 2009, Ten New and Updated Multiplanet Systems and a Survey of Exoplanetary Systems, *The Astrophysical Journal*, **693**:1084–1099

Wright, N. J., & Drake, J. J. 2009, The Massive Star-Forming Region Cygnus OB2. I. Chandra Catalog of Association Members, *Astrophysical Journal Supplement Series*, **184**:84–99

Wright, N. J., & Drake, J. J. 2016, Solar-type dynamo behaviour in fully convective stars without a tachocline, *Nature*, **535**:526–528

Wright, N. J., Drake, J. J., & Civano, F. 2010, Stellar X-ray Sources in the Chandra COSMOS Survey, *The Astrophysical Journal*, **725**:480–491

Wright, N. J., Drake, J. J., Mamajek, E. E., & Henry, G. W. 2011, The Stellar-activity-Rotation Relationship and the Evolution of Stellar Dynamos, *The Astrophysical Journal*, **743**:48

Wright, N. J., Newton, E. R., Williams, P. K. G., Drake, J. J., & Yadav, R. K. 2018, The stellar rotation-activity relationship in fully convective M dwarfs, *Monthly Notices of the Royal Astronomical Society*, **479**:2351–2360

Wyatt, M. C. 2008, Evolution of debris disks., *Annual Review of Astronomy and Astrophysics*, **46**:339–383

Yee, J. C., & Gaudi, B. S. 2008, Characterizing Long-Period Transiting Planets Observed by Kepler, *The Astrophysical Journal*, **688**:616–627

Yorke, H. W., Bodenheimer, P., & Laughlin, G. 1993, The Formation of Protostellar Disks. I. 1 M sub sun, *The Astrophysical Journal*, **411**:274

Youdin, A. N., & Goodman, J. 2005, Streaming Instabilities in Protoplanetary Disks, *The Astrophysical Journal*, **620**:459–469

Yu, L., Donati, J.-F., Hébrard, E. M., et al. 2017, A hot Jupiter around the very active weak-line T Tauri star TAP 26, *Monthly Notices of the Royal Astronomical Society*, **467**:1342–1359

Zhang, K., Blake, G. A., & Bergin, E. A. 2015, Evidence of Fast Pebble Growth Near Condensation Fronts in the HL Tau Protoplanetary Disk, *The Astrophysical Journal Letters*, **806**:L7

Zhang, S., Zhu, Z., Huang, J., et al. 2018, The Disk Substructures at High Angular Resolution Project (DSHARP). VII. The Planet-Disk Interactions Interpretation, *The Astrophysical Journal Letters*, **869**:L47

Danksagung

There are so many people I want to thank.
Barbara for being an incredibly supportive supervisor who has always believed in me.
Giovanni for his impressive patience and always being there to help and support me.
Of course all other members of Barbara's and Til's groups for the great conversations and experiences we've shared.
Ulli, Joseph, Ludwig, Apo and Stefan for being amazing Among Us (and of course office/USM) mates.
Sebastian for your dumb humour that always makes me cringe, and of course the fact that I could rant with you about literally everything.
Joanna for being a great role model, especially for women in science and allowing me to join you and Wini for the road trip through Queensland.
Romy for making it through Uni-time with me from the very beginning, always being my partner for exercise sheets and all the great conversations we had.
My parents for always supporting my decisions and allowing me to follow my own path. My brother Georg for being the best big brother, whom I can always count on. My brother Aljoscha for being the one who initially sparked my interest in Astronomy when I was a child. My sister Katharina for teaching me compassion.
And of course Markus for being my soulmate who understood me, my struggles and my past from the very moment he met me. You're my rock.